JUSTUS-LIEBIG-
UNIVERSITÄT
GIESSEN

Quark Mass and Volume Dependence of the QCD Phase Diagram with DSEs

Quarkmassen- und Volumenabhängigkeit des QCD-Phasendiagramms mit DSEs

Dissertation

zur Erlangung des akademischen Grades eines
Doktors der Naturwissenschaften (Dr. rer. nat.)

Julian Bernhardt

September 2023

Institut für Theoretische Physik
Fachbereich 07:
Mathematik und Informatik, Physik, Geographie
Justus-Liebig-Universität Gießen

Gutachter

Erstgutachten und Betreuung:

Prof. Dr. Christian S. Fischer
Institut für Theoretische Physik
Justus-Liebig-Universität Gießen

Zweitgutachten:

Prof. Dr. Owe Philipsen
Institut für Theoretische Physik
Goethe-Universität Frankfurt

"The way we have to describe Nature is generally incomprehensible to us."

Richard P. Feynman

(in '*QED: The Strange Theory of Light and Matter*')

Abstract

In this work, which is divided into three distinct analyses, we investigate the quark mass and volume dependence of the phase diagram of quantum chromodynamics. To this end, we employ two very similar sets of truncated Dyson–Schwinger equations in Landau gauge for $2+1$ quark flavours in a combination with lattice Yang–Mills theory that have been studied extensively in the past. This system predicts a critical endpoint in the phase diagram at moderate temperature and large chemical potential.

In the first analysis, we study the impact of a finite volume on the location of this critical endpoint. We investigate our system of Dyson–Schwinger equations at small and intermediate volumes and determine the dependence of the location of the critical endpoint on the boundary conditions and the volume of a three-dimensional cube with edge length L. We demonstrate that noticeable volume effects of more than five per cent occur only for $L \lesssim 5\,\mathrm{fm}$ and that volumes as large as $L^3 \gtrsim (8\,\mathrm{fm})^3$ are very close to the infinite-volume limit. Additionally, we present results for the volume dependence of baryon-number fluctuations and ratios thereof up to fourth order in the vicinity of the critical endpoint. Due to the limitations of our truncation, the results are quantitatively meaningful only outside the critical scaling region of the endpoint. We find that the fluctuations are visibly affected by the finite volume, particularly for antiperiodic boundary conditions, whereas their ratios are practically invariant.

In the second analysis, we examine the quality of the extrapolation procedure employed in Ref. [1] to extract the crossover line at real chemical potential from lattice data at imaginary potential. We determine the up/down-quark condensate and chiral susceptibility at imaginary chemical potentials and perform an analytic continuation along the lines described in Ref. [1]. We find that the analytically continued crossover line agrees very well (within one per cent) with the explicitly calculated one for chemical potentials up to about 80 % of the value of the critical endpoint. The method breaks down in the region where the chiral susceptibility as a function of the condensate can no longer be well described by a polynomial.

In the final analysis, we investigate the order of the chiral transition of quantum chromodynamics in the limit of vanishing bare up/down-quark masses for variations of the bare strange-quark mass, $0 \leq m_\mathrm{s} \leq \infty$. In this limit and due to universality, long-range correlations with the quantum numbers of pseudoscalar and scalar mesons may dominate the physics. In order to study the interplay between the microscopic quark and gluon degrees of freedom and these long-range correlations, we extend our set of Dyson–Schwinger equations with a meson-backcoupling approach. The latter has already been studied in the past but this is the first work in a full $(2+1)$-flavour setup. Starting from the physical point, we determine the chiral susceptibilities for decreasing up/down-quark masses and find good agreement with both lattice and functional-renormalization-group results. We then proceed to determine the order of the chiral transition along the left-hand side of the Columbia plot for chemical potentials in the range $-(30\,\mathrm{MeV})^2 \leq \mu_\mathrm{B}^2 \leq (30\,\mathrm{MeV})^2$. We find a second-order phase transition throughout and no trace of a first-order region in the $N_f = 3$ corner of the Columbia plot. This result remains unchanged when an additional Goldstone boson due to a restored axial $\mathrm{U}_A(1)$ symmetry is taken into account.

Kurzreferat

In dieser Arbeit, die in drei getrennte Analysen aufgeteilt ist, untersuchen wir die Quarkmassen- und Volumenabhängigkeit des Phasendiagramms der Quantenchromodynamik. Hierfür verwenden wir zwei sehr ähnlichen Sätze von trunkierten Dyson–Schwinger-Gleichungen in Landau-Eichung für $2+1$ Quark-Flavours in einer Kombination mit Gitter-Yang–Mills-Theorie, die bereits in der Vergangenheit ausgiebig untersucht worden sind. Dieses System sagt einen kritischen Endpunkt im Phasendiagramm bei hohen Temperaturen und moderaten chemischen Potentialen voraus.

In der ersten Analyse erforschen wir den Einfluss eines endlichen Volumens auf die Position dieses kritischen Endpunktes. Wir untersuchen unser System von Dyson–Schwinger-Gleichungen bei kleinen und intermediären Volumina und bestimmen die Abhängigkeit der Position des kritischen Endpunktes von den Randbedingungen und vom Volumen eines dreidimensionalen Würfels mit Kantenlänge L. Wir demonstrieren, dass sichtbare Volumeneffekte von mehr als fünf Prozent nur für $L \lesssim 5\,\mathrm{fm}$ auftreten und dass Volumina größer als $L^3 \gtrsim (8\,\mathrm{fm})^3$ sehr nahe am Grenzwert eines unendlichen Volumens sind. Darüber hinaus präsentieren wir Ergebnisse für die Volumenabhängigkeit von Baryonenzahlfluktuationen und Verhältnisse dieser bis zur vierten Ordnung in der Nähe des kritischen Endpunktes. Durch Limitierungen in unserer Trunkierung sind die Ergebnisse nur außerhalb der kritischen Skalierungsregion des Endpunktes aussagekräftig. Wir stellen fest, dass die Fluktuationen sichtbar durch das endliche Volumen beeinflusst werden, deren Verhältnisse jedoch praktisch invariant sind.

In der zweiten Analyse untersuchen wir die Qualität des Extrapolationsverfahrens, das in Ref. [1] verwendet wurde, um die Crossover-Linie bei reellen chemischen Potentialen aus Gitter-Daten bei imaginären chemischen Potentialen zu extrahieren. Wir bestimmen das Up/Down-Quarkkondensat und die chirale Suszeptibilität bei imaginären chemischen Potentialen und führen eine Analyse nach dem Vorbild der Beschreibungen in Ref. [1] durch. Wir stellen fest, dass die analytisch fortgesetzte Crossover-Linie sehr gut (innerhalb eines Prozents) mit der explizit berechneten bei reellen chemischen Potentialen bis hin zu 80 % des Wertes des kritischen Endpunktes übereinstimmt. Die Methode bricht in jener Region zusammen, in der die chirale Suszeptibilität als Funktion des Kondensates nicht mehr gut als Polynom beschrieben werden kann.

In der letzten Analyse erforschen wir die Ordnung des chiralen Übergangs der Quantenchromodynamik im Grenzwert verschwindender Up/Down-Stromquarkmassen für Variationen der Strange-Stromquarkmasse, $0 \leq m_\mathrm{s} \leq \infty$. In diesem Grenzwert und aufgrund von Universalität könnten langreichweitige Korrelationen mit den Quantenzahlen von pseudoskalaren und skalaren Mesonen die Physik dominieren. Um das Zusammenspiel zwischen mikroskopischen Quark- und Gluon-Freiheitsgraden und diesen langreichweitigen Korrelationen zu studieren, erweitern wir unser System von Dyson–Schwinger-Gleichungen um einen Mesonen-Rückkopplungsansatz. Jener wurde bereits in der Vergangenheit untersucht, aber dies ist die erste Arbeit in einem vollen $(2+1)$-Flavour-Zugang. Beginnend am physikalischen Punkt bestimmen wir die Ordnung des chiralen Überganges entlang der linken Seite des Columbia-Plots für chemische Potentiale im Bereich $-(30\,\mathrm{MeV})^2 \leq \mu_\mathrm{B}^2 \leq (30\,\mathrm{MeV})^2$. Wir finden durchweg einen Phasenübergang zweiter Ordnung und keine Spur einer Region erster Ordnung in der $N_f = 3$-Ecke des Columbia-Plots. Dieses Resultat bleibt unverändert, wenn ein zusätzliches masseloses Goldstone-Boson durch eine wiederhergestellte axiale $\mathrm{U}_A(1)$-Symmetrie in Betracht gezogen wird.

List of Frequently-Used Abbreviations and Acronyms

Throughout this thesis, all abbreviations are defined when they are first introduced or, occasionally, when they are reintroduced after some time. For a quick overview, we collect a list of often-used ones below.

ABC	antiperiodic boundary conditions
BSA	Bethe–Salpeter amplitude
BSE	Bethe–Salpeter equation
CEP	critical endpoint
DCSB	dynamical chiral symmetry breaking
DSE	Dyson–Schwinger equation
FRG	functional renormalization group
IR	infrared
NJL	Nambu–Jona-Lasinio
***n*PI**	n-particle irreducible
O(*n*)	orthogonal group of degree n
PBC	periodic boundary conditions
PBC*	periodic boundary conditions without zero mode
QCD	quantum chromodynamics
QED	quantum electrodynamics
QFT	quantum field theory
QM	quark–meson
SU(*n*)	special unitary group of degree n
U(*n*)	unitary group of degree n
UV	ultraviolet
Z(*n*)	centre of $\mathrm{SU}(n)$

Contents

Chapter 1
Introduction

As of today, we are able to trace back an overwhelming part of the observed phenomena in physics to the four fundamental interactions: the *electromagnetic interaction*, the *weak interaction*, the *strong interaction* and *gravitation*. Apart (infamously) from the latter, we can successfully describe these interactions in the framework of *quantum field theory* (QFT), which combines classical field theory, quantum mechanics and special relativity. Specifically, it describes both matter and interactions uniformly in terms of particles as excitations of ubiquitous quantum fields. That is to say, matter is composed of *fermions* and the interaction between them is mediated by the exchange of force-carrying *bosons*. The distinction is that fermions have half-integer spin whereas bosons possess integer spin.

One of the first applications of this approach was the description of the electromagnetic interaction resulting in *quantum electrodynamics* (QED). This theory was conceived first and foremost by Shin'ichirō Tomonaga, Julian Schwinger and Richard Feynman [2–5], who were jointly awarded the 1965 Nobel Prize in Physics for it. QED describes the interaction of electrically charged particles via the exchange of photons and has been particularly successful. For instance, theoretical QED calculations of the anomalous magnetic moment of the electron coincide with experimental findings up to a relative error of around 10^{-12} [6]. This renders QED – and thus also QFT – one of the most accurate physical theories so far.

Furthermore, QFT gave rise to a theory of the weak interaction proposed by Sheldon Glashow, Steven Weinberg and Abdus Salam [7–9]. The force-carrying bosons between weakly interacting particles are the massive W and Z bosons. The former are also electrically charged and allow for *flavour change*, i.e., the transformation of one quark or lepton species into another. As an intriguing argument for and important result of QFT, the Glashow–Weinberg–Salam theory not only describes the weak interaction but also illuminates its connection with the electromagnetic interaction and that both can be understood as parts of a unified *electroweak interaction*. Additionally, an inherent feature of the Glashow–Weinberg–Salam theory is the *Higgs mechanism* (named after Peter Higgs) [10–12]. It explains the occurrence of the nonzero masses of most elementary particles – namely, of leptons, quarks and the W and Z bosons themselves – due to the existence of and their interaction with a spin-zero field, the *Higgs field*. Its excitation, the *Higgs boson*, was famously verified experimentally at CERN in 2012 [13].

Quantum Chromodynamics

In this thesis, we are exclusively concentrating on the strong interaction whose underlying QFT is *quantum chromodynamics* (QCD). It has its roots in the *quark model* developed by Murray Gell-Mann and George Zweig in the 1960s to classify the plethora of discovered hadrons, i.e., mesons and baryons [14–16]. These are described as composite particles of *quarks* as their elementary constituents. The bosonic mesons can be interpreted as quark–antiquark

bound states while the fermionic baryons are understood as bound states of three quarks.[1] In order to explain all observed properties of hadrons, quarks have to be spin-1/2 fermions with fractional electric charge. As of now, six types of quarks – conventionally called *flavours* – have been found: up (u), down (d), strange (s), charm (c), bottom (b) and top (t) [17–19]. To account for the integer-valued electric charges of hadrons, quarks need to carry a charge of $+2/3$ for the *up-like* quarks (u, c, t) and $-1/3$ for the *down-like* quarks (d, s, b). This way, for instance, the proton is thought of as a uud-bound state.

In spite of being quite successful in classifying existing and predicting new hadrons, the quark model has two major shortcomings. First, it fails to describe the Δ^{++} baryon, a spin-3/2 excitation of the nucleon with electric charge +2, without violating the *Pauli exclusion principle*. Namely, the many-body wavefunction of two fermions in a quantum mechanical system has to be totally antisymmetric, i.e., these cannot be identical in all quantum numbers. Nonetheless, the Δ^{++} baryon is composed of three up quarks with aligned spins in the quark-model picture, so it is symmetric in both spin and flavour. Second, it does not explain the fact that, to this day, no free particle with fractional electric charge has ever been measured [19].

To bypass the first problem, MOO-YOUNG HAN, YOICHIRO NAMBU and OSCAR GREENBERG proposed an additional degree of freedom which can assume three different values [20, 21]. In the simplest approach, that is to say, quarks transform under the (3) representation of an internal SU(3) symmetry and antiquarks under the corresponding $(\overline{3})$ representation. This way, one may compose singlet states with either a quark and an antiquark or three (anti)quarks, i.e., the observed hadrons. Due to a loose analogy of this mechanism with the addition of the three primary colours, this SU(3) quantum number is called *colour charge* and its possible values are correspondingly labelled *red*, *green* and *blue*, hence also the name *chromo*dynamics. Colour-singlet states are consequently also known as *colourless* or *white*.

As a result, the problem that no free quarks have ever been measured can be rephrased to the fact that only colourless states exist as free particles, a phenomenon known as (colour) *confinement*. While there is, as of today, no rigorous mathematical proof from first principles, there are unambiguous QCD calculations that confirm its existence [22]. Additionally, scaling violations hinted at in deep-inelastic scattering experiments suggested *asymptotic freedom*, i.e., the interaction strength between quarks is very large at a long range but decreases significantly for small distances – or equivalently at high energies [23]. It was discovered in 1973 by DAVID GROSS, DAVID POLITZER and FRANK WILCZEK that non-Abelian Yang–Mills theories [24] exhibit this property [25, 26]. Together, this was developed into QCD – the QFT of the strong interaction based on the SU(3) colour gauge group – by HARALD FRITZSCH and HEINRICH LEUTWYLER together with Gell-Mann [27].

Thus, following a similar approach as for QED and replacing the single electrical charge with three colour charges, one ends up with a (superficially) similar-looking theory: Akin to photons, the strong interaction between quarks is mediated by particles called *gluons*, which there are now eight types of rather than one. The key difference, however, is that in contrast to photons, gluons also interact with one another since they carry (colour) charge themselves.

The intricate mathematical structure caused by this self-interaction of the gluons leads

[1] This is the definition of *classical* mesons and baryons. Nowadays, mesons are defined more generally as hadrons with baryon number zero, which also includes *glueballs*, *hybrid mesons* and four-quark states such as, e.g., *tetraquarks*. Likewise, the term "baryon" is now also assigned to all hadrons with nonzero baryon number like, for example, *pentaquarks*.

to arguably very interesting phenomenological implications. Apart from confinement and asymptotic freedom, QCD notably exhibits a third key feature: *dynamical chiral symmetry breaking* (DCSB) which is the major topic of research in this thesis. A tangible consequence of this phenomenon is the dynamical generation of a rather large mass due to the strong interaction. A very prominent example is the fact that baryons – comprising three valence quarks – are much heavier than the sum of the (current-)quark masses generated by the Higgs mechanism. Instead, the quarks acquire a much larger, dynamically generated *constituent-quark mass* being rooted in the strong interaction and making up a huge portion of the nucleon mass and thus of the mass in everyday life. This is also where the name 'chiral symmetry breaking' comes from since *chiral symmetry* is strictly conserved only for massless particles.

In total, also due to many experimental tests [28, 29], QCD is nowadays accepted as the underlying QFT of the strong interaction. We will discuss the mathematical background and properties of QCD in much more detail in Chapter 2.

Non-Perturbative Approaches to QFT

The arguably most practical approach to QFT calculations is the *path-integral* formulation proposed by Feynman [4, 30].[2] Specifically, one can – in principle – obtain all information about a theory from the *generating functional* $\mathcal{Z}$, which serves a similar role in QFT as the partition function in statistical mechanics (see Appendix B.2). In a very simplified notation, the path-integral representation of the generating functional in Euclidean spacetime reads

$$\mathcal{Z}[J] = \int \mathcal{D}\varphi \ \exp\big(-\mathcal{S}[\varphi] + \langle \varphi, J \rangle\big)\,, \tag{1.1}$$

where $\mathcal{S}$ indicates the action of the considered QFT, φ labels a collection of all involved quantum fields, J denotes their respective auxiliary source fields and $\mathcal{D}\varphi$ represents the measure for the infinitely dimensional integration "over all field configurations". For free theories, the path integral can actually be evaluated analytically since it corresponds to a generalized Gaussian integral. However, this looks unpromising if interactions are taken into account.

To this end, a commonly used strategy to describe interactions is to treat them as a perturbation of the free theory. That is, one systematically expands the interaction part of the exponential in Equation (1.1) in powers of the coupling constant g. Interpreting the resulting expressions as graphs, one obtains the rather illustrative description of QFTs in terms of *Feynman diagrams*. For QED, for instance, this approach has been particularly successful since the previously quoted result for the anomalous magnetic moment of the electron was obtained perturbatively. For more background information on path integrals and perturbation theory, see standard textbooks in, e.g., Refs. [33–38]. Perturbation theory, however, ceases to work if the coupling constant is not small, as is the case for QCD at low energies. Consequently, one needs *non-perturbative methods* for the description of strongly coupled QFTs.

[2] Feynman's approach was inspired by a paper by Paul Dirac on the Lagrangian and the action principle in quantum mechanics from 1933 [31]. The earliest notion of a path integral, however, was introduced by Norbert Wiener in the 1920s for the description of Brownian motion. The *Wiener integral* still serves as a basis for the mathematical description of path integrals [32].

One of these is *lattice field theory*, an ab-initio approach to compute the path integral directly in a discretized and finite spacetime. This way, Equation (1.1) reduces to an ordinary – albeit highly dimensional – integral that can be solved numerically. Since the exponential may be interpreted as a probability measure, this is commonly done using Monte Carlo integration. While undoubtedly very successful in areas where applicable,[3] this technique also has a number of drawbacks and especially the treatment of fermions entails difficulties that will be touched upon later. We will cover the basics of particularly *lattice QCD* in Section 2.4.

In contrast, *functional methods* are based on functional manipulations of the path integral in order to obtain equations for the *correlation functions* (also called *n-point functions* or *Green's functions*) of the respective QFTs, which are defined as the expectation values of products of field operators. Since the generating functional can also be expressed as an expansion of these correlation functions, knowing all correlation functions means solving the theory (see Appendix B.2). In addition, a lot of physical information is already encoded in the correlation functions themselves.

There are two frequently used frameworks of functional methods. On one side, *Dyson–Schwinger equations* (DSEs), derived by FREEMAN DYSON and JULIAN SCHWINGER [41, 42], are the quantum equations of motion for these correlation functions and form general relations between them. DSEs are the framework this thesis is centred around and we will discuss them extensively in Chapter 3. At the same time, the idea of the *functional renormalization group* (FRG) is to successively integrate out all quantum fluctuations, i.e., one starts the description at the momentum scale of a renormalization-group fixed point – where the properties are known – and solves a corresponding functional differential equation until the desired quantities are recovered. While no major topic of this work, we still refer to FRG results at several points, which is why we provide some brief background information in Appendix B.7.

In principle, functional methods are exact and circumvent certain shortcomings of lattice field theory. Unfortunately, they imply an infinite number of coupled equations. For practical calculations, this set of equations therefore has to be reduced to a finite number. This process – known as *truncation* – needs to be performed carefully in order not to distort the resulting physics, which is highly non-trivial and the introduced error is usually not quantifiable. Consequently, functional methods and lattice field theory have different up- and downsides and complement each other. Thus, it is beneficial to combine them and compare their results where possible to solidify the physical insights, which will be a recurring theme of this work.

Due to the intricate mathematical structure of QCD, one often resorts to models for exploratory investigations of its non-perturbative region. A prominent example is the *Nambu–Jona-Lasinio* (NJL) model [43, 44] or the closely related *quark–meson* (QM) model [45–47] (see also Appendix B.6.1 for more details). In the simplest approach, they are treated in a *mean-field approximation*, i.e., by neglecting all quantum fluctuations. For more sophisticated studies, these are often also addressed with the functional methods described above.

The Phase Diagram of QCD

In view of its phenomenological features, the phase diagram of QCD is quite an insightful field of research. Namely, the occurrence of its various phases depending on temperature T and

[3] For instance, meson spectra have been calculated to a very high precision in accordance with experiment, see, e.g. Refs. [39, 40] for reviews.

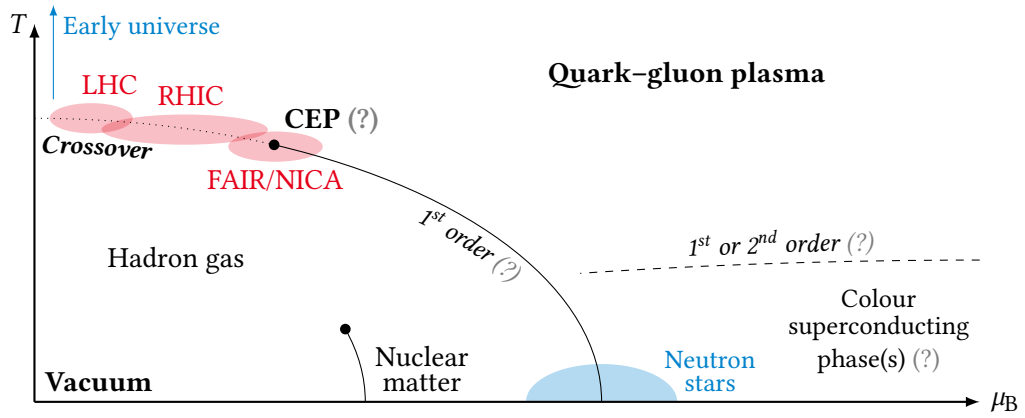

Figure 1.1.: Qualitative sketch of the contemporary view of the QCD phase diagram with respect to temperature T and baryon chemical potential μ_B adapted from Refs. [48–50]. Regions addressed in this thesis are printed in bold. Regions accessible by certain experiments are hinted at in red. Regions of macroscopic QCD matter are indicated in blue. See the main text below for more details.

baryon chemical potential μ_B is caused by an interplay of DCSB, confinement and asymptotic freedom at different energy levels. In advance, we recall that a specific phase diagram is often formulated in terms of a certain physical observable called *order parameter*. A phase transition with respect to some variable, e.g., temperature, is then defined via the behaviour of the order parameter. If it is discontinuous at some point, we speak of a *first-order phase transition*. If the order parameter is continuous but its derivative diverges, we have a *second-order phase transition*. If it stays differentiable arbitrarily often but there is still a transition between two distinct phases, we call this a *crossover*. As a consequence, different order parameters may not always exhibit the same phase transitions and can therefore lead to different phase diagrams in the crossover region. For the QCD phase diagram, there are two common choices: the *quark condensate* (see Sections 2.2.3 and 3.2) and the *Polyakov loop* (see Sections 2.4.2 and 5.1). The former quantifies the strength of DCSB whereas the latter is often employed as a measure for confinement.

In Figure 1.1, we show a qualitative sketch of the contemporary view of the QCD phase diagram that contains elements of both DCSB and confinement. In spite of having been an active field of research for quite some time [51], actually fairly little knowledge about the phase diagram is firmly established. In vacuum and in the region of low temperature and quark chemical potential, of course, QCD matter is confined to hadrons and chiral symmetry is dynamically broken. When moving from vacuum along the temperature axis, this matter undergoes a smooth crossover transition to a chirally symmetric and deconfined *quark–gluon plasma* (QGP) phase at a pseudocritical temperature around $T_c \approx 155\,\mathrm{MeV}$[4] (with a couple of MeV difference between different definitions of the chiral order parameter and the

[4]Recently, there have been discussions that this picture might actually not be correct. It has been argued that true deconfinement is achieved only at much higher temperatures about three times as large [52]. For temperatures between the chiral and deconfinement transitions, it is conjectured that there is a novel phase where chirally symmetric quarks are still bound to each other via colour flux-tubes.

pseudocritical temperature). This is the path the early universe is expected to have taken when cooling down around 10^{-20} s after the big bang [53, 54]. While the crossover is unambiguously confirmed by lattice QCD [55, 56], the existence of QGP is verified for very high energies where QCD can be described perturbatively due to asymptotic freedom [57, 58]. On the other hand, when increasing baryon chemical potential to around the mass of a nucleon, $\mu_B \approx m_N - 16\,\text{MeV}$ [59], we know that baryons coalesce in nuclei where they behave like Fermi liquids [60]. This first-order transition is thus known as the (nuclear) *liquid–gas* transition and is expected to persist for small temperatures to about $T \lesssim 16\,\text{MeV}$ where it then ends in a critical point [60].

The other regions of the phase diagram are still more or less speculative. From NJL [61] or QM [62, 63] model calculations, it is conjectured that the nuclear liquid at some critical μ_B undergoes another first-order phase transition where chiral symmetry is restored. Beyond this point, there are numerous potential scenarios how Cooper pairing between quarks can occur. This is seen as analogous to the one in electrical superconductors at almost absolute zero described by the Bardeen–Cooper–Schrieffer theory, so this is a region of potential *colour superconducting* phases.[5] Especially around the first-order transition, more interesting phenomena are speculated to arise. While cores of neutron stars are reasonably expected to be located in this region for small T [66], areas of inhomogeneous chiral symmetry breaking are hypothesized to exist there for higher temperatures [67] (these are not shown in Figure 1.1).

If this overall picture is true, the chiral first-order and crossover transitions meet in (at least) one *critical endpoint* (CEP). Both the CEP and the crossover transition are our main points of interest in this work, i.e., we are focussing on rather large temperatures and low/intermediate chemical potentials. For this reason, we restrict ourselves exclusively to this region in the following discussions about the current state of research.

On the theoretical side, lattice QCD is able to make reliable predictions at $\mu_B = 0$, such as the pseudocritical temperature and cumulants of the baryon-number distribution (see, e.g., Refs. [55, 56, 68, 69] and Ref. [70] for a review). Furthermore, thermodynamic properties of the hot matter in a broad temperature range around T_c have been determined with great accuracy [71–75]. Unfortunately, the treatment of fermions with a nonzero chemical potential leads to the notorious *sign problem* (see Ref. [76] for a review). Namely, the action in Equation (1.1) becomes complex and the exponential becomes oscillating rather than damping. As a consequence, many cancellations inside the Monte Carlo integration occur and it gets exponentially harder to calculate quantities with a reasonable error. There are numerous strategies to address this limitation, which will be discussed in Section 2.4.3 and Chapter 5 as well as further below. Most of these build on extrapolation schemes which indicate that no CEP is found in the region of the temperature–baryon-chemical-potential plane (T, μ_B) with $\mu_B/T < 2.5$, see, e.g., Refs. [1, 77] and references therein. Beyond this point, errors in lattice extrapolations accumulate rapidly and no definite statements can be made.

Functional approaches, on the other hand, do in principle allow for a mapping of the whole QCD phase diagram but – as stated earlier – inherently depend on approximations and truncations necessary to make the equations tractable. While the precise location of the CEP

[5] Under certain idealized assumptions, the existence of colour superconducting phases can be verified by perturbative QCD calculations. In the case of three-flavour QCD, there is the so-called *colour–flavour locked* phase, i.e., all quarks of a certain flavour have the same colour [64]. For two quark flavours, there is the *two-flavour superconducting* phase [65].

is up to now not unambiguously determined, elaborate functional calculations place it in the region $(\mu_B^{CEP}, T_{CEP}) = (495 \text{ to } 654, 108 \text{ to } 119)$ MeV, i.e., within a narrow temperature range with only moderate spread in chemical potential, which agrees with the lattice extrapolations. These results have been obtained with different techniques, either using DSEs [78–80], the FRG [81] or a combination of both [82, 83]. For recent reviews on the application of functional methods to the QCD phase diagram, see Ref. [84] for DSEs and Ref. [85] for the FRG.

The main experimental tool for the investigation of the QCD phase diagram are heavy-ion collisions. In particular, the quest of finding the CEP is one of the main goals of the experimental Beam Energy Scan program at the Relativistic Heavy-Ion Collider (RHIC) at Brookhaven National Laboratory [86] that probes a large baryon-chemical-potential area of the phase diagram not accessible at the Large Hadron Collider (LHC). Additionally, it is also one of the main motivations for the HADES and future Compressed Baryonic Matter experiments [87–89] at the Facility of Antiproton and Ion Research (FAIR) in Darmstadt and the Nuclotron-based Ion Collider fAcility (NICA) at the Joint Institute for Nuclear Research in Dubna. We roughly indicate the locations of these experiments with red areas in Figure 1.1. Extracting signals for such a CEP from the experimental data is quite delicate and much work is currently being invested to improve the rigorousness of theory–experiment connections (see, e.g., Refs. [90, 91] for reviews).

In the following, we want to briefly outline the chronology of such an experiment. A detailed description is beyond the scope of this work – and especially of this introduction – so we refer to, e.g., Refs. [53, 66, 92] and references therein. Heavy-ion collisions are performed by, as the name suggests, accelerating beams of ionized nuclei with a large number of baryons – such as gold, lead or uranium – to almost the speed of light and letting them collide. Due to the very high energies, the nuclear matter compresses and heats up intensely so that it potentially undergoes a deconfinement transition. Shortly after the collision, the resulting hot and dense matter of quarks and gluons, colloquially called *fireball*, thermalizes and forms the aforementioned quark–gluon-plasma phase. Subsequently, the fireball expands and cools down so much that the QCD matter hadronizes again. Around that time, the formation of new particles ceases to take place, known as *chemical freeze out*. The hadrons are then still able to exchange energy and momentum until the *kinetic freeze out* happens, after which their properties can be measured in detectors. All of this happens within a very short timeframe of about 10^{-21} s. Apart from hadrons, dileptons are an important experimental probe for heavy-ion collisions since these escape the strongly interacting fireball almost undisturbed.

Finite-Volume Effects

The initial fireball of heavy-ion collisions is, of course, only finite in spatial extent. Depending on the size of the colliding ions and the collision's centrality and duration, its size can vary, with typical scales of several femtometres in each direction. To this end, it serves as a crucial crosscheck between theory and experiment to theoretically investigate the impact of this finite volume on experimental observables.

Out of these, fluctuations of the conserved quantities *baryon number*, *electromagnetic charge* and *strangeness* are of special importance [91]. This is due to the fact that they can be extracted on an event-by-event basis from the cumulants of the particle number distribution. They are expected to show signals for the CEP but also for the crossover and the first-order phase

transition at large baryon chemical potential, which may be particularly prominent in higher orders [66, 93–98].

From a theoretical point of view, those fluctuations can be calculated as derivatives of Equation (1.1) with respect to the associated chemical potentials of the conserved charges. Ratios of cumulants have the advantage that the explicit volume dependence of the fluctuations drops out. However, as pointed out and investigated in Refs. [97, 99], implicit volume dependences may remain. While it is still under debate whether these have to be taken into account when comparing theoretical calculations with experimental results, it is interesting to study these implicit dependences on systematic grounds.

At small chemical potentials, fluctuations are accessible through various extrapolation methods applied to lattice QCD. By their very construction, though, these simulations are carried out for cubes with finite edge length and (anti)periodic boundary conditions, so a thorough understanding of the volume dependence of these results is mandatory. Besides lattice QCD, theoretical studies of finite-volume effects on the QCD phase diagram have been carried out in a number of approaches. Model studies in the NJL or the QM models and their Polyakov-loop-enhanced versions serve to highlight important general aspects of small-volume physics. These have been performed using either a mean-field approximation [97, 100, 101] or an FRG treatment [102–105] (see Ref. [106] for a review). Especially the latter allows to study the reaction of fluctuations on changes of the volume.

In the DSE framework, finite-volume effects of (various aspects of) QCD [107–113] or similar theories [114, 115] with varying degrees of sophistication [116–118] have been studied for a long time. Chapter 4 of this thesis is devoted to the investigation of finite-volume effects – both on the phase diagram as a whole and specifically on baryon-number fluctuations around the CEP – in our very advanced setup of DSEs.

Imaginary Chemical Potentials

As stated earlier, the sign problem prevents lattice QCD from investigations of the QCD phase diagram at nonzero chemical potential. There are numerous strategies in order to bypass – or at least to mitigate – this limitation (see also Section 2.4.3). For instance, one might calculate derivatives of, e.g., Equation (1.1) with respect to the chemical potential and employ a *Taylor-expansion* scheme [68, 75, 77, 119–123]. Alternatively, there are *reweighting procedures*, i.e., shifting the imaginary and nonzero contributions from the probability measure to the observable [124–127]. These allow for indirect access to important quantities such as pseudocritical transition temperature, equations of state and fluctuations of conserved charges at moderate chemical potential [128]. Another approach is to consider *imaginary values* for the chemical potential which provide a basis for a number of extrapolation procedures into the real chemical potential domain based on the analytic properties of the QCD partition function, see, e.g., Refs. [1, 69, 129–132] and references therein.

Conveniently, imaginary chemical potentials are also straightforwardly accessible in a Dyson–Schwinger approach besides real chemical potentials. This makes DSE calculations an invaluable tool for gauging the quality of extrapolations as a crosscheck with lattice QCD. In addition, comparing DSE results with lattice QCD in such a controlled environment – where both approaches are applicable – allows to assess the impact of the inherent approximations and truncations of functional methods. These points will be the subject of Chapter 5.

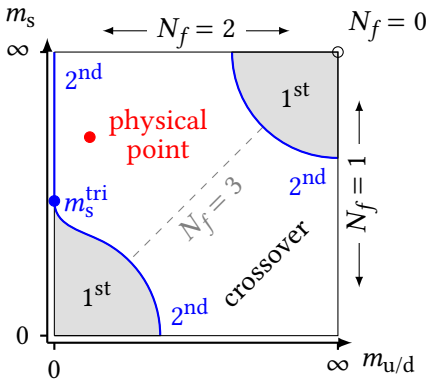

Figure 1.2.: The *Columbia plot* [134] of phase-transition orders at nonzero temperature and vanishing chemical potential as functions of quark masses. See the main text below for details.

The Columbia Plot

As stated earlier, out of the features of QCD, we are mainly interested in DCSB in this thesis. As it turns out, the dynamical generation of a large constituent-quark mass is only one of in total four aspects of the full chiral symmetry. These are actually an interplay between *chirality*, i.e., quarks being massless or not, and *flavour symmetries*, i.e., if and how many quark flavours are mass degenerate. One can show that DCSB occurs even in the limit of massless quarks at low temperatures but ceases to do so at the chiral transition temperature. A similar behaviour – albeit perhaps at a different temperature – is conjectured for the *axial anomaly*, another aspect of chiral symmetry which manifests, e.g., in the differing masses of the η and η' mesons. We discuss the various facets of chiral symmetry in detail in Section 2.2.3.

All previous explanations about the QCD phase diagram were, of course, concerning physical quark masses. In order to study the different mechanisms of chiral symmetry breaking, though, it is therefore also quite interesting to investigate the chiral phase transition at unphysical quark masses, which was first discussed in Ref. [133]. To this end, we consider the *Columbia plot* [134][6] – an illustration indicating the type of phase transition as a function of both up/down- and strange-quark mass, $m_{u/d}$ and m_s, respectively, at vanishing chemical potentials. Here, up and down quarks are assumed to be mass degenerate whereas heavier quark flavours than strange are neglected because they do not play a role at the typical energy scale of the QCD phase diagram.

In Figure 1.2, we display the Columbia plot in its most-commonly found version. The grey areas indicate regions of quark masses where first-order phase transitions might occur, the white area shows the crossover region, while blue lines illustrate the second-order transitions separating the two. The red dot represents the point of physical quark masses where, as explained earlier, we have a crossover transition. Additionally, we highlight the edges of infinitely heavy quarks – where the respective flavours decouple – with the appropriate number of remaining flavours N_f. The upper right corner labelled with $N_f = 0$ consequently corresponds to the case of pure gauge theory, where only gluons drive the dynamics. We also show the $N_f = 3$ diagonal of mass-degenerate up, down and strange quarks.

[6] A group based at the *Columbia University*.

While the pure-gauge corner is understood, the situation on the massless edges is far from being settled. Namely, the limit of massless quarks is another conceptual problem for lattice QCD since full chiral symmetry can only be recovered in the limit of vanishing lattice spacing. Moreover, even for small nonzero quark masses, the considered volumes have to be much larger than the inverse mass which becomes numerically more and more unfeasible as $m \to 0$. As a result, the use of functional methods – where the quark mass just enters as another parameter that can freely be varied – becomes again invaluable.

Additionally, there are different scenarios for the Columbia plot and its precise form is conjectured to depend on whether or not the axial anomaly persists at the chiral transition temperature. For these reasons, even the analysis of unphysical quark masses is a worthwhile way to learn about QCD. The investigation of the left-hand side of the Columbia plot – utilizing a setup of DSEs that is specifically tailored for a description of second-order chiral transitions – will be the topic of Chapter 6. There, we will also revisit background information and generalities of the Columbia plot in much more detail.

Outline

In total, the overarching goal of this thesis is to examine the aforementioned aspects of the QCD phase diagram within the framework of Dyson–Schwinger equations. Before we do so, we first reiterate the most important properties of QCD, elucidate DSEs and motivate the truncation scheme we are using. This serves as the necessary theoretical background for our calculations. Thereafter, we address the topics introduced above and study the impact of finite-volume effects on the QCD phase diagram, gauge the capability of extrapolations from imaginary to real chemical potentials and analyse meson-backcoupling effects on the Columbia plot.

Most results of this work have already been published in Refs. [135–137] or are available as a preprint in Ref. [138]. In advance, we refer to Appendix A for general definitions and conventions of this thesis.

Chapter 2
Quantum Chromodynamics

To set the stage for all following topics, we begin with a discussion of *quantum chromodynamics* (QCD) – the underlying quantum field theory of the strong interaction – since it forms the theoretical foundation for all of our investigations. Building on the historical motivation in Chapter 1, we start with a short explanation of its general mathematical structure. To this end, we discuss the Lagrangian density of QCD, its most important symmetries and their implications on phenomenological features. Finally, we briefly introduce *lattice QCD* as it will serve as a frequent point of reference. To this end, we outline the most important aspects necessary for our comparisons.

This introductory chapter covers topics that are readily available in many standard textbooks on QFT. Since QCD is a highly extensive topic, we restrict ourselves to the fundamentals required for an understanding of the following chapters. Instead, we base our explanations on and refer to Refs. [33–37] for more details and background information.

2.1. Mathematical Structure and Lagrangian Density

As outlined in Chapter 1, QCD is a Yang–Mills theory based on the SU(3) symmetry group of the $N_c = 3$ colour charges. As such, its Lagrangian density can be derived from the respective behaviour of the quarks under these symmetry transformations, i.e., we demand that it be invariant. In this section, we want to briefly sketch this derivation. The procedure itself is generally analogous to QED, which is based on the U(1) group of the single electric charge.

We start by considering SU(3) symmetry transformations of the quark fields. To this end, we recall that every element of an SU(N) group can be expressed as an exponential of the *generators* t and an appropriate choice of transformation parameters ϑ:

$$U_{ij} = \exp\left(\mathrm{i}\vartheta_a t^a_{ij}\right) \in \mathrm{SU}(N)\,. \tag{2.1}$$

Any SU(N) symmetry group possesses $N^2 - 1$ such generators. The SU(3) generators are proportional to the *Gell-Mann matrices*. In general, such symmetry transformations are *local* transformations, i.e., the transformation parameters depend on the spacetime position x. As a consequence, the SU(3) symmetry-transformation law of a quark spinor reads

$$\psi_i(x) \to \psi'_i(x) = \exp\left(\mathrm{i}\vartheta_a(x) t^a_{ij}\right) \psi^j(x)\,. \tag{2.2}$$

Above, $i, j = 1, \ldots, N_c$ indicate colour indices of the fundamental (3) representation whereas $a = 1, \ldots, N_c^2 - 1$ denotes a colour index of the adjoint ($\overline{8}$) representation. To keep the notation concise, we will in the following spare both the (3) colour indices and all position arguments and instead assume them to be present implicitly.

A Yang–Mills theory based on the SU(3) symmetry group is called *non-Abelian* since its generators do not commute. Instead, they define the $\mathfrak{su}(3)$ *Lie algebra*. That is, they form the basis of a vector space $\mathfrak{g}$ equipped with the *Lie bracket* $[\cdot,\cdot] : \mathfrak{g} \times \mathfrak{g} \to \mathfrak{g}$ that fulfils

$$\left[t^a, t^b\right] = \mathrm{i} f^{ab}{}_d \, t^d \,, \tag{2.3}$$

where the Lie bracket is given by the commutator, f labels the associated $\mathfrak{su}(3)$ *structure constants* and b, d are further $(\overline{8})$ colour indices.

Analogously to QED, the derivative of the quark field appearing in the Lagrangian density of a free spin-1/2 field does not transform in the same way the quark field does. To this end, it is replaced with the appropriately transforming *covariant derivative*:

$$D_\nu \coloneqq \partial_\nu + \mathrm{i} g A^a_\nu t_a \,, \tag{2.4}$$

which introduces both the *gauge field*, i.e., the *gluon field* A^a_ν, and the *strong coupling constant* g where ν denotes a Lorentz index. As a consequence, the covariant derivative governs the interaction between quarks and gluons.

Just like for photons, we may express the gauge part of the Lagrangian in terms of a *field-strength tensor* F. However, due to the non-Abelian nature of the SU(3) generators and the existence of structure constants in Equation (2.3), the gluon field-strength tensor has to take the following form in order to result in the correct transformation behaviour of the Lagrangian (where we gain an additional Lorentz index ρ):

$$F^a_{\nu\rho} = \partial_\nu A^a_\rho - \partial_\rho A^a_\nu - g f^a{}_{bd} \, A^b_\nu A^d_\rho \,. \tag{2.5}$$

Apart from the number of gauge bosons, this is the central difference between QCD and QED. Since F not only contains derivatives of the gauge fields but also the fields themselves, Equation (2.5) implies the existence of three- and four-gluon vertices. Therefore, gluons also couple to gluons – as opposed to photons which do not couple to other photons.

Together, the Lagrangian density of QCD in Euclidean spacetime reads

$$\mathcal{L}_{\mathrm{QCD}} = \overline{\Psi}\left(\not{D} + M\right)\Psi - \frac{1}{4} F^a_{\nu\rho} F_a^{\nu\rho} \,. \tag{2.6}$$

Here, we utilized a heavily condensed notation where $\Psi \coloneqq (\psi_f)$ denotes a generalized spinor consisting of the spinors of all six contributing quark flavours, $M \coloneqq \mathrm{diag}\{m_f\}$ labels a diagonal mass matrix containing all current-quark masses, while $f \in \{\mathrm{u}, \mathrm{d}, \mathrm{s}, \mathrm{c}, \mathrm{b}, \mathrm{t}\}$ indicates the respective flavour index.

Since we started our derivation of the QCD Lagrangian at the SU(3) symmetry transformations and frequently referred to them, it is only consequential to now look at its transformation behaviour. Building on Equation (2.2), the quark spinor and its Dirac adjoint transform as

$$\Psi \to \Psi' = U\Psi \,, \quad \overline{\Psi} \to \overline{\Psi}' = \overline{\Psi} U^{-1} \,, \quad U \in \mathrm{SU}(3) \,. \tag{2.7}$$

The transformation behaviour of the gluon field follows directly from the condition that the covariant derivative of the quark field must transform in the same way as the quark field itself. Employing the frequently utilized abbreviation $A_\nu \coloneqq A^a_\nu t_a$, we find

$$A_\nu \to A'_\nu = U A_\nu U^{-1} + \frac{\mathrm{i}}{g} (\partial_\nu U) U^{-1} \,. \tag{2.8}$$

Indeed, it is a straightforward exercise to show that the Lagrangian in Equation (2.6) is invariant under these gauge transformations.

For practical calculations, however, the QCD Lagrangian in Equation (2.6) suffers from similar defects as the QED Lagrangian. In order to reconstruct these, we consider the partition function $\mathcal{Z}$ in its path-integral formulation:

$$\mathcal{Z}_{\mathrm{QCD}} = \int \mathcal{D}[\overline{\Psi}\Psi A]\ \exp\bigl(-\mathcal{S}_{\mathrm{QCD}}[\Psi, \overline{\Psi}, A]\bigr)\,, \tag{2.9}$$

where the QCD action $\mathcal{S}_{\mathrm{QCD}}$ is given by a spacetime integral over the Lagrangian:

$$\mathcal{S}_{\mathrm{QCD}}[\Psi, \overline{\Psi}, A] = \int \mathrm{d}^4x\, \mathcal{L}_{\mathrm{QCD}}[\Psi, \overline{\Psi}, A]\,. \tag{2.10}$$

The problem is that $\mathcal{D}A$ in Equation (2.9) integrates over all possible field configurations including ones that are equivalent via the gauge transformations of Equation (2.8), which leads to the respective gluon propagator not being well-defined.

This problem can be overcome by *gauge fixing*. That is, we need to single out precisely one field configuration among all equivalent ones. This is done using the well-known *Faddeev–Popov procedure* [139, 140]. For a sketched derivation and information on intricacies, we refer to Appendix B.3.

Eventually, we arrive at the gauge-fixed QCD Lagrangian that will serve as the basis for all investigations throughout this thesis:

$$\mathcal{L}_{\mathrm{QCD}} = \overline{\Psi}\bigl(\not{D} + M\bigr)\Psi - \frac{1}{4}F^a_{\nu\rho}F_a^{\nu\rho} - \frac{(\partial_\nu A^\nu)^2}{2\xi} + \mathrm{i}(\partial^\nu \overline{c})(D_\nu c)\,. \tag{2.11}$$

Here, the auxiliary fields $\overline{c}$ and c are the so-called *Faddeev–Popov ghosts*. As Grassmann-valued, scalar fields, they have spin zero but are anticommuting in violation of the *spin–statistics theorem* [141, 142]. As a consequence, they cannot correspond to physical particles but rather serve as a mathematical tool to cancel unphysical degrees of freedom of the gluon fields [34, 37]. Additionally, ξ labels the gauge-fixing parameter that specifies a whole class of gauges, the so-called R_ξ gauges. Prominent examples include the *Feynman–'t Hooft gauge* for $\xi = 1$ or *Landau gauge* corresponding to the limit $\xi \to 0$ at the very end of the calculations. In this thesis, we will exclusively work in Landau gauge.

2.1.1. Regularization and Renormalization

As is very common for QFTs in general, the integrals occurring, e.g., inside loop diagrams are divergent. Therefore, they have to be *regularized* in order to render them finite and *renormalized* to remove the regulator dependence from the results.

There is a plethora of different regularization schemes. The most straightforward approach is to simply introduce some hard, numerical cutoff Λ to eliminate the problematic part of the respective integral. For a UV-divergent integral of some integrand f in momentum space, for instance, this corresponds to the replacement

$$\int_0^\infty f(q)\,\mathrm{d}q \to \int_0^\Lambda f(q)\,\mathrm{d}q\,. \tag{2.12}$$

While usually easiest to implement, a hard-cutoff regularization implies several downsides, like breaking of translational invariance and violation of *Ward–Takahashi identities* (WTIs) [143, 144]. To this end, e.g., *Pauli–Villars* (PV) regularization serves as a better alternative [145]. Its idea is to introduce one or more fictitious mass terms that suppress the diverging parts of the integral without altering the integral bounds. For our numerical calculations, it will be the regularization scheme of choice. Introducing the regularization scale Λ_{PV}, we employ the form

$$\int_0^\infty f(q)\,\mathrm{d}q \to \int_0^\infty f(q)\frac{\Lambda_{\mathrm{PV}}^2}{\Lambda_{\mathrm{PV}}^2+q^2}\,\mathrm{d}q\,. \tag{2.13}$$

While regularization solves the problem of diverging integrals, it introduces another one: The results now depend on the regularization parameters. To remove this dependence, the calculated quantities have to be *renormalized*. In this respect, a certain class of theories – one of which is gauge-fixed QCD – exhibits the beneficial property of being *muliplicatively renormalizable* [146–150]. That is to say, it suffices to rescale the fields and parameters in the Lagrangian with associated *renormalization constants* which consequently carry the dependence on the regularization parameter. In the case of QCD, this rescaling reads

$$\begin{aligned} \psi \to Z_2^{1/2}\psi\,, \quad \overline{\psi} \to Z_2^{1/2}\overline{\psi}\,, \quad A_\nu^a \to Z_3^{1/2}A_\nu^a\,, \\ m \to Z_m m\,, \quad g \to Z_g g\,, \quad c^a \to \tilde{Z}_3^{1/2}c^a\,, \quad \overline{c}^a \to \tilde{Z}_3^{1/2}\overline{c}^a\,, \end{aligned} \tag{2.14}$$

where Z_2 is the quark, Z_3 the gluon, Z_m the quark-mass, Z_g the coupling and $\tilde{Z}_3$ the ghost renormalization constant, respectively. Above, quantities on the left-hand sides are unrenormalized whereas those on the right-hand sides are renormalized.

Further, the different renormalization constants can be interrelated by utilizing *Slavnov–Taylor identitites* (STIs) [151, 152]. These are non-Abelian generalizations of the WTIs and relate the correlation functions of QCD to one another. That is, one may derive the relations

$$Z_{1F} = Z_g Z_2 Z_3^{1/2}\,, \quad Z_1 = Z_g Z_3^{3/2}\,, \quad \tilde{Z}_1 = Z_g \tilde{Z}_3 Z_3^{1/2}\,, \quad \tilde{Z}_4 = Z_g^2 Z_3^2\,, \tag{2.15}$$

where Z_{1F} labels the quark–gluon-vertex, Z_1 the three-gluon-vertex, $\tilde{Z}_1$ the ghost–gluon-vertex and $\tilde{Z}_4$ the four-gluon-vertex renormalization constant, respectively.

In the following, we will mostly refrain from explicitly showing the renormalization constants in intermediate calculations for the sake of brevity. However, they can always be inserted at the appropriate positions utilizing the relations above which will be done explicitly in relevant places. An example of the QCD Lagrangian with renormalization constants inserted can be found in Equation (81) in Ref. [153].

2.2. Global Symmetries

Apart from the local gauge symmetry – which is the defining property of the QCD Lagrangian – it also exhibits various global symmetries that have interesting implications. The investigation of (non-)conservation of symmetries is generally a very important tool in the analysis of QFTs which is why we start with some general considerations and theorems.

Inherited from classical physics, we recall *Noether's (first) theorem* that can be derived from the principle of least action [154]. It states that each continuous, global, unbroken symmetry of the Lagrangian implies the existence of an associated current j^ν being conserved: $\partial_\nu j^\nu = 0$. Consequentially, this also leads to a conserved charge: $Q = \int j^0 \, \mathrm{d}V$, $\partial_t Q = 0$. Classically, symmetries can be broken in two ways:

Explicit symmetry breaking occurs if the Lagrangian is not actually invariant under the corresponding transformations, i.e., there are explicit terms in the Lagrangian that break the symmetry. In this case, the corresponding Noether current is, of course, not conserved.

Spontaneous symmetry breaking labels a situation where the Lagrangian is invariant under a symmetry transformation, i.e., the Noether current is conserved, but the ground state of the theory $|0\rangle$ is not invariant under the effect of the corresponding charge operator: $\hat{Q}\,|0\rangle \neq 0$. Since the associated mechanisms originate in dynamical processes of the theory, it is also called *dynamical symmetry breaking*.[1]

Transitioning to QFT, *Goldstone's theorem* [155, 156] outlines important consequences: Each generator of a spontaneously broken symmetry leads to the existence of a massless particle. These are usually spin-zero bosons, the so-called *(Nambu–)Goldstone bosons* [157]. In addition, a third mechanism of symmetry breaking arises in QFT (see, e.g., Refs. [158, 159] for reviews):

Anomalous symmetry breaking describes a symmetry of both the Lagrangian and the classical theory that is broken by the quantization process. This can happen, for instance, if the path-integral measure is not invariant under the respective symmetry transformation. The corresponding classical Noether current is conserved while the one of the quantized theory is not.

Having this in mind, we briefly go through the most important symmetries of QCD as well as potential mechanisms of their breaking in this section and elucidate the respective implications.

2.2.1. Discrete Symmetries

The QCD Lagrangian in Equation (2.11) is invariant under the discrete symmetry transformations of *charge conjugation* (C), *parity transformation* (P) and *time reversal* (T). Additionally, as is true for any physical theory, this also holds for simultaneous C, P and T transformations (CPT). In principle, however, one is allowed to add a term compatible with SU(3) colour symmetry that is not invariant under simultaneous C and P transformations (CP):

$$\mathcal{L}_\theta = \overline{\theta}\frac{g^2 N_f}{64\pi^2}\,\mathrm{tr}\big(\tilde{F}^a_{\nu\rho}F_a^{\nu\rho}\big)\,, \quad \text{where} \quad \tilde{F}^a_{\nu\rho} = \varepsilon_{\nu\rho}{}^{\lambda\sigma}F^a_{\lambda\sigma}\,. \tag{2.16}$$

Here, $\overline{\theta}$ labels the strength parameter of the CP violation, $\tilde{F}^a_{\nu\rho}$ indicates the dual gluon field-strength tensor, whereas ε is the Levi-Civita symbol. While there is no reason for this term not to be present, no CP violating process involving only the strong interaction has been found as of today, and the upper experimental bound for $\overline{\theta}$ is $\overline{\theta} \lesssim 10^{-10}$ [160][2] (known as the infamous *strong CP problem*). Therefore, we omit this term from now on.

[1] A prominent example from classical physics is the magnetization of ferromagnets: While Maxwell's equations are invariant under spatial rotations, the magnetization of ferromagnets for low temperatures is not.

[2] $\overline{\theta}$ is related to the electric dipole moment of the neutron d_N via $d_N = \big(5.2 \times 10^{-16}\,\mathrm{e}\cdot\mathrm{cm}\big)\overline{\theta}$ [161].

2.2.2. BRST and Global Gauge Symmetry

Since the Lagrangian is invariant under local gauge symmetry, it is trivially also invariant under *global* gauge transformations. That is, we replace the space-dependent gauge parameter in Equation (2.2) by a constant one, $\vartheta_a \neq \vartheta_a(x)$.

A closely related symmetry transformation was described by Carlo Becchi, Alain Rouet and Raymond Stora [162–164] and independently by Igor Tyutin [165, 166] (BRST). It can be obtained by a gauge transformation where the gauge parameter is replaced by the (rescaled) ghost field, $\vartheta_a(x) \to \lambda c_a(x)$, where λ labels a Grassmann-valued parameter. Introducing the BRST operator $\hat{\mathrm{s}}$, the fields transform according to (where we again drop the position arguments):[3]

$$\hat{\mathrm{s}}\,\psi = -\mathrm{i}gt^a c_a \psi\,, \quad \hat{\mathrm{s}}\,A^a_\nu = D^{ab}_\nu c_b\,, \quad \hat{\mathrm{s}}\,c^a = -gf^{abd}c_b c_d/2\,, \quad \hat{\mathrm{s}}\,\overline{c}^a = \xi^{-1}\partial^\nu A^a_\nu\,. \tag{2.17}$$

Since the ghost field is determined globally and so is the transformation parameter λ, spacetime points cannot be transformed independently from each other and thus BRST transformations are global. More on the BRST formalism can be found, e.g., in the textbook in Ref. [167].

The Noether currents of both global gauge and BRST symmetry are conserved but is not clear whether or not they are spontaneously broken, which may be relevant for the *Kugo–Ojima scenario* of confinement (see Section 2.3.2 below).

2.2.3. Chiral and Flavour Symmetries

Next, we want to cover a class of symmetries that lies at very heart of our investigations in this thesis and will consequently be treated in more detail. Our motivation is the N_f-dimensional generalized spinor Ψ in Equation (2.11). In principle, all quark flavours are treated equally by the strong interaction so the Lagrangian should be invariant under a $\mathrm{U}(N_f)$ transformation of Ψ. However, while it will certainly hold for N_f *massless* quark flavours, one can intuitively conjecture that this symmetry is spoiled by the non-degenerate current-quark masses of the different flavours. At the same time, the Lagrangian of even a single massless Dirac fields exhibits additional symmetries in Dirac space. We will mathematically formalize these considerations below.

In advance, we remark that the symmetries in this section are a delicate interplay between two different spaces, namely four-dimensional Dirac space and N_f-dimensional flavour space. Since matrices – especially unit matrices – of both spaces will appear simultaneously, we clarify that $\mathbb{1}_D, \gamma_\nu \in \mathbb{C}^{4\times 4}$ live in Dirac space while $\mathbb{1}_f, t_a \in \mathbb{C}^{N_f \times N_f}$ act on flavour space.

As the first step towards a mathematical treatment of chiral and flavour symmetries, we consider the Dirac equation of N_f massless quark flavours: $\not{\partial}\Psi = 0$. For reasons that will become apparent shortly, we introduce the matrix γ_5 defined to be Hermitian, unitary and anticommuting with all Dirac matrices:[4]

$$(\gamma_5)^\dagger = \gamma_5\,, \quad (\gamma_5)^2 = \mathbb{1}_D\,, \quad \{\gamma_\nu, \gamma_5\} = 0\,. \tag{2.18}$$

[3] These are the *on-shell transformations*, i.e., assuming that the ghost equations of motion hold.

[4] In four-dimensional Euclidean spacetime, one can explicitly construct such a matrix in terms of the Dirac matrices, $\gamma_5 = \gamma_1\gamma_2\gamma_3\gamma_4$, assuming a representation of Hermitian γ_ν.

Using this definition, one can now find that $\gamma_5 \not{\partial} \Psi = -\not{\partial} \gamma_5 \Psi = 0$. That is, both Ψ and $\gamma_5 \Psi$ are solutions of the massless Dirac equation. However, the properties in Equation (2.18) also imply that we can utilize γ_5 to define two projection operators, P_R and P_L, such that:

$$P_{L/R} = \big(\mathbb{1}_D \mp \gamma_5\big)/2 \quad \Rightarrow \quad P_{L/R}^2 = P_{L/R}\,, \quad P_L P_R = 0 = P_R P_L\,, \quad P_L + P_R = \mathbb{1}_D\,. \tag{2.19}$$

These operators are commonly interpreted to project out the respective left- and right-handed parts of a spinor, i.e., $\Psi_L = P_L \Psi$ and $\Psi_R = P_R \Psi$. Due to this property, γ_5 is also called *chiral matrix*. Additionally, this implies that Ψ_L and Ψ_R independently satisfy the massless Dirac equation, which leads to the well-known *Weyl equations*.

As a consequence, the classical action of QCD in the limit of massless quarks (colloquially termed *chiral limit*) is trivially invariant under independent global $\mathrm{U}(N_f)$ transformations of the left- and right-handed spinor components (the *chiral symmetry transformations*):

$$\Psi_L \to U_L \Psi_L\,, \ \Psi_R \to U_R \Psi_R \quad \text{or} \quad \Psi \to U_L U_R \Psi\,, \quad U_L \in \mathrm{U}_L(N_f)\,, \ U_R \in \mathrm{U}_R(N_f)\,. \tag{2.20}$$

As an abbreviation, we say the Lagrangian is invariant under a $\mathrm{U}_L(N_f) \otimes \mathrm{U}_R(N_f)$ symmetry transformation where the subscript indicates that the transformation acts only on the left- and right-handed spinor component, respectively. It is more convenient to separate the $\mathrm{U}(1)$ and $\mathrm{SU}(N_f)$ components of these transformations,[5]

$$U_{L/R} = \exp\big(\mathrm{i}\alpha_{L/R} \mathbb{1}_f P_{L/R}\big) \cdot \exp\big(\mathrm{i}\beta^a_{L/R} t_a P_{L/R}\big) \in \mathrm{U}_{L/R}(1) \otimes \mathrm{SU}_{L/R}(N_f)\,, \tag{2.21}$$

with α and β being some transformation parameters, since it allows us to disentangle flavour-singlet from flavour-multiplet effects. Moreover, we change the basis of our transformations from left- and right-handed projectors to the unit and chiral matrices, i.e., $\{P_L, P_R\} \to \{\mathbb{1}_D, \gamma_5\}$. This is due to the fact that the associated transformations correspond to vector and axialvector currents (see below) indexed by V and A, respectively. Consequently, the symmetry group of chiral and flavour transformations can be decomposed in the following way:

$$\mathrm{U}_L(N_f) \otimes \mathrm{U}_R(N_f) = \mathrm{U}_V(1) \otimes \mathrm{SU}_V(N_f) \otimes \mathrm{SU}_A(N_f) \otimes \mathrm{U}_A(1)\,. \tag{2.22}$$

Therefore, there are in total four distinct aspects of chiral symmetry and – as it turns out – the vector transformations are not even tied to the quarks being chiral or not.

For a formal analysis, we investigate if and when the respective Noether currents are conserved. To this end, it is convenient to again to express the elements of the symmetry groups in terms of exponential representations:

$$\begin{aligned} \exp\big(\mathrm{i}\alpha_V \mathbb{1}_f \mathbb{1}_D\big) &\in \mathrm{U}_V(1)\,, & \exp\big(\mathrm{i}\beta^a_V t_a \mathbb{1}_D\big) &\in \mathrm{SU}_V(N_f)\,, \\ \exp\big(\mathrm{i}\alpha_A \mathbb{1}_f \gamma_5\big) &\in \mathrm{U}_A(1)\,, & \exp\big(\mathrm{i}\beta^a_A t_a \gamma_5\big) &\in \mathrm{SU}_A(N_f)\,. \end{aligned} \tag{2.23}$$

This way, one easily finds that the associated currents read

$$j^\nu = \overline{\Psi} \gamma^\nu \mathbb{1}_f \Psi\,, \quad j^\nu_a = \overline{\Psi} \gamma^\nu t_a \Psi\,, \quad j^\nu_5 = \overline{\Psi} \gamma^\nu \gamma_5 \mathbb{1}_f \Psi\,, \quad j^\nu_{5,a} = \overline{\Psi} \gamma^\nu \gamma_5 t_a \Psi\,. \tag{2.24}$$

[5] This is due to the fact that any $\mathrm{U}(N)$ matrix can be written as an $\mathrm{SU}(N)$ matrix multiplied with a complex phase ($\mathrm{U}(1)$). Strictly and mathematically speaking, there is an isomorphy $\mathrm{U}(N) \simeq (\mathrm{U}(1) \otimes \mathrm{SU}(N))/\mathbb{Z}_n$ where $\mathbb{Z}_n$ is the cyclic group of n integers. However, we neglect this subtlety and just write $\mathrm{U}(N) = \mathrm{U}(1) \otimes \mathrm{SU}(N)$.

If a current is conserved, its four-divergence has to vanish. In order to calculate the respective four-divergences, we consider the Dirac equations for Ψ and $\gamma_5\Psi$ for arbitrary quark masses,

$$\big(\not{\partial} + M\big)\Psi = 0 \quad \Leftrightarrow \quad \big(\not{\partial} - M\big)\gamma_5\Psi = 0\,, \tag{2.25}$$

which leads us to

$$\partial_\nu j^\nu = 0\,, \quad \partial_\nu j_a^\nu = \overline{\Psi}\mathbb{1}_D[M, t_a]\Psi\,, \quad \partial_\nu j_5^\nu = 2\overline{\Psi}\gamma_5 M\Psi\,, \quad \partial_\nu j_{5,a}^\nu = \overline{\Psi}\gamma_5\{M, t_a\}\Psi\,. \tag{2.26}$$

Using these, we can now discuss each of the four aspects of chiral symmetry in detail:

$\mathrm{U}_V(1)$ symmetry is conserved both classically and in the quantized theory since it corresponds to a mere global phase of the quark fields. It is thus a true and exact symmetry of QCD and the unbroken charge associated with its current is the *baryon number* which is consequently conserved in all processes of the strong interaction.

$\mathrm{SU}_V(N_f)$ symmetry is broken not by nonzero quark masses but rather by *non-degenerate* quark masses, i.e., $M \neq m\mathbb{1}_f$.[6] This leads to non-degenerate meson masses inside the same $\mathrm{SU}(N_f)$ multiplet. Since the masses of the three lightest quark flavours $m_\mathrm{u} \lesssim m_\mathrm{d} \ll m_\mathrm{s}$ are still smaller than the scale of the strong interaction $\Lambda_\mathrm{QCD} \approx 200-300\,\mathrm{MeV}$ (see Section 2.3.1), $\mathrm{SU}_V(3)$ remains an approximate symmetry of QCD. For example, the masses of kaons and pions in the SU(3) pseudoscalar octet are different but in the same order of magnitude. On the other hand, due to almost mass-degenerate up and down quarks, all pions have approximately the same mass corresponding to an almost exact $\mathrm{SU}_V(2)$ *isospin symmetry*. In total, $\mathrm{SU}_V(N_f)$ is therefore more a flavour rather than a chiral symmetry.

$\mathrm{U}_A(1)$ symmetry is explicitly broken by nonzero quark masses. However, even in the chiral limit, it is anomalously broken in QCD – a phenomenon known as *axial anomaly*. Analogous to the *Adler–Bell–Jackiw anomaly* [168, 169] already present in QED [170–172], one can show that the path-integral measure is not invariant under $\mathrm{U}_A(1)$ transformations. As a consequence, the four-divergence of the quantized theory gains an additional term:

$$\partial_\nu j_5^\nu = \frac{g^2 N_f}{16\pi^2}\,\mathrm{tr}\big(\tilde{F}^a_{\nu\rho}F_a^{\nu\rho}\big)\,. \tag{2.27}$$

Since this term does not involve any quark masses, $\mathrm{U}_A(1)$ symmetry is indeed broken even in the chiral limit. A phenomenological consequence of the axial anomaly is the mass splitting between the η and η' mesons, i.e., $m_\eta = 548\,\mathrm{MeV}$ vs. $m_{\eta'} = 958\,\mathrm{MeV}$ [19].

$\mathrm{SU}_A(N_f)$ symmetry is the one usually implied when talking about *chiral symmetry*. Just like $\mathrm{U}_A(1)$ symmetry, it is also broken explicitly by nonzero quark masses. A phenomenological consequence is that *chiral partners* – i.e., hadrons with the same quark content but different parity – are not degenerate in mass. However, the magnitude of the observed mass splitting[7] cannot be attributed to the small current-quark masses generated by the Higgs mechanism. This is due to the fact that the strong interaction between quarks and gluons breaks $\mathrm{SU}_A(N_f)$

[6] Since the mass matrix is diagonal, the diagonal currents corresponding to t_3 and t_8 are also always conserved making their charges, the *third isospin component* and *hypercharge*, also good quantum numbers.

[7] For example, the vector–axialvector partners $\rho(770)$ and $a_1(1260)$ deviate about 490 MeV in mass while the difference is about 380 MeV for $K^*(892)$ and $K_1(1270)$ [19].

symmetry spontaneously, a phenomenon known as *dynamical chiral symmetry breaking* (DCSB) which will pose a central topic of this work.

A rather haptic manifestation of DCSB is the quite large *constituent-quark mass*, i.e., the mass valence quarks in hadrons appear to have if the total mass were evenly distributed among them. For the light quarks, this constituent-quark mass of about 300 MeV is orders of magnitude larger than the current-quark masses of about 3 MeV to 5 MeV. The (pseudo-)Nambu–Goldstone bosons associated with the spontaneously broken $\mathrm{SU}_A(N_f)$ symmetry are the pions which are consequently much lighter than other hadrons and even the constituent-quark mass (the same, albeit to a lesser extend, also applies to the kaons). They are not massless, though, due to the nonzero current-quark masses. In fact, one can show that the largest part of the hadron masses m_H is due to gluonic effects. That is because they are related to the trace of the energy–momentum tensor $T^{\nu\rho}$: $m_H \sim \langle H|T^{\nu}{}_{\nu}|H\rangle$ [173], where $|H\rangle$ labels the hadronic state. The *trace anomaly* of QCD [174, 175] shows that this trace remains nonzero even in the chiral limit: $T^{\nu}{}_{\nu} \sim F_a^{\nu\rho}F^a_{\nu\rho}$.

Another consequence of DCSB is the emergence of a nonzero quark condensate that mixes left- and right-handed spinor components:

$$\langle\overline{\Psi}\Psi\rangle = \langle 0|\overline{\Psi}\Psi|0\rangle = \langle 0|\overline{\Psi}_L\Psi_R|0\rangle + \langle 0|\overline{\Psi}_R\Psi_L|0\rangle\,. \tag{2.28}$$

On the one hand, if chiral symmetry were realized exactly, such a condensate would naturally vanish. On the other hand, if chiral symmetry were not broken spontaneously, the light-quark condensate would be of the order of the nonzero current-quark masses: $\langle\overline{q}q\rangle \sim m_{\mathrm{u}}, m_{\mathrm{d}}$, $q = \mathrm{u}, \mathrm{d}$ [176]. The physical value of the condensate, however, can be determined from the *Gell-Mann–Oakes–Renner* (GMOR) relation [177] and yields $\langle\overline{q}q\rangle \approx -(240\,\mathrm{MeV})^3$ which is confirmed by lattice calculations [178]. Therefore, the by far largest contribution is due to DCSB. For these reasons, the quark condensate serves as an order parameter for DCSB and its dependence on temperature and quark chemical potential forms the basis of our investigations of the QCD phase diagram.

2.3. Phenomenological Features

Apart from DCSB, there are two other very prominent key features of QCD phenomenology: *asymptotic freedom* and *confinement*. Even though both are not immediately at the centre of the investigations in this thesis, we still want to outline them briefly in this section for the sake of completeness and since they will be referenced several times.

2.3.1. Asymptotic Freedom

Due to the observation that quarks and gluons are always tightly bound in hadrons with a small spatial extent, one can already infer that the coupling constant of QCD is large at a long range (and thus small energies, the *infrared* (IR) momentum regime). On the other hand, there is nowadays abundant evidence from deep-inelastic scattering experiments that the coupling is much weaker at high energies [29] (the *ultraviolet* (UV)). From a theoretical point of view, the dependence of the coupling constant on the energy scale Q is encoded in the β function,

$$\frac{\partial g}{\partial \ln(Q)} = \beta(g)\,, \tag{2.29}$$

which can be obtained from renormalization-group calculations. Therefore, the coupling strength increases with energy for $\beta > 0$, decreases for $\beta < 0$, while it is scale invariant for $\beta = 0$. At large energies, where experiment finds a weak coupling of QCD, we may therefore apply perturbation theory to calculate the β function. To lowest order, one can derive [34]:

$$\beta(g) = -\left(11 - \frac{2N_f}{3}\right)\frac{g^3}{16\pi^2}\,, \tag{2.30}$$

which is negative for $N_f \leq 16$ quark flavours, a number far larger than observed. Consequently, the coupling constant of QCD indeed decreases with rising energy, a property called *asymptotic freedom*. Solving explicitly for g yields

$$\alpha_s(Q) \coloneqq \frac{g^2(Q)}{4\pi} = \frac{6\pi}{(33 - 2N_f)\ln(Q/\Lambda_{\mathrm{QCD}})}\,, \tag{2.31}$$

where we introduce the dimensionless quantity α_s inspired by the fine-structure constant of QED and where the scale Λ_{QCD} enters as an integration parameter. Its value can be extracted from measurements of α_s and depends on the energy scale of the experiment. Considering the β function up to third order, a value of $\Lambda_{\mathrm{QCD}} \approx 250\,\mathrm{MeV}$ is obtained for $\alpha_S(m_Z) = 0.1179(9)$, where $m_Z = 91.1876(21)\,\mathrm{GeV}$ denotes the Z-boson mass, which corresponds to $N_f = 5$ since $m_\mathrm{b} < m_Z < m_\mathrm{t}$ [19, 34]. Because α_s has a pole at $Q = \Lambda_{\mathrm{QCD}}$, the latter serves as a rough estimate of the border between the perturbative and non-perturbative regimes. That is, QCD can be treated perturbatively at high energies $Q \gg \Lambda_{\mathrm{QCD}}$ whereas one has to resort to non-perturbative descriptions otherwise.

2.3.2. Confinement

Arguably one of the most-prominent non-perturbative features of QCD is *confinement*. In the narrower sense, confinement in QCD describes the existense of a linearly rising potential between static (i.e, infinitely heavy) quarks for large distances [22]. There are multiple phenomenological manifestations:[8] First, due to the linearly rising potential, trying to remove a quark from a hadron takes so much energy that eventually another quark–antiquark pair is produced which then forms new hadrons, a process called *string breaking*. Closely related is that neither quarks nor gluons occur outside of hadrons. That is, one does not observe coloured states in the physical spectrum of particles. This feature is labelled *colour confinement*.

From a theoretical point of view, confinement is an especially delicate feature of QCD since – to this day – there is no mathematical proof for it from first principles. However, there are multiple conjectured scenarios of how confinement comes about and we want to briefly discuss the two most notable ones in the following. On the one hand, the *Kugo–Ojima scenario* [179] argues that if both BRST and global gauge symmetry are unbroken, the physical state space of QCD contains only colourless states (see Ref. [167] for more details). On the other hand, the *Gribov–Zwanziger scenario* [180] links confinement to the *Gribov horizon* [181] (see Appendix B.3). In Coulomb gauge, it can be shown that its presence triggers an (almost) linearly rising potential [182–185]. In Landau gauge, one can formulate *Zwanziger's horizon*

[8] Sometimes, these are also cited as definitions for confinement. However, the linearly rising potential is the most rigorous definition from which the other manifestations follow.

conditions linked to the infrared behaviour of a properly gauge-fixed continuum gauge theory: The non-perturbative ghost propagator has to be more singular in the infrared than a simple pole and the dressed gluon propagator has to vanish in the infrared [186, 187].

From lattice-QCD calculations of the *Wilson loop* (see Section 2.4), though, there are unambiguous indications that the linear potential between static quarks exists [22, 188]. Additionally, the *Polyakov loop* serves as an order parameter for confinement in pure gauge theory and has often been applied to systems with dynamical fermions at nonzero temperature and chemical potential (see Sections 2.4 and 5.1).

2.4. Lattice QCD

We end our discussion of QCD with a brief introduction of the most-commonly used technique for actual non-perturbative calculations, namely *lattice QCD*. It is an ab initio approach, i.e., it does not require any additional input or modelling but only the theory itself. For this reason, lattice QCD has been the method of choice for non-perturbative QCD calculations in the past and has been applied quite successfully to, e.g., QCD at nonzero temperature or hadron spectroscopy (see, e.g., Refs. [39, 40, 70, 189] for reviews). Nevertheless, it naturally also has its downsides. Therefore, it serves as a recurring point of reference in this thesis, which is why we want to outline the basic concepts behind lattice QCD in this section. The following statements will later serve as a motivation why and how it can complement our Dyson–Schwinger framework and vice versa. The explanations below are oriented towards those in Ref. [188]. As with QCD in general, lattice QCD is a highly exhaustive topic, so covering all of its aspects, subtleties and technical details lies far beyond the scope of this thesis. Instead, we treat only those points necessary for our analyses and comparisons and refer to aforementioned textbook and references therein for further reading.

2.4.1. Generalities of Lattice Field Theories

The general idea behind lattice field theories is rather straightforward. That is, the infinite and continuous spacetime QFTs are usually formulated in is replaced by a discretized one with a finite number of spacetime points N that have a small but nonzero distance a. To this end, we define a (four-dimensional) lattice Λ with N_τ temporal and N_s spatial, i.e., $N = N_\tau \times N_s^3$ total points:

$$\Lambda \coloneqq \left\{ n = (n_4, \boldsymbol{n}) : n_4 \in \{0, \dots, N_\tau - 1\}, \boldsymbol{n} \in \{0, \dots, N_s - 1\}^3 \right\}. \tag{2.32}$$

We note that conventionally one works with the lattice position n rather than the spacetime position $x = an$. Many advantages of the spacetime discretization are apparent immediately. First, due to the finite number of lattice points, any path integral becomes an ordinary finitely dimensional integral:

$$\mathcal{Z} = \int \mathcal{D}[\Phi] \ \exp\bigl(-\mathcal{S}[\Phi]\bigr), \quad \text{where} \quad \mathcal{D}[\Phi] = \prod_{n \in \Lambda} \mathrm{d}\Phi(n). \tag{2.33}$$

Since the action consequently becomes a (highly but finitely dimensional) polynomial that is positive definite and at least quadratic in the fields, this renders the partition function mathematically well-defined. Together, these properties already suggest *Monte Carlo methods*

as a possible way to solve the resulting highly dimensional integral where the exponential serves as some kind of probability measure. Moreover, the nonzero lattice spacing a naturally regularizes the theory since it automatically introduces a finite ultraviolet cutoff in momentum space. An infrared cutoff, on the other hand, is induced by the finite lattice volume $V = a^3 N_s^3$.

However, this procedure, of course, also introduces numerous disadvantages. One of the most apparent ones is that the lattice discretization breaks Poincaré invariance of the vacuum, one of the fundamental symmetries of nature. Additionally, lattice field theories are by their very construction formulated in a finite volume and involve only a finite number of points. As a consequence, the results suffer from finite-volume and finite-size effects and numerous limits have to be taken carefully to remove these properly and recover the full theory. Most prominently, there are the infinite-volume and the continuum limit, $N \to \infty$ and $a \to 0$, respectively. In this regard, one also has to appropriately set a scale in order to relate lattice units to physical ones. A number of further difficulties – especially concerning fermions – will be elucidated in the following.

2.4.2. Pure Gauge Theory

We begin our discussion of lattice QCD with pure gauge theory, i.e., we are neglecting the fermions in this subsection since their inclusion entails much more subtleties. Nevertheless, some mathematical details are still rooted in a theory with fermions, which are conventionally defined to be located on the lattice sites. For instance, due to the demand that $\overline{\Psi} \not{D} \Psi$ in the discretized QCD action be gauge invariant, it turns out that it is more natural to work in terms of *link variables* U instead of the gauge fields themselves:

$$U_\nu(n) = \exp\bigl(\mathrm{i} a A_\nu(n)\bigr) \approx \mathbb{1} + \mathrm{i} a A_\nu(n) + O(a^2)\,. \tag{2.34}$$

These matrix-valued variables are elements of the gauge group. Their name comes from the fact that they are oriented with respect to the Lorentz index ν and are commonly interpreted to live on the links between the sites n and $n + \hat{\nu} \coloneqq n + \hat{e}_\nu$.

Using these, one can define paths as ordered products of links. It is a straightforward exercise to show that the trace over closed paths, i.e., loops, is gauge invariant. To this end, a very useful quantity to define is the so-called *plaquette*,

$$U_{\nu\rho}(n) = U_\nu(n) U_\rho(n + \hat{\nu}) U_\nu(n + \hat{\rho})^\dagger U_\rho(n)^\dagger\,, \tag{2.35}$$

which is the shortest, nontrivial closed loop on the lattice. This is due to the fact that one can find a pure lattice gauge action $\mathcal{S}_G$ that recovers the correct Yang–Mills action in the continuum and infinite-volume limits using only plaquettes:

$$\mathcal{S}_G[U] = \frac{2}{g^2} \sum_{n \in \Lambda} \sum_{\nu < \rho} \mathrm{Re}\,\mathrm{tr}\bigl[\mathbb{1} - U_{\nu\rho}(n)\bigr]\,. \tag{2.36}$$

Moreover, the use of link variables enables us to perform the integrals over the gauge fields in a mathematically well-defined manner. Namely, integration over the elements of a continuous compact group is formalized by the *Haar measure* [190]. This way, integrals over products of plaquettes can be performed algebraically.

Wilson and Polyakov Loops

Apart from plaquettes, there are two other special kinds of loops: the *Wilson* and the *Polyakov loops*, which serve as physical observables related to confinement. In advance, we define *Wilson lines* S as paths connecting two spacetime points along some path $C_{\boldsymbol{m},\boldsymbol{n}}$ with different spatial but identical temporal components and *temporal transporters* T as straight lines between two spacetime points with identical spatial but different temporal components:

$$S(n_\tau, \boldsymbol{m}, \boldsymbol{n}) = \prod_{(\boldsymbol{k},j)\in C_{\boldsymbol{m},\boldsymbol{n}}} U_j(n_\tau, \boldsymbol{k})\,, \quad T(n_\tau, \boldsymbol{n}) = \prod_{j=0}^{n_\tau-1} U_4(j, \boldsymbol{n})\,. \tag{2.37}$$

A Wilson loop $W_{\mathcal{L}}$ now consists of two Wilson lines connected by two temporal transporters:

$$W_{\mathcal{L}}[U] = \operatorname{tr}\big[S(n_\tau, \boldsymbol{m}, \boldsymbol{n})T(n_\tau, \boldsymbol{n})^\dagger S(0, \boldsymbol{m}, \boldsymbol{n})^\dagger T(n_\tau, \boldsymbol{m})\big] = \operatorname{tr}\bigg[\prod_{(k,\nu)\in\mathcal{L}} U_\nu(k)\bigg]\,. \tag{2.38}$$

Utilizing *temporal gauge*,[9] it can be argued that its expectation value is related to the static quark potential (cf. Section 2.3.2) between the two spacetime points $\boldsymbol{n}$ and $\boldsymbol{m}$:

$$\langle W_{\mathcal{L}}\rangle \propto \exp\big(-\tau V(r)\big) + O\big(\exp(-\tau\Delta E)\big)\,, \quad r = a|\boldsymbol{m}-\boldsymbol{n}|\,, \quad \tau = an_\tau\,. \tag{2.39}$$

Here, ΔE labels the difference between $V(r)$ and the first excited energy level of the quark–antiquark pair.

The Polyakov loop (or thermal Wilson line), on the other hand, is a special Wilson loop where the temporal extent is as large as possible, i.e., from $n_\tau = 0$ to $n_\tau = N_\tau - 1$. Utilizing periodic temporal boundary conditions for the bosonic gauge fields and choosing a gauge where this time the spatial lines become $\mathbb{1}$, one finds that this Wilson loop decomposes into two gauge-invariant, disconnected parts winding around the temporal direction with opposite orientations. This leads us to a quantity also called (and usually implied when referred to the) Polyakov loop:

$$P(\boldsymbol{n}) = \operatorname{tr}\bigg[\prod_{j=0}^{N_\tau-1} U_4(j, \boldsymbol{n})\bigg]\,. \tag{2.40}$$

Since it is a (special) Wilson loop, it is also connected with the static quark potential. In fact, at nonzero temperature $T^{-1} = \beta = aN_\tau$, the expectation value of the Polyakov loop's spatial average P may be related to the free energy F_q of a single colour charge, i.e., of a free quark:

$$|\langle P\rangle| \sim \exp\big(-F_q/T\big)\,, \quad P = N_s^{-3}\sum_{\boldsymbol{n}} P(\boldsymbol{n})\,. \tag{2.41}$$

In the confined phase, where there are no free colour charges, the free energy is basically infinite, $F_q \to \infty$, and so the Polyakov loop vanishes, $\langle P\rangle = 0$. In the deconfined phase, the free energy is finite and so is $\langle P\rangle \neq 0$. Therefore, the Polyakov loop serves as an order parameter for the deconfinement transition in pure gauge theory at nonzero temperature. We will come back to this later in Section 5.1 where we also provide a continuum version.

[9] On an lattice with infinite temporal extent or if $n_\tau \neq N_\tau - 1$, temporal gauge corresponds to $U_4(n) = \mathbb{1}$, $\forall n$.

2.4.3. Fermions (and Their Problems)

A priori, the naïve discretization of a fermionic path integral for a description on the lattice is rather formulaic. The functional integration over infinitely many Grassmann numbers turns into $2N$ discrete ones.[10] Employing the standard calculation rules for differentiation, integration and coordinate transformation of Grassmann numbers and the resulting identity for a multidimensional Gaussian integral, one can then perform the integration over the fermion fields analytically [36]:

$$\mathcal{Z} = \int \mathcal{D}[U]\ \mathcal{Z}_F[U] \exp\bigl(-\mathcal{S}_G[U]\bigr)\,, \quad \mathcal{Z}_F[U] = \int \mathcal{D}[\overline{\Psi}\Psi]\ \exp\bigl(-\mathcal{S}_F[\Psi, \overline{\Psi}, U]\bigr)\,. \tag{2.42}$$

Here, $\mathcal{S}_F$ denotes the fermionic part of the action while $\mathcal{Z}_F$ is the so-called *fermion determinant* which is the determinant of the *fermion matrix*, i.e., the discretized Dirac operator.

These quantities, however, are responsible for most of the problems of lattice QCD with fermions. One of the directly apparent reasons is that the fermion matrix scales with the number of lattice points, $O(N^2)$, and – depending on the gauge configuration – spans several orders of magnitude which renders an explicit calculation of the determinant almost impossible. While for an even number of mass-degenerate quarks the determinant is positive (semi)definite and can be interpreted as part of the probability measure for the Monte Carlo methods, one often has to resort to approximations in the general case. For these reasons, many lattice calculations have been performed in a *quenched* approximation of static quarks where the fermion determinant is set to unity, which simplifies matters tremendously.

Fermion Doubling and Chiral Symmetry

Another conceptual difficulty emerges when considering massless fermions. Namely, the Dirac operator of the naïve fermion discretization has poles if each component of the four-momentum is either $p_\nu = 0$ or $p_\nu = \pi/a$. Therefore, in addition to the physical pole, there are 15 unphysical ones called *doublers*. This phenomenon is consequently called *fermion doubling problem*. Kenneth Wilson proposed a solution by adding a term to the Dirac operator that cancels the unphysical contributions while vanishing for both $p_\nu = 0$ and in the limit $a \to 0$, a description known as *Wilson fermions* [191].

While Wilson fermions remove the doublers, they explicitly break chiral symmetry. In fact, this turns out to be a fundamental property of lattice QCD since the *Nielsen–Ninomiya theorem* [192–194] states that one cannot preserve chiral symmetry on the lattice without also having doublers.[11] There is, however, a relation which allows for a description of chiral symmetry on the lattice for finite a and recovers the proper continuum relation in the limit $a \to 0$. It is given by the *Ginsparg–Wilson equation* [195]:

$$D\gamma_5 + \gamma_5 D = aD\gamma_5 D \quad \Leftrightarrow \quad \{D^{-1}, \gamma_5\} = a\gamma_5\,. \tag{2.43}$$

[10] For each of the N lattice points, we have a Grassmann number and its adjoint, e.g., θ and θ^*, that are derived from the spinor and its Dirac adjoint, respectively.

[11] More precisely, it states that for a Dirac operator that is translational invariant, Hermitian and local, there has to be an equal number of left- and right-handed fermions.

The problem of chiral symmetry on the lattice has spawned a whole range of different fermion types – e.g., *overlap* [196, 197], *staggered* [198], *Domain Wall* [199, 200] or *Twisted Mass fermions* [201] – all having their own respective up- and downsides.

Regardless of the fermion formulation and even if the Ginsparg–Wilson equation is fulfilled, one can show analytically that chiral symmetry cannot be broken spontaneously in a finite volume V in the chiral limit $m \to 0$. Nevertheless, even in a finite volume, DCSB still occurs if the following relation holds [202]:

$$Vm|\langle\overline{q}q\rangle| \gg 1\,, \tag{2.44}$$

where $\langle\overline{q}q\rangle$ is the infinite-volume quark condensate. For this reason, one has to perform the infinite-volume limit, $V \to \infty$, before the chiral limit, $m \to 0$, and small quark masses on the lattice can only be meaningfully described if the considered volume is large enough. Consequentially, it is numerically quite involved to investigate small quark masses in lattice QCD.

Nonzero Temperature and Chemical Potential

In view of an analysis of the QCD phase diagram, we last want to elucidate how nonzero temperatures and chemical potentials are treated in the framework of lattice QCD. In principle, their inclusion is no different from the continuum theory and analogous to the procedure in Appendix B.1. Due to the finite extend of the lattice in configuration space, there is actually an intrinsic nonzero temperature $\beta = aN_\tau$. In order to obtain results for a specific temperature, one therefore has to adjust the number of temporal lattice points to the lattice spacing while peforming the continuum limit.

The much larger complication by far are fermionic chemical potentials μ. In a naïve implementation, which corresponds to the statements in Appendix B.1, the chemical potential corresponds to an imaginary shift of the Euclidean energy component. As it turns out, however, this approach leads to a divergent energy density ε in the continuum limit: $\varepsilon(\mu)-\varepsilon(0) \propto (\mu/a)^2$. This can be overcome by adding terms proportional to $\exp(\pm a\mu)$ to the temporal part of the Dirac operator [203] which, however, breaks γ_5 *Hermiticity*:

$$\gamma_5 D \gamma_5 = D^\dagger \quad \to \quad \gamma_5 D(\mu)\gamma_5 = D^\dagger(-\mu)\,. \tag{2.45}$$

As a consequence, this procedure also results in a complex fermion determinant – just as the naïve implementation would – with grave implications. First, the integrand in Equation (2.33) becomes oscillating and many cancellations occur rendering the observables small but their numerical errors large, which is the infamous *sign problem* (see Ref. [76] for a review). In fact, one can show that the numerical effort for the calculation of oberservables scales exponentially with increasing chemical potential. Second, due to the negative and imaginary parts, the probability interpretation of the fermion determinant is definitely no longer applicable adding to the numerical difficulties.

There is a number of approaches trying to to bypass or at least mitigate the sign problem. One of these, for example, is *reweighting* [124–127]. The general idea behind this is to collect the problematic, i.e., complex and nonzero, contributions of the fermion determinant and shift

these from the probability measure to an additional weighting function(al) $w(\mu)$. This way, the expectation value of some observable O at $\mu \neq 0$ becomes

$$\langle O \rangle_\mu = \frac{\langle O w(\mu) \rangle_0}{\langle w(\mu) \rangle_0}, \quad \text{with, e.g.,} \quad w(\mu) = \frac{\mathcal{Z}_F(\mu)}{\mathcal{Z}_F(0)} \exp\big(-\mathcal{S}_G(\mu) + \mathcal{S}_G(0)\big) . \tag{2.46}$$

Unfortunately, this procedure exchanges the sign problem with the *overlap problem*. That is to say, there is a mismatch between the distribution of $w(\mu)$ and the probability measure in $\mathcal{Z}(0)$ which gets worse for larger μ. In general, the overlap problem therefore leads to systematic errors since the tails of the distribution of $w(\mu)$ get cut off by the importance sampling of $\mathcal{Z}(0)$.

On the other hand, a commonly used strategy is to employ *Taylor expansions* of observables around $\mu = 0$, where there is no sign problem [68, 75, 77, 119–123]. For the grand potential, e.g., this expansion reads

$$\ln \mathcal{Z}(T,\mu) = \sum_{k=0}^{\infty} C_k(T) \left(\frac{\mu}{T}\right)^k, \quad C_k(T) = \frac{T^k}{k!} \frac{\partial^k}{\partial \mu^k} \ln \mathcal{Z}(T,\mu) \bigg|_{\mu=0} . \tag{2.47}$$

Here, C_k labels the (temperature-dependent) Taylor coefficients. While the overall idea is straightforward, it entails many downsides. First, Taylor expansions build on analyticity of the underlying function. This is fine for the crossover region in the QCD phase diagram but fails in the vicinity of the CEP and the first-order phase transition. In general, the radius of convergence is restricted by non-analyticities in the complex imaginary μ plane (see Section 5.3). Additionally, higher-order derivatives get increasingly difficult to calculate.

Finally, one can consider *imaginary values* for the chemical potential, obtain results there and consequently perform an extrapolation to real values [1, 69, 129–132]. Imaginary chemical potentials are conceptually unproblematic since they retain γ_5 Hermiticity. This way, they do not induce an imaginary part in the fermion determinant and thus do not lead to a sign problem. We will elucidate those and the associated extrapolation methods in more detail in Chapter 5.

Chapter 3
Dyson–Schwinger Equations

In this chapter, we want to build on the brief introduction in Chapter 1 and outline *Dyson–Schwinger equations* (DSEs) as the central framework our calculations are based on in detail. In contrast to lattice field theories, they do not rely on a direct calculation of the path integral but are rather derived from functional derivatives of the generating functional(s). This procedure results in the exact, non-perturbative equations of motion for the correlation functions of a QFT. As a very versatile approach, there is a wide range of applications apart from investigations of the QCD phase diagram. DSEs are often combined with *Bethe–Salpeter equations* (BSEs) [204] and/or *Faddeev equations* [205] to describe bound states. Famously and successfully, this allows to study hadron spectroscopy of, e.g., mesons [206], baryons [207], tetraquarks [208] and glueballs [209]. In addition, DSEs have been applied – among other things – to QED in $2+1$ dimensions [115, 210], the anomalous magnetic moment of the muon [211, 212], form factors and electromagnetic decays of hadrons [213, 214].

This chapter is aimed at conveying the most important background information, concepts and terminology of DSEs especially in view of the calculations to come. To this end, we begin with an outline of the basic idea and central relations. We proceed with a revision of the *quark condensate* as the order parameter of chiral symmetry breaking and the main quantity of interest for the calculations in this thesis. Thereafter, we specify our discussion by the examples of the QCD propagators, which we also use to establish *dressing functions*. Together, this enables us to elucidate different *truncation schemes* for QCD centred around the quark propagator in more detail and motivate the truncation employed for our investigations.

3.1. Background and Fundamentals

Since the generalities of DSEs are topics readily available in standard textbook like [36, 38] and the reviews [153, 215, 216], we keep this first section rather concise. The underlying idea of Dyson–Schwinger equations is based on the fact that the integral over a total derivative evaluates to zero if the integrand vanishes on the integration bounds. Quantum fields have to vanish at infinity for normalization purposes so we are able to apply this idea to the path-integral formulation of the generating functional of a QFT, which yields

$$0 = \int \mathcal{D}\varphi \, \frac{\delta}{\delta\varphi_i} \exp\bigl(-\mathcal{S}[\varphi] + \langle \varphi, J\rangle\bigr) = \int \mathcal{D}\varphi \left(-\frac{\delta \mathcal{S}[\varphi]}{\delta\varphi_i} + J_i\right) \exp\bigl(-\mathcal{S}[\varphi] + \langle \varphi, J\rangle\bigr)\,, \tag{3.1}$$

where $\mathcal{S}$ denotes the Euclidean action, $\varphi = (\varphi_i)$ is a generalized quantum field and $J = (J_i)$ labels a generalized source field. In the case of QCD, we have $\varphi_i \in \{\psi, \overline{\psi}, A, c, \overline{c}\}$ and $J_i \in \{\overline{\eta}, \eta, j, \overline{\sigma}, \sigma\}$ where all indices (colour, flavour and Lorentz) are again implicit. Rewriting above expression into a more convenient and familiar form, we already arrive at the central relation

for Dyson–Schwinger equations:[1]

$$\left\langle \frac{\delta \mathcal{S}[\varphi]}{\delta \varphi_i} - J_i \right\rangle = \left(\frac{\delta \mathcal{S}}{\delta \varphi_i} \left[\frac{\delta}{\delta J_k} \right] - J_i \right) \mathcal{Z}[J] = 0 \,. \tag{3.2}$$

This equation has the form of a one-point function of the source field. One can derive the corresponding DSEs for all higher correlation functions by taking an appropriate number of functional derivatives with respect to J_i, decomposing higher connected correlation functions into vertices and and finally setting $J \to 0$.[2] For this reason, it is often also called *master DSE*.

Since Equation (3.2) is derived from the generating functional $\mathcal{Z}$, the procedure described above results in the DSEs for *all* correlation functions – both connected and disconnected. Likewise, we are able to obtain the DSEs for other classes of correlation functions via analogous master DSEs for the respective generating functionals. We provide more detailed information on the ones mentioned here in Appendix B.2. Using $\mathcal{W} = \ln \mathcal{Z}$ as a basis, for instance, one obtains the master DSE of the connected correlation functions:

$$\frac{\delta \mathcal{S}}{\delta \varphi_i} \left[\frac{\delta \mathcal{W}[J]}{\delta J_k} + \frac{\delta}{\delta J_k} \right] \cdot 1 - J_i = 0 \,. \tag{3.3}$$

Additionally, we also want to address another often-used class of correlation functions corresponding to the *one-particle irreducible* (1PI) Feynman diagrams. These are defined as those graphs that cannot be made disconnected by cutting a single internal line. Their generating functional is the *effective action* Γ defined as the Legendre transform of $\mathcal{W}$ with respect to J, which leads to the definition of the *classical field* $\Phi \coloneqq \langle \varphi \rangle_J$ as the transformed variable. The corresponding master DSE for Γ reads

$$\frac{\delta \mathcal{S}}{\delta \varphi_i} \left[\Phi_k + \left\langle \left(\frac{\delta^2 \Gamma[\Phi]}{\delta \Phi_k \delta \Phi_\ell} \right)^{-1}, \frac{\delta}{\delta \Phi_\ell} \right\rangle \right] \cdot 1 - \frac{\delta \Gamma[\Phi]}{\delta \Phi_i} = 0 \,. \tag{3.4}$$

Sometimes, it is useful to work with *n-particle irreducible* (*n*PI) correlation functions to, for instance, construct truncation schemes or to show analytical relations. These are an extension of the 1PI idea and are defined analogously by demanding that their Feynman diagrams cannot be made disconnected by cutting n internal lines. The associated generating functionals are obtained by performing further Legendre transforms of the effective action with respect to source fields for higher n-point functions. One can find analogous equations of motion for those as well [219, 220].

At this point, a short clarification of commonly used nomenclature is beneficial. When dealing with DSEs, both perturbative and non-perturbative quantities appear. On the one hand, perturbative quantities will also be denoted with the adjectives *free* or *bare*. On the other hand, non-perturbative quantities will equivalently be called *full* or *dressed*. All of these expressions may be used interchangeably and do not carry a special meaning.

[1] Here and in the following, the argument of the action with index k is to be understood as a replacement rule for all contributing fields, e.g., $\mathcal{S}\left[\partial/\partial J_k\right] \coloneqq \mathcal{S}[\varphi]\big|_{\varphi_k \to \partial/\partial J_k}$.

[2] Due to this formulaic approach, there are numerous programs that automate the derivation of DSEs both algebraically and numerically [217, 218].

3.2. Interlude: Chiral Phase Diagram and Quark Condensate

As a motivation for everything to come, we recall the main goal of this thesis: investigating the QCD phase diagram using Dyson–Schwinger equations. As is well-known from statistical mechanics, a thermodynamic system can be completely described by its *thermodynamic potential*. In our case – studying a system of QCD matter allowed to exchange both energy and particles with a heat bath – it is given by the *grand potential* which depends on temperature T and the chemical potentials of all particle flavours f in the system $(\mu_f) \in \mu$:

$$\Omega(T,\mu) = -\frac{T}{V} \ln \mathcal{Z}(T,\mu) \,. \tag{3.5}$$

In principle, it would therefore suffice to calculate Ω. However, doing so is a highly non-trivial task since a direct calculation of the path integral is out of the question for interacting theories. Unfortunately, DSEs themselves are also not ideally qualified for this purpose since – by their very definition – they only involve derivatives of the grand-canonical partition function $\mathcal{Z}$. As a consequence, many thermodynamical observables – such as pressure or entropy – are not directly accessible utilizing DSEs (apart from simple truncations), although there has been some effort in this direction recently [48, 221].

The *quark condensate* being the order parameter for DCSB, however, is very well suited for an analysis using DSE calculations since it can be obtained directly from the dressed quark propagator S_f (see Appendix B.5):

$$\langle\overline{\psi}\psi\rangle_f(T,\mu) = \frac{\partial\Omega(T,\mu)}{\partial m_f} = -N_c Z_2^f Z_m^f \sum\!\!\!\!\!\!\int_q \mathrm{tr}\left[S_f(q_4 + \mathrm{i}\mu_f, \boldsymbol{q})\right] . \tag{3.6}$$

Here, m_f labels the bare (i.e., current-)quark mass, $N_c = 3$ denotes the number of colours, whereas Z_2^f and Z_m^f are the quark and quark-mass renormalization constants,[3] respectively. The summation over the Matsubara frequencies introduces both an explicit and an implicit dependence on temperature. As a result, we will focus exclusively on the quark condensate as an order parameter thoughout this thesis, instead of the Polyakov loop. Thus, whenever we refer to the QCD phase diagram, we imply the *chiral phase diagram* with respect to the quark condensate. In addition, this renders the dressed quark propagator one of our pivotal quantities of interest.

At this point, we want to make two remarks about the quark condensate for nonzero quark masses, $m_f > 0$. First, the integral in Equation (3.6) is quadratically divergent in the UV. For meaningful results, we consequently have to regularize the condensate. The precise regularization scheme will differ for the different investigations in Chapters 4 to 6. Second, for small chemical potentials, there is no classical phase transition between the chirally broken and symmetric phases but rather a smooth *crossover transition*. To be more specific, neither the condensate nor any of its derivatives become discontinuous. As a consequence, we instead define a *pseudo*critical transition temperature. Again, the definition of the pseudocritical temperature will depend on the respective analysis in Chapters 4 to 6.

[3] Due to the renormalization constants, Equation (3.6) represents the renormalized quark condensate.

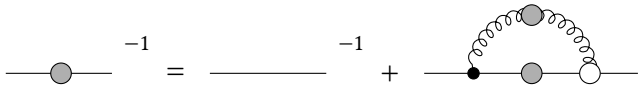

Figure 3.1.: Pictorial representation of the quark-propagator DSE. Gray dots represent dressed propagators, the white dots indicate dressed vertices, while small blacks dot denote bare vertices. Straight and curly lines illustrate quark and gluon propagators, respectively. Here, factors of i have already been absorbed in the sign of the quark self-energy.

Additionally, we clarify that setups at $T = 0$ will be referred to as *vacuum* whereas nonzero temperatures imply the existence of a heat bath and so they describe systems in *medium*.

3.3. DSEs of the QCD Propagators

Since we are interested in the dressed quark propagator, we concretize the considerations of Section 3.1 explicitly with the aid of the QCD propagators being the connected two-point correlation functions. As such, their corresponding DSEs can be obtained by one functional derivative of Equation (3.3). We do so sketchily by example of the quark-propagator DSE in Appendix B.4. Alternatively, a derivation of all QCD-propagator DSEs starting at Equation (3.2) can be found, e.g., in Ref. [153]. The resulting DSEs are displayed pictorially in Figures 3.1 to 3.3. In the following, we discuss each of them briefly.

In advance, we remark that all prefactors and signs are absorbed in the respective Feynman diagrams as a means of simplification. Additionally, the diagrams shown there not only comprise perturbative quantities but also non-perturbative ones indicated by large grey and white dots. Nonetheless, all Feynman rules apply to those equivalently. Moreover, we clarify that we will from now on implicitly assume propagator DSEs if not stated otherwise and just indicate the respective quantum field, e.g., ‘quark DSE’ instead of ‘quark-propagator DSE’.

The quark DSE is illustrated in Figure 3.1. For the quark propagator S_f of flavour f in vacuum, it reads (with Z_2^f, Z_m^f and m_f as in Equation (3.6))

$$S_f^{-1}(p) = S_{0f}^{-1}(p) + \Sigma_f(p)\,, \qquad S_{0f}^{-1}(p) = Z_2^f \cdot \left(\mathrm{i}\not{p} + Z_m^f m_f\right), \tag{3.7}$$

$$\Sigma_f(p) = g^2 C_F \frac{Z_2^f}{\tilde{Z}_3} \int \frac{\mathrm{d}^4 q}{(2\pi)^4} \gamma^\nu S_f(q) D_{\nu\rho}(k) \Gamma_f^\rho(p,q)\,. \tag{3.8}$$

Here, S_{0f}^{-1} labels the inverse, bare quark propagator and Σ_f represents the quark self-energy. Moreover, p denotes the external quark momentum, q the internal quark momentum and $k = p - q$ the gluon momentum. Additionally, γ^ν is a bare quark–gluon vertex, g indicates the strong coupling, while $\tilde{Z}_3$ labels the ghost renormalization constant.[4] The prefactor of $C_F = 4/3$ arises from performing the contractions over the colour indices (cf. Appendix C.3).

The quark DSE is self-consistent, i.e., the dressed quark propagator appears both on the left- and on the right-hand side. In addition, one also requires the dressed gluon propagator

[4] In Landau gauge, the ghost–gluon vertex is not ultraviolet divergent, so we can choose $\tilde{Z}_1 = 1$ [222]. This way, the STI for the quark–gluon vertex in Equation (2.15) simplifies to: $Z_{1F} = Z_2/\tilde{Z}_3$.

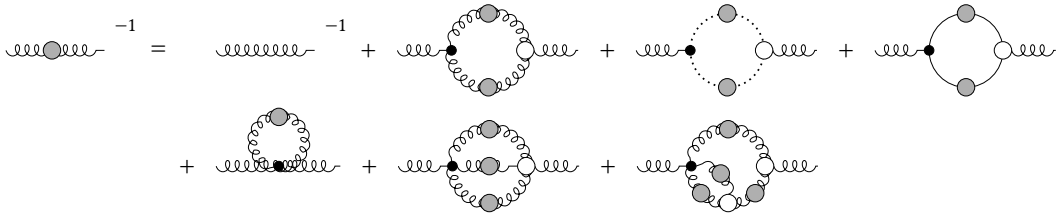

Figure 3.2.: Pictorial representation of the full gluon-propagator DSE. Dotted lines illustrate ghost propagators. Other lines and dots are to be understood as in Figure 3.1. All prefactors are absorbed in the respective diagrams.

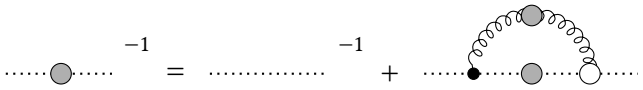

Figure 3.3.: Pictorial representation of the ghost-propagator DSE. Lines and dots are to be understood as in Figures 3.1 and 3.2.

$D_{\nu\rho}$ and the dressed quark–gluon vertex Γ_f^ρ in order to calculate the quark self-energy.

The gluon DSE in Figure 3.2, in contrast, is far more intricate due to all possible diagrams originating in the three- and four-gluon interactions inherited from the QCD Lagrangian. In addition to the purely gluonic diagrams, it also contains a quark and a ghost loop. As a consequence of this complicated nature, the full expression of the gluon DSE is rather lengthy which is why we refrain from showing explicit expressions here. However, a simplified version will be considered later in Section 3.5.2.

The ghost DSE in Figure 3.3, on the other hand, looks similar to the one of the quark propagator, except that quark propagators and the quark–gluon vertex are replaced by ghost propagators and a ghost–gluon vertex, respectively. For this reason and because it plays a negligible role in this thesis anyway, we also do not show a mathematical equation.

So far, all relations are exact, i.e., they have been derived directly from the generating functional(s) without any approximations.[5] The main complication, though, becomes apparent already at the level of the QCD propagators: Not only do the propagators themselves appear also on the right-hand side – i.e., all DSEs are self-consistent – but so do dressed vertices. These satisfy their own DSEs which, in turn, contain even higher correlation functions. As a consequence, the full system of DSEs implies a set of infinitely many, coupled equations. Only in certain limits can these be solved explicitly, e.g., in the deep infrared [180, 223–226]. For practical applications, one therefore has to reduce the set of considered DSEs to a finite number. It is vital that this process known as *truncation* be performed carefully in order not to distort the resulting physics, which is highly non-trivial. As a consequence, finding an appropriate truncation scheme is essential for obtaining a solvable set of equations that yields accurate results. In Section 3.5, we will elucidate the truncation scheme(s) employed in this work.

[5] One could argue, however, that the DSE of the gluon propagator still suffers from *Gribov copies* (see Appendix B.3) since it is a problem already at the path-integral level.

3.4. Dressing Functions

A commonly used strategy to parametrize dressed correlation functions is to resort to scalar functions that carry all non-perturbative information, the so-called *dressing functions*. That is, each possible tensor structure is multiplied with a corresponding dressing function that describes its momentum-dependent behaviour. Depending on the symmetries, the number of distinct dressing functions necessary for a description of the problem may be reduced significantly.

They also play an invaluable role when it comes to DSEs. This is due to the fact that one can project each equation onto the different tensor structures to obtain (scalar) DSEs for the dressing functions. The resulting *projected DSEs* are sets of coupled, self-consistent integral equations that are usually solved with a fixed-point iteration. Since the bare correlation functions have to be recovered in the UV, the asymptotic behaviour of the dressing functions is known, which is often used as a renormalization condition.

In the following, we explicate the statements from above by taking the example of the quark–gluon vertex in vacuum. Thereafter, we introduce and briefly explain the dressing functions of the quark and gluon propagators both in vacuum and in presence of a heat bath. This is mainly because their projected DSEs are the ones which are actually solved in the course of our calculations. Explicit expressions are provided in Appendix C.

3.4.1. Example: Quark–Gluon Vertex in Vacuum

While the bare quark–gluon vertex is proportional to γ^ν, the full vertex can generally comprise all kinematically possible tensor structures. It has two quark legs carrying a Dirac index each that couple to a gluon leg with a Lorentz index. The quark momenta are p^ν (ingoing) and q^ν (outgoing), while the gluon momentum is $k^\nu = p^\nu - q^\nu$ due to momentum conservation. Therefore, the possible structures are made up of the direct product between four Lorentz scalars, $\{\mathbb{1}, \not{p}, \not{q}, [\not{p}, \not{q}]\}$, and three four-vectors, $\{\gamma^\nu, p^\nu, q^\nu\}$. In total, the basis of all tensor structures is thus given by

$$\Gamma^\nu \propto \{\gamma^\nu, p^\nu, q^\nu\} \otimes \{\mathbb{1}, \not{p}, \not{q}, [\not{p}, \not{q}]\}\,, \tag{3.9}$$

which amounts to twelve basis elements in vacuum. Consequently, the full vertex could be parametrized as follows:

$$\Gamma^\nu(p,q) = h_1(p,q)\gamma^\nu + \sum_{i=2}^{12} h_i(p,q) T_i^\nu(p,q)\,. \tag{3.10}$$

Here, h_i denotes the dressing functions while T_i^ν labels the basis elements of the vertex decomposition. Due to the known perturbative behaviour, we can infer the ultraviolet running of the dressing functions, i.e., $h_1 \sim Z_{1F}$ and $h_i \sim 0$ otherwise. Since the choice of the basis elements is not unique, neither is the definition of the dressing functions and their precise form depends on the chosen decomposition [227].

3.4.2. Quark and Gluon Propagators

Vacuum

A dressed (inverse) quark propagator with momentum p^ν in vacuum has two tensor structures, proportional to $\not{p}$ and $\mathbb{1}$, respectively. As a consequence, we introduce two dressing functions A_f and B_f, such that

$$S_f^{-1}(p) = \mathrm{i}\not{p}A_f(p) + B_f(p)\,. \tag{3.11}$$

The interpretation of these dressing functions becomes apparent by looking at the actual propagator rather than its inverse. This way, we can identify the momentum-dependent quark wavefunction $Z_f = A_f^{-1}$ and mass function $M_f = B_f/A_f$ in a well-known parametrization:

$$S_f(p) = Z_f(p)\big(\mathrm{i}\not{p} + M_f(p)\big)^{-1}\,. \tag{3.12}$$

The latter can be interpreted as the constituent-quark mass for small momenta while it approaches the current-quark mass in the ultraviolet. Therefore, both B_f and M_f serve as measures for the strength of (dynamical) chiral symmetry breaking at momentum p.[6]

Next, we consider the free gluon propagator in an arbitrary R_ξ gauge with implicit colour indices,

$$D^0_{\nu\rho}(k) = \left(\delta_{\nu\rho} - \frac{k_\nu k_\rho}{k^2}\right)\frac{1}{k^2} + \xi\frac{k_\nu k_\rho}{k^2}\frac{1}{k^2} =: P^{\mathcal{T}}_{\nu\rho}\frac{1}{k^2} + \xi P^{\mathcal{L}}_{\nu\rho}\frac{1}{k^2}\,. \tag{3.13}$$

Here, the gluon propagator was decomposed into parts transversal and longitudinal to the four-momentum. To this end, we introduced the transverse and longitudinal projectors, $P^{\mathcal{T}}$ and $P^{\mathcal{L}}$, respectively. Since we always work in Landau gauge, $\xi \to 0$, the longitudinal part vanishes and we need only one gluon dressing function Z in vacuum. Thus, the dressed gluon propagator is parametrized as

$$D_{\nu\rho}(k) = P^{\mathcal{T}}_{\nu\rho}\frac{Z(k)}{k^2}\,. \tag{3.14}$$

Medium

As outlined in Appendix B.1.1, the Euclidean energy variable at a nonzero temperature is only able to assume values of the discrete Matsubara frequencies. This special treatment of the fourth momentum component, though, breaks O(4) momentum symmetry. This can also be interpreted as the need to fix a frame of reference due to the presence of the heat bath. In our case, it is most convenient to work in its rest frame, i.e., we choose $u = (1, \mathbf{0})$ for the heat-bath velocity vector.[7]

In medium, the inverse quark propagator therefore gains an additional dressing function C_f to account for the behaviour of the temporal part:

$$S_f^{-1}(p_4, \boldsymbol{p}) = \mathrm{i}\gamma_4 p_4 C_f(p_4, \boldsymbol{p}) + \mathrm{i}\boldsymbol{\gamma}\cdot\boldsymbol{p}A_f(p_4, \boldsymbol{p}) + B_f(p_4, \boldsymbol{p})\,. \tag{3.15}$$

[6] This is underpinned by the fact that the quark condensate is predominantly driven by the scalar part of the quark propagator, i.e., the B_f function.

[7] Sometimes, it is beneficial to work in another frame and choose $u \neq (1, \mathbf{0})$, e.g., for treating in-medium bound states.

In principle, another tensor structure proportional to $\gamma_4 \boldsymbol{\gamma}$ would also be possible. However, it turns out that its associated dressing function is heavily suppressed [228] and will thus be neglected henceforth.

Likewise, the gluon propagator splits into two parts, one transversal and one longitudinal to the heat bath,

$$D_{\nu\rho}(k) = P^T_{\nu\rho} \frac{Z^T(k)}{k^2} + P^L_{\nu\rho} \frac{Z^L(k)}{k^2} , \tag{3.16}$$

$$\text{where} \quad P^{\mathcal{T}}_{\nu\rho} = P^T_{\nu\rho} + P^L_{\nu\rho} \quad \text{with} \quad P^T_{\nu\rho} = \left(\delta^{ij} - \frac{k^i k^j}{\boldsymbol{k}^2} \right) \delta_{i\nu} \delta_{j\rho} . \tag{3.17}$$

Here and in the following, longitudinal and transversal always refer to the three-dimensional finite-temperature kinematics with respect to the heat bath and not the four-dimensional vacuum one as a means of simplification.

3.5. Truncations

Based on the previous explanations, we conclude by motivating the truncation(s) we utilize for our investigations of the QCD phase diagram. To do so, we first elucidate different truncation schemes centred around the quark DSE in general.

3.5.1. Truncation Schemes of the Quark DSE

In the long run, the aim is to construct a self-consistent, parameter-free truncation to get results for QCD from first principles. A possible way to do so is to include all correlation functions up to a certain order and approximate higher-order ones until some kind of convergence is achieved [207]. Systematically, a self-consistent set of m-point functions can be obtained with an l-loop expansion of the nPI effective action (where $l \geq n$ and $m \geq n$) [229]. There are indications that a restriction of this procedure to all primitively divergent correlation functions, i.e., all correlation functions that appear explicitly inside the Lagrangian, is a reasonable cutoff point [230]. While this would also include the four-gluon vertex, results of a pure-Yang–Mills system up to the three-gluon vertex in vacuum have been obtained for the glueball spectrum in Ref. [231]. These match lattice results within error bars which is a highly encouraging result.

For systems with quarks, however, the main obstacle to this is the quark–gluon vertex due to its complicated nature (see Section 3.4.1). While it has been investigated in some detail in vacuum with the DSE framework using highly elaborate truncation schemes (see, e.g., Refs. [227, 232, 233] and the review Ref. [207]), the situation is much more dire at nonzero temperature. There, only a few exploratory studies exist [234, 235], which is also the case for other types of vertices [236]. As a consequence, the quark–gluon vertex has to be approximated somehow and we elucidate ways to do so below. For this reason, all of the following truncation schemes still necessitate some degree of modelling.

Rainbow–Ladder Truncation

Historically the first and still an often-used approach is to neglect any dynamics of the quark–gluon vertex in the quark DSE, consider only its leading tensor structure γ^ν and make a

model ansatz for the corresponding vertex dressing function. This procedure is known as the *rainbow–ladder truncation*.[8] Frequently and for reasons of simplicity, the gluon DSE is also not solved explicitly but a model ansatz for the gluon dressing function is chosen instead. This way, one is able to effectively treat the vertex as being bare and combine the product of gluon and vertex dressing functions to an effective interaction strength α. Its form is then motivated by physics such as the correct perturbative behaviour in the UV and required features in the IR. One famous model for the interaction strength in the rainbow–ladder truncation of DSEs is the *Maris–Tandy model* (see Appendix B.6).

In connection with our initial statements, the rainbow–ladder truncation can be identified with the leading-order term in a systematic loop expansion, so it is indeed a reasonable starting point. Additionally, it fulfils the axialvector WTI, thus preserving chiral symmetry breaking and the Goldstone-boson nature of the pion. It is therefore often used in a Bethe–Salpeter framework to study hadron spectroscopy and is able to, e.g., successfully reproduce the experimental masses of pseudoscalar and vector mesons [207]. Additionally, the structure of the rainbow–ladder truncation allows for an expression of the grand potential involving only the quark and gluon propagators that can be derived from the 2PI effective action [237]. This way, one may investigate, e.g., both thermodynamics [238] and inhomogeneous phases using a stability analysis based on differences in the grand potential [239].

Beyond Rainbow–Ladder

In spite of these successes, the rainbow–ladder truncation is still a very rough simplification and also has many shortcomings. For instance, it fails to accurately describe scalar and axialvector mesons due to missing tensor structures in the quark–gluon interaction [84]. On the other hand, the quality of results for the QCD phase diagram depends heavily on the features of the employed rainbow–ladder model. The non-trivial temperature and chemical potential dependence may not be accounted for appropriately without some modelled gluon screening mass. Additionally, the same model may yield accurate vacuum hadron physics but a wrong pseudocritical temperature for the same set of parameters [240].

There are different approaches trying to improve the vertex ansatz, which are usually referred to as truncations *beyond rainbow–ladder*. Their precise form depends both on the goal and the context they are supposed to be used in. As an example, one has the aforementioned constructions from nPI effective actions. In this work, on the other hand, we utilize an ansatz based on the *Ball–Chiu vertex construction* [241], which we will introduce and motivate in detail in the next section.

3.5.2. Unquenched Gluon Truncation

Finally, we are going to discuss the truncation that serves as the basis for all of our investigations. Its general idea is inspired by the fact that it is possible to separate the gluon DSE into a part of pure-Yang–Mills diagrams and a quark loop. The Yang–Mills part corresponds to

[8] Its name is inspired by certain properties of the Feynman diagrams resulting from this truncation. The first part stems from the fact that the Dyson series of the quark DSE consists only of a quark propagator emitting and absorbing an increasing number of gluon propagators which resembles a rainbow. Analogously, the BSE meson kernel comprises only gluon propagators between the internal quarks which looks like a ladder.

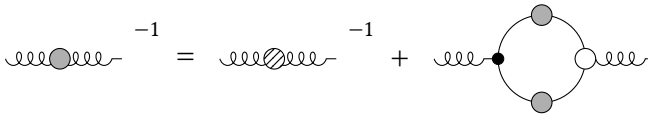

Figure 3.4.: Gluon-propagator DSE of Figure 3.2 split into quenched part and quark loop. The striped dot indicates the DSE of the quenched gluon propagator containing all pure-Yang–Mills diagrams.

the limit of infinitely heavy quarks, i.e., a *quenched* approximation. We recall that quenched calculations are comparably easy to perform in the framework of lattice QCD, so high-quality data for the corresponding gluon propagator at nonzero temperature is available. Since it is quite involved to investigate the temperature dependence of the full gluon DSE [242, 243], one may hence use the lattice data of the quenched propagator as a basis and perform only the explicit unquenching caused by the quark loop in the DSE framework.

As a result, the full gluon DSE displayed in Figure 3.2 reduces to the one in Figure 3.4. Introducing the quenched gluon propagator $D^{\text{que}}_{\nu\rho}(k)$, the unquenching gluon DSE in vacuum is explicitly given by

$$D^{-1}_{\nu\rho}(k) = \left(D^{\text{que}}_{\nu\rho}(k)\right)^{-1} + \Pi_{\nu\rho}(k)\,, \tag{3.18}$$

$$\Pi_{\nu\rho}(k) = -\frac{g^2}{2}\frac{1}{\tilde{Z}_3}\sum_f Z_2^f \int \frac{\mathrm{d}^4 q}{(2\pi)^4}\,\mathrm{tr}\left[\gamma_\nu S_f(p)\Gamma^f_\rho(p,q)S_f(q)\right]. \tag{3.19}$$

Here, $\Pi_{\nu\rho}$ labels the quark loop with the factor of $1/2$ originating in the trace over colour space (cf. Appendix C.3) that has already been performed. The flavour sum, $f \in \{\mathrm{u/d}, \mathrm{s}\}$, runs over the investigated $N_f = 2 + 1$ quark flavours.[9] We work in the isospin-symmetric limit of degenerate up and down quarks ($m_\mathrm{u} = m_\mathrm{d}$, $\mu_\mathrm{u} = \mu_\mathrm{d}$). In the current setup, the quark masses are fixed using results for the pion and kaon masses in vacuum obtained from the Bethe–Salpeter formalism developed in Ref. [244]. This leads to values of $m_\mathrm{u} = 0.8\,\mathrm{MeV}$ and $m_\mathrm{s} = 20.56\,\mathrm{MeV}$ at a renormalization point of 80 GeV.

As a consequence of the explicit unquenching, the quark DSE in Equations (3.7) and (3.8) and the gluon DSE in Equations (3.18) and (3.19) are coupled nontrivially. Therefore, the gluon depends on both temperature and (implicitly) quark chemical potential as well as the chiral dynamics of the quarks beyond modelling. Moreover, the different quark flavours also influence each other indirectly via the gluon. In order to render this system of equations self-consistent and thus solvable, we consequently require parametrizations of the quenched gluon propagator and the quark–gluon vertex as input. We discuss both of these in detail below. Since the ghost loop is accounted for by the quenched gluon propagator, the ghosts decouple completely in our truncation and their DSE does not have to be calculated.

This approach was first introduced in Ref. [111] – yet without unquenching and based on an SU(2) gluon – for a study of the deconfinement transition of $N_f = 2$ flavours. Ever since, the present truncation has evolved greatly [78, 245, 246] and has been applied very successfully to

[9] The influence of the charm quark on the QCD phase diagram has been addressed in [78] and found to be negligible. Thus, we will not consider heavier flavours than strange quarks from now on.

different aspects of the QCD phase diagram (for a review, see Ref. [84]). This includes – among others – hadronic backcoupling effects [80, 247–249], different regions of the Columbia plot, the Polyakov loop and imaginary chemical potentials [112, 250–253], as well as an exploratory study of thermodynamics in the DSE framework [221]. As a consequence, there have also been many previous PhD theses centred around this truncation [48, 49, 228, 234, 254–257], which makes it a very sophisticated and well-studied approach.

Quenched Gluon

The modelled dressing function of the quenched gluon comprises two parts: the lattice fit in the IR and the known perturbative UV behaviour. In total, it is given by [245]

$$Z_{\mathrm{que}}^{T/L}(k) = \frac{y}{(1+y)^2}\left[\left(\frac{c}{y + a_{T/L}(T)}\right)^{b_{T/L}(T)} + y \cdot \left(\frac{\beta_0 \alpha_s}{4\pi}\ln(1+y)\right)^{\gamma}\right], \quad y = \frac{k^2}{\Lambda^2}, \tag{3.20}$$

where k denotes the gluon four-momentum. In the ultraviolet part, $\gamma = (-13N_c{+}4N_f)/(22N_c - 4N_f)$ represents the anomalous dimension of the gluon, $\alpha_s = 0.3$ labels the running coupling at some chosen scale, while $\beta_0 = (11N_c - 2N_f)/3$ denotes the QCD beta function to lowest order perturbation theory, where of course $N_c = 3$. In the case of an explicit unquenching, Equation (3.20) describes a genuine quenched gluon, i.e., $N_f = 0$. If the quark loop is neglected, one has to adjust N_f to the number of considered quark flavours to ensure the correct running in the UV.

The infrared parameters are obtained by fits to the lattice data in Ref. [258]. Above, $c = 5.87$ and $\Lambda = 1.4\,\mathrm{GeV}$ label temperature-independent scales while the crucial part of the parametrization is given by the temperature-dependent parameters a and b which come in a transversal and longitudinal version each [245, 255],

$$a_T(T) = \begin{cases} 1.1010 \cdot t^2 + 0.5950 & t \leq 1 \\ 0.8505 \cdot t - 0.2965 & t > 1 \end{cases}, \quad a_L(T) = \begin{cases} 0.4005 \cdot t^2 - 0.9025 \cdot t + 0.5950 & t \leq 1 \\ 3.6199 \cdot t - 3.4835 & t > 1 \end{cases}, \tag{3.21}$$

$$b_T(T) = \begin{cases} 0.5548 \cdot t^2 + 1.3550 & t \leq 1 \\ 0.4296 \cdot t + 0.7103 & t > 1 \end{cases}, \quad b_L(T) = \begin{cases} 0.3287 \cdot t^2 - 0.5741 \cdot t + 1.3550 & t \leq 1 \\ 0.1131 \cdot t + 0.9319 & t > 1 \end{cases}, \tag{3.22}$$

where $t = T/T_{\mathrm{c}}^{\mathrm{YM}}$ denotes the reduced temperature with respect to the pure-Yang–Mills transition temperature, $T_{\mathrm{c}}^{\mathrm{YM}} = 277\,\mathrm{MeV}$.

One downside of our unquenching procedure is that Equation (3.20) neglects potential backcoupling effects of the quarks onto the quenched gluon propagator. However, there are numerous studies of a pure-Yang–Mills system with DSEs in vacuum (see Ref. [217] for a review), so this effect has already been investigated in Ref. [222] and found to be well below five per cent [84]. Nevertheless, it is unfortunately unknown how this changes at nonzero temperature and especially chemical potential.

Ansatz for the Quark–Gluon Vertex

In contrast to the quenched gluon propagator, lattice studies of the quark–gluon vertex – especially in medium – are still exploratory and currently underway [259, 260] so they cannot serve as input, yet. As an alternative, it was proposed in Refs. [82, 83, 261] to instead use the vacuum result of FRG calculations and employ difference DSEs for the corrections due to medium effects.

In our truncation, however, we utilize an extension of the bare vertex based on WTI-inspired proposals put forward by James S. Ball and Ting-Wai Chiu in Ref. [241]. For the vacuum-fermion–photon vertex of QED, they employed the Ward–Takahashi identity

$$\mathrm{i}k_\nu \Gamma_f^\nu(p,q) = S_f^{-1}(p) - S_f^{-1}(q) = \mathrm{i}\not{p} A_f(p) - \mathrm{i}\not{q} A_f(q) + B_f(p) - B_f(q)\,, \tag{3.23}$$

and the absence of kinematic singularities in order to reduce the number of independent dressing functions in the longitudinal part of the vertex down to eight (recall the vertex decomposition in Section 3.4.1). The part of the full vertex that fulfils Equation (3.23) and is free of kinematic singularities in the limit $k \longrightarrow 0$ can be parametrized as

$$\Gamma_{0,f}^\nu(p,q) = \frac{A_f(p)+A_f(q)}{2}\gamma^\nu + \frac{A_f(p)-A_f(q)}{p^2-q^2}\frac{\not{p}+\not{q}}{2}(p+q)^\nu + \frac{B_f(p)-B_f(q)}{\mathrm{i}\left(p^2-q^2\right)}(p+q)^\nu\,. \tag{3.24}$$

As a consequence, the full QED vertex is given by

$$\Gamma_f^\nu(p,q) = \Gamma_{0,f}^\nu(p,q) + \sum_i h_{i,f}(p,q) T_i^\nu(p,q)\,, \quad \text{with} \quad k_\nu T_i^\nu(p,q) = 0\,. \tag{3.25}$$

Here, T_i labels the remaining transverse tensor structures that are not constrained by above WTI and $h_{i,f}$ their respective dressing functions.

Moving from QED to QCD, the non-Abelian STI equivalent of Equation (3.23) reads [262]

$$\mathrm{i}k_\nu \Gamma_f^\nu(p,q) = G\left(k^2\right)\left[H_f(p,q)S_f^{-1}(p) - S_f^{-1}(q)\tilde{H}_f(p,q)\right], \tag{3.26}$$

where G labels the ghost dressing function while H and its conjugate $\tilde{H}$ are non-standard vertices related to the quark–ghost scattering kernel [263].

We use Equation (3.24) as the basis for an improvement of the bare quark–gluon vertex. Still, we make some simplifications. That is, we only consider the leading γ^ν tensor structure of the Abelian Ball–Chiu vertex Γ_0^ν and neglect all other terms and tensor structures. We try to account for the non-Abelian effects and the missing tensor structures with an appropriate choice for a vertex dressing function $\Gamma(x)$ where x labels a momentum argument, which we will come to shortly. In vacuum, our ansatz for the vertex is thus given by

$$\frac{1}{\tilde{Z}_3}\Gamma_f^\nu(p,q) = \Gamma(x)\frac{A_f(p)+A_f(q)}{2}\gamma^\nu\,, \tag{3.27}$$

where the momentum x is specified below. In medium, all involved tensor structures again split up into a part transversal and longitudinal to the heat bath. Consequently, our Ball–Chiu-inspired quark–gluon-vertex ansatz reads

$$\frac{1}{\tilde{Z}_3}\Gamma_f^\nu(p,q) = \Gamma(x)\left(\delta^{\nu i}\gamma_i\Gamma_f^s(p,q) + \delta^{\nu 4}\gamma^4\Gamma_f^4(p,q)\right) =: \Gamma(x)\Gamma^\nu_{\mathrm{BC},f}(p,q)\,, \tag{3.28}$$

$$\text{where}\quad \Gamma_f^s(p,q) = \frac{A_f(p)+A_f(q)}{2}\quad\text{and}\quad \Gamma_f^4(p,q) = \frac{C_f(p)+C_f(q)}{2}\,. \tag{3.29}$$

Here $p \to \tilde{p} = (\boldsymbol{p}, p_4 + \mathrm{i}\mu)$ and $q \to \tilde{q} = (\boldsymbol{q}, q_4 + \mathrm{i}\mu)$ label the quark momenta in medium [111].

Just as for the quenched gluon propagator, the parametrization of the quark–gluon-vertex dressing function Γ is made up of an infrared and an ultraviolet part. The latter is again based on knowledge about the perturbative behaviour, which entails the non-perturbative and renormalization-group invariant definition of the corresponding running coupling of the quark–gluon vertex, $\alpha_{QG} \sim \alpha_s\Gamma^2 Z/A^2$ [111, 263]. For the infrared part, we compare Equations (3.23) and (3.26) to find that we require knowledge about the behaviour of G, H and $\tilde{H}$. In vacuum, the ghost dressing function G is well-known and exhibits an enhancement in the IR [217, 264]. While generally less investigated, there are indications that H and $\tilde{H}$ show an IR enhancement as well [265, 266]. Additionally, G is found to be largely independent from temperature across a broad temperature range [245, 267–269]. Therefore, we extract the momentum running from explicit results for the vertex DSE in vacuum [78].

Together, our quark–gluon-vertex dressing function should account both for non-Abelian dressing effects as well as for the correct ultraviolet momentum running of the vertex:

$$\Gamma(x) = \frac{d_1}{d_2+x} + \frac{x}{\Lambda^2+x}\left(\frac{\beta_0\alpha_s}{4\pi}\ln\left(1+x/\Lambda^2\right)\right)^{2\delta}\,. \tag{3.30}$$

In order to maintain multiplicative renormalizability of the gluon DSE, the momentum argument x is either given by the gluon momentum in the quark self-energy, $x = k^2$, or by the sum of the squared quark momenta in the quark loop, $x = p^2 + q^2$ [222]. In addition to the parameters β_0, α_s and Λ that appear identically also in Equation (3.20), $d_2 = 0.5\,\mathrm{GeV}^2$ is fixed to match its corresponding scale in the gluon lattice data whereas $\delta = -9N_c/(44N_c - 8N_f)$ denotes the perturbative anomalous dimension of the vertex.

The infrared vertex strength d_1, on the other hand, is the only free model parameter which is fixed to yield the desired pseudocritical temperature of the quark condensate. Since we will use varying definitions of the pseudocritical temperature in different contexts (cf. Section 3.2), the choice of d_1 will vary between the analyses in Chapters 4 to 6 and we comment on the precise parameter fixing in each chapter. See Table 3.1 for an overview.

Even though the modelled dressing function is independent of quark flavour, temperature and quark chemical potential, this information is (at least partially) accounted for by the quark dressing functions in the leading Ball–Chiu term. One major success of this approach is that it is able reproduce the unquenched gluon propagator from lattice calculations very well [84]. Additionally, we recover the desired perturbative running of the propagators and the quark condensate.

On the other hand, even this improved vertex ansatz is still a very rough approximation. First, we neglect all tensor structures except for γ^i and γ^4, even though especially scalar contributions are linked to the correct scaling behaviour in the vicinity of second-order phase

transitions [251]. Second, the infrared vertex-strength model parameter d_1 is taken to be independent of temperature and chemical potential. However, it should become smaller at high T and μ, which leads to discrepancies in observables obtained in DSE calculations as compared to lattice results [48, 79, 221]. In Chapter 6, we propose an improvement of the vertex that takes long-range correlations corresponding to an exchange of (pseudo)scalar mesons into account.

Hybrid Truncation

Last, we want to discuss a rainbow–ladder-like variation of the unquenched truncation originally conceived for uses in bound-state equations inside the QCD phase diagram in Ref. [248]. This is due to the fact that it fulfils the axialvector WTI (see Section 3.5.1). In order to keep as much of the improved Ball–Chiu vertex as possible, though, a bare vertex is employed only in the quark self-energy. As a consequence, the precise form of the vertex differs between quark self-energy and quark loop, indicated by subscripts Q and G, respectively. The resulting ansatz reads

$$\Gamma_f^\nu(p,q) \to \begin{cases} \Gamma_f^\nu(p,q)_Q = Z_2^f \gamma^\nu \Gamma\left(k^2\right) & \text{in the quark self-energy} \\ \Gamma_f^\nu(p,q)_G = \Gamma_{f,\mathrm{BC}}^\nu(p,q) \Gamma\left(q^2+p^2\right) & \text{in the quark loop} \end{cases} . \tag{3.31}$$

In addition, the vertex-strength parameter d_1 inside the vertex dressing function Γ also splits up. That is, we have d_{1G} in the quark loop, which is left unchanged as compared to the unmodified unquenched gluon truncation, and d_{1Q} in the quark self-energy, that is tuned to obtain the correct pseudocritical temperature, see again Table 3.1. Moreover, the quark masses have to be adjusted to $m_\mathrm{u} = 1.47\,\mathrm{MeV}$ and $m_\mathrm{s} = 37.8\,\mathrm{MeV}$ at a renormalization point of 80 GeV. The precise parameter-fixing procedure has been outlined in great detail in Ref. [49]. Due to the nonuniform treatment of the quark–gluon vertex, we refer to this setup as *hybrid truncation*. Even though designed for bound-state calculations, it turns out that the hybrid truncation yields a curvature of the pseudocritical crossover-transition line more consistent with lattice results [80].

Analysis	Truncation	Regulator	d_1 [GeV^2]
Section 4.2	Unquenched	Hard Cutoff	8.26
Section 4.3	Unquenched	Pauli–Villars	8.49
Chapter 5	Hybrid	Pauli–Villars	$d_{1Q} = 12.71$, $d_{1G} = 8.49$
Chapter 6	Unquenched + Mesons	Pauli–Villars	8.98

Table 3.1.: Overview of vertex-strength parameter(s) (d_1 for unquenched and d_{1Q}, d_{1G} for hybrid) for all combinations of truncations and regulators used throughout this thesis; see main text for details. The precise parameter-fixing criteria are detailed in the respective analyses.

Chapter 4
Finite-Volume Effects

In this first ouf our three results chapters, we investigate finite-volume effects on the QCD phase diagram. We recall from Chapter 1 that heavy-ion collisions naturally take place in a finite spatial volume. Therefore, theoretical finite-volume calculations serve as an important crosscheck with experiment for at least two reasons. First, the location of all phase boundaries – including the crossover at zero chemical potential, the CEP and the chiral first-order transition – will certainly become volume dependent for small-enough volumes. Second, volume effects on important observables such as fluctuations of conserved charges may be considerable and need to be taken into account. However, apart from that, effects due to changes in the volume are not only annoying artefacts but interesting in themselves from an academic point of view because they serve to probe the reaction of a physical system on one of its external parameters. This is what this chapter is devoted to and it is structured as follows.

We begin with an explanation how we implement a finite, three-dimensional box of equal edge lengths L into the DSE framework introduced in the last chapter, which also includes technical subtleties like the treatment of a zero mode. In particular, we motivate and introduce a method to get rid of cubic artefacts at large momenta in the ultraviolet that drastically improves the infinite-volume limit of our approach as compared to a naïve implementation. As a first numerical result, we illustrate finite-volume effects on the level of the quark propagator.

Next, we discuss our results for the volume dependence of the chiral crossover, its curvature and the CEP and compare improved with unimproved calculations. We contrast periodic and antiperiodic boundary conditions and vary the box size between $L = 3\,\text{fm}$ and $L = 8\,\text{fm}$. We trace the location of the CEP in the QCD phase diagram for various volumes and determine the box size necessary to approach the infinite-volume results. Furthermore, we discuss volume effects on the curvature of the crossover line at small chemical potential and compare with lattice QCD. This analysis is based on the one performed in Ref. [135]. In addition, we comment on two approximations/simplifications of finite-volume calculations found in the literature and compare it to our more sophisticated treatment.

Thereafter, we study the explicit and implicit volume effects in baryon-number fluctuations and ratios thereof for a similar range of different volumes around the location of the CEP. Before, we reiterate some background information about fluctuations of conserved charges in general and explicate how fluctuations are determined in this framework. Specifically, this includes a discussion of the regularization of the finite-volume quark-number density in our setup. This second half of the chapter was published to a large extend in Ref. [136].

4.1. Finite-Volume Setup

In this first section, we introduce the specifics about our finite-volume setup. While the first subsection covers some fundamental analytical details of the volume we are about to study,

the subsections therafter are necessary to properly adjust this setup to a practical treatment within our DSE framework.

4.1.1. Cubical Volumes

In order to study QFTs in a finite three-dimensional volume V, one is in principle free to choose an arbitrary shape so long as it is a subset of $\mathbb{R}^3$. This is due to the fact that introducing a finite volume into QFT corresponds mathematically "merely" to bounding the spatial integral inside the action in position space. At some nonzero temperature $T = \beta^{-1}$, this replacement reads

$$\int_0^\beta \mathrm{d}\tau \int_{\mathbb{R}^3} \mathrm{d}^3x \; \mathcal{L} \to \int_0^\beta \mathrm{d}\tau \int_V \mathrm{d}^3x \; \mathcal{L} \,. \tag{4.1}$$

In practice, however, the choice of suitable shapes is heavily constraint by computational feasibility. Among the few adequate options are cuboids, i.e., $V = [0, L_x] \times [0, L_y] \times [0, L_z]$, where L_i labels the edge length in i-direction, $i \in \{x, y, z\}$. As a means of simplification, we restrict ourselves to cubes with edge length $L = L_x = L_y = L_z$, which will serve as the shape of choice throughout this thesis. Still, choosing a shape alone is not sufficient, one also needs to specify boundary conditions on the fields.[1] While in temporal direction these are dictated by the spin–statistics theorem, there is no such restriction on the spatial components.[2] Again, for the sake of feasability, we therefore restrict ourselves to the description of *periodic boundary conditions* (PBC) and *antiperiodic boundary conditions* (ABC).

Employing a setup as described above, the introduction of finite-volume effects into the mathematical framework of QFT has close similarities with discribing a nonzero temperature with the Matsubara formalism (see Appendix B.1). That is, a discrete interval in position space combined with (anti)periodic boundary conditions leads to a discretization of the corresponding three-momentum components. Specifically, given some integrand f fulfilling above boundary conditions, one can introduce a finite three-dimensional volume by replacing all momentum integrals by their corresponding sums,

$$\int_{\mathbb{R}^3} \frac{\mathrm{d}^3q}{(2\pi)^3} \, f(\boldsymbol{q}) \to \frac{1}{L^3} \sum_{\boldsymbol{z} \in \mathbb{Z}^3} f(\boldsymbol{q}_{\boldsymbol{z}}) \,, \tag{4.2}$$

with $\boldsymbol{q}_{\boldsymbol{z}} = \sum_{i=1}^3 \omega_{z_i}^L \hat{e}_i$ denoting the possible momentum vectors, where $\{\hat{e}_1, \hat{e}_2, \hat{e}_3\}$ labels the Cartesian basis and $\omega_{z_i}^L$ indicates the *spatial Matsubara modes*:

$$\omega_m^L := \begin{cases} 2m\pi/L & \text{for PBC} \\ (2m+1)\pi/L & \text{for ABC} \end{cases}, \quad m \in \mathbb{Z} \,. \tag{4.3}$$

This underlines the resemblance between the mathematical structures of a nonzero temperature and a finite volume. Judging from that alone, one may already hypothesize that a decrease

[1] As stated in Section 3.1, these are fixed automatically in an infinite volume by normalization conditions, i.e., the fields have to vanish at infinity.

[2] It turns out that there are kinematic constraints on the gluon due to the structure of the quark self-energy and the quark-loop diagrams in our DSEs. For this reason, gluons are, in fact, restricted to PBC.

of the system size should have similar effects as an increase of the temperature due to the similar roles of L and β.

Above, we focused on the nonzero-temperature case and thus on three-dimensional volumes as this will pose the main part of our analysis. The vacuum, on the other hand, is characterized by O(4) invariance. That is, we treat the temporal component in the same way as the spatial components and consequently consider a finite *four-dimensional* volume. This way, the replacement in position space becomes

$$\int_{\mathbb{R}^4} \mathrm{d}^4x \; \mathcal{L} \to \int_{V_4} \mathrm{d}^4x \; \mathcal{L} \,. \tag{4.4}$$

As a result, the temporal momentum component – which is no longer specially distinguished – is also described by spatial Matsubara modes.

In advance, we remark on commonly used nomenclature in the context of finite-volume studies. Geometrically, a finite (four- or) three-dimensional volume with (anti)periodic boundary conditions corresponds to a *(hyper)torus*. Therefore, we frequently refer to a torus when talking about our finite-volume summations over the discrete grid of momentum vectors.

4.1.2. (Hyper)Cubic Artefacts

In view of the Dyson–Schwinger equations we are about to investigate, it is numerically beneficial to rewrite the summations in Equation (4.2) such that they resemble a spherical coordinate system [107]. This is due to the symmetries of the quark and gluon DSEs, i.e., they only ever depend on the magnitude of the momentum vectors and their angular distribution (see Appendix C.1). Therefore, we define:

$$\frac{1}{L^3} \sum_{\boldsymbol{z} \in \mathbb{Z}^3} f(\boldsymbol{q}_{\boldsymbol{z}}) =: \frac{1}{L^3} \sum_{j,m} f(\boldsymbol{q}_{jm}) \,. \tag{4.5}$$

Here, j denotes an index for spheres in momentum space that contain momentum vectors with an identical radius, $|\boldsymbol{q}_{\boldsymbol{z}}| = |\boldsymbol{q}_{jm}|$, and $m = m(j)$ labels the multiplicity of the individual momentum vectors on a given sphere j. The corresponding vectors are denoted by $\boldsymbol{q}_{jm}$.

At this point, we remark that a naïvely constructed momentum grid, which has an equal number of points in each direction, possesses the problem of *(hyper)cubic artefacts*. They are rooted in the mismatch between the cubic geometry of the finite momentum grid and the O(3)-symmetric continuum at large momenta. Due to the similar setup of lattice calculations compared to the framework described here, these also suffer from hypercubic artefacts and a number of methods has been developed to reduce them [270–272].

In our case, hypercubic artefacts are numerical inaccuracies caused by summing over *incomplete spheres*, which are characterized by gaining more points if the grid is enlarged. In Figure 4.1, we illustrate this phenomenon with the aid of two small two-dimensional grids – the left one for ABC and the right one for PBC. The possible momentum-grid points are depicted as black dots while complete spheres are represented by red, solid circles and the incomplete ones are blue and dashed. As one can see, we have a large number of complete spheres in the innermost region whereas the outermost spheres are necessarily incomplete.

Due to the momentum symmetries of our DSEs, they necessitate an O(3)-symmetric UV cutoff. Utilizing the replacement of Equation (4.2) and having identified the intricacies of

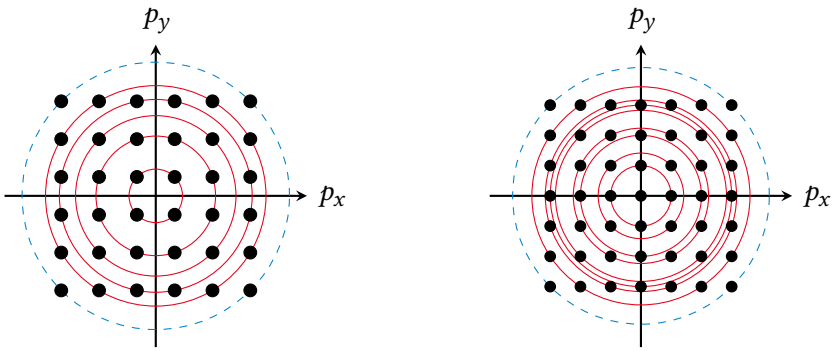

Figure 4.1.: Illustration of two-dimensional momentum grids with ABC (left) and PBC (right) adapted from those in Refs. [107, 109, 135, 273]. Red, solid circles represent complete spheres while the blue, dashed ones are incomplete (see text for details).

hypercubic artefacts, it is, however, straightforward to implement such a cutoff. That is to say, we only take complete spheres into account and discard the incomplete ones. As can be seen in Figure 4.1, this procedure corresponds geometrically to "cutting the edges" of the momentum grid and has long been used in earlier finite-volume DSE studies [107, 109].

4.1.3. Inclusion of the Zero Mode into DSEs

The next technicality we have to discuss in advance is how to include the PBC zero mode into our DSE framework. This is necessary since the projected DSE of the vector dressing function A is of the form (see Appendix C.1) (for the summation/integration symbol, see Appendix A.5)

$$A(p_4, \boldsymbol{p}) = Z_2 + Z_2 \frac{4\pi C_F}{\boldsymbol{p}^2} \sum\!\!\!\!\!\!\int_q \frac{A(q_4, \boldsymbol{q})(\Gamma_s K_{AAs} + \Gamma_4 K_{AA4}) + q_4 C(q_4, \boldsymbol{q})(\Gamma_s + \Gamma_4) K_{AC}}{q_4^2 C^2(q_4, \boldsymbol{q}) + \boldsymbol{q}^2 A^2(q_4, \boldsymbol{q}) + B^2(q_4, \boldsymbol{q})} \,. \tag{4.6}$$

Therefore, we have to show analytically that this expression stays well-defined in the limit $\boldsymbol{p} \to 0$. To this end, we analyse the limits of its angular integral kernels in the following. We recall that at nonzero temperature these read (with $k = (k_4, \boldsymbol{k}) = p - q$)

$$K_{AAs}(p, q) = (\boldsymbol{p} \cdot \boldsymbol{q}) \frac{k_4^2}{k^2} \frac{\alpha_L(k)}{k^2} + 2 \left(\frac{\alpha_T(k)}{k^2} - \frac{k_4^2}{k^2} \frac{\alpha_L(k)}{k^2} \right) \frac{(\boldsymbol{p} \cdot \boldsymbol{k})(\boldsymbol{q} \cdot \boldsymbol{k})}{\boldsymbol{k}^2} \,, \tag{4.7}$$

$$K_{AA4}(p, q) = (\boldsymbol{p} \cdot \boldsymbol{q}) \frac{k_4^2}{k^2} \frac{\alpha_L(k)}{k^2} \,, \quad K_{AC}(p, q) = (\boldsymbol{p} \cdot \boldsymbol{k}) \frac{k_4}{k^2} \frac{\alpha_L(k)}{k^2} \,. \tag{4.8}$$

It turns out that there are terms proportional to $|\boldsymbol{p}|^{-1}$, namely the ones containing dot products between $\boldsymbol{p}$ and $\boldsymbol{q}$. However, utilizing the symmetry of the angular sums, i.e., we always sum over both $\boldsymbol{q}$ and $-\boldsymbol{q}$, we can find that these terms cancel:[3]

$$\lim_{\boldsymbol{p} \to 0} \sum_m \frac{\boldsymbol{p} \cdot \boldsymbol{q}_{jm}}{\boldsymbol{p}^2} f(\boldsymbol{p} \cdot \boldsymbol{q}_{jm}) = 0 \,, \quad \text{with} \quad f(x) = f(0) + O(x) \,, \; f(0) \neq 0 \,. \tag{4.9}$$

[3] Actually, the same holds in infinite volume where the angular integrals of the dot products always vanish in this limit due to symmetry reasons.

Using these limits, we consequently obtain the following well-defined angular integrals:

$$\lim_{\boldsymbol{p}\to 0}\sum_m \frac{K_{AAs}(p,q)}{\boldsymbol{p}^2} = -2\left(\frac{\alpha_T(q)}{k_4^2+\boldsymbol{q}^2} - \frac{k_4^2}{k_4^2+\boldsymbol{q}^2}\frac{\alpha_L(q)}{k_4^2+\boldsymbol{q}^2}\right)\sum_m (1+z_m^2)\,, \quad z_m := \cos\sphericalangle(\boldsymbol{p},\boldsymbol{q}_m)\,, \tag{4.10}$$

$$\lim_{\boldsymbol{p}\to 0}\sum_m \frac{K_{AA4}(p,q)}{\boldsymbol{p}^2} = 0\,, \quad \lim_{\boldsymbol{p}\to 0}\sum_m \frac{K_{AC}(p,q)}{\boldsymbol{p}^2} = \frac{k_4}{k_4^2+\boldsymbol{q}^2}\frac{\alpha_L(q)}{k_4^2+\boldsymbol{q}^2}\,. \tag{4.11}$$

The same chain of reasoning also holds true even more straightforwardly in vacuum. As a consequence, there is no conceptual problem with the PBC zero mode within our DSE framework. For practical calculations, though, we have to treat it with special care nonetheless:

(i) Our kernels are not well-defined at $\boldsymbol{q} = \boldsymbol{0}$ for $k_4 = 0$, but smooth in the limit $|\boldsymbol{q}| \to 0$. Additionally, we always use a logarithmic mapping for the absolute value of our momentum vectors. Therefore, we set the magnitude of the zero mode to a small but nonzero value, $|\boldsymbol{q}_{\text{zero}}| = \varepsilon$, introducing an effective infrared cutoff. We have checked explicitly that variations of ε over several orders of magnitude from $\varepsilon = 1\,\text{MeV}$ down to $\varepsilon = 10^{-7}\,\text{MeV}$ lead to no noticeable differences in our results.

(ii) As seen above, the DSE kernels depend not only on the internal loop momentum $\boldsymbol{q}$ but also on the external momentum $\boldsymbol{p}$ and their dot product, which contains information on directions. The evaluation of this expression has to be modified if either $\boldsymbol{p}$ or $\boldsymbol{q}$ corresponds to a zero mode. In case of an internal zero mode, $\boldsymbol{q} = \boldsymbol{0}$, we set $\boldsymbol{p}\cdot\boldsymbol{q} = 0$. On the other hand, in case of an external zero mode, $\boldsymbol{p} = \boldsymbol{0}$, the angular information contained in $\boldsymbol{p}\cdot\boldsymbol{q}$ is important for the spherical sum over the loop momentum $\boldsymbol{q}$ with multiplicity index m in Equation (4.2). Therefore, in this case, we use $|\boldsymbol{p}_{\text{zero}}| = \varepsilon$ and employ the same directions/angles for the zero-mode momenta as for the first nonzero momentum shell. This due to the fact that the convergence of the expressions above depends on summing over both $\boldsymbol{q}$ and $-\boldsymbol{q}$.

In the literature, the zero mode frequently leads to numerical problems and its role for volume effects is often debated (see Section 4.3.3). To account for that and to investigate its influence, we also consider a setup of periodic boundary conditions with a discarded zero mode denoted by PBC*.

4.1.4. Naïve Approach: Pure Torus

In principle, the investigation of finite-volume effects in the framework of Dyson–Schwinger equations is now very straightforward. That is, one starts at the usual infinite-volume DSEs and replaces all occurring momentum integrals by their respective momentum sums as outlined above. In practice, however, restrictions of this naïve approach arise rather quickly. Since we require information about the angular distribution of the possible momentum vectors because of the scalar products inside the DSEs, one needs to keep information not only about the multiplicities but also about their angular dependence in memory for numerical calculations. While, due to symmetries of the possible momentum vectors, the total number of points required to store does not quite scale like $O(N^3)$ – where N is the number of spatial Matsubara

modes in each direction – large UV cutoffs Λ still become quickly unfeasible. Typically, we choose a value of $\Lambda = 10\,\mathrm{GeV}$. As a consequence, we have to adjust the renormalization procedure in this setup (see Appendix C.1.3).

As the very first foray into our investigations, we exemplarily show results for the dressing functions obtained in a finite volume in the left panels of Figure 4.2. More specifically, we display the momentum-dependent up-quark mass function $M_\mathrm{u} = B_\mathrm{u}/A_\mathrm{u}$ for the (temporal) Matsubara frequency with the smallest absolute value, ω_0^T, at a temperature of $T = 130\,\mathrm{MeV}$ for box sizes of $L = 3$, 5 and 8 fm.

Qualitatively, we immediately notice some features of the torus summation. First, one can see the emergence of discrete momentum shells which lie relatively far apart for the smallest momenta but become increasingly dense afterwards.[4] Second, ABC and PBC* develop an effective IR cutoff since the innermost possible momentum shell has a nonzero radius, $p_\mathrm{min}^\mathrm{ABC} \neq 0 \neq p_\mathrm{min}^{\mathrm{PBC}^*}$. In addition, the conjecture from above that L and β act similarly proved to be true. That is, a decreasing L acts chirally restoring which is obvious from the $L = 3\,\mathrm{fm}$ lines, especially for PBC*. Quantitatively, however, it is apparent that there is no consistent infinite-volume limit. While the behaviour for increasing system sizes is consistent within the finite-volume calculations, the $L = 8\,\mathrm{fm}$ line overshoots the infinite-volume one.

4.1.5. UV Improvement

Technically, the lack of an infinite-volume limit in the setup above can be attributed to two reasons that are hard to disentangle. First, the necessarily rather small UV cutoff leads to non-negligible cubic artefacts as already discussed above. Second, the renormalization point is inevitably located at even smaller momenta (8 GeV in our calculations) than the already small cutoff and thus too close to the infrared momentum region, where medium and finite-volume effects become important (see Appendix C.1.3). As a consequence, the renormalization constants are contaminated by medium and finite-volume artefacts.

In addition, the spherical finite-volume summation introduced above has a severe drawback in terms of numerical cost. The larger the grid the more dense are the complete outer spheres and the more points are on every one of these. Moreover, since the dressing functions run logarithmically as functions of large squared momenta in the UV, they do not change much from sphere to sphere in this region. Therefore, a lot of numerical effort is spent to integrate an almost constant function. Nevertheless, the effects due to the torus summation should only affect the infrared region anyway.

In order to remove all of the problems addressed above, we therefore proposed the following procedure. We consider discrete spheres only up to some matching cutoff Λ_vol and replace the spheres with radii between $\Lambda_\mathrm{vol}^2 < q^2 < \Lambda^2$ with a continuous momentum integral. As a consequence, the original replacement Equation (4.5) is modified such that an additional integral over the continuous momenta is added to the sum over the spatial modes:

[4] In the plot, it appears as if the shells become equidistant beyond some point. This is caused by numerical optimizations where higher momenta are interpolated (see Appendix D.1).

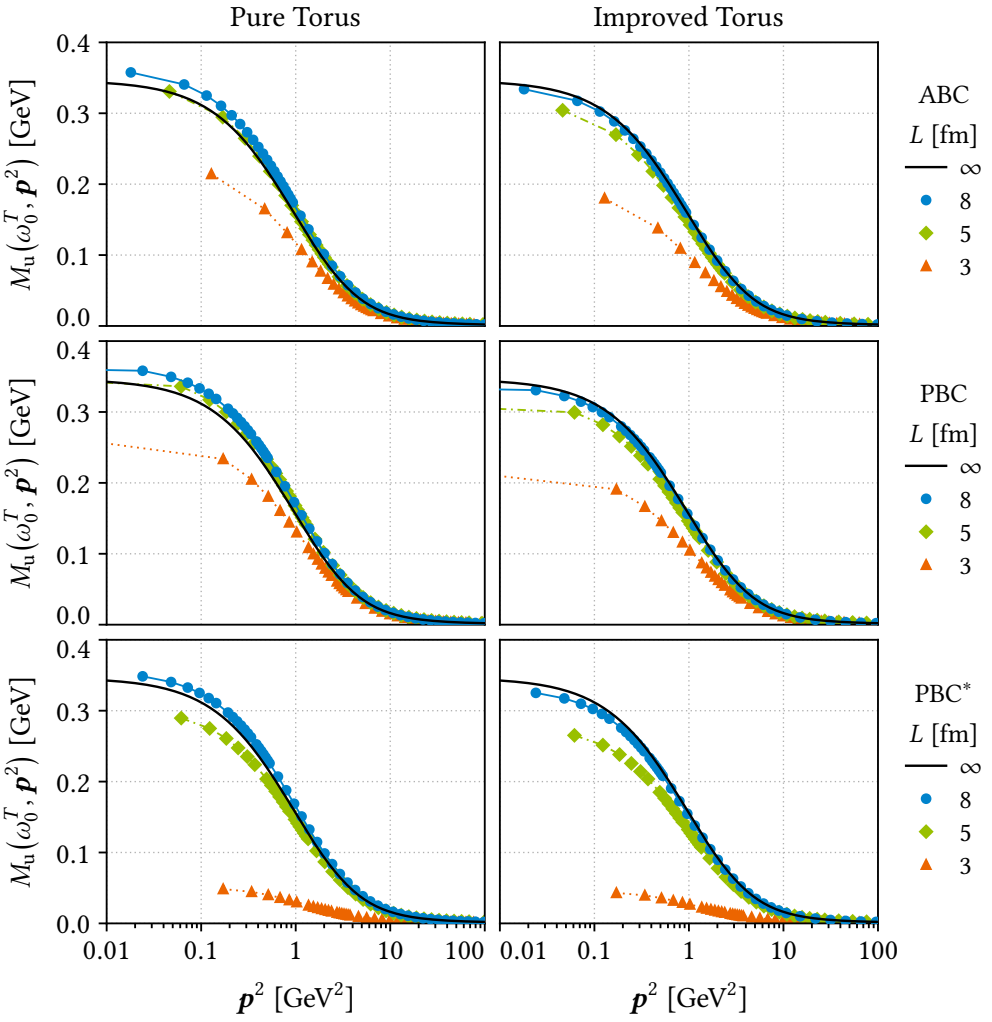

Figure 4.2.: Up-quark mass function $M_u = B_u/A_u$ as a function of momentum for different box sizes at $T = 130$ MeV and $\mu_B = 0$ compared to the infinite-volume result. We display results for both the pure torus (left) and the UV improvement (right) with ABC (top), PBC (middle) and PBC* (bottom). Finite-volume data points are connected by lines to guide the eye.

$$\int \frac{\mathrm{d}^3 q}{(2\pi)^3} f(\boldsymbol{q}) \;\to\; \frac{1}{L^3} \sum_{q_i \in \{\omega_{m_i}^L\}}^{|\boldsymbol{q}|<\Lambda_{\mathrm{vol}}} f(\boldsymbol{q}) + \int_{|\boldsymbol{q}|>\Lambda_{\mathrm{vol}}} \frac{\mathrm{d}^3 q}{(2\pi)^3} f(\boldsymbol{q})\,. \tag{4.12}$$

This modification – in the following called "(UV) improvement" – allows for arbitrarily large values for the ultraviolet cutoff Λ, which should mitigate artefacts that are caused by a potentially too small cutoff. In addition, this improvement also allows to renormalize the system at a large subtraction point where medium and volume effects are negligible. Thus, the renormalization procedure can be carried out identically as in infinite-volume calculations. Recently, a similar treatment has been used in Ref. [118] within a simpler truncation of the

corresponding DSEs.

The cutoff Λ_{vol} is chosen large enough that any further increase does not change the results. Typically, this is the case if it is larger than any other characteristic scale of the system like temperature, chemical potential and quark masses. In practice, we always generate a torus with the same size, e.g., $N = 25$ spatial Matsubara modes in each direction, and use the radius of the outermost complete sphere as Λ_{vol}. For more technical details, we refer to Appendix D.1.

In the right panels of Figure 4.2, we show results for the up-quark mass function obtained in our improved framework. As can be seen, the qualitative behaviour does not change at all, so the UV improvement preserves all important features of a pure torus. However, one can also observe that the $L = 8\,\text{fm}$ line is now much closer to the one for $L \to \infty$. We also performed calculations at even larger box sizes but since the results are similar to the infinite-volume ones on the per-mill level, we did not include them in the plot. As a consequence, we indeed now have a consistent infinite-volume limit.

We also investigated the gluon dressing functions. However, these are much less affected by the finite volume than the quark is.[5] The ones in the pure-torus setup can be found in Ref. [48] while the improved ones look essentially identical except for a better mid-momentum behaviour. For these reasons, we refrain from showing them here.

4.2. Numerical Results for the Quark Condensate

This completes our explanations about the general finite-volume setup and technicalities. Before we begin proceed with our investigation of finite-volume effects on the QCD phase diagram, we need to make some final clarifying remarks. First, the small UV cutoff of the pure torus prevents usage of a Pauli–Villars regulator. In order to properly compare all setups, we therefore employ a hard-cutoff regulator for any calculation in this section. To obtain the correct pseudocritical temperature in an infinite volume (see Section 4.2.2), our vertex-strength parameter is thus given by $d_1 = 8.26\,\text{GeV}^2$ (see also Table 3.1). Second, we need to specify how to regularize our order parameter, the quadratically divergent (up-)quark condensate in Equation (3.6). In our $(2+1)$-flavour framework, we can subtract the strange-quark condensate weighted with the up-to-strange mass ratio from the up-quark condensate which cancels the divergence. This defines the regularized condensate:

$$\Delta_{\text{us}} \coloneqq \langle\bar{\psi}\psi\rangle_{\text{u}} - \frac{Z_m^{\text{u}}}{Z_m^{\text{s}}}\frac{m_{\text{u}}}{m_{\text{s}}}\langle\bar{\psi}\psi\rangle_{\text{s}}\,. \tag{4.13}$$

Note that we are working with renormalized quantities, hence the appearance of the renormalization constants Z_m^f in order to preserve multiplicative renormalizability. Both for the improved torus and in infinite volume, the mass renormalization constants of all quark flavours are identical. For a pure torus, however, this is not the case so their ratio becomes important.

In the following, we now discuss and compare our numerical results for finite-volume effects on the QCD phase diagram without UV improvement with the ones including the UV improvement as discussed in Sections 4.1.4 and 4.1.5. We studied systems in boxes with edge

[5] Due to our ansatz, we neglected volume effects on the quenched gluon propagator. For the volumes investigated here, lattice calculations suggest that this approximation seems to be acceptable [245, 274–276].

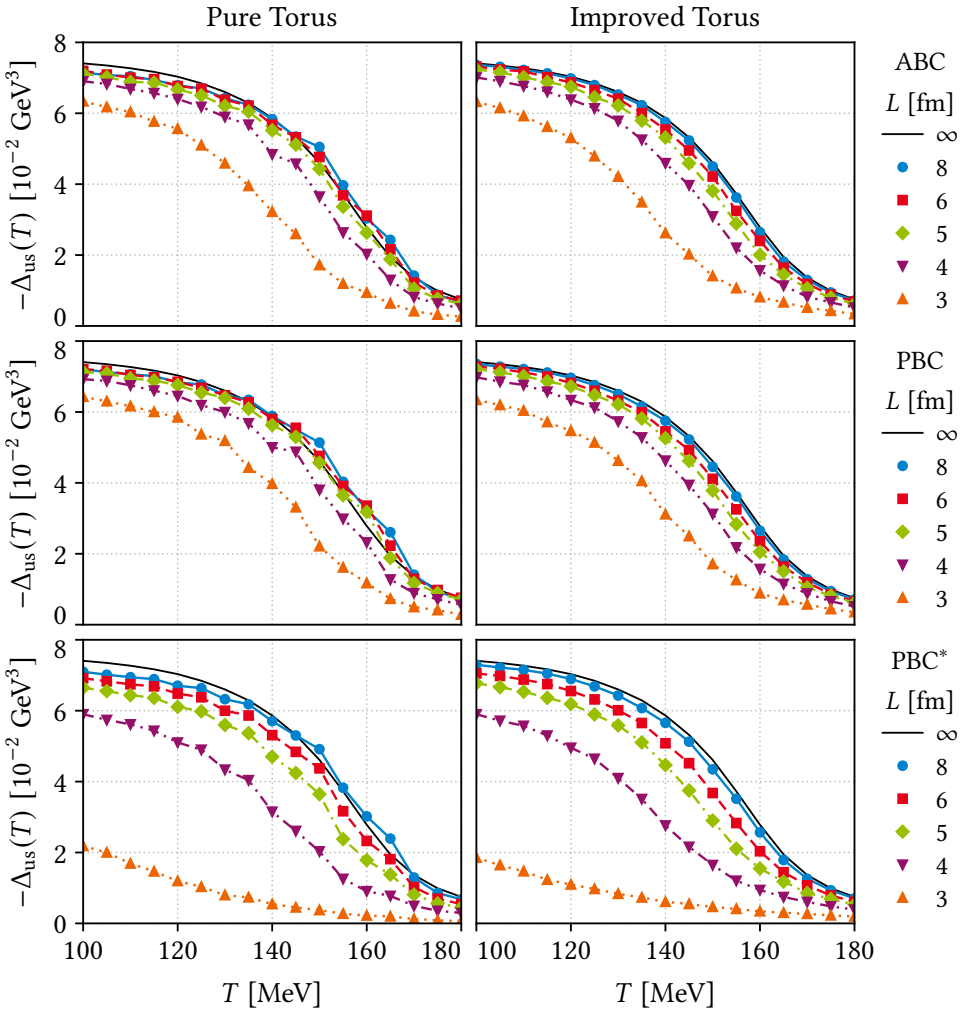

Figure 4.3.: Finite-volume effects of the quark condensate at vanishing chemical potential for different box sizes. We display results for both the pure torus (left) and the UV improvement (right). The phase diagrams are obtained with ABC (top), PBC (middle) and PBC* (bottom).

lengths of $L = 3, 4, 5, 6$ and 8 fm and contrast them to the infinite-volume limit. We do so for all boundary conditions, i.e., ABC, PBC and PBC*. A large part of this section is based on the published work in Ref. [135].

4.2.1. Quark Condensate at Vanishing Chemical Potential

We start our analysis with a brief discussion of the regularized condensate at vanishing chemical potential shown in Figure 4.3 as a function of temperature. We display results both in the unimproved (left column) and the improved setup (right column) for ABC (top row), PBC (middle row) and PBC* (bottom row), respectively.

Overall, we notice the following common features. First, the behaviour with resepect to decreasing system sizes is qualitatively identical, i.e., one can observe both a decrease of

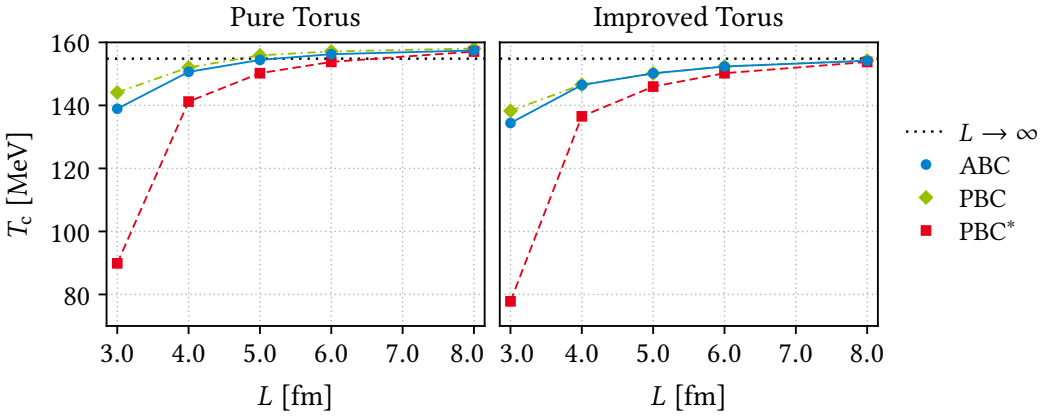

Figure 4.4.: Finite-volume effects without (left) and with (right) UV improvement. We display the dependence of the pseudocritical chiral transition temperature on the box size for ABC (blue circles), PBC* (red squares) and PBC (green diamonds). The black, dotted line is the infinite-volume result. Data points are connected by lines to guide the eye.

the magnitude of the condensate and a shift of the position of its inflection point to lower temperatures. While the curves of ABC and PBC are always very similar, the volume effects for PBC* are most pronounced. Additionally, we observe that the condensates of the pure-torus setup are rather unstable in temperature direction whereas they are very smooth for the improved torus. Again, the improved results exhibit a consistent infinite-volume limit.

4.2.2. Pseudocritical Temperature at Vanishing Chemical Potential

In view of our analysis of the crossover line, let us remark how we determine the pseudocritical chiral transition temperature T_c. Very commonly, one defines T_c is as the inflection point of the regularized quark condensate with respect to temperature:

$$T_c \coloneqq \arg\max_T \left| \frac{\partial \Delta_{us}}{\partial T} \right| . \tag{4.14}$$

To damp numerical instabilities in the condensates at finite volumes in temperature direction, especially in the pure-torus setup, we employ a hyperbolic-tangent fit that represents the condensate very well up to chemical potentials around the CEP, i.e., in the crossover region. The inflection point of the fit function determines T_c (see Ref. [48] for details on the precise procedure). For the sake of consistency, we also apply this fit procedure to the infinite-volume analysis. This, in turn, leads to (very) small changes in the transition temperatures as compared to previous works. For example, within the same truncation scheme, we find $T_c(L \to \infty) = 155(1)$ MeV at zero chemical potential in this work compared to $T_c(L \to \infty) = 156(1)$ MeV in the infinite-volume calculation of Ref. [79]. We emphasize that the difference is purely technical and very small.

In Figure 4.4, we display the pseudocritical chiral transition temperature T_c at vanishing chemical potential in both setups for antiperiodic and periodic spatial boundary conditions with and without zero mode for the quarks. For comparison, the infinite-volume result is indicated by a black, dotted line. Comparing both figures, we clearly see the effect of the UV

improvement at large volumes. In the unimproved case, our results for both ABC and PBC suffer from cubic artefacts and overshoot the infinite-volume line. In contrast, the improved results approach the infinite-volume results smoothly as discussed earlier.

At smaller box sizes, T_c decreases monotonically. While the decrease is rather moderate down to $L \approx 5\,\mathrm{fm}$, volume effects become much more pronounced for even smaller volumes. For example, at $L = 3\,\mathrm{fm}$ and PBC*, we find that T_c is almost halved as compared to infinite volume. In general, one can observe that quarks with PBC* are much more sensitive to finite-volume effects across all investigated box sizes. This is caused by the missing zero mode and the associated larger infrared cutoff introduced by the discrete momentum grid. From Equation (4.2), the ratio of the smallest possible momentum magnitude p_{min} between antiperiodic and periodic boundary conditions is given by $p_{\mathrm{min}}^{\mathrm{ABC}}/p_{\mathrm{min}}^{\mathrm{PBC}^*} = \sqrt{3/4} \approx 0.866$.

From Figure 4.4, it becomes apparent that the full PBC results, i.e., with zero mode, resemble closely the ones for ABC. Down to $L = 4\,\mathrm{fm}$, the ABC results lie on top of the PBC results with zero mode, and they differ only by around three per cent at our smallest investigated box size of $L = 3\,\mathrm{fm}$. This is true for both the unimproved and the improved setup.

For volumes as small as a box size of $L = 3\,\mathrm{fm}$, the system begins to enter what is called the epsilon regime in chiral perturbation theory [202]. In this region, the product $\alpha = m_f V \langle\bar{\psi}\psi\rangle_f^{L\to\infty}$ of quark mass, four-volume V and infinite-volume quark condensate becomes of order one and smaller and chiral symmetry starts to get restored already in the vacuum theory. While the full effect (including critical scaling with α) sets in only at much smaller volumes ($L \lesssim 2\,\mathrm{fm}$), first effects are already seen at our smallest box size of $L = 3\,\mathrm{fm}$ (see Section 4.2.5).

4.2.3. Crossover Line and Critical Endpoint

The finite-volume modifications on the phase structure are summarized in Figure 4.5. We show the phase diagrams for ABC (upper row), PBC (centre row) and PBC* (lower row) of the quarks. For comparison, the infinite-volume crossover line including the CEP is added, too. The left diagrams correspond to results without UV improvement while the diagrams on the right are obtained with UV improvement.

Similar to the results at zero chemical potential, we note the drastic effects of the UV improvement. Whereas the CEPs of the series of larger and larger box sizes do not approach the infinite-volume CEP without improvement (diagrams on the left), they do so after the improvement has been implemented (diagrams on the right). Both the crossover line and the CEP at $L = 8\,\mathrm{fm}$ are very close to the infinite-volume limit. The remaining discrepancy is within the numerical error of the infinite-volume calculation.[6] Furthermore, the volume-dependent shift of the crossover line and the CEP for increasing box size approach the infinite-volume result uniformly. Thus, while the overall qualitative behaviour with and without improvement is the same, quantitative aspects can only be discussed in the improved framework.

For ABC and PBC*, both phase diagrams show a similar trend when the box size is decreased: The CEP moves towards smaller temperatures and larger chemical potentials. In more detail, we find that the increase of its location in μ_B direction is larger than the decrease in T direction

[6] Note that the numerical error of the finite-volume calculations is of the order of machine precision because no integrations are involved, only sums.

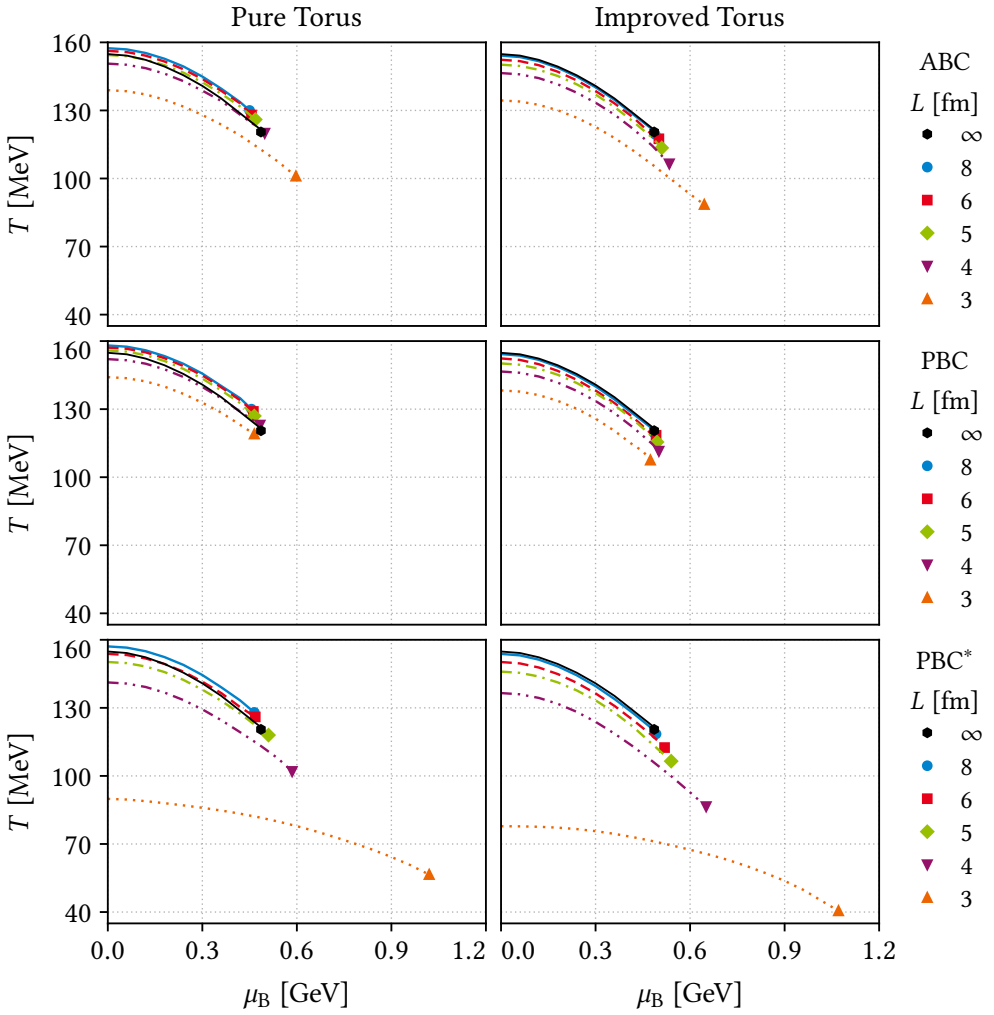

Figure 4.5.: Finite-volume effects of the crossover lines and locations of the CEPs (symbols) in the QCD phase diagram for different box sizes. We display results for both the pure torus (left) and the UV improvement (right). The phase diagrams are obtained with ABC (top), PBC (middle) and PBC* (bottom).

leading to a flattening of the chiral crossover line; see Section 4.2.4 below where we discuss the volume dependence of the curvature of the crossover line for different boundary conditions.

Down to $L = 4\,\mathrm{fm}$, the PBC results are generally very similar to the corresponding ABC results. However, the volume-dependent movement of the CEP is slightly slower and the endpoint values are closer to infinite volume. The differences to ABC are around/below the ten-per-cent level, though. On the other hand, at small volumes, we observe a qualitative difference for full PBC including the zero mode: The shift of the CEP in μ_B direction inverts. In particular, the CEP in our smallest volume of $L^3 = (3\,\mathrm{fm})^3$ is located at smaller chemical potential than the infinite-volume result. Nonetheless, the crossover lines again become flatter for decreasing system sizes, which is in agreement with ABC and PBC*.

Overall, the temperature dependence of the crossover line and CEP is analogous to that of

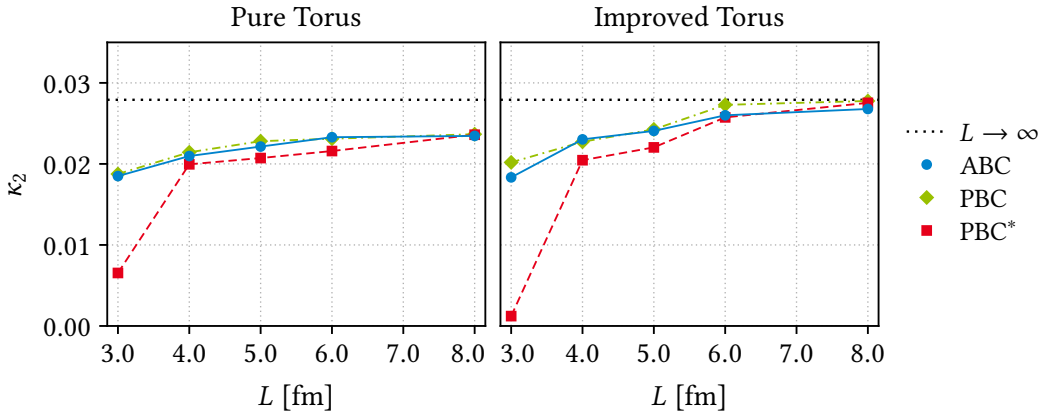

Figure 4.6.: L dependence of the curvature of the crossover line for ABC (blue circles), PBC* (red squares) and PBC (green diamonds). We display results for both the pure torus (left) and the UV improvement (right). Data points are connected by lines to guide the eye.

the pseudocritical temperature at vanishing chemical potential discussed above in Section 4.2.2. Results for box sizes $L \gtrsim 5\,\text{fm}$ are rather similar to one another for the different boundary conditions while the phase diagrams for ABC, PBC* and PBC display markedly different structures for small system sizes $L \lesssim 4\,\text{fm}$. Again, finite-volume effects are much more pronounced for PBC*. Especially, the result for $L = 3\,\text{fm}$ stands out with a very flat crossover line and a CEP at $(\mu_B, T) \approx (1070, 40)\,\text{MeV}$ with UV improvement.

The volume dependence of the location of the CEP has been investigated also in an FRG treatment within a two-flavour quark–meson-model truncation [103]. In this work, the position of the CEP has been extracted from the maximum of the scalar susceptibility and its shift with L has been calculated for PBC between $L = 4\,\text{fm}$ and $L = 10\,\text{fm}$. Compared to the DSE calculation presented here, the infinite-volume CEP of the FRG analysis is generally located at (much) higher chemical potential and lower temperature since its precise location depends on the chosen infrared input parameters, in particular on the value of the sigma-meson mass. However, a qualitative comparison of the results of Ref. [103] with the ones presented here yields a satisfying agreement between the present DSE and the FRG findings. Specifically, both the L-dependent relative shift of the CEP as well as the onset of finite-volume effects below $L = 8\,\text{fm}$ coincide well. Below $L = 4\,\text{fm}$, the CEP disappeared completely in the FRG framework.

4.2.4. Curvature of the Chiral Crossover Line

As our final point of the QCD phase diagram, we discuss the volume dependence of the curvature of the crossover line. At small baryon chemical potential μ_B, the crossover line can be parameterized as:

$$\frac{T_c(\mu_B)}{T_c} = 1 - \kappa_2 \left(\frac{\mu_B}{T_c}\right)^2 - \kappa_4 \left(\frac{\mu_B}{T_c}\right)^4 + \cdots . \tag{4.15}$$

Here, $T_c(\mu_B)$ and $T_c = T_c(0)$ are the pseudocritical temperatures at nonzero and vanishing chemical potential, respectively, while the coefficient κ_2 is the curvature of the transition line.

We obtain κ_2 by fitting the values of the crossover line at small baryon chemical potentials, $\mu_B \leq 240\,\text{MeV}$, to the parametrization given in Equation (4.15). For comparison, lattice calculations yield a curvature in the range $0.0120 \leq \kappa_2 \leq 0.0153$ [1, 77, 277, 278] (see also Figure 5.3 later).

Our results for κ_2 are shown in Figure 4.6. As already apparent from the phase diagrams (see Figure 4.5), the curvature is consistently smaller than the infinite-volume result and decreases for smaller box sizes. Since this is especially true for the pure-torus setup, we focus on the improved results below. Overall, this flattening resembles the volume dependence of the pseudocritical temperature. That is, the results for $L = 8\,\text{fm}$ are closest to the infinite-volume value and drop monotonically with decreasing L for all boundary conditions.

Compared to the pseudocritical temperatures shown in Figure 4.6, we find that the curvature displays a somewhat stronger reaction to a finite volume. Whereas the ABC temperatures are already close to the infinite-volume result for $L = 6\,\text{fm}$, the curvature parameter κ_2 for both ABC and PBC* is still off by more than ten per cent. Only for very large box sizes of $L \gtrsim 8\,\text{fm}$, we observe agreement with the infinite-volume limit within errors. Here, it is important to note that the fit is quite sensitive to details in the input data and choices of fit intervals such that κ_2 can only be extracted within a margin of several per cent.

In contrast to ABC and PBC*, the PBC curvature is very close to the infinite-volume result already above $L \gtrsim 6\,\text{fm}$. For $L = 5\,\text{fm}$ and below, the PBC results are again very similar to the ABC ones with slightly less pronounced finite-volume effects for $L = 3\,\text{fm}$.

The curvature for PBC between $L = 2\,\text{fm}$ and $L = 5\,\text{fm}$ was studied with FRG techniques in Ref. [102]. Above $L \approx 3\,\text{fm}$, there is qualitative agreement with our results: The curvature increases with L. However, for smaller box sizes, an interesting discrepancy occurs. In our case, we find a monotonic decrease for smaller and smaller box sizes whereas the FRG results show an increase of the curvature when L gets smaller than $L \approx 3.5\,\text{fm}$, resulting in an overall non-monotonic behaviour. Even though this increase occurs for L lower than we have investigated here, the sharp drop of κ_2 for $L = 3\,\text{fm}$ appears to contradict such a scenario in our calculations. The reason for this deviation is unknown. While the PBC zero mode is attributed to be the driving force in the small-volume limit of Ref. [102], its inclusion does not qualitatively change the behaviour of the curvature at small L in our case. However, there are indications that these deviations might be rooted in truncation/model artefacts and we comment on this in the following.

4.2.5. (Very) Small Volumes and Influence of the Zero Mode

In this subsection, we want to discuss intricacies of including the zero mode $\boldsymbol{q} = \mathbf{0}$ for PBC since there have been discussions about its influence. In model calculations, one can find that its inclusion leads to an increase of chiral symmetry breaking for small box sizes $L \lesssim 3\,\text{fm}$ compared to large volumes, see, e.g., Refs. [99, 102, 105, 279]. In particular, the amount of chiral symmetry breaking for small box sizes is found to be significantly larger than in infinite volume. In our analysis above, however, we have found that PBC with a zero mode behave qualitatively and quantitatively almost identically to ABC for box sizes larger than $L = 3\,\text{fm}$.

In order to investigate this discrepancy, we performed calculations for PBC with zero mode at $T = 100\,\text{MeV}$ also in two simpler truncations. The first one is the quenched version of the truncation scheme discussed in Section 3.5.2, i.e., the gluon in the quark DSE is solely given

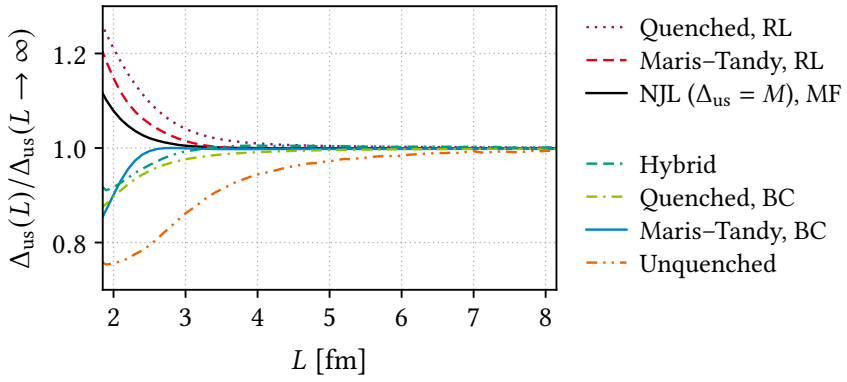

Figure 4.7.: L dependence of the subtracted quark condensate at $T = 100\,\text{MeV}$ normalized to its infinite-volume value for different models/truncations.

by our fits $D_{\nu\rho}^{\text{YM}}$ to quenched lattice data with $N_c = 3$ in the parametrization instead of $N_c = 0$. For the second one, we resort to the well-established Maris–Tandy model [280]. Both take no backcoupling of quarks onto the gluon into account, so the gluon can be seen as a static input for the quark DSE and unquenching effects are either absent (quenched gluon) or modelled (Maris–Tandy). Furthermore, within both truncations, we also varied the vertex ansatz by employing both the Ball–Chiu-inspired vertex (BC) and the bare Rainbow–Ladder vertex (RL) $\Gamma_\nu^{f,(\text{RL})} = Z_2^f \gamma_\nu$. In addition, we considered the hybrid truncation and a *Nambu–Jona-Lasinio* (NJL) model in a mean-field (MF) approximation as well. For more details on the Maris–Tandy and NJL model, see Appendix B.6.

In Figure 4.7, we show the L dependence of the subtracted quark condensate from Equation (4.13) at $T = 100\,\text{MeV}$ normalized to its infinite-volume value for all truncations and vertex ansätze, respectively. We investigated system sizes in the range of $L = 2\,\text{fm}$ to $8\,\text{fm}$ since visible volume effects generally occur at smaller L for these truncations. In the large-L limit, we notice that all results tend to the infinite-volume value regardless of truncation and vertex. For small L, however, especially below $L \lesssim 3\,\text{fm}$, the qualitative behaviour depends crucially on the vertex ansatz. In case of the RL vertex and the NJL model in MF approximation, we are able to reproduce the effects seen in model calculations: an increasing condensate with decreasing system size in both truncations and the mean-field NJL model. In case of the BC-inspired vertex and the hybrid truncation, though, the L dependence of the condensate is in line with our findings in this work.

It was argued analytically in Ref. [202] that the behaviour of the condensate for small L is driven entirely by the zero mode. Additionally, it was shown (in a mean-field approximation) in Ref. [99] that the zero-mode condensate even diverges for $L \to 0$. To this end, we also studied the behaviour of the regularized condensate in the unquenched truncation for very small volumes and all boundary conditions both in vacuum and at $T = 100\,\text{MeV}$ as well as both for the pure and the improved torus. Shown in Figure 4.8, we considered volumes down to $L = 0.6\,\text{fm}$, below of which convergence issues prevented further investigations. Since the curves for both types of tori look essentially identical, we refrain from referring to each in detail but rather describe the overall behaviour below.

For ABC, the condensate responds to a decrase in L similarly to an increase in T. That is, it

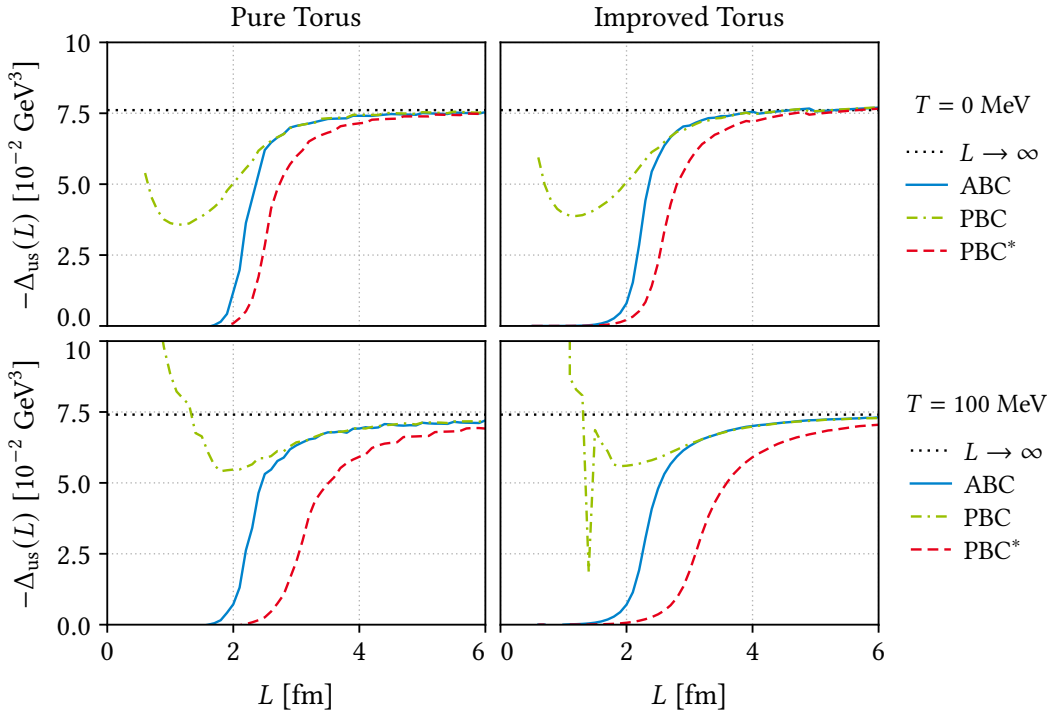

Figure 4.8.: L dependence of the subtracted quark condensate compared to its infinite-volume value. We display results for both the pure torus (left) and the UV improvement (right) and all boundary conditions. These were obtained in vacuum (upper) and at $T = 100$ MeV (lower).

undergoes a (narrow) smooth crossover transition from large values at high L to small values at low T, where the inflection point is located at around $L \approx 2.25$ fm. We observe basically the same behaviour for PBC*, even though the inflection point of the condensate is at larger L, i.e., $L \approx 2.5$ fm in vacuum and $L \approx 3$ fm at $T = 100$ MeV. Apart from a slight deviation in the onset box length of chiral restoration, these findings are generally in line with, e.g., Refs. [109, 113]. For PBC, though, the small-L behaviour changes drastically, i.e., one observes a steep increase, where the condensate exhibits a minimum[7] with respect to L located at $L \approx 1$ fm in vacuum and $L \approx 2$ fm at $T = 100$ MeV. Therefore, we can indeed also see the full effect of the epsilon regime as decribed in Ref. [99] in our calculations. Nevertheless, we note that we cannot make any quantitative statements since the results become numerically very unstable in this region.

As a consequence, we suppose that the monotonic, i.e., stricly increasing, behaviour of the condensate in the small-L limit seen in Refs. [99, 102, 105, 279] is either a model artefact or an artefact induced by approximations (e.g., mean field) within the models. In any case, however, we have demonstrated that the PBC zero mode must not be neglected: For volumes $L \gtrsim 4$ fm, it assures that PBC and ABC behave almost identically, while for $L \lesssim 3$ fm, it triggers the expected behaviour of the epsilon regime.

[7] Actually, for the improved torus, a second minimum/sharp dip occurs at around $L \approx 1.5$ fm. However, due to the general unstable behaviour in the region of very small volumes for both tori, it is most likely numerical in origin.

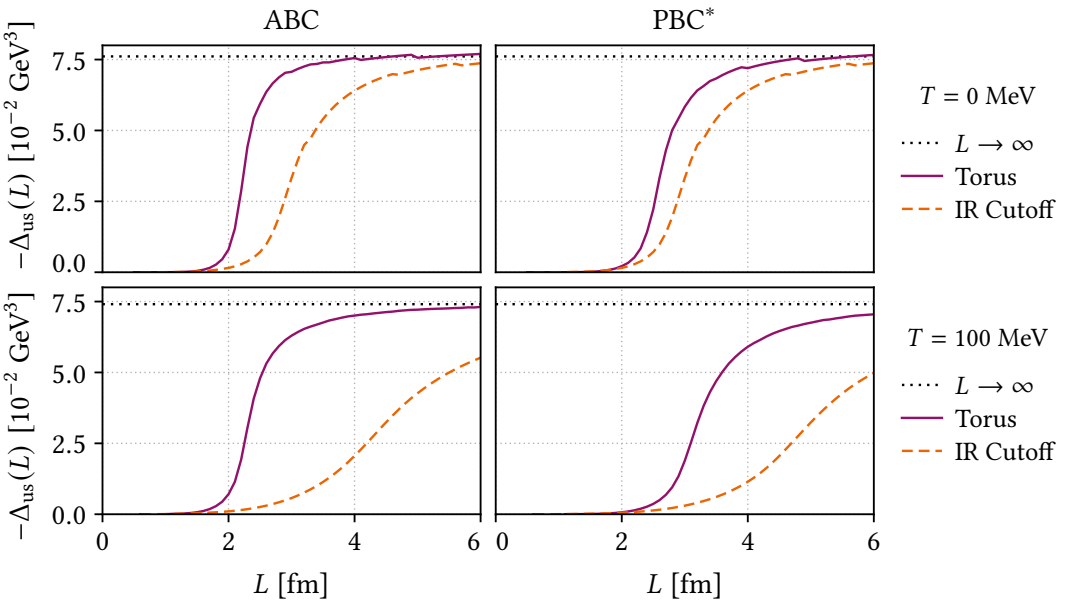

Figure 4.9.: L dependence of the subtracted quark condensate compared to its infinite-volume value. We display results for ABC (left) and PBC (right) for the improved torus and an IR cutoff. These were obtained in vacuum (upper) and at $T = 100\,\text{MeV}$ (lower).

4.2.6. Approximation of the Finite Volume with an IR Cutoff

Finally, we want to analyse an (over)simplification of finite-volume setups that is sometimes used in the literature instead of a proper torus summation. That is, rather than taking the discretized momentum summation explicitly into account, one uses a continuous integration with an effective IR cutoff that corresponds to the innermost torus momentum. Such an approach has been persued, e.g., for (P)NJL model calculations in a mean-field approximation [100, 101] and for rainbow–ladder DSE investigations [116, 117]. Clearly, it cannot describe PBC with zero mode at all since these do not introduce a smallest nonzero momentum value.

We contrast the volume dependence of the regularized condensate obtained in our setup for the improved torus with the IR cutoff in Figure 4.9. We show results for both ABC and PBC* again in vacuum and at $T = 100\,\text{MeV}$. While the qualtitative behaviour is similar, we observe visible quantitative differences in all setups. In vacuum, the shapes of the torus and IR-cutoff curves coincide albeit with an inflection point at larger L for the latter. At $T = 100\,\text{MeV}$, though, the cutoff curves are significantly flatter and their inflection point is also at drastically larger L than for the improved torus. In total, we can say that the effective IR cutoff is quantitatively not a justified approximation for a full finite-volume calculation in our sophisticated framework, especially for small volumes and nonzero temperature.

4.3. Baryon-Number Fluctuations

Apart from the quark condensate, there are other quantities of interest to investigate the QCD phase diagram with. As stated earlier, fluctuations of the conserved quantities baryon

number, electromagnetic charge and strangeness are important quantities for locating the CEP in the QCD phase diagram because they are sensitive to phase transitions [66, 93, 94]. More specifically, the correlation length ξ_{cor} of the system diverges at the critical endpoint (at least in an infinite volume) and the second-order baryon-number fluctuation χ_2^{B} is proportional to it, $\chi_2^{\mathrm{B}} \propto \xi_{\mathrm{cor}}^{\varepsilon}$, with some exponent $\varepsilon > 0$. Therefore, we first briefly summarize some general aspects of fluctuations (see, e.g., Refs. [91, 281] for reviews) and then detail how we determine these from our solutions of the DSEs.

In three-flavour QCD with quark chemical potentials μ_{u}, μ_{d} and μ_{s}, the *quark-number fluctuations* are derivatives of QCD's grand potential Ω (see Equation (3.5)) with respect to these chemical potentials:[8]

$$\chi^{\mathrm{uds}}_{ijk}(T,\mu_{\mathrm{u}},\mu_{\mathrm{d}},\mu_{\mathrm{s}}) = -\frac{1}{T^{4-(i+j+k)}}\frac{\partial^{i+j+k}}{\partial\mu_{\mathrm{u}}^{i}\partial\mu_{\mathrm{d}}^{j}\partial\mu_{\mathrm{s}}^{k}}\Omega(T,\mu_{\mathrm{u}},\mu_{\mathrm{d}},\mu_{\mathrm{s}})\,, \quad i,j,k\in\mathbb{N}\,, \tag{4.16}$$

where the prefactor of $T^{-(4-i+j+k)}$ serves normalization purposes and also renders all $\chi^{\mathrm{uds}}_{ijk}$ dimensionless quantities. The quark chemical potentials are related to the ones for baryon number (B), strangeness (S) and electric charge (Q) via:

$$\mu_{\mathrm{u}} = \frac{1}{3}\mu_{\mathrm{B}} + \frac{2}{3}\mu_{\mathrm{Q}}\,, \quad \mu_{\mathrm{d}} = \frac{1}{3}\mu_{\mathrm{B}} - \frac{1}{3}\mu_{\mathrm{Q}}\,, \quad \mu_{\mathrm{s}} = \frac{1}{3}\mu_{\mathrm{B}} - \frac{1}{3}\mu_{\mathrm{Q}} - \mu_{\mathrm{S}}\,. \tag{4.17}$$

With these relations, we can define corresponding fluctuations $\chi^{\mathrm{BQS}}_{ijk}$ which can be expressed as linear combinations of quark-number fluctuations. For example:

$$\chi_2^{\mathrm{B}} = -\frac{1}{T^2}\frac{\partial^2\Omega}{\partial\mu_{\mathrm{B}}^2} = \frac{1}{9}\left[\chi_2^{\mathrm{u}} + \chi_2^{\mathrm{d}} + \chi_2^{\mathrm{s}} + 2\left(\chi_{11}^{\mathrm{ud}} + \chi_{11}^{\mathrm{us}} + \chi_{11}^{\mathrm{ds}}\right)\right]. \tag{4.18}$$

Here, we remark two notational details for all following statements. First, we suppress all T and μ_f arguments for the sake of brevity and always assume them to be present implicitly. Second, whenever certain indices are left out, the associated fluctuation is of order zero in that index, e.g., $\chi_2^{\mathrm{B}} = \chi_{200}^{\mathrm{BSQ}}$.

Fluctuations of conserved charges also bridge the gap between theory and experiment as they have a one-to-one correspondence to the *cumulants* C_n of the associated probability distribution. For the baryon number, this relation reads:

$$C_n^{\mathrm{B}} = VT^3\chi_B^{\mathrm{n}} \tag{4.19}$$

while analogous expressions hold for strangeness and electric charge. More useful to work with are the statistical quantities that can be extracted from heavy-ion collisions by means of event-by-event analyses; see Refs. [86, 91, 281, 282] and references therein for more details. These are connected to the cumulants via:

$$M_{\mathrm{B}} = C_1^{\mathrm{B}}\,, \quad \sigma_{\mathrm{B}}^2 = C_2^{\mathrm{B}}\,, \quad S_{\mathrm{B}} = C_3^{\mathrm{B}}\left(C_2^{\mathrm{B}}\right)^{-3/2}, \quad \kappa_{\mathrm{B}} = C_4^{\mathrm{B}}\left(C_2^{\mathrm{B}}\right)^{-2}, \tag{4.20}$$

where M_{B}, σ_{B}^2, S_{B} and κ_{B} denote mean, variance, skewness and kurtosis of the net-baryon distribution, respectively.

[8] Alternatively, they are sometimes equivalently defined as derivatives with respect to the normalized chemical potentials $\tilde{\mu}_f := \mu_f/T$, i.e., $\chi^{\mathrm{uds}}_{ijk} = -T^{-4}\,\partial^{i+j+k}\Omega/\left(\partial\tilde{\mu}_{\mathrm{u}}^{i}\partial\tilde{\mu}_{\mathrm{d}}^{j}\partial\tilde{\mu}_{\mathrm{s}}^{k}\right)$.

Apparently, ratios of fluctuations are particularly interesting because they are equal to ratios of cumulants of the corresponding probability distributions and all explicit volume dependences drop out. However, implicit volume dependences may remain [97, 99]. Whether these have to be taken into account when comparing theoretical calculations with experimental results is under debate and will constitute one of the topics of the following analysis. For the baryon-number fluctuations, for instance, prominent ratios read:

$$\frac{\chi_4^{\mathrm{B}}}{\chi_2^{\mathrm{B}}} = \kappa_{\mathrm{B}}\sigma_{\mathrm{B}}^2\,, \quad \frac{\chi_3^{\mathrm{B}}}{\chi_2^{\mathrm{B}}} = S_{\mathrm{B}}\sigma_{\mathrm{B}}\,, \quad \frac{\chi_1^{\mathrm{B}}}{\chi_2^{\mathrm{B}}} = \frac{M_{\mathrm{B}}}{\sigma_{\mathrm{B}}^2}\,. \tag{4.21}$$

Now that we have outlined generalities about fluctuations and their ratios, we want to specify how these can be calculated in our DSE framework. As was already established in Section 3.2, the grand potential Ω is not directly accessible with DSEs. Rather analogous to the quark condensate, however, one can derive from the 2PI effective action (see Appendix B.5) that the quark-number density n_f may be expressed with the aid of the quark propagator:

$$n_f = -\frac{\partial\Omega}{\partial\mu_f} = -N_c Z_2^f \int\!\!\!\!\!\!\sum_q \mathrm{tr}\big[\gamma_4 S_f(q)\big]\,. \tag{4.22}$$

4.3.1. Regularization of the (Finite-Volume) Quark-Number Density

In principle, we can now take Equation (4.22), perform the trace (see Appendix C.1.4) and calculate the integrals/sums. Similar to the quark condensate, though, the quark-number density entails a UV divergence and needs to be regularized. Due to γ_4 appearing in the trace, the divergence arises in the temporal part of the propagator and is thus rooted in the Matsubara sum. For regularization, we therefore utilize a subtraction scheme employed in Refs. [79, 238, 283]. In infinite volume, the regularized quark-number density is then given by:

$$n_f^{\mathrm{reg,inf}} = -N_c Z_2^f \big(K_f^{n,\mathrm{inf}} - K_f^{\mathrm{reg}}\big)\,, \quad K_f^{n,\mathrm{inf}} = T\sum_{q_4\in\{\omega_n^T\}} K_f^{\mathrm{inf}}(q_4)\,, \quad K_f^{\mathrm{reg}} = \int_{-\infty}^{\infty}\frac{\mathrm{d}q_4}{2\pi}\,K_f^{\mathrm{inf}}(q_4)\,, \tag{4.23}$$

$$K_f^{\mathrm{inf}}(q_4) = \int\frac{\mathrm{d}^3q}{(2\pi)^3}\,\mathrm{tr}\big[\gamma_4 S_f(q_4,\boldsymbol{q})\big]\,. \tag{4.24}$$

The term $K_f^{n,\mathrm{inf}}$ contains a sum over the temporal Matsubara frequencies and is the one expected to yield the quark-number density. The subtracted, regularizing term K_f^{reg} does not depend explicitly on temperature or chemical potential and is therefore known as a "vacuum contribution" [284]. This procedure is based on the Euclidean version of the contour-integration technique for Matsubara sums and we refer to Ref. [79] for a detailed discussion.

Due to its definition in Equation (4.22), the integrand of the quark-number density is mainly governed by the C_f dressing function. A hard UV cutoff, though, induces an unphysical nonzero imaginary part $\mathrm{Im}\,C_f$ in the UV [48, 234, 285]. For this reason, we have to use a Pauli–Villars regulator for the calculation of the quark-number density and thus we are

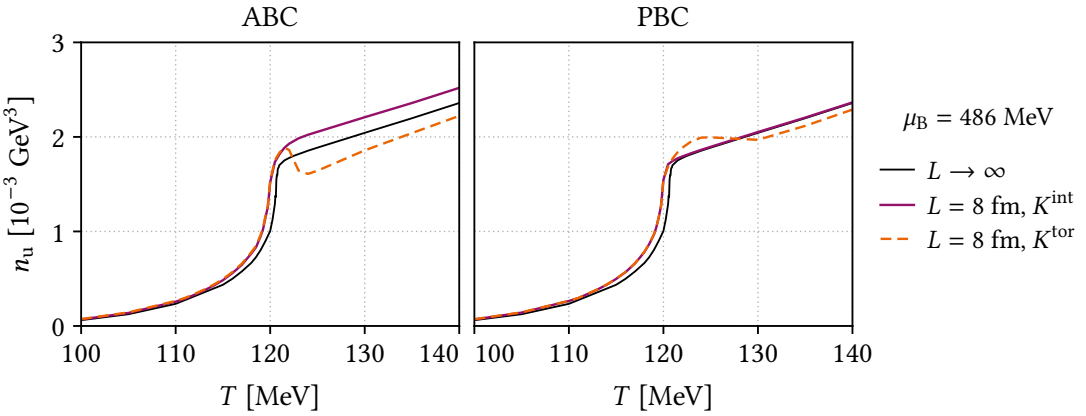

Figure 4.10.: Temperature dependence of the $L = 8\,\mathrm{fm}$ quark-number density at μ_B^{CEP} for ABC (left) and PBC (right) compared to the infinite-volume result. We display results for the regularization term obtained with a continuous integration (K^{int}) or (improved) torus summation (K^{tor}), respectively.

restricted to the improved-torus setup. Consequentially, the temporal integrand in a finite volume is then given by:

$$K_f^{vol}(q_4) = \frac{1}{L^3} \sum_{q_i \in \{\omega_{m_i}^L\}}^{|\boldsymbol{q}|<\Lambda_{vol}} \mathrm{tr}\left[\gamma_4 S_f(q_4, \boldsymbol{q})\right] + \int_{|\boldsymbol{q}|>\Lambda_{vol}} \frac{\mathrm{d}^3 q}{(2\pi)^3}\ \mathrm{tr}\left[\gamma_4 S_f(q_4, \boldsymbol{q})\right]. \tag{4.25}$$

Naïvely, one would expect that the finite-volume quark-number density can be regularized analogously to the infinite-volume case, i.e., by subtracting a term K_f^{tor} where the spatial integral is performed on the improved torus and the temporal part is integrated continuously:

$$K_f^{n,inf} \to K_f^{n,vol} = T \sum_{q_4 \in \{\omega_n^T\}} K_f^{vol}(q_4), \quad K_f^{reg} \to K_f^{tor} = \int_{-\infty}^{\infty} \frac{\mathrm{d}q_4}{2\pi}\, K_f^{vol}(q_4). \tag{4.26}$$

Unfortunately, it turns out that this apporach leads to artefacts in the resulting densities related to the high-momentum behaviour of the subtraction term. In order to avoid these, we do not replace the infinite-volume integral with the torus summation in the subtraction term but rather use a term K_f^{int} with a continuous integral in the spatial part as well:

$$K_f^{reg} \to K_f^{int} = \int_{-\infty}^{\infty} \frac{\mathrm{d}q_4}{2\pi} \int_{|\boldsymbol{q}|>|\boldsymbol{q}_{z=0}|} \frac{\mathrm{d}^3 q}{(2\pi)^3}\ \mathrm{tr}\left[\gamma_4 S_f(q_4, \boldsymbol{q})\right]. \tag{4.27}$$

The subscript of the integral indicates that we treat the radial integral differently for different boundary conditions: Whereas there is no momentum gap for PBC and the integral consequently starts at zero, for ABC we have $\boldsymbol{q}_{z=0}^{ABC} \neq \boldsymbol{0}$ and therefore set the lower integration limit to the value of the smallest possible momentum magnitude.

We illustrate aforementioned artefacts in Figure 4.10 for $L = 8\,\mathrm{fm}$ – where the results should essentially coincide with the infinite-volume limit – at the critical baryon chemical

potential, $\mu_{\mathrm{B}}^{\mathrm{CEP}} = 486\,\mathrm{MeV}$, and temperatures around the CEP, $T_{\mathrm{CEP}} = 121\,\mathrm{MeV}$. We display the up-quark-number density regularized either with K^{int} or K^{tor} for both ABC and PBC as a function of temperature compared to the infinite-volume result. Whereas for $T < T_{\mathrm{CEP}}$, the regularization term is immaterial, one notices significant differences above T_{CEP}. That is, for both boundary conditions, the K^{tor}-regularized result develops a dip, which is deeper and steeper for ABC than for PBC, and consequently undershoots the infinite-volume curve. While K^{int} resolves this problem entirely for PBC – where the infinite-volume limit is recovered – the ABC curve now no longer exhibits a dip albeit with an overshoot of the $L \longrightarrow \infty$ result. Since the main difference between ABC and PBC is the IR cutoff in the continuous spatial integration for ABC, the remaining artefacts are probably linked to this IR behaviour.

In total, we therefore obtain the regularized quark-number density in a finite volume with the aid of the relation:

$$n_f^{\mathrm{reg,vol}} = -N_c Z_2^f \left(K_f^{n,\mathrm{vol}} - K_f^{\mathrm{int}}\right) . \tag{4.28}$$

Apart from this special regularization procedure, there are several numerical subtleties when it comes to the calculation of the quark-number density in Equation (4.22) – both in finite and in infinite volume. We discuss them in detail in Appendix D.1.

4.3.2. Setup and Up-Front Remarks

In advance of the discussion of our results for finite-volume baryon-number fluctuations and their ratios, we comment on some details of our setup. First, since we have argued earlier that the omission of the zero mode is a rather unphysical approximation, we will no longer consider PBC* below. Second, as elucidated in the previous subsection, we necessitate a Pauli–Villars regularization scheme. To again obtain the correct infinite-volume pseudocritical temperature of $T_{\mathrm{c}} = 155\,\mathrm{MeV}$, the vertex-strength parameter is given by $d_1 = 8.49\,\mathrm{GeV}^2$ (see Table 3.1) in line with, e.g., Ref. [79].

Moreover, we neglect mixed derivatives in Equation (4.16) for all of our considerations as a means of simplification.[9] Such being the case, our baryon-number fluctuations of arbitrary order n read [79]:

$$\chi_n^{\mathrm{B}} = \frac{1}{3^n}\left(2\chi_n^{\mathrm{u}} + \chi_n^{\mathrm{s}}\right) , \quad \chi_n^f = \frac{1}{T^{4-n}} \frac{\partial^{n-1}}{\partial \mu_f^{n-1}} n_f^{\mathrm{reg}} . \tag{4.29}$$

Although this approach formally also neglects mixed derivatives with respect to (the degenerate) up and down quarks which could be identified with diagonal ones, e.g., $\chi_{11}^{\mathrm{ud}} = \chi_2^{\mathrm{u}}$, we have checked explicitly that this makes only a small quantitiave and no qualitative difference in our results.

Additionally, we would like to discuss the issue of the potential effects of (spacelike) correlations with the quantum numbers of mesons in the quark DSE. Within the DSE framework,

[9] This approximation appears to be justified as lattice results indicate that these are subleading [286].

these correlations appear as part of a particular diagram in the DSE for the quark–gluon vertex and therefore feed back into the quark DSE. These correlations have been identified and explored in a number of works in the vacuum [287–289] as well as at nonzero temperature and chemical potential [80, 251]. In Ref. [80], it was found that the inclusion of meson-backcoupling effects onto the quark has only very little effect on the location of the CEP in the QCD phase diagram. On the other hand, though, these degrees of freedom will develop long-range correlations inside the critical regions around second-order transitions and will therefore be crucial when it comes to the calculation of anomalous dimensions and critical scaling.

Since our truncation outlined in Section 3.5.2 does not take these effects (e.g., those with the quantum numbers of the σ meson) into account, we do not expect to be able to study the full volume dependence inside the critical scaling region. However, we believe that the scheme at hand provides a meaningful starting point for the study of fluctuations outside the critical scaling region. Furthermore, the truncation can be improved systematically along the lines of the (more involved) scheme explored in Refs. [80, 251], which will be one of the topics in Chapter 6.

Due to the substantial technical complications that arise when including these contributions, we ignore those in the present exploratory analysis in this chapter. Therefore, we do not expect to be able to study all (and likely not even the most important) contributions to volume effects inside the critical scaling region around the CEP. However, outside this region, these contributions are known to be subleading. Thus, our results should be meaningful and relevant – in particular since beyond-mean-field calculations indicate that the size of the critical region is rather small [62, 290]. Nevertheless, long-range correlations with the quantum numbers of pseudoscalar and scalar mesons will be included systematically in Chapter 6 where we also demonstrate that this approach is, in principle, applicable also to finite-volume calculations.

With this in mind, we discuss finite-volume baryon-number fluctuations and their ratios around the CEP and compare them to their infinite-volume limit below. We study cubes with edge lengths of $L = 2.5$, 3, 4, 5, 6 and 8 fm for both ABC and PBC. We recall from the last section that the location of the CEP in the phase diagram is volume-dependent. Sizable effects only occur for volumes $V \lesssim (5\,\mathrm{fm})^3$ and are much larger for ABC than for PBC. For the sake of comparability, we always show results obtained around the respective critical chemical potential for each system size below. Additionally, we also normalize all temperatures to the corresponding critical temperatures. Since fluctuations around the CEP vary rapidly with temperature, a dense numerical grid is necessary to avoid misalignments. We accomplish this by using steps of one MeV in temperature. A large part of this analysis has been published in Ref. [136].

4.3.3. Results for the Fluctuations

We begin our discussion with the results for the baryon-number fluctuations. In Fig. 4.11, we show baryon-number fluctuations of orders one to four, χ_1^B to χ_4^B, from the topmost to the bottommost row, respectively, for both ABC (left) and PBC (right) at finite volume as well as the infinite-volume results in black for comparison.

Before we discuss the details, another general comment is in order. As visible in both plots, the infinite-volume result of χ_2^B does not show the expected divergence at the critical

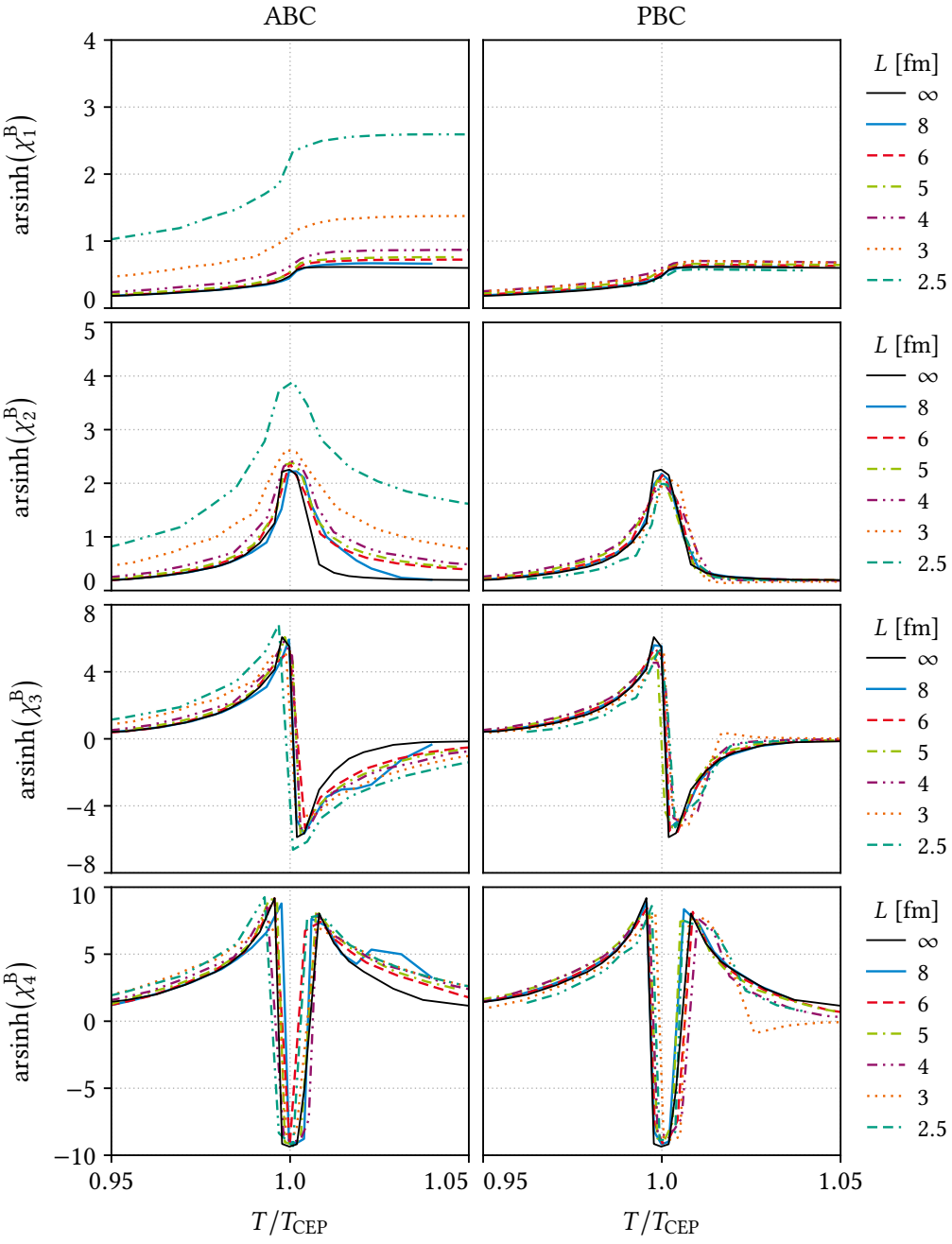

Figure 4.11.: Baryon number fluctuations of order one (topmost row) to four (bottommost row) against normalized temperature for antiperiodic (left) and periodic (right) boundary conditions in different box sizes L.

temperature. This is entirely due to our limited resolution in temperature. Given an unlimited amount of CPU time, we could determine the location of the CEP with arbitrary precision and perform calculations arbitrarily close to the CEP, thereby extracting the point of divergence exactly. In practice, for now, this is the best we could do and thus the finite width and height

of the peak at infinite volume serves as our control quantity for the size of potential effects at finite volume.

Starting with the ABC results, we find clearly visible volume effects, especially for the lower-order fluctuations. First, we see monotonous increases of χ_1^{B} and χ_2^{B} with decreasing system size across the whole temperature range. Second, we find that the ratio of the peak height to the tails of the peaks, e.g., $\chi_2^{\mathrm{B}}(1.00)/\chi_2^{\mathrm{B}}(1.05)$, grows continuously with increasing system size (even within the resolution limits discussed above). The $L = 2.5\,\mathrm{fm}$ lines especially stand out with the arsinh of the peak value of χ_2^{B} nearly being doubled as compared to the infinite-volume result – its peak-to-tail ratio, however, is much smaller. At T_{CEP}, the arsinh of χ_1^{B} is even almost five times as large. For $T < T_{\mathrm{CEP}}$, we find a consistent infinite-volume limit, i.e., the results for $L \gtrsim 5\,\mathrm{fm}$ are very similar to one another while the $L = 8\,\mathrm{fm}$ lines essentially coincide with the infinite-volume ones. For $T > T_{\mathrm{CEP}}$, however, we see noticeable deviations between the finite- and infinite-volume results. We have not succeeded to track down these deviations unambiguously, but we believe they originate from the finite-volume adjusted subtraction procedure of the density outlined in Section 4.3.1 either as remnants or as an overcompensation of the initial problem.

In contrast, the fluctuations using PBC shown in the right diagram of Figure 4.11 are much less dependent on the volume of the system than the fluctuations with ABC. This resembles similar differences between PBC and ABC effects on the location of the CEP discussed above. In fact, the volume dependence of the fluctuations with PBC are within our margin of error. Nonetheless, for χ_1^{B} and χ_2^{B} at $T < T_{\mathrm{CEP}}$, one can observe a monotonous increase of χ_2^{B} with decreasing system size down to $L = 4\,\mathrm{fm}$. For smaller box sizes, the values start decreasing again. This behaviour is similar to the non-monotonic volume dependence of the location of the CEP around $L = 3\,\mathrm{fm}$ that has been already noticed in Section 4.2. Again, it may be linked to the onset of the epsilon regime at very small volumes. In total, we also find that volume dependences in the higher-order fluctuations are generally much less pronounced.

In addition, as seen before, the infinite-volume limit of the PBC fluctuations is much more consistent for $T > T_{\mathrm{CEP}}$ as compared to ABC. That is, there are no substantial deviations between the $L = 8\,\mathrm{fm}$ and the $L \to \infty$ lines. As a consequence, one might conjecture that the numerical problems of ABC for $T > T_{\mathrm{CEP}}$ are connected to infrared momentum modes because ABC introduce an effective infrared cutoff, $\boldsymbol{q}_{z=0}^{\mathrm{ABC}} \neq \mathbf{0}$, while PBC do not, $\boldsymbol{q}_{z=0}^{\mathrm{PBC}} = \mathbf{0}$.

4.3.4. Finite-Volume Scaling

We also extracted the peak heights of the ABC and PBC results for χ_2^{B} as a function of volume and analysed their behaviour in terms of power laws which is shown as a log–log plot in Figure 4.12. The peak heights were determined using Gaussian fits to our data. Whereas the PBC results are virtually independent of volume, i.e., roughly proportional to V^0, there is no clear power-law behaviour visible for the ABC results if all volumes are considered. This may or may not be connected to the numerical error discussed in Section 4.3.1. However, as we argued earlier, it is far more likely that the lack of a consistent scaling behaviour inside the critical region is linked to the omission of correlations with the quantum numbers of mesons in the quark DSE (see Section 4.3.2).

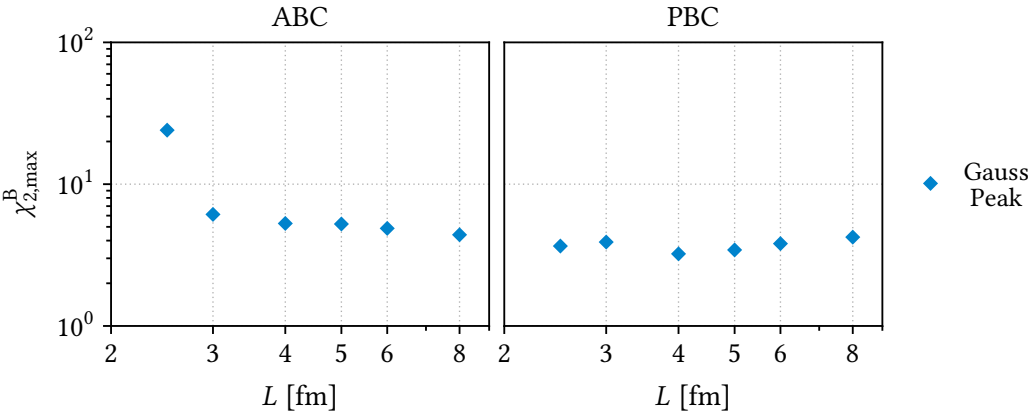

Figure 4.12.: L dependence of the peak position of χ_2^{B} obtained with a Gaussian fit. We display results for both ABC (left) and PBC (right).

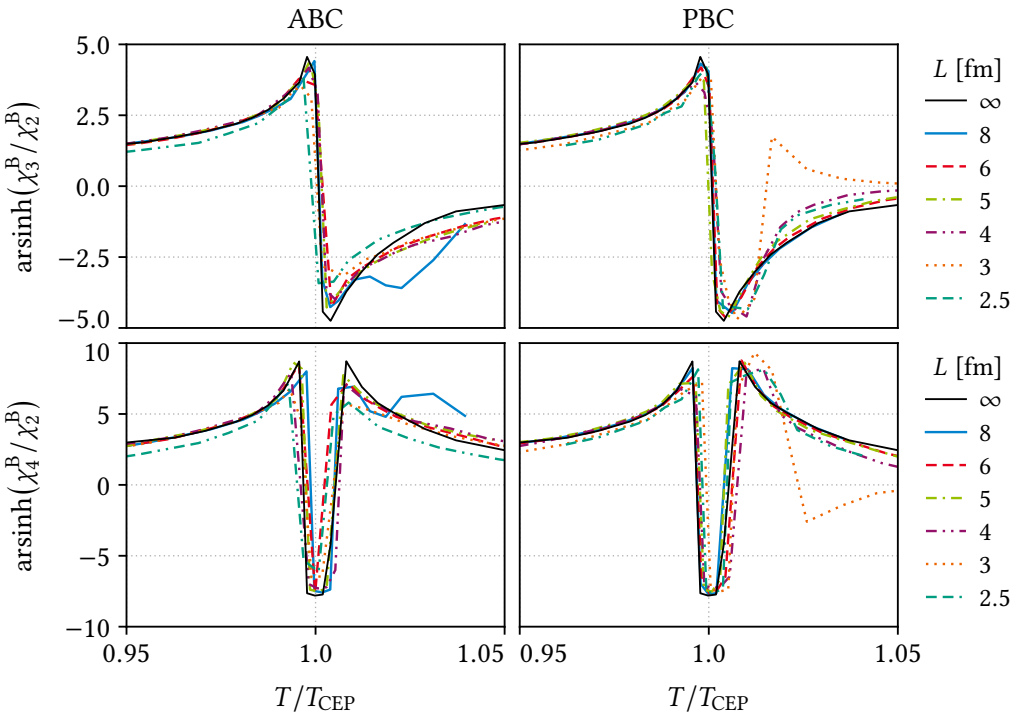

Figure 4.13.: Baryon number fluctuation ratios χ_3/χ_2 (top row) and χ_4/χ_2 (bottom row) against normalized temperature for different for antiperiodic (left) and periodic (right) boundary conditions in different box sizes L.

4.3.5. Results for the Fluctuation Ratios

Finally, we turn to ratios of baryon-number fluctuation. To this end, we display (the inverse hyperbolic sine of) both the skewness and kurtosis ratios for ABC and PBC in Figure 4.13. For comparison, the infinite-volume result is again shown as a black line. In general, one can observe that ratios for both boundary conditions and all system sizes qualitatively coincide

very well for $T \leq T_{\mathrm{CEP}}$. Additionally, they are also compatible with the respective infinite-volume results. Furthermore, the sign changes in both ratios are consistent with predictions based upon general grounds [95, 96].

For ABC, however, we find again slight inconsistencies between the finite- and infinite-volume data for $T > T_{\mathrm{CEP}}$. Neglecting the obvious outlier at $L = 8\,\mathrm{fm}$, the lines of the larger volumes deviate qualitatively from the $L \to \infty$ one, especially for larger temperatures. This deviation is more pronounced for the skewness ratio. Contrary to this, the PBC results exhibit once more no such behaviour and we observe a consistent infinite-volume limit also for $T > T_{\mathrm{CEP}}$. In fact, the $L = 8\,\mathrm{fm}$ and the infinite-volume curves are almost indistinguishable. This seems to corroborate our assumption that the infrared cutoff of ABC leads to some numerical problems for $T > T_{\mathrm{CEP}}$. In addition to that, there are two notable outliers which were already present in the higher-order fluctuations: the curves for ABC at $L = 8\,\mathrm{fm}$ and PBC at $L = 3\,\mathrm{fm}$. Due to the randomness in their occurrence, they are most likely of purely numerical origin. We remark that the deviation from the rest of the curves in both cases occurs again for $T > T_{\mathrm{CEP}}$, which makes a connection to the subtraction procedure plausible. This also implies that PBC are not completely immune to these numerical problems.

Overall, we find the remarkable result that all individual volume dependences of the fluctuations cancel once ratios are studied. This not only true for large volumes but also for our smallest system sizes of $L = 5$, 4, 3 and 2.5 fm. This is somewhat in contrast to the results of Ref. [99], where significant volume effects in the kurtosis ratio have been found for volumes $V \lesssim (5\,\mathrm{fm})^3$ within an FRG treatment of the quark–meson model. Since the two approaches are rather different, e.g., our approach treats the gluonic sector explicitly but neglects a class of mesonic fluctuations and vice versa in their approach, it may be interesting to provide a systematic comparison in the future.

4.4. Outlook: Spherical Volume

While cubical volumes with (anti)periodic boundary conditions are very convenient for a mathematical description, they certainly do not describe the real-world physics of heavy-ion collisions. Depending on the centrality of the collision, the interacting fireball is rather spherical (high centrality) or almond-like (low centrality) in shape with a fuzzy boundary. When trying to impose Dirichlet boundary conditions on fermions in a sphere, though, one can show that these are too strict and that no solutions can exist [291].

As has been advocated in Ref. [118] within a DSE-model framework, this situation may be better represented in a calculation in a sphere with *MIT boundary conditions*. These were first proposed in the context of the *MIT bag model* [292, 293], a model for baryons which enforces confinement of its fermionic constituents inside by demanding that the normal component of their current $j^\nu = \overline{\psi}\gamma^\nu\psi$ be zero at the baryon's surface.

For a spherical shape with radius R, MIT boundary conditions can be written as

$$-\mathrm{i}\hat{r}\cdot\boldsymbol{\gamma}\psi(t,r,\theta,\phi)\big|_{r=R} = \psi(t,r,\theta,\phi)\big|_{r=R}\,, \tag{4.30}$$

where $\hat{r}$ denotes the unit vector on the surface of the sphere, whereas t, r, θ, ϕ label time, radial and angular components of the sphere, respectively.

A first approximation used sometimes is to assume that the fermions inside the sphere have some constant mass M and fulfil the free Dirac equation. This is naturally the case in mean-field models, e.g., in the NJL-model calculations in Ref. [294]. However, such an ansatz was also persued in the rainbow–ladder-DSE study in Ref. [118], where M was given by the constituent-quark mass $M_f(p \to 0)$. In this case, the magnitudes of possible (again discrete) momentum vectors $|\boldsymbol{p}| = p_i$ are given by the solutions of the following equation [295]:

$$j_{\ell_\kappa}(pR) = -\operatorname{sgn}(\kappa)\frac{p}{E+M} j_{\bar{\ell}_\kappa}(pR)\,, \quad E = \sqrt{p^2+M^2}\,, \tag{4.31}$$

where $j_\ell(x)$ labels the spherical Bessel functions and

$$\ell_\kappa = \begin{cases} -\kappa - 1 & \text{for } \kappa < 0 \\ \kappa & \text{for } \kappa > 0 \end{cases}, \quad \bar{\ell}_\kappa = \begin{cases} -\kappa & \text{for } \kappa < 0 \\ \kappa - 1 & \text{for } \kappa > 0 \end{cases}, \quad \kappa \in \mathbb{Z}\backslash\{0\}\,. \tag{4.32}$$

With the discrete momentum vectors at hand, the momentum summation for MIT boundary condition then reads [294]

$$\int_{\mathbb{R}^3} \frac{\mathrm{d}^3 q}{(2\pi)^3} f(\boldsymbol{q}) \to \frac{1}{2V} \sum_{|q|\in\{p_i\}} f(\boldsymbol{q})\,. \tag{4.33}$$

In principle, the general course of action described above should be unproblematic to perform in our framework. Nevertheless, two complications for a proper treatment come to mind. First, one needs to find an appropriate version of Equation (4.31) for the full momentum-dependent mass function. Second, it needs to be clarified if and how the gluon can be described with MIT our analogous boundary conditions. This is left for future work.

4.5. Summary and Conclusion

In this first results chapter, we studied the effects of a finite, uniform, three-dimensional cubic volume with equal edge lengths L and (anti)periodic boundary conditions on the phase diagram of QCD. To this end, we employed the truncation scheme elucidated in the last chapter and extracted the volume dependence of the chiral order parameter. In order to do so properly, we found two technical procedures to be mandatory: the first being the removal of cubic artefacts due to a UV improvement of the setup and the second being the explicit inclusion of the zero mode for periodic boundary conditions. The zero mode ensures the correct and analytically expected onset of the epsilon regime for small volumes while it turns out to render results almost identical to antiperiodic boundary conditions for large volumes.

For both types – periodic and antiperiodic boundary conditions – we then find similar and only moderate volume effects of the order of ten MeV and smaller for box sizes $L \gtrsim 5\,\mathrm{fm}$. Only for very small volumes, sizable shifts of the CEP and the associated crossover line occur. These shifts are almost monotonous: Smaller volumes correspond to smaller transition temperatures and the CEP shifts towards larger chemical potential. The only deviation from this general behaviour occurs for periodic boundary conditions at very small box sizes, which may be linked to the epsilon regime. Our findings are consistent with corresponding results from an FRG treatment of the quark–meson model.

Furthermore, we investigated a simplification of full finite-volume calculations that is sometimes used in literature, i.e., the usage of an IR cutoff instead of a proper torus summation. In our setup, this turns out to be a very poor approximation especially at nonzero temperatures, so the torus summation is mandatory for quantitative descriptions of finite volumes.

Additionally, we determined the volume dependence of the skewness and kurtosis ratios of baryon-number fluctuations within the same setup. For a wide range of cubic spatial volumes with edge lengths between $L = 2.5\,\mathrm{fm}$ and $L = 8\,\mathrm{fm}$ and our two boundary conditions, we observe almost no volume dependence of these ratios. This is a highly nontrivial outcome because the individual results for the different fluctuations, both for ABC and PBC, reveal a pattern that is at odds with the general expectation of linear dependence on volume: Whereas the PBC results for χ_2^{B} do not change with volume, the ones for ABC are even inversely proportional to $V = L^3$. Nevertheless, all these dependences cancel in the ratios, which is important when comparing with experimental results from heavy-ion collisions. We consider this a very encouraging and relevant finding.

As explained in Section 4.3.4, these results still need to be put into perspective. Mesonic degrees of freedom are not yet included but are crucial to obtain the correct critical scaling inside the critical region around the CEP. However, they have been taken into account in the infinite-volume calculation of the location of the CEP in Ref. [80]. We will revisit this issue later in Section 6.4. As a last point, we also introduced MIT boundary conditions and outlined that it may be necessary to adapt our current framework to those in order to bridge the gap towards more direct applications in the context of heavy-ion collisions.

Chapter 5

Extrapolations from Imaginary Chemical Potentials

In the following, we want to investigate the behaviour of the quark condensate for *imaginary* values of the quark chemical potential. As outlined in Chapters 1 and 2, the main motivation to consider imaginary chemical potentials is to bypass the sign problem of lattice QCD by using them for extrapolations to real chemical potentials. Unfortunately, the quality of such extrapolations cannot be assessed within the framework of lattice QCD. Dyson–Schwinger equations, on the other hand, are well suited for this task since both real and imaginary chemical potentials are accessible. Conversely, the extent of uncertainties caused by the inherent truncations of DSEs might be assessed by comparisons with first-principle lattice results in regions where both methods are applicable. For these reasons, imaginary chemical potentials provide an excellent environment for both frameworks to complement each other.

Notwithstanding the above, imaginary chemical potentials have a priori no real-world meaning. The mathematical structure of the QCD partition function in the plane of complex chemical potentials, however, possesses some interesting features. For example, it turns out that QCD exhibits a special symmetry with respect to imaginary values of the baryon chemical potential – the so-called *Roberge–Weiss symmetry*. This symmetry leads to periodicity of the partition function in imaginary μ_B direction and consequently restricts the range of potential input values for extrapolations. Therefore, imaginary chemical potentials are not only a mere mathematical tool but also an interesting subject to study for their own sake.

To specify the statements of the last paragraph, we begin this chapter with some short elucidations about Roberge–Weiss symmetry and how it influences extrapolation procedures. Thereafter, we present results of our DSE calculations obtained for imaginary chemical potentials and gauge the quality of the extrapolation procedure put forward in Ref. [1]. That is, we perform calculations at appropriate values of imaginary μ_B, where direct comparison with corresponding lattice results is possible. We then employ a similar extrapolation procedure as on the lattice and compare the extrapolated results for the crossover-transition line with the ones explicitly calculated in our functional approach. Large parts of the results in this chapter have been published in Ref. [137].

5.1. Roberge–Weiss Symmetry

In addition to the defining SU(N_c) gauge symmetry, the pure-Yang–Mills part of QCD actually exhibits another symmetry [296]. To see this, we consider gauge transformations of the form

$$U(\tau+\beta,\boldsymbol{x}) = z_k U(\tau,\boldsymbol{x})\,, \quad U \in \mathrm{SU}(3)\,, \tag{5.1}$$

where U are elements of the gauge group, β denotes the inverse temperature, while $\boldsymbol{x}$ and τ label the Euclidean space and time variables, respectively. Specifically, the elements of the gauge group are therefore allowed to be periodic with respect to Euclidean time only up to an element of the *centre*[1] of SU(3): $z_k \in \mathrm{Z}(3)$. This is why such transformations are called *centre transformations* and the corresponding symmetry is labelled *centre symmetry*. The centre elements of SU(N) are given by the N-th roots of the unit matrix:[2]

$$\mathrm{Z}(N) \coloneqq \mathrm{Z}\big(\mathrm{SU}(N)\big) = \left\{ z_k = \exp(2\pi \mathrm{i} k/N) \cdot \mathbb{1}_N : k = 0, 1, \ldots, N-1 \right\} . \tag{5.2}$$

Using the definition in Equation (2.8), one can easily verify that the gauge fields A do not change under the transformations in Equation (5.1) and still fulfil the Kubo–Martin–Schwinger (KMS) condition (see Appendix B.1.1).

While the gauge fields – and thus the pure-Yang–Mills action – are invariant under centre transformations, it is straightforward to show on the lattice that the Polyakov loop (introduced in Section 2.4.2) is not but rather transforms as

$$P(\boldsymbol{n}) \to P'(\boldsymbol{n}) = z_k P(\boldsymbol{n}) . \tag{5.3}$$

In case Z(3) symmetry is unbroken, one hence must have $\langle P \rangle = 0$ (corresponding to the confined phase as explained in Section 2.4.2). If $\langle P \rangle \neq 0$, on the other hand, this necessitates a broken centre symmetry. As a consequence, we may identify the confinement–deconfinement transition in pure Yang–Mills theory with a breaking of Z(3) symmetry. Actually, the same chain of reasoning holds true also in the continuous theory if one considers the Polyakov loop from Equation (2.40) in continuum [297],

$$P(\boldsymbol{x}) = \frac{1}{N_c} \operatorname{tr}\left[\hat{\mathcal{P}} \exp\left(\int_0^\beta \mathrm{d}\tau \, A_4(\tau, \boldsymbol{x}) \right) \right] , \tag{5.4}$$

where the trace is performed in colour space only and $\hat{\mathcal{P}}$ denotes *path ordering* which results from the definition of the path integral. For more background information on the Polyakov loop, see, e.g., the textbooks in Refs. [22, 188] or the review in Ref. [298].

The quark sector of QCD, though, does not exhibit centre symmetry since the transformed quark fields would violate the KMS condition:

$$\Psi(\tau, \boldsymbol{x}) \to \Psi'(\tau, \boldsymbol{x}) = U(\tau, \boldsymbol{x}) \Psi(\tau, \boldsymbol{x}) \quad \Rightarrow \quad \Psi'(\tau + \beta, \boldsymbol{x}) = -z_k \Psi'(\tau, \boldsymbol{x}) . \tag{5.5}$$

As a consequence, dynamical quarks break Z(3) centre symmetry explicitly which renders the Polyakov loop smooth with respect to temperature for small enough quark masses, i.e., when moving away from the upper right corner of the Columbia plot. The resulting crossover behaviour of the Polyakov loop is similar to the one of the quark condensate caused by the explicit breaking of (the chiral) $\mathrm{SU}_A(N_f)$ symmetry by nonzero quark masses.

André Roberge and Nathan Weiss, however, argued that a remnant of centre symmetry is still left in a theory with dynamical fermions [299]. To see this, we start at the partition function for imaginary chemical potentials:

$$\mathcal{Z}(\theta) = \mathcal{N} \operatorname{tr}\left[\exp\left(-\beta \hat{H} + \mathrm{i}\theta \hat{N} \right) \right] , \quad \theta = \beta \operatorname{Im} \mu , \quad \hat{N} = \int \mathrm{d}^3 x \, \left(\Psi^\dagger \Psi \right) . \tag{5.6}$$

[1] Let G be some group. Then, the centre of this group is defined as the set of all group elements that commute with any other group element: $\mathrm{Z}(G) = \{ z \in G : \forall g \in G, \, zg = gz \}$.

[2] Equivalently, we can define the centre elements of SU(N) by $\mathrm{Z}(N) = \{ M = c \cdot \mathbb{1}_N : c \in \mathbb{C}, \, \det(M) = 1 \}$.

Here, $\hat{H}$ labels the system's Hamiltonian operator, $\mathcal{N}$ is some normalization factor and μ denotes the (quark) chemical potential. Heuristically, if there is colour confinement, the eigenvalues of the particle-number operator $\hat{N}$ are always multiplies of N_c, so $\mathcal{Z}(\theta)$ has a period of $2\pi/N_c$ rather than 2π.

More rigorously and connecting with the explanations about centre symmetry from above, we consider the partition function in its path-integral representation:

$$\mathcal{Z}(\theta) = \int \mathcal{D}[\overline{\Psi}, \Psi, A] \ \exp\left(-\int_0^\beta \mathrm{d}\tau \int \mathrm{d}^3x \left[\mathcal{L}[\overline{\Psi}, \Psi, A] - \mathrm{i}\theta\left(\Psi^\dagger\Psi\right)\right]\right). \tag{5.7}$$

The explicit θ dependence can be transferred from the action to the boundary conditions via a change of variables:

$$\Psi(\tau, \boldsymbol{x}) \longrightarrow \Psi'(\tau, \boldsymbol{x}) = \exp(\mathrm{i}\beta/\theta)\Psi(\tau, \boldsymbol{x}) \quad \Rightarrow \quad \Psi'(\tau + \beta, \boldsymbol{x}) = -\exp(\mathrm{i}\theta)\Psi'(\tau, \boldsymbol{x})\,. \tag{5.8}$$

If we perform a centre transformation like before, we find that both the action and the path-integral measure are invariant. The altered boundary conditions of the quarks, which break centre symmetry,

$$\Psi(\tau + \beta, \boldsymbol{x}) = -\exp(2\pi\mathrm{i}k/N_c)\exp(\mathrm{i}\theta)\Psi(\tau, \boldsymbol{x})\,, \tag{5.9}$$

however, we can now absorb via an analogous change of variables to conclude that indeed

$$\mathcal{Z}(\theta) = \mathcal{Z}(\theta + 2\pi k/N_c)\,. \tag{5.10}$$

Therefore, centre symmetry of pure gauge theory turns into a $2\pi k/N_c$ periodicity with respect to imaginary quark chemical potential, the *Roberge–Weiss symmetry*. As it turns out, this symmetry is smoothly realized at low temperature associated with the $\langle L\rangle = 0$ confining phase of pure Yang–Mills theory. For high temperatures, on the other hand, there are discontinuities at $\theta = (\pi + 2\pi k)/N_c$ corresponding to the broken centre symmetry [299]. For all temperatures, though, there is a reflection symmetry around $\theta = \pi$, so one is restricted to values $\mathrm{Im}\,\mu_\mathrm{B}/T < \pi$ for extrapolation procedures.

In this work, we do not incorporate contributions of the Polyakov loop, so we are actually not able to observe Roberge–Weiss symmetry in our results. While this might have some quantitative impact, it should not be troublesome qualitatively for our extrapolations, though, since we restrict ourselves to values of $\mathrm{Im}\,\mu_\mathrm{B}/T < \pi$ anyway. Nevertheless, studies of imaginary chemical potentials including the Polyakov loop have already been performed within our DSE framework in Ref. [253] for heavy quarks, i.e., in the context of the upper right (pure gauge) corner of the Columbia plot (see Chapter 6). There, Roberge–Weiss symmetry appears as expected.

5.2. Numerical Results: Quality of Extrapolations

Now, we turn to the results of our numerical DSE calculations at imaginary chemical potentials. In advance, we remark that we employ the *hybrid truncation* in this chapter. This is due to the fact that we work very closely with lattice results in the following analysis and the hybrid truncation yields a curvature of the crossover line more consistent with the one found on the

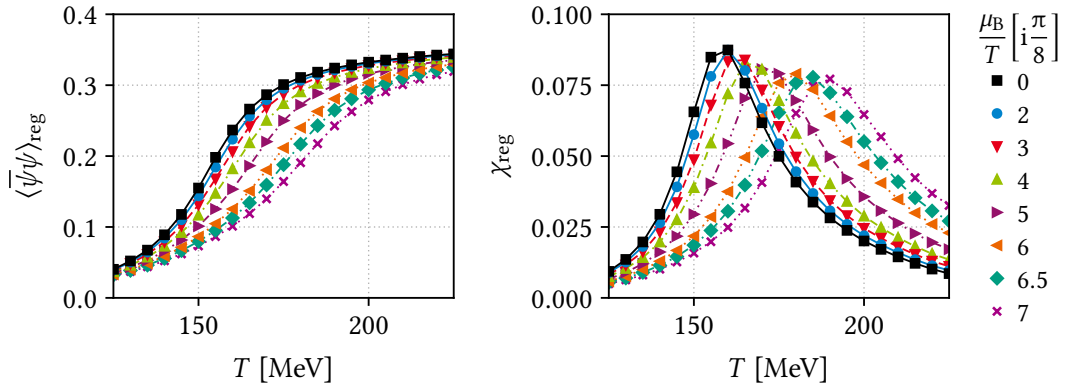

Figure 5.1.: Temperature dependence of the quark condensate (left) and chiral susceptibility (right) for imaginary chemical potentials. Data points are connected by lines to guide the eye.

lattice. In this work, we use a slightly different value for the vertex strength parameter in the quark self-energy, d_{1Q}, as compared to previous works, though. Our value is adapted to yield the same pseudocritical temperature as in Ref. [1] where different conventions for its determination were used from the ones we employ normally in our framework (see below for details and Table 3.1 for a comparison). This leads to $d_{1Q} = 12.71\,\mathrm{GeV}^2$ (instead of $d_{1Q} = 12.85\,\mathrm{GeV}^2$ as in [80]) in the quark self-energy and $d_{1G} = 8.49\,\mathrm{GeV}^2$ (same as in [80]) in the quark loop.

The up-quark condensate is determined via Equation (3.6) while the corresponding chiral quark susceptibility is defined as its derivative with respect to the quark mass:

$$\langle\bar{\psi}\psi\rangle(T,\mu_{\mathrm{B}}) = \langle\bar{\psi}\psi\rangle_{\mathrm{u}}(T,\mu_{\mathrm{B}})\,, \tag{5.11}$$

$$\chi(T,\mu_{\mathrm{B}}) = \frac{\partial\langle\bar{\psi}\psi\rangle(T,\mu_{\mathrm{B}})}{\partial m_{\mathrm{u}}}\,. \tag{5.12}$$

The derivative is numerically determined in our approach via a finite-difference formula (see Appendix D.2.2).

As outlined in Section 3.2, the expression for the condensate in Equation (3.6) is divergent and needs to be regularized. Similarly to Ref. [1], we define the regularized condensate and susceptibility in the following way:

$$\langle\bar{\psi}\psi\rangle_{\mathrm{reg}}(T,\mu_{\mathrm{B}}) = \left[\langle\bar{\psi}\psi\rangle(T,\mu_{\mathrm{B}}) - \langle\bar{\psi}\psi\rangle(0,0)\right]\frac{m_{\mathrm{u}}}{f_\pi^4}\,, \tag{5.13}$$

$$\chi_{\mathrm{reg}}(T,\mu_{\mathrm{B}}) = \left[\chi(T,\mu_{\mathrm{B}}) - \chi(0,0)\right]\frac{m_{\mathrm{u}}^2}{f_\pi^4}\,, \tag{5.14}$$

where $f_\pi = 130.41\,\mathrm{MeV}$ indicates the pion decay constant in vacuum.

5.2.1. Temperature Dependence of Condensate and Susceptibility

We begin our discussion with the numerical results for the regularized quark condensate and chiral susceptibility. These are displayed in Figure 5.1 as functions of temperature for

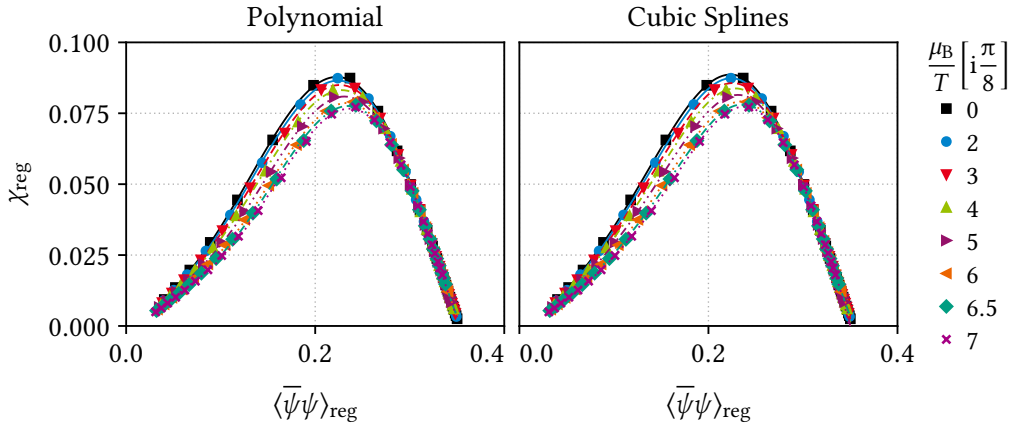

Figure 5.2.: Chiral susceptibility as a function of the quark condensate for imaginary chemical potentials. The points indicate the DSE data while the curves represent polynomial fits (left panel) or cubic spline interpolations (right panel), respectively.

imaginary chemical potentials in the range $\mu_B/T = (0, \ldots, 7) \times \mathrm{i}\pi/8$. For the condensate in the left panel, we observe that all curves behave very similarly. Only the position of the respective inflection point increases with larger $\mathrm{Im}\,\mu_B$ whereas the slope decreases at the same time. The associated susceptibilities in the right panel show an analogous behaviour. That is, their maximum moves towards larger temperature for increasing imaginary chemical potential while their width increases. All of these findings agree qualititatively very well with those of Ref. [1].

Quantitatively, there are some differences. On the one hand, the positions of the inflection points/maxima deviate. While the values for $\mu_B = 0$ coincide (by construction) with a value of $T \approx 155\,\mathrm{MeV}$, they spread between $T \approx 188\,\mathrm{MeV}$ (DSE) and $T \approx 178\,\mathrm{MeV}$ (lattice) at $\mu_B/T = 7/8\pi\mathrm{i}$. On the other hand, the magnitudes of condensate and susceptibility differ between the lattice and our framework. Namely, the lattice condensates are about 40 % larger than the DSE ones across the whole temperature range, while the peak susceptibilities differ by roughly 38 % ($\mu_B = 0$) to 56 % ($\mu_B/T = 7/8\pi\mathrm{i}$). This is mainly due to two reasons. First, the values of the renormalized quark masses do not coincide which leads to some disparities. Second, because of the numerically dissimilar treatment of medium and vacuum in the DSE calculations (see Appendices A.5 and C), the subtracted vacuum value is not perfectly comparable with the associated $T \to 0$ limit in medium.

5.2.2. Determination of the Pseudocritical Temperature

In the following, we now summarize the analysis of the up-quark condensate and the chiral susceptibility employed in Ref. [1] to extrapolate from imaginary to real chemical potentials and adapt it to our DSE framework. Analogously to the procedure described therein, we determine the pseudocritical transition temperature as follows:

1. We calculate the regularized condensate $\langle\bar{\psi}\psi\rangle(T)$ and susceptibility $\chi(T)$ for a discrete set of temperatures at each value of imaginary/real chemical potential.

2. This data is converted to a discrete set of points with the dependence $\chi\big(\langle\bar{\psi}\psi\rangle\big)$.

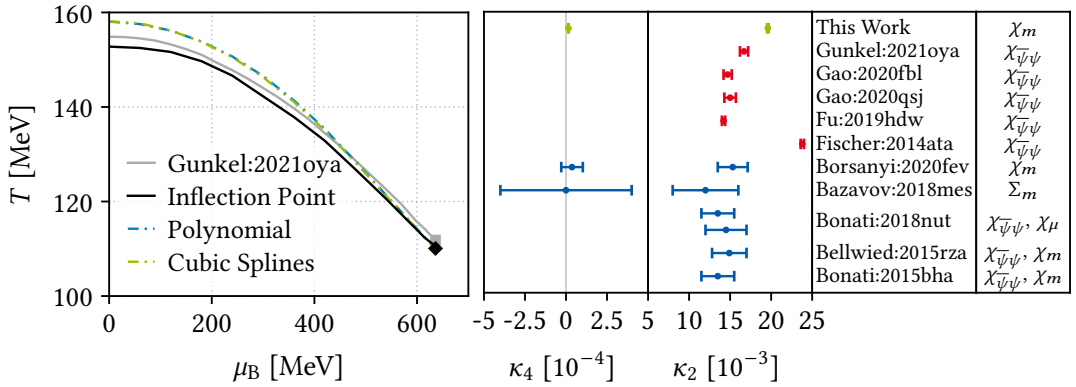

Figure 5.3.: *Left panel*: Phase diagram for different definitions of the pseudocritical temperature (see main text for explanations). *Right panel*: Expansion coefficients κ_2 and κ_4 for the pseudocritical chiral transition line parametrized in Equation (5.15)) from different sources and definitions. Lattice QCD results [1, 77, 277, 278, 300] are displayed in blue, DSE/FRG results [78, 80–83] in red, this work in green. References are denoted by their INSPIRE-HEP citation keys.

3. We use either a fit to a polynomial of order five or a cubic-spline interpolation to determine the peak position of these curves. This yields the value of the condensate at the pseudocritical temperature $\langle\bar{\psi}\psi\rangle(T_c)$.

4. Going back to the discrete set of values for $\langle\bar{\psi}\psi\rangle(T)$ determined in step 1, we use an appropriate interpolation procedure to extract T_c from $\langle\bar{\psi}\psi\rangle(T_c)$.

In Figure 5.2, we display the datasets and resulting curves of $\chi\big(\langle\bar{\psi}\psi\rangle\big)$ obtained from steps 2 and 3 for imaginary chemical potentials in the range $\mu_B/T = (0,\ldots,7)\times i\pi/8$. The points indicate DSE data whereas the curves represent polynomial fits in the left panel and cubic-spline interpolations in the right panel, respectively. We first notice that both the polynomial fits and the cubic splines match the DSE data almost perfectly and yield very similar results. In fact, this observation holds true for real chemical potentials up to rather large values. As a consequence and for the sake of comparability with the lattice results, we restrict ourselves to the polynomial fit results except when noted otherwise.

From Figure 5.2, it is obvious that our curves $\chi\big(\langle\bar{\psi}\psi\rangle\big)$ at different rescaled imaginary chemical potential μ_B/T are close to each other but do not collapse to one curve. We rather find that both peak height and peak position vary slightly with imaginary μ_B. That is, the peak position is at the largest χ but smallest $\langle\bar{\psi}\psi\rangle$ for $\mu_B/T = 0$ while it moves to smallest χ but largest $\langle\bar{\psi}\psi\rangle$ for $\mu_B/T = 7/8\pi i$. We, therefore, do not confirm the apparent collapse (within error bars) observed in Ref. [1] without attaching great significance to this observation, though. Indeed, in later works, μ_B-dependent corrections to simple rescaling laws have been successfully explored [69, 132].

5.2.3. Extrapolation of the Crossover Line

In the next step, we gauge the quality of extrapolations from imaginary to real chemical potentials. In the DSE approach, this is possible since explicit results at real chemical potential

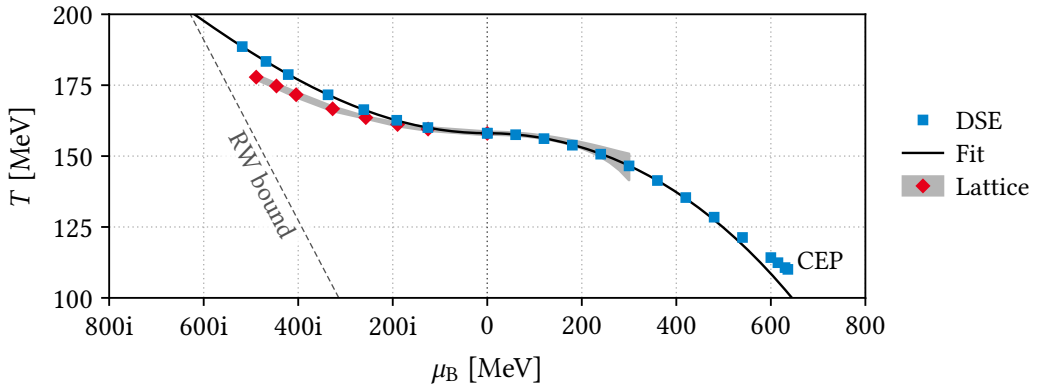

Figure 5.4.: Pseudocritical transition temperature at both imaginary and real chemical potentials from DSEs (points) and fit (line). The grey band and the red diamonds correspond to the lattice results from Ref. [1]. We also show the Roberge–Weiss (RW) bound, $\mathrm{Im}\,\mu_B/T = \pi$.

have been determined already in Ref. [80] and have been verified independently for this work. Using first the inflection point of the subtracted condensate as the crossover criterion, the phase diagram for the setup of Ref. [80] (labelled "Gunkel:2021oya" in Figure 5.3) and the one of this work with the slightly adapted vertex-strength parameter d_{1Q} ("Inflection Point") are shown in the left panel of Figure 5.3. We find an almost uniformly shifted phase boundary to slightly lower temperatures as expected due to the reduced vertex strength. Using the peak of the susceptibility, Equation (5.13), as criterion, we find a crossover line at somewhat larger temperatures that merges with the previous one, of course, at the critical endpoint. The fits to the condensate using polynomials as well as the cubic-spline interpolations end up in very similar results.

Now, we are in a position to compare results obtained from extrapolations with explicitly calculated values. To this end, we fit our phase boundary at imaginary chemical potentials to the well-known parametrization of the pseudocritical transition temperature (see Equation (4.15)),

$$\frac{T_c(\mu_B)}{T_c} = 1 - \kappa_2\left(\frac{\mu_B}{T_c}\right)^2 - \kappa_4\left(\frac{\mu_B}{T_c}\right)^4, \tag{5.15}$$

where $T_c = T_c(\mu_B = 0)$ and κ_2 labels the curvature. In Figure 5.4, we illustrate the pseudocritical temperature obtained for polynomial fits at imaginary chemical potentials. The blue square boxes show the results of the DSE calculations whereas the black curve indicates the fit to the parametrization given in Equation (5.15). The resulting fit parameters are given by

$$\kappa_2^{\mathrm{poly}} = 0.0196 \pm 0.0001\,, \quad \kappa_4^{\mathrm{poly}} = 0.00015 \pm 0.00001\,, \tag{5.16}$$

with very small error and almost vanishing χ^2 value due to the non-statistical nature of the data. The fit very accurately represents the DSE data. If we use cubic-spline interpolations, we again end up at very similar results, i.e., $\kappa_2^{\mathrm{spln}} = 0.0196 \pm 0.0001$ and $\kappa_4^{\mathrm{spln}} = 0.00014 \pm 0.00001$. This underpins the fact that our data points are very well represented by the polynomial fit at imaginary chemical potentials. The difference of the values for κ_2 in Equation (5.16) as compared to

$$\kappa_2^{\mathrm{infl}} = 0.0173 \tag{5.17}$$

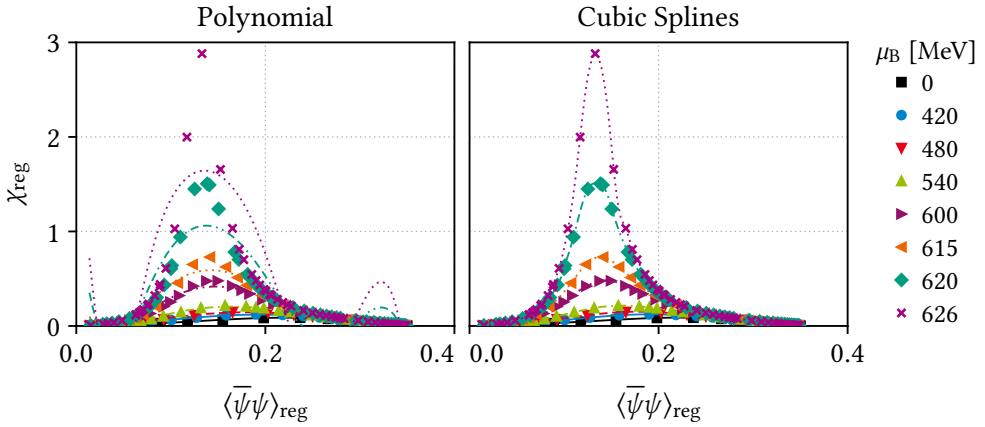

Figure 5.5.: Chiral susceptibility as a function of the quark condensate for real chemical potentials near the CEP. The points indicate the DSE data while the curves represent polynomial fits (left panel) or cubic spline interpolations (right panel), respectively.

presented in Ref. [80] and obtained in the same truncation scheme as used in this work is entirely due to the difference in the definition of the pseudocritical temperature from a different regularized order parameter. The resulting shifts of the transition lines seen in the left panel of Figure 5.3 has been discussed above. Since pseudocritical transition lines from different definitions all end up in the same critical endpoint, they naturally have different curvatures. For completeness, we show results from different sources in the right panel of Figure 5.3. The curvatures therein were determined either by using different definitions of the pseudocritical temperature, i.e., from susceptibilities with respect to temperature or mass $\left(\chi_{\bar{\psi}\psi}, \chi_m, \Sigma_m\right)$, respectively, or by demanding that $\mathrm{d}\langle\bar{\psi}\psi\rangle_{\mathrm{reg}} = 0$ along the crossover line $\left(\chi_\mu\right)$.

Now, we can analytically continue this fit to real chemical potentials and compare to DSE results obtained there. For a discussion of the quality of the fit, see Section 5.2.4. In Figure 5.4, we show our best fit result together with the lattice data of Ref. [1] (red diamonds) and their fit result (grey band). The discrepancy of our data and the lattice data at large imaginary chemical potential is a measure of the systematic error of our calculation and therefore of our data points. This systematic error is small by construction in the vicinity of zero chemical potential but grows into the five-per-cent region for largest imaginary chemical potential. (Naïvely) assuming the error to be symmetric in μ_B, our CEP could be accurate on the level of ten per cent. But, of course, we cannot exclude that new-physics effects at large real chemical potential might invalidate this naïve estimate.

In general, we observe a remarkable coincidence between our fit and the DSE data up to rather large chemical potentials. Deviations of more than one per cent in temperature occur only for $\mu_{\mathrm{B}} > 510\,\mathrm{MeV}$, i.e., for chemical potential larger than 80 % of the one of the CEP, which in the present truncation is located at around $\mu_{\mathrm{B}}^{\mathrm{CEP}} \approx 636\,\mathrm{MeV}$. We can infer that the extrapolation from imaginary chemical potentials works excellently for a large part of the crossover region well towards the CEP.

In the vicinity of the CEP, however, not only does the extrapolation of T_{c} cease to be valid, the $\chi\left(\langle\bar{\psi}\psi\rangle\right)$ curves also can no longer be approximated by a polynomial as is illustrated in Figure 5.5. There, we show the chiral susceptibility as a function of the chiral condensate

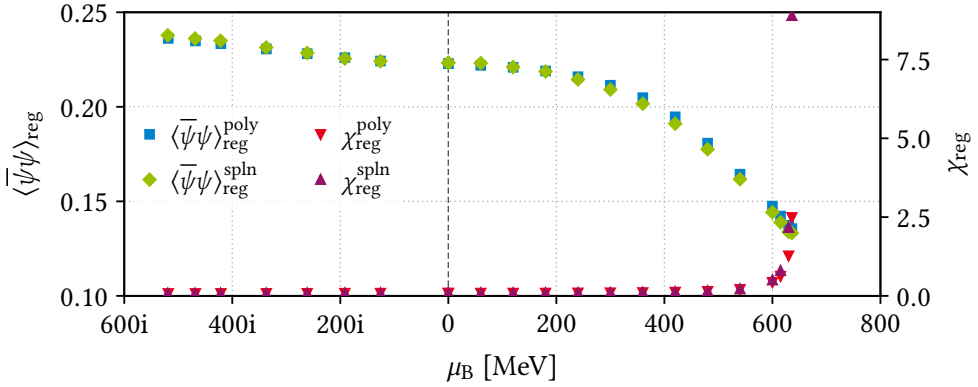

Figure 5.6.: Condensate (blue and green) and susceptibility (red and purple) at the pseudocritical temperature for both imaginary and real chemical potentials obtained both with polynomial fits and cubic spline interpolations.

analogously to Figure 5.2, this time for real chemical potentials $\mu_{\mathrm{B}} > 420\,\mathrm{MeV}$ and $\mu_{\mathrm{B}} = 0$ as a reference. We depict the polynomial fits and cubic-spline interpolations in the left and right panels, respectively. Obviously, the approximation of a fifth-order polynomial breaks down completely at around $\mu_{\mathrm{B}} \gtrsim 600\,\mathrm{MeV}$. In this region, only the splines reliably coincide with the DSE data.

This discrepancy is also visible in Figure 5.6, where we plot peak height and peak position of $\chi\big(\langle\bar{\psi}\psi\rangle\big)$ as a function of negative and positive values of $\big(\mu_{\mathrm{B}}/T\big)^2$. We show results for the polynomial fits as well as the cubic-spline interpolations for the sake of comparison. We notice again that both peak position and height are not entirely constant at imaginary chemical potentials in slight contrast to the lattice results discussed in Ref. [1]. While the change of the condensate is more or less constant for real μ_{B}, the critical susceptibility does not change much for small chemical potentials but drastically in the vicinity of the CEP, which is expected. This is also the region where the polynomial fit and the spline interpolation deviate substantially, i.e., where the assumption of a low-order polynomial breaks down. Again, this is to be expected since the susceptibility is singular at the CEP.

We would like to finish our analysis by pointing out that our results fully support the analysis performed in Ref. [1]. In the imaginary chemical potential region where the lattice fits have been done, there is no difference in quality in using polynomial or spline fits. This is also true for the region of real chemical potential covered by the lattice extrapolation. The (expected) problems with the polynomial fits emerge only at much larger real chemical potential, close to the CEP.

5.2.4. Sensitivity of the Fit

Since the main goal of this analysis is to gauge the quality of extrapolations from imaginary to real chemical potentials and since our extrapolation is based on a fit to Equation (5.15), it is mandatory to quantify the sensitivity of our fit to the input points. This is done and depicted in Figure 5.7 in two different ways.

First, we investigate the dependence of the fit on the number and the interval of the input

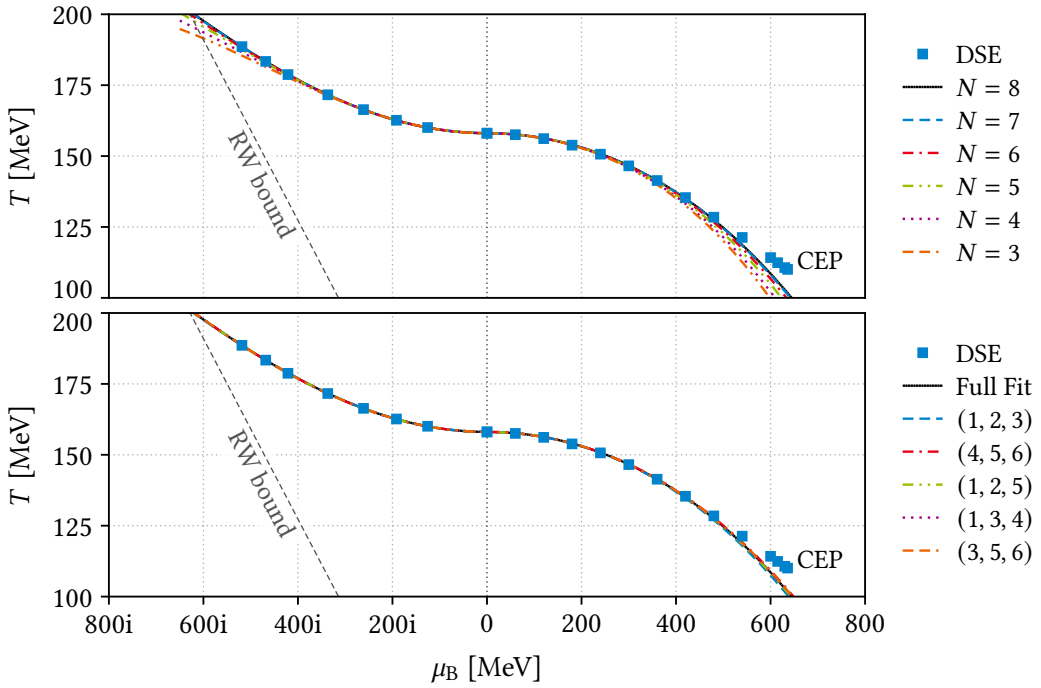

Figure 5.7.: *Upper panel*: Results for fits to different numbers of point at imaginary potential. N counts the number of points starting with 1 at zero chemical potential and adding point-by-point in direction of increasing imaginary chemical potential. *Lower panel*: Results for fits to different combinations of input points at imaginary potential with three points left out compared with the full fit that includes all points. The tuples given here label the indices that were left out from the input points for the fit.

points displayed in the upper panel. Starting with fits to $N = 3$ points at zero chemical potential and the two smallest imaginary values, we add point-by-point in the direction of increasing imaginary chemical potential until we include all data at $N = 8$. We clearly observe that the quality of the fits improves rapidly until it settles down at about $N = 6$. Adding further points enhances the fit very little. We conclude from this that a large imaginary-chemical-potential range is important but going all the way to the Roberge–Weiss bound is not necessary. Therefore, we could have stopped at $N = 6$ to obtain an appropriate fit.

Furthermore, we studied what happens to the fit when leaving out three arbitrary input points between zero chemical potential and the largest imaginary value. This is exemplarily shown in the lower panel for five different combinations of omitted indices in comparison with the full fit which includes all points. One can clearly see that this changes neither the quality of the fit nor of the extrapolation at all. We have verified that this holds true for all possible combinations of three omitted indices.

5.3. Outlook: Lee–Yang Zeroes

With both real and imaginary chemical potentials at our disposal, the next logical step is to consider *complex chemical potentials*. As already pointed out in the introduction of this

chapter, the QCD partition function in the plane of complex chemical potentials exhibits interesting mathematical structure with physical implications.

To understand this, we follow the line of argument put forward by Tsung-Dao Lee and Chen-Ning Yang [301, 302]. Namely, the grand-canonical partition function $\mathcal{Z}_V$ of a lattice theory is a (highly dimensional) polynomial of the fugacity y for any finite volume V. This polynomial exhibits many roots (i.e., zeroes) y_i in the complex chemical-potential plane, the so-called *Lee–Yang zeroes*:

$$\mathcal{Z}_V(y) = \prod_{i=1}^{N}\left(1 - \frac{y}{y_i}\right), \quad \mathcal{Z}_V(y_i) = 0\,, \quad y \propto \exp(\mu/T)\,, \quad N \in \mathbb{N}\,. \tag{5.18}$$

Due to the structure of the partition function in a finite volume, none of these roots can be real and positive. The distribution of y_i now provides information about the phase structure of the underlying theory. That is, the grand potential, $\Omega_V = \ln \mathcal{Z}_V$, naturally has singularities at roots of $\mathcal{Z}_V$. If there is a region in the complex plane that does not contain any y_i and encloses a strip R of the real axis, Lee and Yang have proven that all of the following functions stay analytic for $y \in R$:

$$f_n(y) = \lim_{V\to\infty}\left(\frac{\partial}{\partial \ln y}\right)^n \frac{1}{V}\Omega_V(y)\,, \quad n \in \mathbb{N}\,. \tag{5.19}$$

For this reason, phase transitions of the system can occur only at the points on the positive real y axis onto which the roots y_i close in for $V \to \infty$.

As we will see shortly, the location of these zeroes entails information about phase transitions even if they are not located on the real axis. Namely, for temperatures larger than the critical one, $T > T_\mathrm{c}$, one has no phase transition in μ direction and so there only exist zeroes with nonzero imaginary part, $\operatorname{Im} y_i \neq 0$. As a consequence, there is a gap of width $2y_0$ between the two zeroes closest to the real axis, y_0, and the partition function is analytic for values in between, $|\operatorname{Im} y| < y_0$. In this context, it was pointed out by Michael E. Fisher [303] that the edges of this gap, $y = \pm \mathrm{i}y_0$,[3] must be branch points and termed them *Lee–Yang edge singularities*. Moreover, he highlighted that an order parameter $M(y)$ obeys a scaling behaviour in the vicinity of these edge singularities,

$$m \propto h^\sigma\,, \quad m = M(y) - M(\mathrm{i}y_0)\,, \quad h = y - \mathrm{i}y_0\,, \tag{5.20}$$

where σ labels some critical exponent. Phrased alternatively and building on the explanations in Ref. [130], the universal scaling function of the order parameter $f_G(z)$ exhibits a branch cut singularity at a universal position $z = z_\mathrm{c}$. We can embed this into a more general context by considering the following parametrization of an order parameter in the vicinity of a second-order phase transition:

$$M = h^{1/\delta} f_G(z) + M_\mathrm{reg}\,, \quad z = t/|h|^{1/(\beta\delta)}\,, \tag{5.21}$$

where t is the reduced temperature, h labels a symmetry-breaking field, β and δ denote critical exponents, while M_reg accounts for regular contributions of the order parameter. From the

[3] Here, we assumed without loss of generality that the real part of the zeroes vanishes.

temperature scaling associated with the Roberge–Weiss critical point, for example, one can identify

$$t = t_0^{-1}\left(\frac{T_{\mathrm{RW}} - T}{T_{\mathrm{RW}}}\right), \quad h = h_0^{-1}\left(\frac{\hat{\mu}_{\mathrm{B}} - \mathrm{i}\pi}{\mathrm{i}\pi}\right), \tag{5.22}$$

where $\hat{\mu}_{\mathrm{B}} = \mu_{\mathrm{B}}/T$, t_0, h_0 and the Roberge–Weiss transition temperature T_{RW} are non-universal parameters. We can now calculate the location of the corresponding Lee–Yang edge singularities $\hat{\mu}_{\mathrm{B}}^{\mathrm{LY}}$ by solving

$$t/|h|^{1/(\beta\delta)} = z_{\mathrm{c}}\,, \quad \text{with} \quad z_{\mathrm{c}} = |z_{\mathrm{c}}|\exp\bigl(\mathrm{i}\pi/(2\beta\delta)\bigr)\,, \tag{5.23}$$

for $\hat{\mu}_{\mathrm{B}}$ to obtain

$$\mathrm{Re}\,\hat{\mu}_{\mathrm{B}}^{\mathrm{LY}} = \pm\pi\left(\frac{z_0}{|z_c|}\right)^{\beta\delta}\left(\frac{T_{\mathrm{RW}} - T}{T_{\mathrm{RW}}}\right)^{\beta\delta}, \quad \mathrm{Im}\,\hat{\mu}_{\mathrm{B}}^{\mathrm{LY}} = \pm\pi\,, \tag{5.24}$$

where we define a normalization constant $z_0 = h_0^{1/(\delta\beta)}/t_0$. Similar analyses can be performed for the second-order transition in the chiral limit, $m_{\mathrm{u}} \to 0$, or at the QCD critical endpoint.

As a consequence, a worthwhile option for future investigations is to determine the location of Lee–Young zeroes inside the complex chemical-potential plane in order to study potentially different kinds of phase transitions. This is also interesting in view of extrapolation procedures since Lee–Yang zeroes – as singularities of the grand potential – limit their radius of convergence. Additionally, we can link to the analysis in the last chapter. Namely, a different extrapolation procedure was brought forward in [130] which builds on using Padé approximants of the baryon-number fluctuations around the RW point. For this reason, an attractive further possibility for future studies would be to reproduce this extrapolation procedure within our framework.

5.4. Summary

In this chapter, we first motivated imaginary chemical potentials and reiterated some basics about Roberge–Weiss symmetry and its implications. Thereafter, we studied whether the extrapolation procedure from imaginary to real chemical potentials introduced in Ref. [1] in the context of lattice QCD is capable to reproduce explicit results for the phase-transition line at real chemical potentials obtained with functional methods. The result is very encouraging: Up to quite large chemical potentials not very much smaller ($\approx 20\,\%$) than the one of the critical endpoint, the extrapolation works extremely well. For larger chemical potentials, the extrapolated transition line undershoots the calculated one; at the critical chemical potential $\mu_{\mathrm{B}}^{\mathrm{CEP}} \approx 636\,\mathrm{MeV}$, the resulting temperature of the extrapolation is about 13 MeV too small. Also, of course, it is not possible to extract the location of the CEP from the extrapolation procedure. However, comparing the lattice results with the ones of our framework at large imaginary chemical potential and taking this as a (naïve) measure for the corresponding systematic error of our framework at corresponding values for real chemical potential, this indicates a systematic error of the order of five to ten per cent for the location of the CEP. Finally, we have argued that the investigation of Lee–Yang zeroes is an interesting option for future work that can build on the results and methods in this chapter.

Chapter 6
The Columbia Plot

In our final and second eponymous analysis, we investigate the quark mass dependence of the QCD phase diagram by means of the left-hand side of the Columbia plot. Building on explanations in Chapter 1 and Sections 2.2.3 and 5.1, we start this chapter with an in-depth revision of the Columbia plot that will serve as a motivation for the studies to come.

Afterwards, we explicate the inclusion of long-range-fluctuation effects with quantum numbers of mesons on the quark–gluon vertex that were already hinted at in Section 4.3.2. We discuss our treatment of the corresponding meson masses and decay constants for varying strange-quark mass, taking particular care of the limits $m_s \to \infty$ and $m_s \to 0$. In Section 6.3, we then present our results for the order of the phase transition along the left-hand side (i.e., chiral up/down quarks but varying strange-quark mass) of the Columbia plot for zero and small nonzero real and imaginary chemical potentials as well as the bottom edge (i.e., chiral strange quarks but varying up/down-quark mass). We discuss critical temperatures, the resulting Columbia plot and the dependence of our result on the restoration temperature of the $\mathrm{U}_A(1)$ symmetry. The majority of this chapter is – as of the writing of this thesis – available as a preprint in Ref. [138].

6.1. Motivation and Background

To start, we want to deepen and extend the discussion of the Columbia plot from Chapter 1. To this end, we now display the three most-probable scenarios for the Columbia plot in Figure 6.1. Each of the phase transitions seen there (first order, second order or crossover) is related to an underlying symmetry of QCD: chiral symmetry and centre symmetry. Their explicit breaking due to non-vanishing (chiral) or non-infinite (centre) quark masses generates possible patterns for the order of the transition at nonzero temperature and vanishing chemical potential as a function of the quark masses.

As explained in Section 5.1, centre symmetry of pure gauge theory is unbroken for low temperatures while it gets broken at some critical temperature. Therefore, in the upper right corner of each of the three plots, we find the first-order deconfinement transition in the pure-gauge limit of infinite quark masses, separated by a second-order critical line from the crossover region. The second-order separation line in the upper right corner of the Columbia plot is in the $\mathrm{Z}(2)$ universality class and its location in the up/down–strange-quark mass plane has been mapped out by lattice gauge theory [304–309], effective models [310, 311], the DSE approach [253] and background-field techniques [312, 313]. Thus, although the precise location of the second-order critical line may differ between the approaches, the qualitative picture is undisputed.

This is different for the chiral upper left and lower left corners of the Columbia plot as well as the left edge of varying strange-quark masses in the up/down-quark chiral limit. This

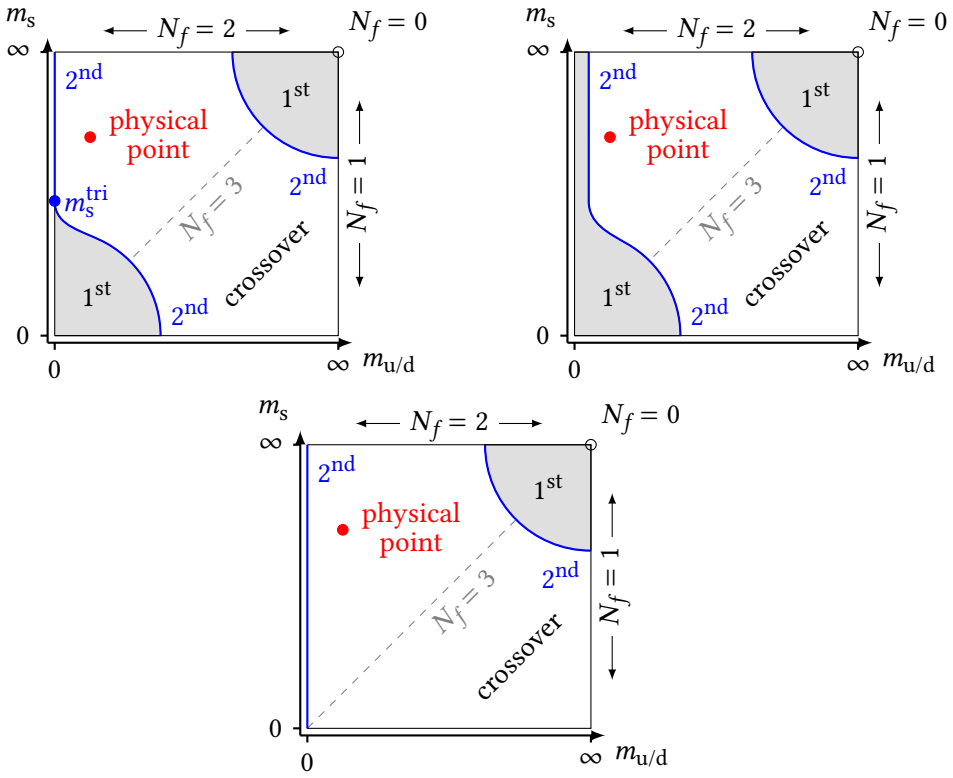

Figure 6.1.: Three different versions of the Columbia plot [134] of phase-transition orders at nonzero temperature and vanishing chemical potential as functions of quark masses. We display the 'standard plot' with anomalously broken $U_A(1)$ symmetry (upper left), a possible version with restored $U_A(1)$ (upper right) and an alternative version without chiral first order regions (bottom).

region is governed by the chiral axial and axialvector symmetries, $U_A(1) \times SU_A(N_f)$. Whereas the latter is broken dynamically at low temperatures (and always explicitly by nonzero quark masses), the former is broken anomalously as outlined in Section 2.2.3. Both the dynamical and anomalous breaking can be restored at large temperatures, even though the corresponding transition temperatures may very well differ from each other. Whether $U_A(1)$ remains broken at the temperature of the chiral $SU_A(N_f)$ transition is an open question with conflicting indications in both directions [314–322].

The fate of the $U_A(1)$ symmetry is expected to affect the order of the chiral $SU_A(N_f)$ transition. With an anomalously broken $U_A(1)$ at all temperatures, it has been conjectured that the chiral transition for the two-flavour theory (upper left corner) is second order and in the universality class of the O(4) theory, whereas the chiral three-flavour theory (lower left corner) is expected to be first order [133] since no three-dimensional $SU(N_f \leq 3)$ second-order universality class is known [323, 324]. Consequently, the left edge of the Columbia plot features a tricritical strange-quark mass m_s^{tri} where the first-order region around the chiral three-flavour point merges into the second-order line connected to the chiral two-flavour point. This is the 'standard' plot, i.e., the scenario found most often in the literature, seen on

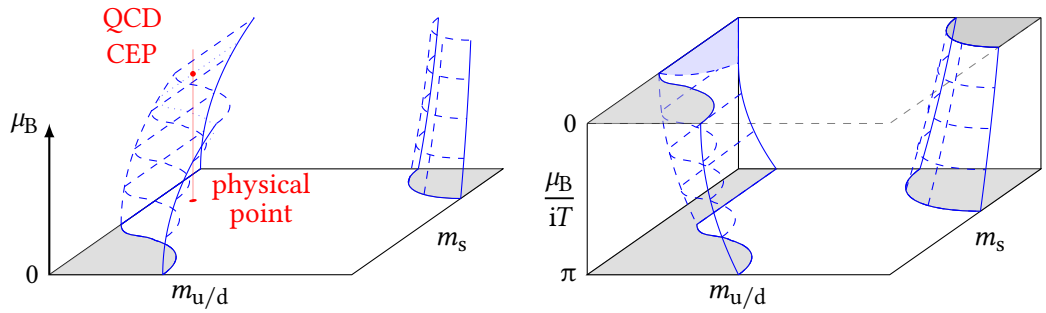

Figure 6.2.: Three-dimensional extensions of the 'standard' Columbia plot with respect to real (left) and imaginary (right) chemical potentials.

the upper left of Figure 6.1. The upper right panel shows a possible scenario with restored $U_A(1)$. There, the $N_f = 2$ corner may remain first order [133] and the two first-order corners are expected to be connected along the left-hand side of the plot.

As of now, it is still an open question which of these scenarios is realized in QCD. The situation in the upper left corner and, relatedly, along the left edge of the $N_f = 2 + 1$ theory is not clear and indications from lattice simulations vary between favouring either of the two upper scenarios of Figure 6.1 [320, 325–332]. Both of these scenarios can also be realized in effective low-energy QCD models such as the PQM or PNJL model, see, e.g., Refs. [333–340] and references therein, and FRG approaches to QCD [341, 342]. In Ref. [340], it has been demonstrated that results for the Columbia plot from mean-field approaches are substantially modified once fluctuations are included.

For the theory with three mass-degenerate flavours, lattice studies seem to support the existence of a first-order transition for light quark masses on coarse lattices [343–349]. However, the size of the first-order region depends strongly on the formulation of the lattice action and the temporal extend of the lattice and has not yet been determined unambiguously. Thus, it has been conjectured [324] that the third option for the Columbia plot shown in the bottom panel of Figure 6.1 is a realistic possibility. Indeed, recent results on the lattice clearly point in this direction [350] and have been followed up in Ref. [351] with similar results. In Ref. [352], it has been suggested that a second-order $N_f = 3$ transition may not be at odds with previous FRG results, see Ref. [340] and references therein.

Apart from insights about the general nature of chiral symmetry breaking, investigations of the Columbia plot might actually also tell us something about the phase diagram at physical quark masses more directly. In order to see this, we consider a three-dimensional extension with respect to real and imaginary chemical potentials. In this case, the critical second-order lines turn into critical surfaces. As an example, we illustrate a commonly found extension of the 'standard plot' in Figure 6.2. In the scenario seen there, the critical line at $m_{u/d} \to 0$ and $\mu_B \to 0$ turns into a critical sheet that bends towards larger $m_{u/d}$ for increasing μ_B until it intersects the physical point at $\mu_B = \mu_B^{CEP}$. If this is true, the chiral second-order phase transition and the second-order physical CEP are connected to each other. On the other hand, there are alternative scenarios of a restored $U_A(1)$ where the critical sheets bends towards lower $m_{u/d}$ until it vanishes [353]. Such a scenario could potentially rule out the existence of a physical CEP or at least render it unrelated to the chiral transition. The behaviour of

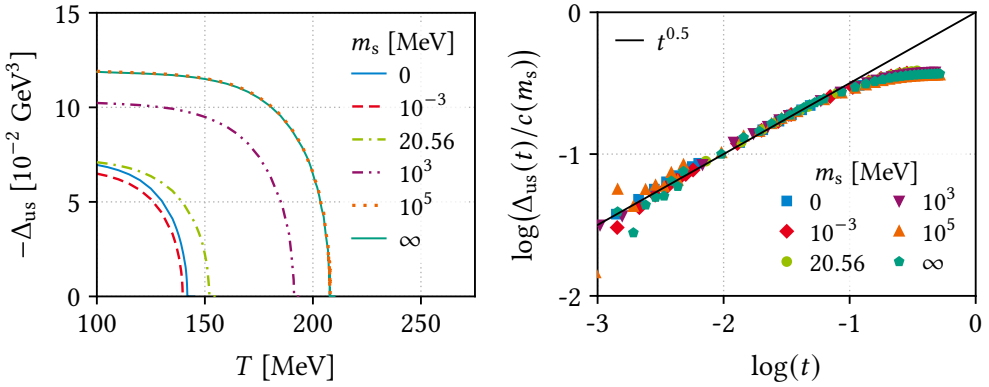

Figure 6.3.: Regularized quark condensate obtained in the unquenched truncation without long-range correlations for different strange-quark masses in the up/down-quark chiral limit. *Left*: Condensate as a function of temperature. *Right*: Scaling behaviour of the (normalized) condensate as a function of the reduced temperature.

the critical sheet in the pure-gauge corner as seen in Figure 6.2, on the other hand, is again confirmed by several different approaches [253, 304, 306, 311–313].

The purpose of this chapter is to re-examine the situation of the Columbia plot in a functional continuum framework that takes both microscopic quark and gluon degrees of freedom as well as effective, long-range degrees of freedom with the quantum numbers of pseudoscalar and scalar mesons into account. In the framework of DSEs that we employ, the latter appear naturally as part of fermion four-point functions in the DSE for the quark–gluon vertex [287, 289]. At nonzero temperature and chemical potential, the corresponding setup has already been explored for physical quark masses [80, 248, 249] and has led to a prediction of the location of the critical endpoint in agreement with recent FRG studies [81–83]. Here, quarks have been taken into account on the $N_f = 2 + 1$ level but the mesonic sector remained $N_f = 2$ [80, 248, 249]. In this chapter, we extend the framework to a consistent $N_f = 2 + 1$ setup and therefore make it suitable for a study of the left-hand side of the Columbia plot.

6.1.1. Unquenched Truncation in the Up-Quark Chiral Limit

As a first step and proof of principle, we analyse the left edge of the Columbia plot within the unquenched (not hybrid) truncation of Section 3.5.2 yet without long-range correlations. In Figure 6.3, we show the regularized quark condensate as a function of temperature in the up-quark chiral limit, $m_u \to 0$, for several strange-quark masses ranging between $m_s = 0$ and $m_s \to \infty$. As can be seen, we find a second-order phase transition for all investigated strange-quark masses. Therefore, the second-order line extends across all of the left edge of the Columbia plot and there is no chiral corner on the bottom left in our truncation corresponding to the scenario in the lower panel of Figure 6.1.

In the vicinity of a second-order phase transition, the order parameter obeys a power law with respect to some (universal) reduced quantity. For the regularized condensate, we expect

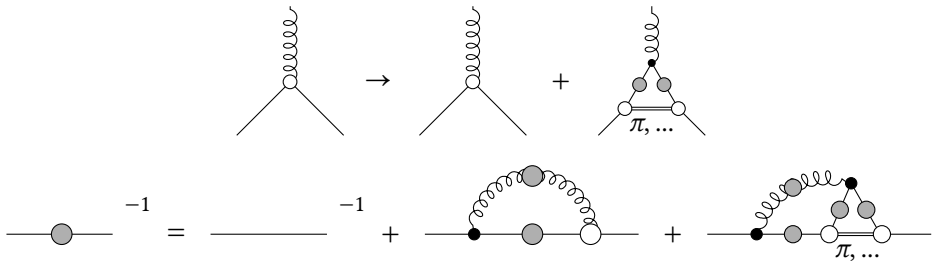

Figure 6.4.: *Top*: Vertex ansatz for including long-range correlations originating the in the skeleton expansion of the quark–gluon-vertex DSE. *Bottom*: Resulting DSE for the quark propagator.

the following behaviour:

$$\Delta_{\ell s}(T, m_u \to 0, m_s) \sim c(m_s) \cdot t^{\beta}, \quad \text{where} \quad t = \frac{T_c(m_s) - T}{T_c(m_s)} \tag{6.1}$$

labels the reduced temperature, β indicates the critical exponent depending on the underlying universality class and c denotes a non-universal constant, while the critical temperature T_c is also non-universal. To analyse the scaling behaviour, we display the regularized condensate as a function of the reduced temperature as a log–log plot in the right panel of Figure 6.3. In order to compare the curves for different strange-quark masses, we divide by $c(m_s)$ for normalization. We find that all curves align very nicely along $t^{0.5}$ for $t \lesssim -1.1$. Therefore, we obtain the 4D-Ising mean-field exponent, $\beta = 0.5$, and not the (at least in the $N_f = 2$ corner) expected O(4) one of $\beta = 0.73/2$. In fact, this behaviour has been found in rainbow–ladder-type truncations already very early and has been reviewed in Ref. [216]. Without the extension of our truncation we are about to introduce, we are therefore not able to describe the correct scaling behaviour.

6.2. Long-Range Correlations: Meson-Backcoupling Diagrams

Since the correlation length diverges in the vicinity of a second-order phase transition, long-range correlations in the quark–gluon vertex become important. These arise from a specific diagram in the DSE for the quark–gluon vertex that involves a four-quark kernel. In pole approximation, this diagram is shown in the upper equation of Figure 6.4. Said diagram provides contributions to all tensor components of the quark–gluon vertex [287]. In the quark DSE in the lower equation, the resulting two-loop diagram can be simplified to a one-loop diagram using a homogenous Bethe–Salpeter equation (BSE), see Refs. [80, 287] for details. The effect of this specific contribution to the quark–gluon interaction has been studied in a number of works at zero temperature/chemical potential including a discussion of the analytic structure of the quark propagator [289], a discussion of its effect onto the meson spectrum [288] and an exploratory study of meson-cloud effects in baryons [354]. In all of these studies, it has been noted that meson-backcoupling effects typically provide contributions of the order of 10–20 % as compared with other components of the quark–gluon interaction. The effect of this contribution on the location of the CEP has been studied in Ref. [80].

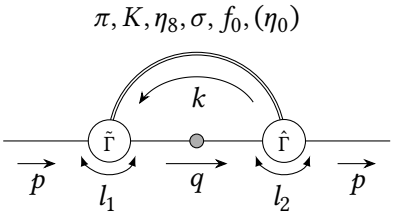

Figure 6.5.: One-loop meson-backcoupling diagram in the quark self-energy as an approximation of the two-loop diagram of Figure 6.4.

The quark–gluon vertex, split into a non-hadronic (NH) and a mesonic (M) part and inserted into the quark DSE leads to the following expression for an analogous splitting of the quark self-energy:

$$\Sigma_f(p) = \Sigma_f^{\mathrm{NH}}(p) + \Sigma_f^{\mathrm{M}}(p)\,, \tag{6.2}$$

The non-hadronic part of the quark self-energy corresponds to the usual quark self-energy from Equation (3.8). The new element of the truncation used in this chapter – as compared to Ref. [80] – is the inclusion of the strange-quark contributions to the mesonic part of the vertex. While the quark–gluon vertex would formally also have to be replaced in the quark-loop diagram of the gluon DSE of our truncation, we do not take the mesonic effects explicitly into account there. The main reason is feasibility: In the quark loop, the meson-exchange diagram remains two-loop and is therefore too expensive in terms of CPU time. However, these contributions are also irrelevant when it comes to critical exponents [251].

In the following, we discuss the mesonic part of the quark self-energy in more detail. To this end, we begin again with the two-loop expression in the quark DSE in the lower equation of Figure 6.4. This diagram originates from the meson-pole approximation of a fermion four-point function in the DSE for the quark–gluon vertex [287]. The corresponding meson propagator in the diagram is therefore bare and accompanied by two Bethe–Salpeter amplitudes (BSAs) that connect the quark lines with the exchanged meson in question. In Ref. [287], it has been realized that the left half of the two-loop diagram displayed in Figure 6.4 can be interpreted as the interaction diagram in a homogeneous BSE and therefore can be replaced with a BSA. This way, the mesonic part of the quark self-energy reduces to a one-loop diagram illustrated in Figure 6.5. Of course, this simplifies calculations tremendously.

In principle, this diagram contains mesons with all quantum numbers that can be build from a quark–antiquark pair. In practice, we are only interested in those mesons that have the potential to become massless at phase transitions, i.e., the pseudoscalar meson octet, its critical chiral-partner modes and the pseudoscalar singlet in case the axial $\mathrm{U}_A(1)$ is restored at the transition temperature. All of these are potentially long ranged and are expected to become the dominant degrees of freedom at second-order phase transitions. All other meson contributions are subleading due to their large masses in the meson propagator and are therefore omitted in our approach.

We thus end up with the lightest pseudoscalar octet, i.e., pions, kaons and the η_8, as well as the η_0 in a crosscheck calculation (see Section 6.3). Additionally, we consider the scalar σ meson (i.e., the $f_0(500)$) as it is vital for the correct $\mathrm{O}(4)$ scaling behaviour in the upper left corner of the Columbia plot and the $\mathrm{s\bar{s}}$ partner of the σ (which we identify with the $f_0(980)$)

that may be important in the $N_f = 3$ chiral limit. As detailed below in Equation (6.5), we assume the f_0 to be massless in the chiral $N_f = 3$ limit since it has the quantum numbers of the strange-quark condensate. In order to obtain a consistent $N_f = 3$ limit, we alter its flavour factor by hand to match the one of the σ meson in order to obtain three identical DSEs for the up, the down and the strange quark in this limit (cf. Table 6.1).[1]

Restricting to the pions and σ meson, this type of meson backcoupling was discussed in detail, e.g., in Refs. [80, 251]. Building on the explanations therein, we generalize this to the $N_f = 2 + 1$ case to arrive at the following mesonic contribution to the quark self-energy:

$$\Sigma_f^{\mathrm{M}}(p) = \sum_X F_X^f \int\!\!\!\!\!\!\sum_q D_X(P)\tilde{\Gamma}_X^f(l_1, -P)\, S_X^f(q)\, \hat{\Gamma}_X^f(l_2, P)\,. \tag{6.3}$$

Here, $P = p - q$ denotes the total meson momentum, whereas l_i represents the relative momenta of the Bethe–Salpeter amplitudes. Using an appropriate momentum routing, we can identify $l_1 = p$ and $l_2 = q$.[2] As always, we work in the isospin-symmetric limit of degenerate up and down quarks ($m_{\mathrm{u}} = m_{\mathrm{d}}$, $\mu_{\mathrm{u}} = \mu_{\mathrm{d}}$). For the sake of brevity and simplicity, we will from now on mostly refer to a 'light' quark, $\ell = \mathrm{u} = \mathrm{d}$, instead of up/down quarks. This way, for instance, we do not have differentiate between different pion and kaon species.

Most quantities in Equation (6.3) are specific to the flavour of the external quark, $f \in \{\ell, \mathrm{s}\}$, and the exchanged meson, $X \in \{\pi, K, \eta_8, \sigma, f_0, (\eta_0)\}$. First, there are the multiplicities F_X^f of the respective meson-backcoupling diagram obtained by performing the trace over flavour space (see Appendix C.4.3). Second, we have the quark propagator of the internal quark S_X^f which differs from the external one for the kaon, i.e., $S_K^\ell = S_{\mathrm{s}}$ and $S_K^{\mathrm{s}} = S_\ell$.

The (inverse) meson propagator at nonzero temperature reads [355]

$$D_X^{-1}(P) = P_4^2 + u_X^2\left(\boldsymbol{P}^2 + m_X^2\right), \tag{6.4}$$

with $u_X = f_X^s/f_X^t$ being the meson velocity which is given by the ratio of the spatial and temporal meson decay constants, f_X^s and f_X^t, respectively. Again, we restrict ourselves to potentially critical modes and consider only the zeroth Matsubara frequency of the meson propagator, i.e., $P_4 = 0$. All other Matsubara frequencies act as an effective meson mass that leads to suppression of the respective contribution. This restriction implies $q_4 = p_4$ in Equation (6.3) and consequently cancels the Matsubara sum [356].

For the meson masses m_X, we choose the vacuum values:

$$\begin{aligned} m_\pi &= 156.525\,\mathrm{MeV}^{1/2}\cdot m_\ell^{1/2}\,, \quad m_\sigma = 2m_\pi\,, \\ m_K &= 74.2\,\mathrm{MeV}^{1/2}\cdot m_{\mathrm{s}}^{1/2} + 1.54\cdot m_{\mathrm{s}}\,, \quad m_{\eta_8} = m_{f_0} = 2m_K\,. \end{aligned} \tag{6.5}$$

[1] In a more complete framework, we would additionally include the a_0 as well as all other members of the scalar meson multiplets and determine their masses, wave functions and decay constants dynamically. In this case, adjusting flavour factors by hand would not be necessary.

[2] This somewhat unusual choice of the routing parameter has two major advantages. First, if one BSA only depends on the external momentum p, it does not have to be integrated over. Second, in view of (potential) finite-volume calculations, the relative momenta always stay valid torus points. Nevertheless, we have checked explicitly that a change of the momentum routing makes only a small quantitative and no qualitative difference.

These have been obtained in the following way: We have solved the coupled system of $N_f = 2 + 1$ DSEs without meson-backcoupling effects in the vacuum for complex quark momenta. Then, we extracted the associated meson masses from the solutions of their corresponding Bethe–Salpeter equations for different light- and strange-quark masses. The resulting mass curves for the pion and the kaon have been fitted with the expressions above, which correspond to the expected behaviour from Gell-Mann–Oakes–Renner relations. The remaining masses are expressed in terms of these for the sake of simplicity in such a way that the correct massless modes appear in the $N_f = 2$ and $N_f = 3$ chiral flavour limits.

Note that this treatment overestimates the effects of the critical modes in the chirally broken low-temperature phase since the critical modes are always massless by construction instead of becoming massless only at the critical temperature. We have checked that this simplification does not affect the order of the transition but it may affect its location, i.e., the critical temperature. We discuss this further in Section 6.3, when we present our results. In principle, one could solve the temperature-dependent Bethe–Salpeter equations also at nonzero temperature along the lines of Ref. [356]. There, it has been shown explicitly that the pion and sigma modes follow the correct pattern of symmetry breaking and restoration in the $N_f = 2$ chiral limit. In practice, this would add an extra layer of complications and an order of magnitude more in computing time to an already demanding endeavour and we therefore resort to the simplifications expressed in Equation (6.5).

The central unknown quantities are the meson Bethe–Salpeter amplitudes $\hat{\Gamma}_X$. In the chiral limit, it is an exact property of QCD [357, 358] that the leading BSA of the Goldstone boson can be expressed through the scalar dressing function B of the quark propagator and the Goldstone-boson decay constant via $\hat{\Gamma}_X(l, P) = \gamma_5 B(l)/f_X$, with relative momentum l between the quark and the antiquark, see Ref. [207] for a review and a detailed explanation of this property. This behaviour persists approximately also away from the chiral limit with the caveat that the quark dressing function then develops a logarithmic tail at large momenta whereas the Bethe–Salpeter amplitude always falls like a power in momentum. We therefore adopt the following prescription for our meson amplitudes:

$$\hat{\Gamma}^f_X(l, P) = \gamma_X \frac{B^r_f(l)}{f^{f,t}_X} \coloneqq \gamma_X \frac{B_f(l)}{f^{f,t}_X} \cdot \frac{a}{a + l^2}\,, \quad a = 80\,\mathrm{GeV}^2\,, \tag{6.6}$$

where $f^{f,t}_X$ labels the respective temporal meson decay constant with $\gamma_X = \gamma_5$ for the pseudoscalar mesons and $\gamma_X = \mathbb{1}$ for the scalar mesons. Additionally, we also apply these relations to mesons comprising non-chiral strange quarks. To account for the correct power-law behaviour in the large-momentum limit, we supplement the quark dressing function with a Pauli–Villars-like term with a scale that matches our renormalization point [255]. As a consequence, this also renders the meson-backcoupling diagrams ultraviolet finite so that no further regularization is necessary. Note that for mesons with mixed flavour content we always use the B function of the quark external to the loop the BSA appears in. This turned out to be numerically advantageous for a consistent $N_f = 3$ limit.

Additionally, we introduce the closely related quantity $\tilde{\Gamma}_X$ originating in the two-loop diagram of the vertex expansion. Apart from a non-trivial sign, which is a result of its two-loop background (see Appendix C.4.2), we identify it with the BSA $\hat{\Gamma}_X$:

$$\tilde{\Gamma}^f_X(l, P) = (-1)^X \hat{\Gamma}^f_X(l, P)\,, \tag{6.7}$$

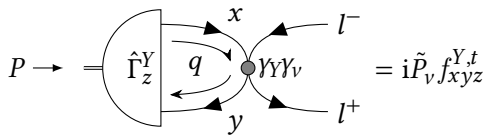

Figure 6.6.: Pictorial representation of the generalized Pagels–Stokar formula in Equation (6.9) we use to calculate the pseudoscalar and scalar meson decay constants.

where $(-1)^X = -1$ for the pseudoscalar mesons and $(-1)^X = +1$ for the scalar mesons.

Last, we also require the meson decay constants. These are calculated using a generalization of the Pagels–Stokar formula [359] for the pion decay constant. From the pion BSE, the axialvector WTI and the pion-pole contribution to the axialvector vacuum polarization, as was shown in Ref. [358], one can derive the following vacuum expression [251] for the pion decay constant:

$$\mathrm{i}P_\nu f_\pi = 3\int \frac{\mathrm{d}^4 q}{(2\pi)^4}\,\mathrm{tr}\Big[S_\ell(q+P)\gamma_5\gamma_\nu S_\ell(q)\hat{\Gamma}_\pi(q,P)\Big]\,. \tag{6.8}$$

Translating this equation to a scenario of different quark flavours, nonzero temperature and potentially also scalar mesons, we arrive at the generalized Pagels–Stokar formula we utilize to calculate the required meson decay constants:

$$\mathrm{i}\tilde{P}_\nu \big(f^{Y,t}_{xyz}\big)^2 = 3\sum\!\!\!\!\!\!\int_q \mathrm{tr}\Big[S_x(q+P)\gamma_Y\gamma_\nu S_y(q)\gamma_Y B^r_z(q)\Big]\,, \tag{6.9}$$

which merits some explanations. In above equation, we use the abbreviation $\tilde{P}_\nu = (P_4, u_X \boldsymbol{P})$, whereas x and y label the flavour indices of the quarks contributing to the meson in question. The temporal and spatial decay constants are then obtained in the limit $P_\nu \to 0$ from the temporal and spatial momentum component, respectively. The index z labels the quark flavour of the external quark of the associated meson-backcoupling diagram and $Y \in \{\mathrm{ps}, \mathrm{sc}\}$ represents the parity of the meson.

The interpretation of Equations (6.8) and (6.9) can by facilitated by example of the pion in vacuum. Namely, one finds a similar expression for its decay constant via a parametrization of the matrix element of the axialvector current, $j_{5\nu} = \bar{\ell}\gamma_5\gamma_\nu\ell$, between the vacuum $|0\rangle$ and an on-shell pion $|\pi(P)\rangle$ [37, 360]:

$$\mathrm{i}P_\nu f_\pi \mathrm{e}^{-\mathrm{i}P\cdot x} = \langle 0|j_{5\nu}(x)|\pi(P)\rangle\,, \quad P_\nu \to 0\,. \tag{6.10}$$

As a consequence, Equation (6.9) describes a generalization of such a process with the aid of a Bethe–Salpeter amplitude, which is illustrated in Figure 6.6. Since f_π can also be determined from the π decay rate through the weak interaction [37], we additionally indicate two (charged) leptons, l^+ and l^-, attached to the axialvector current.[3]

[3] Since we always work in the isospin-symmetric limit, we note that we again ignore the charges of the quarks for the sake of simplicity. Therefore, we restrict ourselves to uncharged mesons in the course of the explanations above.

$N_f = 2$:

	$f = \ell$		
X	F_X^f	S_X^f	f_X^f
π	$3/2$	S_ℓ	$f_{\ell\ell}^{\mathrm{ps}}$
(η_0)	$1/3$	S_ℓ	$f_{\ell\ell}^{\mathrm{ps}}$
σ	$1/2$	S_ℓ	$f_{\ell\ell}^{\mathrm{sc}}$

$N_f = 2+1$:

	$f = \ell$			$f = \mathrm{s}$		
X	F_X^f	S_X^f	f_X^f	F_X^f	S_X^f	f_X^f
π	$3/2$	S_ℓ	$f_{\ell\ell}^{\mathrm{ps}}$	$-$	$-$	$-$
K	1	S_{s}	$f_{\ell\mathrm{s}}^{\mathrm{ps}}$	2	S_ℓ	$f_{\mathrm{s}\ell}^{\mathrm{ps}}$
η_8	$1/6$	S_ℓ	$f_{\ell\ell}^{\mathrm{ps}}$	$2/3$	S_{s}	$f_{\mathrm{ss}}^{\mathrm{ps}}$
(η_0)	$1/3$	S_ℓ	$f_{\ell\ell}^{\mathrm{ps}}$	$1/3$	S_{s}	$f_{\mathrm{ss}}^{\mathrm{ps}}$
σ	$1/2$	S_ℓ	$f_{\ell\ell}^{\mathrm{sc}}$	$-$	$-$	$-$
f_0	$-$	$-$	$-$	$1/2$	S_{s}	$f_{\mathrm{ss}}^{\mathrm{sc}}$

$N_f = 3$:

	$f = \ell$		
X	F_X^f	S_X^f	f_X^f
π, K, η_8	$8/3$	S_ℓ	$f_{\ell\ell}^{\mathrm{ps}}$
(η_0)	$1/3$	S_ℓ	$f_{\ell\ell}^{\mathrm{ps}}$
σ, f_0	$1/2$	S_ℓ	$f_{\ell\ell}^{\mathrm{sc}}$

Table 6.1.: Information of multiplicities, internal quark propagators and decay constants for all considered meson-backcoupling diagrams in all setups.

The somewhat complicated notation introduced above is necessary for the following reason: All decay constants in our diagrams do not depend on the mesons directly but rather on the contributing quark propagators of the backcoupling diagram. Furthermore, they have to match the type of the scalar dressing function used in the BSA. For hidden-flavour mesons, this is unproblematic and Equation (6.9) matches the usual Pagels–Stokar approximations. For open-flavour mesons, i.e., the four kaons in our approach, however, this has the consequence that the decay constant appearing in the light-quark DSE is different from the one in the strange-quark DSE since the external quark differs. Equation (6.9) accounts for this. Furthermore, we symmetrize the equation in a mathematically well-defined manner[4] with the arithmetic mean of the exchanged quark flavours. This way, we arrive at the following definitions (see also Appendix C.4.5 for more information and explicit expressions):

$$f_{xy}^{Y,s} f_{xy}^{Y,t} = \left(f_{xyx}^{Y,s} f_{xyx}^{Y,t} + f_{yxx}^{Y,s} f_{yxx}^{Y,t}\right)/2\,, \quad \left(f_{xy}^{Y,t}\right)^2 = \left(\left(f_{xyx}^{Y,t}\right)^2 + \left(f_{yxx}^{Y,t}\right)^2\right)/2\,, \tag{6.11}$$

from which we can obtain the required (temporal) meson decay constants used in our calculations:

$$f_{xy}^{Y} := f_{xy}^{Y,t} = f_{xy}^{Y,s} f_{xy}^{Y,t} / \sqrt{\left(f_{xy}^{Y,t}\right)^2}\,. \tag{6.12}$$

Of course, this procedure is only relevant for finite, nonzero strange-quark masses along the left-hand side of the Columbia plot. In the chiral $N_f = 2$ and $N_f = 3$ limits (lower and upper left corners), it becomes immaterial. In total, we summarize all necessary information for our meson-backcoupling procedure compactly in Table 6.1.

Before we turn to our results for the condensate, we want to comment on the role of the meson decay constants in our setup. It turns out to be crucial for the meson-backcoupling truncation to solve for the decay constants self-consistently during the DSE iteration. This is due to the fact that they govern the strength of individual backcoupling diagrams by appearing inversely quadratic as a prefactor. Therefore, a self-consistent calculation of the decay constants dynamically adjusts the influence of the respective diagrams. In order to

[4] This is done by a shift of the integration momentum which can be compensated in the BSA with a different momentum routing.

illustrate some important consequences of this for our framework, we exemplarily show results for the decay constants obtained with $m_\ell \to 0$ and $m_\mathrm{s} = 1\,\mathrm{GeV}$ in Figure 6.7.

In the upper left panel, we display the temperature dependence of all calculated decay constants. As can be seen, these spread across one order of magnitude and follow a certain hierarchy: The decay constants with external (non-chiral) strange quarks are heaviest so that these diagrams are consequently suppressed more strongly than the ones with external (chiral) light quarks. Additionally, the temperature dependence differs between these two classes of decay constants, which is depicted in the upper right and lower left panels. That is, the decay constants with external strange quarks are more or less temperature independent whereas the ones with external light quarks smoothly undergo a second-order transition to zero at T_c. This behaviour is inherited from the underlying external quarks. As a consequence, the dynamics of the light quarks around the critical temperature are clearly dominated by the (chirally restoring) meson-backcoupling diagrams rather than the non-hadronic self-energy, which in total lowers T_c. At the second-order transition, the (light-quark) decay constants obey a scaling behaviour, i.e., $f_{\ell\ell}^Y$ scale with the critical exponent of the condensate whereas the one of $f_{\ell s}^\mathrm{ps}$ is halved. This, however, is perfectly in line with the scaling analysis of Ref. [251] when extended to $N_f = 2 + 1$ flavours (see also Section 6.3.3).

6.3. Numerical Results

In this section, we present the numerical results obtained in our framework. Before doing so, we make some clarifying remarks about the general setup. Just as for the previous analyses, our investigation of the Columbia plot is based on monitoring the behaviour of the light-quark condensate as the order parameter for chiral symmetry breaking, which is once more obtained from Equation (3.6). For nonzero light-quark masses, the ultraviolet divergence is again cancelled with the corresponding one of the strange-quark condensate by means of the subtracted condensate from Equation (4.13):

$$\Delta_{\ell\mathrm{s}} = \langle\bar{\psi}\psi\rangle_\ell - \frac{Z_m^\ell}{Z_m^\mathrm{s}}\frac{m_\ell}{m_\mathrm{s}}\langle\bar{\psi}\psi\rangle_\mathrm{s}\,. \tag{6.13}$$

Therefore, we return to the definition of the order parameter utilized in Chapter 4 as opposed to the slightly different definition in Chapter 5. In the case of massless light quarks, the subtracted condensate reduces to the unsubtracted one which is consequently well-defined, i.e., ultraviolet finite. The chiral susceptibility is then defined as the derivative of the regularized condensate with respect to the light-quark mass:

$$\chi_{\ell\mathrm{s}}^m = \frac{\partial}{\partial m_\ell}\Delta_{\ell\mathrm{s}}\,. \tag{6.14}$$

Up to normalization factors and for $m_\ell = m_\mathrm{u} = m_\mathrm{d}$, this definition is equivalent to the ones used in Refs. [342, 361].

In this chapter, we are back in the full unquenched (not hybrid) truncation. Since the meson-backcoupling diagrams originate in a modification of the vertex, we once more need to adjust the vertex-strength parameter d_1. We tune d_1 such that the pseudocritical temperature obtained from the chiral susceptibility at the physical point, i.e., the maximum of $m_\pi = 139\,\mathrm{MeV}$ in

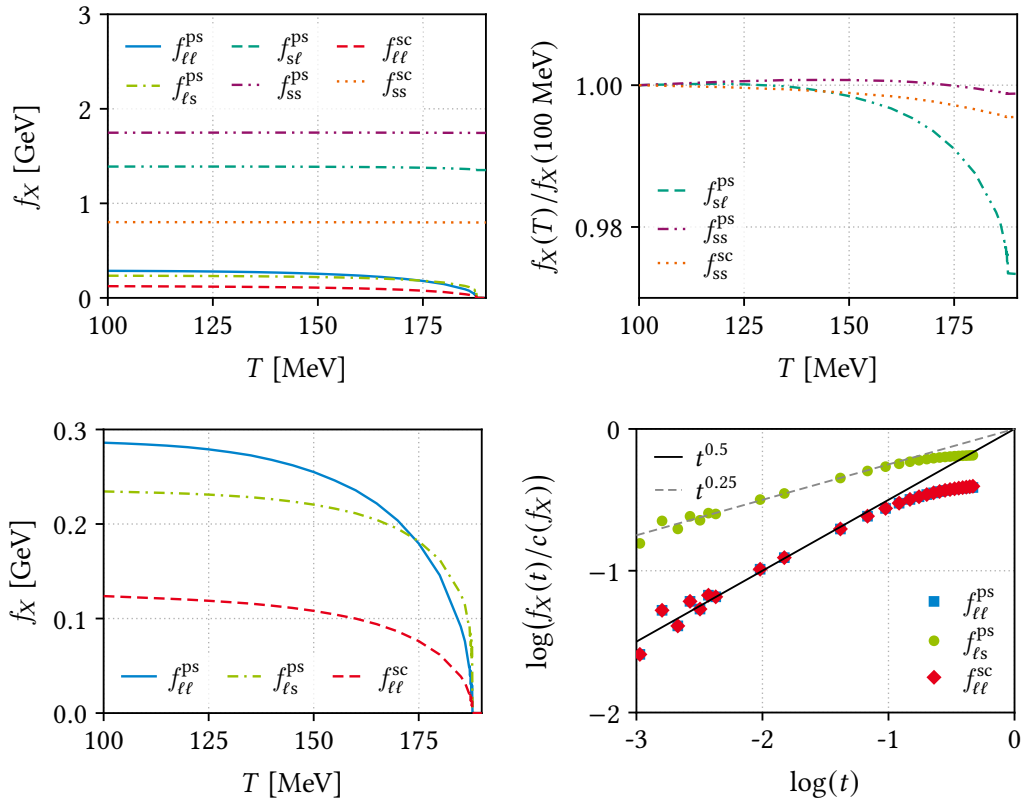

Figure 6.7.: Results for meson-backcoupling truncation in the light-quark chiral limit, $m_\ell \to 0$, for $m_s = 1\,\mathrm{GeV}$. *Upper left*: Temperature dependence of all calculated decay constants. *Upper right*: Temperature dependence of all decay constants involving strange quarks normalized to their value at $T = 100\,\mathrm{MeV}$. *Lower left*: Temperature dependence of all scaling decay constants. *Lower right*: Scaling behaviour of all scaling uu decay constants.

Figure 6.8, corresponds to the one from the lattice $T_c^p = 156.5\,\mathrm{MeV}$. This yields $d_1 = 8.98\,\mathrm{GeV}^2$ as opposed to $d_1 = 8.49\,\mathrm{GeV}^2$ without mesonic contributions [79] (see again Table 3.1).

The remainder of this section is structured as follows. First, we study the line between the physical point and the left-hand side of the Columbia plot by analysing the dependence of the chiral susceptibility on the pion (and thus the light-quark) mass. Second, we investigate the type of the chiral phase transition across the whole left edge of the Columbia plot, i.e., for chiral light quarks and strange-quark masses in the range $m_s \in [0, \infty)$. We also quantify the dependence of the critical temperature on the strange-quark mass. Third, we study the scaling behaviour of the light-quark condensate. Fourth, we extend our analysis of the left-hand side of the Columbia plot to small but nonzero chemical potentials, both real and imaginary, i.e., we consider the three-dimensional Columbia plot. Last, we perform a first, exploratory study of the bottom edge (i.e., chiral strange quarks but varying light-quark mass).

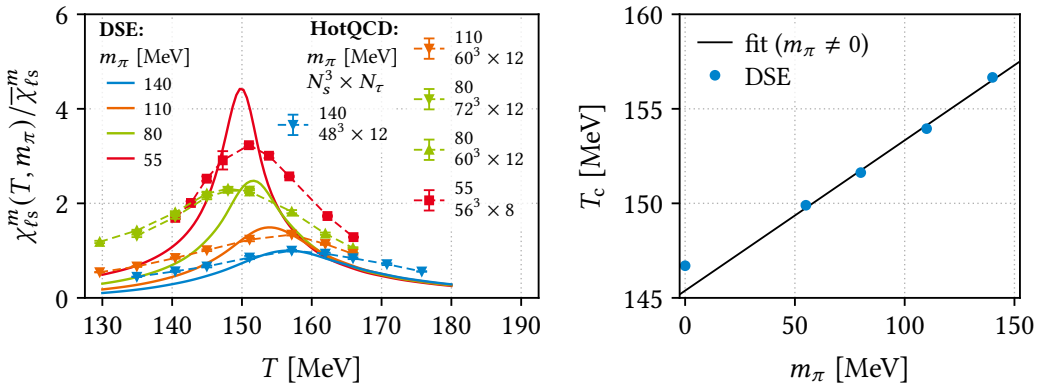

Figure 6.8.: *Left*: Chiral susceptibility as a function of temperature for fixed, physical strange-quark mass but different light-quark masses corresponding to different pion masses. The susceptibilities are normalized to the maximal value of $m_\pi = 140$ MeV. The lattice data have been taken from Ref. [361]. *Right*: Critical temperatures for the same pion masses shown in a linear extrapolation down to zero mass with input for data at $m_\pi \neq 0$ compared with the result of an explicit calculation at zero pion mass.

m_π [MeV]		0	55	80	110	140
T_c [MeV]	DSE	146.7	149.9	151.6	154.0	156.7
	FRG [342]	142	148.0	150.5	153.6	156.3
	FRG–DSE [261]	141.3	146.5	149.1	152.1	155.4
	HotQCD ($N_\tau = 12$) [361]	-	-	$149.7^{+0.3}_{-0.3}$	$155.6^{+0.6}_{-0.6}$	$158.2^{+0.5}_{-0.5}$
	HotQCD ($N_\tau = 8$) [361]	-	$150.9^{+0.4}_{-0.4}$	$153.9^{+0.3}_{-0.3}$	$157.9^{+0.3}_{-0.3}$	$161.0^{+0.1}_{-0.1}$

Table 6.2.: Comparison of critical temperatures for different up/down-quark masses corresponding to different pion masses and fixed physical strange quark masses between our DSE findings, the FRG, FRG–DSE and the lattice results, respectively.

6.3.1. Towards the Chiral Limit

We start our investigation of the Columbia plot with the line between the physical point and the left-hand side. That is, we keep the strange-quark mass physical, $m_s = m_s^p$, and decrease the light-quark mass from its physical value down to zero. This path has been explored already by the HotQCD collaboration [361] with lattice-QCD methods, the fQCD collaboration using the FRG [342] as well as with a combined FRG–DSE approach in Ref. [261].

In the left diagram of Figure 6.8, we show the chiral susceptibility as a function of temperature for four different pion masses compared to the lattice results of Ref. [361]. Analogously to Ref. [342], we normalize the susceptibilities to the maximal value at a physical pion mass:

$$\overline{\chi}^m_{\ell s} = -\max_T \left|\chi^m_{\ell s}(T, m_\pi = 140\,\text{MeV})\right| . \tag{6.15}$$

Qualitatively, we find similar results as both the lattice, the FRG and the FRG–DSE approach

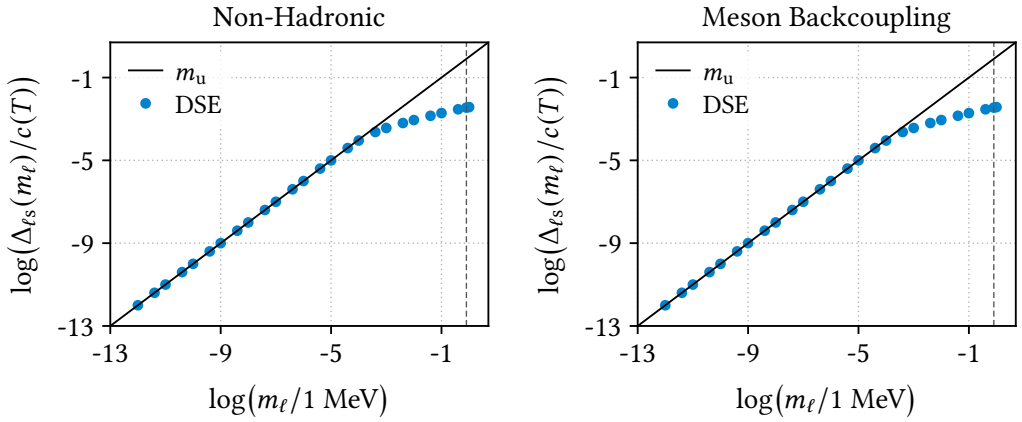

Figure 6.9.: Scaling behaviour of the regularized quark condensate as a function of the light-quark mass for physical strange-quark masses at the critical temperature of $m_\ell = 0$. We display results for the non-hadronic vertex (left) and meson-backcoupling diagrams (right).

in Refs. [261, 342, 361]. That is, for decreasing pion masses, the peak of the susceptibilities increases in height and moves towards lower temperatures monotonically. Quantitatively, the results are also very similar. Namely, the peak heights are comparable with the FRG and FRG–DSE findings for all investigated pion masses and the (pseudo)critical temperatures away from the chiral limit do not deviate more than 2 MeV and 3.5 MeV, respectively, see Table 6.2. It is, however, interesting to note that the linear extrapolation of our results towards the chiral limit, shown in right diagram of Figure 6.8, underestimates the chiral transition temperature calculated explicitly in the light-quark chiral limit by about two MeV. The linear extrapolation results in 145.4 MeV whereas we find the value

$$T_c(m_\ell = 0) = 146.7\,\mathrm{MeV}\,, \tag{6.16}$$

which is about 5 MeV to 5.5 MeV larger than the FRG and FRG–DSE results, respectively, and more than ten MeV larger than the extrapolated lattice value $T_c^{\mathrm{HotQCD}} = 132^{+3}_{-6}$ MeV. We attribute this in part to our vertex construction, where the vertex-strength parameter d_1 is fixed at the physical point and not changed with quark mass. We therefore marginally overestimate the interaction strength in the chiral limit leading to slightly too large transition temperatures. This will be discussed again also in the next section.

The (almost) linear behaviour in the right panel of Figure 6.8 is based on a general scaling analysis [342, 361] derived from scaling relations for both the condensate and the chiral susceptibility. This way, the (pseudo)critical temperature as a function of the pion mass is given by:

$$T_c(m_\pi) \approx T_c(m_\pi = 0) + c \cdot m_\pi^{2/(\beta\delta)}\,, \tag{6.17}$$

where again c labels some non-universal parameter and the critical exponent $2/(\beta\delta)$ is expected to be very close to 1 [342].

Of course, such a scaling analysis is only valid inside the critical region in the vicinity of a second-order transition. In order to estimate the size of the scaling region in our framework, we show the scaling behaviour of the regularized condensate as a function of the light-quark mass

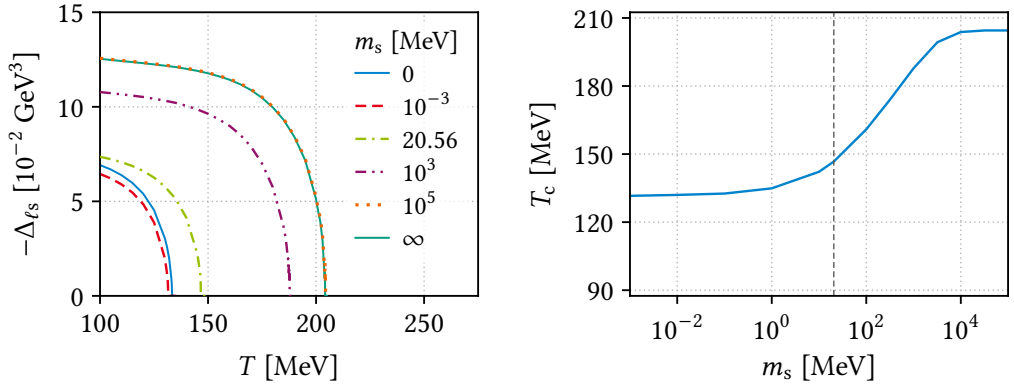

Figure 6.10.: *Left*: Regularized quark condensate as a function of temperature for different strange-quark masses in the light-quark chiral limit. *Right*: Dependence of the critical temperature on the strange-quark mass in the same limit. The dashed vertical line indicates the physical strange-quark mass.

at a physical strange-quark mass in Figure 6.9 with the physical light-quark mass indicated by a vertical line. In addition to the meson-backcoupling diagrams, we display results for the non-hadronic vertex as a crosscheck (also to assess the impact of the nonzero-quark-mass regularization in Equation (6.6)). In both cases, we find a perfectly linear behaviour up to about $m_\ell \lesssim 10^{-5}$ MeV, i.e., $m_\pi \lesssim 0.5$ MeV, with increasing deviations for larger masses. If we take this as a measure for the size of our critical region, the assumption of the scaling behaviour in Equation (6.17) is not really justified and the linear behaviour is not unlikely to have a different origin. This may also explain parts of the deviation of the extrapolation for $m_\ell \to 0$ in the right panel of Figure 6.8. A similar size of $m_\pi \lesssim 1$ MeV for the scaling region was also determined in an FRG study using the QM model in Ref. [362].

6.3.2. Left Edge of the Columbia Plot

Next, we turn our analysis to the left edge of the Columbia plot. To this end, we display the temperature dependence of the quark condensate for chiral light quarks and a set of six selected strange-quark masses in the range $m_s \in [0, \infty)$ in the left diagram of Figure 6.10. One can immediately notice that we again observe a second-order phase transition for all investigated strange-quark masses. That is, the quark condensate continuously changes from a nonzero value to zero for increasing temperature with no (apparent) jumps. As we will see in Section 6.3.3, it is indeed a genuine second-order transition since the condensate exhibits a scaling behaviour in the vicinity of the respective critical temperatures. We emphasize that this also holds true for the $N_f = 3$ corner where we consequently find no first-order region at all. In general, the condensate is smaller for smaller strange-quark masses at all temperatures. The only exception occurs close to the three-flavour limit at around $m_s \sim 10^{-9}$ MeV where we do find a sudden and small increase in the condensate for all temperatures which then remains constant until $m_s \to 0$. In the left diagram of Figure 6.10, this increase is visible when comparing the $m_s = 10^{-3}$ MeV result with the one at $m_s = 0$ MeV. Since we neither found a technical nor a physical reason for this glitch, we attribute it (for the moment) to a purely numerical artefact of the three-flavour limit. It total, we find the same situation as in Figure 6.3

m_s		0	m_s^p	∞
T_c [MeV]	DSE	133.4	146.7	204.2
	Lattice	98^{+3}_{-6} [351]	132^{+3}_{-6} [361]	$174 \pm 3 \pm 6$ [363]

Table 6.3.: Comparison of critical temperatures for different strange-quark masses between our DSE findings and lattice results.

again corresponding to the lower scenario of Figure 6.1.

The dependence of the critical temperature on the strange-quark mass is illustrated in the right diagram of Figure 6.10. Qualitatively, we find that T_c varies only little for very small and very high strange-quark masses but increases monotonically in the range $m_s =$ 1 MeV to 10^4 MeV. In Table 6.3, we compare our findings of the critical temperature quantitatively to the most-recent lattice results available for zero, physical and infinite strange-quark masses. We observe that our values for T_c are consistently larger than the ones found on the lattice, with the smallest difference at the physical strange-quark mass. Our explanation for this discrepancy is based on the discussion above: We fix the interaction strength d_1 for the non-hadronic part of our quark–gluon interaction, Equation (3.30), at the physical point and do not take any changes of the vertex strength with variation of the quark masses into account. Presumably, this leads to the small discrepancy in transition temperature in the light-quark chiral limit with physical strange quarks already discussed above and larger discrepancies in the chiral corners of the Columbia plot. We have explicitly checked what happens in the $N_f = 3$ limit if we adapt the vertex strength. With $d_1 = 7.13\,\mathrm{GeV}^2$, we reproduce the transition temperature of $T_c = 98$ MeV given in Ref. [351] while the transition is still second order. Thus, the value of d_1 (at least within the range studied here) had no material influence on the order of the transition.

Finally, we investigated whether the fate of the $\mathrm{U}_A(1)$ symmetry has any influence on the order of the transition. On the complexity level of the present truncation, an anomalously broken $\mathrm{U}_A(1)$ at the critical temperature results in a massive η' meson whereas a restored $\mathrm{U}_A(1)$ renders the η' meson massless. So far, we assumed the first case and neglected the η' meson in the backcoupling diagrams completely together with all other mesons that remain massive in the chiral $N_f = 3$ limit. In order to gauge the influence of the η' on the order of the transition in this limit, we repeated our calculation with a massive η' of $m_{\eta'} = 800$ MeV and – even more importantly – with a massless η' explicitly present in the loops. As a result, we find only a very small reduction of the transition temperature of about 0.3 MeV when including a massive η' with no changes in the second-order nature of the transition. This result confirms our notion that additional massive mesons barely have any influence on our results and their omission, therefore, is a good approximation. Including a massless η' reduces the transition temperature further by about 1.5 MeV but again does not change the second-order nature of the phase transition. As a consequence, we conclude that within the framework presented here the fate of the anomalously broken axial $\mathrm{U}_A(1)$ symmetry with temperature has no relevant effect on the order of the chiral phase transition.

6.3.3. Scaling Behaviour

The scaling properties of the quark DSE and, related, that of the condensate have been studied in Ref. [251] in the chiral $N_f = 2$ limit. Here, we expect a second-order phase transition in the O(4) universality class of the Heisenberg antiferromagnet, see, e.g., Ref. [133]. Indeed, it has been shown in Ref. [251] that the correct scaling is obtained if (and only if) the scaling of the temporal meson decay constants is taken into account. Therefore, in order to obtain self-consistent scaling from the quark DSE, one would need to explicitly include the BSE for the relevant long-range degrees of freedom – the pion and the sigma – as well as the corresponding equations for their decay constants in a self-consistent manner. This is beyond the present truncation and would require extensive additional work. A shortcut, also used in Ref. [251], is to assume the critical scaling of the decay constants and only check for consistency in the quark DSE using an appropriate ansatz for this scaling. Indeed, one then finds that the diagrams with long-range, massless, mesonic degrees of freedom dominate over the gluonic ones, i.e., universality sets in and scaling is observed. On the other hand, any setup without scaling decay constants delivers the usual mean-field scaling as seen and discussed in Section 6.1.1.

For completeness, we have checked both mean-field scaling without and O(4) scaling with properly scaling decay constants. For the former, we use the Pagels–Stokar approximation for the decay constants discussed in Equation (6.9); for the latter, we use the following ansatz:[5]

$$\tilde{f}^Y_{\ell\ell}(T) = f^Y_{\ell\ell}(T_0)\left(\frac{T_c - T}{T_c - T_0}\right)^{\beta}, \quad \tilde{f}^{\mathrm{ps}}_{\ell s}(T) = f^{\mathrm{ps}}_{\ell s}(T_0)\left(\frac{T_c - T}{T_c - T_0}\right)^{\beta/2}, \quad \tilde{f}^Y_{xy}(T) = f^Y_{xy}(T_0)\,. \tag{6.18}$$

Here, we use the decay constants from the Pagels–Stokar setup at some temperature $T_0 = 100\,\mathrm{MeV}$ as input, while the critical temperatures T_c are the ones from Figure 6.10. The scaling law for $f^Y_{\ell\ell}$ is taken from Ref. [251] whereas the scaling law for $f^{\mathrm{ps}}_{\ell s}$, valid for $m_s \neq 0$, is obtained from an analogous scaling analysis as in Ref. [251] for the kaon diagrams. All other decay constants do not exhibit any critical scaling. In the limit of $m_s \to 0$, we just assume the same critical scaling for $f^Y_{\ell\ell}$, $f^{\mathrm{ps}}_{\ell s}$ and f^{ps}_{ss} also found in the Pagel–Stokar setup. This is, however, for simplicity only since the universality class in this limit is not known.

In Figure 6.11, we display our results as log–log plots. In the left panel, we show (the logarithm of) the regularized condensates in the light-quark chiral limit and for the same strange-quark masses as in Figure 6.10 as functions of (the logarithm of) the reduced temperature t. For the sake of comparability, we fit each dataset to the relation in Equation (6.1) and divide by their respective constant c. As can be seen, all curves collapse nicely onto each other and align along the line $t^{0.5}$ for $\log(t) \lesssim -1.5$. The spread of data points below $\log(t) \lesssim -2$ is entirely due to our numerical uncertainty of $\Delta T_c = 0.1\,\mathrm{MeV}$ in the determination of T_c. We observe the expected mean-field scaling behaviour for all investigated strange-quark masses. As a consequence, the meson-backcoupling diagrams do not change the scaling behaviour from Figure 6.3.

[5] Indeed, this is precisely the behaviour we also find when calculating the decay constants using the Pagels–Stokar formula except with a mean-field critical exponent of $\beta = 0.5$, cf. Figure 6.7.

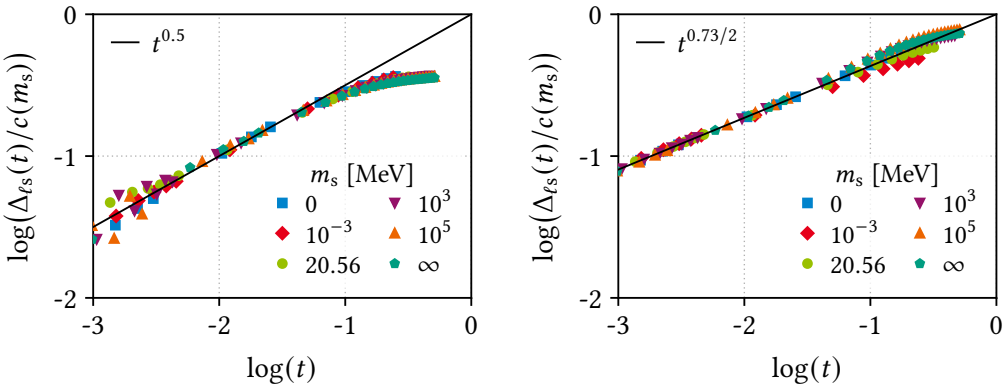

Figure 6.11.: *Left*: Scaling behaviour of the regularized quark condensate as a function of the reduced temperature for different strange-quark masses in the light-quark chiral limit without scaling decay constants. *Right*: Same scaling behaviour with scaling decay constants (see main text for discussion).

In the right diagram of Figure 6.11, we show corresponding results under the assumption that the decay constants scale according to Equation (6.18) with the correct O(4) critical exponents of QCD, where $\beta = 0.73/2$. As expected, the scaling behaviour of the decay constants induces a corresponding, consistent scaling of the order parameter. Furthermore, with induced scaling, the collapse of all datasets for $\log(t) \lesssim -1.5$ is almost perfect and the spread for low $\log(t)$ vanishes completely. This is due to the fact that the additional appearance of T_c in the scaling ansatz stabilizes the numerics considerably.

In fact, it is mandatory that T_c in Equation (6.18) be chosen appropriately in order to observe the correct scaling behaviour. That is, T_c needs to be smaller than the critical temperature obtained with only the non-hadronic self-energy T_c^{NH}. If $T_c > T_c^{\mathrm{NH}}$, the phase transition is triggered by the non-hadronic diagram and one again only observes mean-field scaling. If $T_c = T_c^{\mathrm{NH}}$, both effects occur concurrently and one retains the sum of the mean-field and induced critical exponents. A correct value of T_c, however, is guaranteed by taking the one obtained with the Pagels–Stokar setup. This makes sense since the meson-backcoupling diagrams act chirally restoring so their inclusion automatically also lowers T_c such that it always becomes smaller than T_c^{NH}.

Of course, since $\beta = 0.73/2$ is an input, this setup reveals nothing about the universality class in the chiral three-flavour limit. In order to study this issue with DSEs, as discussed above, one needs to solve the corresponding Bethe–Salpeter equations and the defining equations for the decay constants without further approximations. This is possible, in principle, and should be attempted in future work. In practice, it may however be more straightforward to perform this calculation in the framework of the functional renormalization group, where scaling properties are more directly approachable [62, 336, 340, 342, 364–366].

6.3.4. Small Chemical Potentials: Three-Dimensional Columbia Plot

As the penultimate part of our analysis, we would like to explore the fate of the second-order phase transition along the left-hand side of the Columbia plot when we switch on chemical potential, i.e., in the three-dimensional Columbia plot. Is there a second-order critical sheet?

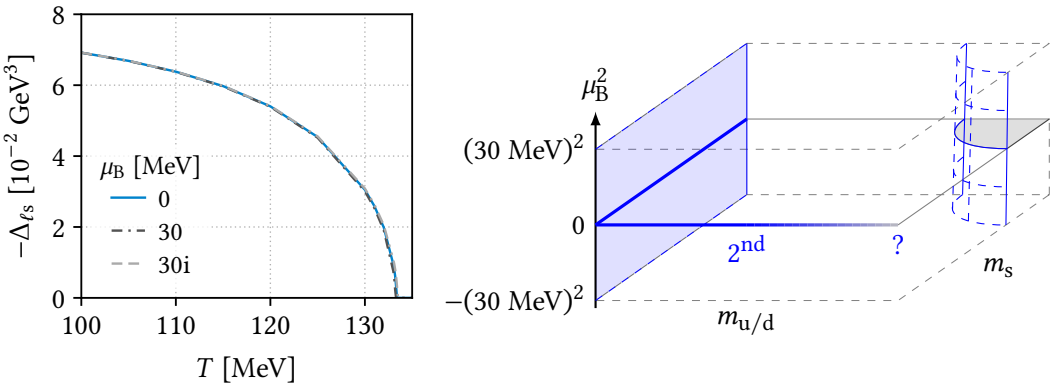

Figure 6.12.: Results for (small) real and imaginary chemical potentials in the light- and strange-quark chiral limits. *Left*: Regularized quark condensate as a function of temperature. *Right*: Illustration of the three-dimensional Columbia plot we find.

And if yes, does it bend at some point towards nonzero quark masses and is it connected to the CEP that we find at physical quark masses [79, 80, 246]?

Unfortunately, these questions are difficult to study. Our current approximation for the meson Bethe–Salpeter amplitudes, Equation (6.6), is known to be accurate at vanishing chemical potential. From the explicit calculation in Ref.[248, 249], however, it is established that the amplitudes are modified substantially at large chemical potential. We can therefore only trust the approximation in Equation (6.6) at small chemical potentials.

As a consequence, we restrict ourselves to real and imaginary baryon chemical potentials of $|\mu_B| = 30\,\text{MeV}$. The corresponding results are shown in Figure 6.12 together with results for $\mu_B = 0$ as a comparison. The calculations have been performed for vanishing, physical and infinite strange-quark masses: $m_s = 0$, $m_s = m_s^p$, $m_s = \infty$. In the left panel, we display the condensate as a function of temperature in the $N_f = 3$ chiral limit, i.e., $m_\ell = m_s = 0$. We find no significant changes within this range of chemical potential. Similar results are obtained for all investigated strange-quark masses. In total, we find little quantitative and no qualitative difference between the results for vanishing and small chemical potentials. That is, one can still observe a second-order phase transition with identical scaling behaviour and an almost unchanged critical temperature. We therefore arrive at the slice of the three-dimensional Columbia plot shown in the right panel of Figure 6.12, i.e., without any curvature of the second-order critical sheet on the left edge. For zero chemical potential, this ties in with the lattice results of Ref. [350, 351] and for imaginary chemical potential with Ref. [367]. It also agrees with one of the scenarios displayed in the FRG approach in Ref. [340] (their right diagram of Fig. 3) but disagrees with the other scenarios they give. This needs to be re-examined in some detail. In any case, the analyticity of the second-order transition plane from small imaginary to small real chemical potential visible in Figure 6.12 is – to our knowledge – shown for the first time.

6.3.5. Bottom Edge of the Columbia Plot

Finally, we perform a first exploration of the 'bottom' edge of the Columbia plot, i.e., the line of zero chemical potential with a massless strange quark and up/down-quark masses in the range $m_\ell = 0, \ldots, m_\ell^p, \ldots, \infty$. Since the strange quarks are now the lightest flavour, their condensate becomes the corresponding order parameter for the chiral transition at nonzero temperature. In this setup, merely a $\mathrm{U}_A(1)$ subgroup of the flavour $\mathrm{SU}_A(3)$ is dynamically broken, so we include one massless Goldstone boson with $\mathrm{s\bar{s}}$ quark content. Moreover, we expect the isoscalar, scalar f_0 with $\mathrm{s\bar{s}}$ content to be the only additional massless mode at the critical temperature since it has the quantum numbers of the strange-quark condensate. To obtain such a mixing inside the SU(3) pseudoscalar multiplet, we assume a restored anomaly at the chiral transition temperature. The precise mixing/quark content as well as the corresponding meson masses, flavour coefficients and decay constants are detailed in Appendix C.4.4.

For this setup, we indeed find again a second-order phase transition, also indicated in our three-dimensional Columbia plot in the right panel of Figure 6.12. Such a behaviour is in contrast to all of the scenarios in Figure 6.1 which, however, always assume the up/down-quark condensate as the chiral order parameter. This second-order transition persists to large but not infinite up/down-quark masses. At some large up/down-quark mass, $m_\ell > 100\,\mathrm{GeV}$, our calculation breaks down indicating that we are approaching the one-flavour limit of QCD with different symmetries. The detailed study of this limit is non-trivial and deferred to future work. The same also applies to an investigation of the bottom edge in the three-dimensional Columbia plot, i.e., at nonzero baryon chemical potential.

6.4. Outlook: Volume-Effects with Meson Backcoupling

We have argued in Section 4.3.2 that the lack of an appropriate volume scaling inside the critical region around the CEP is caused by missing long-range correlations with the quantum numbers of scalar mesons. In this chapter, however, we have introduced a setup that explicitly includes the according diagrams into the quark self-energy of our truncation. As was demonstrated in Section 6.3.3, these diagrams are also necessary to ensure the correct scaling behaviour with respect to temperature in the vicinity of the second-order chiral transition. Therefore, we can now apply the improved meson-backcoupling truncation to our finite-volume framework of Chapter 4 in order to potentially account for previously missing contributions.

To this end, we display the volume dependence of the regularized condensate normalized to its infinite-volume value in Figure 6.13. We show results at $T = 100\,\mathrm{MeV}$ for both boundary conditions as a function of L calculated both with a non-hadronic vertex and meson-backcoupling diagrams as a proof of principle. As can be seen, the additional diagrams have a negligible influence above $L \gtrsim 3\,\mathrm{fm}$ where the results are essentially unchanged. For very small volumes, however, (slight) discrepancies between the two setups begin to appear. At $L = 2\,\mathrm{fm}$, that is, we see the values deviate between the approaches for both PBC and (more so) ABC, which is somewhat expected since chiral restoration sets in and the mesons become lighter and thus more important. Nevertheless, these findings are very promising for future analyses since – as stated earlier – the contributions of the sigma meson become dominant only in the vicinity of a second-order transition but we see effects already here around a crossover.

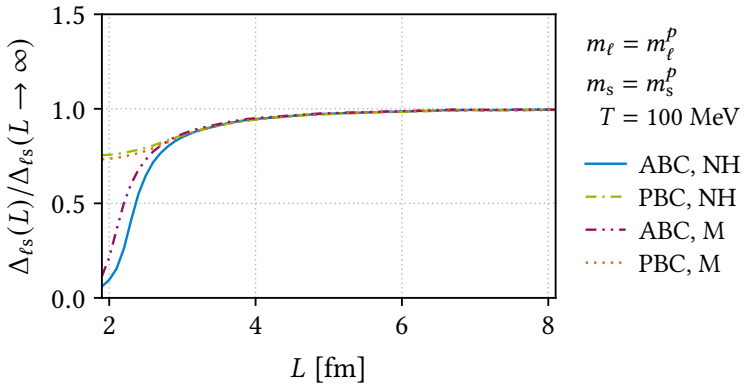

Figure 6.13.: Dependence of subtracted condensate on the system size including meson-backcoupling diagrams at the physical point for antiperiodic and periodic boundary conditions at $T = 100\,\mathrm{MeV}$. We compare results for the non-hadronic vertex (NH) with the meson-backcoupling diagrams (M).

In total, we have demonstrated that our setup is, in principle, capable of describing volume and meson-backcoupling effects at the same time and that the mesons do influence the small-volume behaviour. Therefore, a revision of the scaling analysis from Section 4.3.4 with mesonic degrees of freedom is a highly interesting option for a future work.

6.5. Summary

In this chapter, we studied the order of the phase transition in the light chiral limit of massless up/down quarks as a function of the strange-quark mass both at zero and small nonzero values for the baryon chemical potential. Using an extended truncation of Dyson–Schwinger equations that takes into account microscopic degrees of freedom as well as potential long-range correlations with the quantum numbers of pseudoscalar and scalar mesons, we obtain a chiral crossover as long as the light-quark masses remain nonzero but a second-order phase transition in the light-quark chiral limit. We find this behaviour along the left-hand side of the Columbia plot, i.e., for all strange-quark masses in $0 \leq m_s \leq \infty$ and also for (small) imaginary and real chemical potentials. Furthermore, it persists regardless of whether we include a massive η' meson (in case the axial $\mathrm{U}_A(1)$ remains anomalously broken at T_c) or a massless η' meson (in case the axial $\mathrm{U}_A(1)$ is restored at T_c). Our findings do not support the long-standing notion of a chiral first-order $N_f = 3$ corner in the Columbia plot [133] but agree with recent findings from lattice QCD [350, 351] and notions from effective models [352]. Beyond that, we also investigated behaviour of the strange-quark condensate at the bottom edge of the Columbia plot, i.e., for chiral strange quarks, and find a second-order transition there as well. Additionally, we demonstrated that this setup is, in principle, able to also be applied to finite-volume investigations. For this reason, the framework introduced in this chapter may be applied to the analysis in Section 4.3 in a future work in order to study whether or not it enables the correct volume scaling around the physical CEP.

Chapter 7
Summary, Conclusion and Outlook

In this thesis, we investigated the quark mass and volume dependence of the phase diagram of quantum chromodynamics. We did so using the functional framework of Dyson–Schwinger equations. We employed two very similar sets of truncated DSEs in Landau gauge for 2 + 1 quark flavours that have been studied extensively in the past. In the introductory chapter, we motivated the subjects of this thesis. This comprises the QCD phase diagram as a whole as well as non-perturbative approaches to QFT and the topics of the individual analyses. Thereafter, we reiterated the most important basics and characteristics of QCD that are relevant for our investigations. Before we presented our results, we introduced the framework of Dyson–Schwinger equations. We reconstructed their derivation from the generating functionals, explained the structure of the QCD-propagator DSEs and motivated the necessity and properties of dressing functions by their examples. Afterwards, we illustrated different truncation schemes centred around the quark propagator since our main observable is the quark condensate.

This then enabled us to explain our truncation(s) in general. In addition to the well-known quark DSE, these are based on a temperature-dependent fit of the quenched gluon propagator to data obtained by lattice Yang–Mills theory. The unquenching of the gluon is calculated explicitly within our framework by taking the quark-loop contribution of the gluon self-energy into account. The last remaining quantity to render this set of equations self-contained is the quark–gluon vertex which is inspired by the Slavnov–Taylor identities of the full vertex in the infrared while it ensures the correct perturbative behaviour of the propagators in the ultraviolet momentum region. The only difference between our two very similar truncations is whether or not a backcoupling of the quarks into the vertex is taken into account in the quark DSE. Consequently, we have the fully non-perturbative quark and gluon propagators at nonzero temperature and chemical potential at our disposal. The vertex strength being the only free parameter in our truncation can be adjusted to recover the desired pseudocritical temperature and may vary depending on the definition of the latter.

Finite-Volume Effects

In the first of our three results chapters, we covered the volume dependence of the QCD phase diagram. That is, we studied the effects of a finite, uniform, three-dimensional cubic volume with equal edge lengths L and (anti)periodic boundary conditions on both the chiral order parameter as well as baryon-number fluctuations and their ratios. For a proper treatment of our setup, we found two technical procedures to be mandatory. First, one has to approximate the analytical summation over a pure torus in the ultraviolet with a continuous integral to remove cubic artefacts and simultaneously get a numerically feasible system. Second, one explicitly needs to include the zero mode for periodic boundary conditions. This is important to ensure the correct and analytically expected onset of the epsilon regime for small volumes

while it renders results almost identical to antiperiodic boundary conditions for large volumes. We demonstrated that an omission of this zero mode – an approximation commonly found in the literature – is not justified. In addition, we investigated a further simplification of full finite-volume calculations, namely, the usage of an IR cutoff instead of a proper torus summation. In our setup, this turns out to be a very poor approximation especially at nonzero temperatures, so the torus summation is required for quantitative descriptions of finite volumes.

For both types of boundary conditions, we consequently find similar volume effects on the quark condensate and the QCD phase diagram. These are only moderate (of the order of ten MeV and smaller) for box sizes $L \gtrsim 5\,\mathrm{fm}$, whereas sizable shifts of the CEP and the associated crossover line occur for very small volumes. These shifts are almost monotonous: Smaller volumes correspond to smaller transition temperatures and the CEP shifts towards larger chemical potential. The only deviation from this general behaviour occurs for periodic boundary conditions at very small box sizes which is not unexpected considering aforementioned epsilon regime. Our findings are consistent with corresponding results from FRG calculations within a quark–meson-model truncation.

Within the same setup, we also determined the volume dependence of the skewness and kurtosis ratios of baryon-number fluctuations. For a wide range of cubic spatial volumes with edge lengths between $L = 2.5\,\mathrm{fm}$ and $L = 8\,\mathrm{fm}$ and both boundary conditions, we observe a visible volume dependence of the fluctuations especially in the lower orders while the ratios show practically none. This is a highly nontrivial outcome because the individual results for the different fluctuations reveal a pattern that is at odds with the general expectation of linear dependence on volume: Whereas the PBC results for χ_2^{B} do not change with volume, the ones for ABC are even inversely proportional to $V = L^3$. In view of comparisons with experimental results from heavy-ion collisions, it is nevertheless a very encouraging and relevant finding that all explicit and implicit volume dependences cancel in the ratios.

The results in the finite-volume chapter did not include the mesonic degrees of freedom that are crucial to obtain the correct volume-scaling behaviour inside the critical region around the CEP. A prescription how these can be treated in our approach, however, has been provided in Chapter 6 where we also demonstrated the principal technical feasability of their usage in finite-volume calculations. As a consequence, an analysis in this direction is a logical next step for future investigations. In addition, we also briefly introduced MIT boundary conditions for the description of spherical volumes. In order to enable more direct applications in the context of heavy-ion collisions, they might have to be incorporated into our framework in a future work.

Imaginary Chemical Potentials

In the course of our second and intermediate analysis, we returned to the infinite-volume phase diagram albeit in a broader sense, i.e., we considered imaginary chemical potentials. We began with a discussion why these are an interesting object of investigation as well as a reiteration about the associated Roberge–Weiss symmetry and its implications. Afterwards, our main study was to gauge the quality the extrapolation procedure introduced in Ref. [1] in the context of lattice QCD. To this end, we applied it to our functional framework – where both regimes are accessible – and compared the extrapolation from imaginary chemical potentials to values explicitly obtained at real chemical potentials. The findings are highly promising: The

extrapolation performs exceptionally well for chemical potentials nearly as large (up to 80 %) as the critical endpoint. For larger chemical potentials, however, the extrapolated transition line falls slightly below the calculated one, with the temperature at the critical chemical potential $\mu_{\mathrm{B}}^{\mathrm{CEP}} \approx 636\,\mathrm{MeV}$ being about 13 MeV too low. Additionally, the extrapolation procedure, of course, cannot determine the location of the CEP. Nevertheless, by comparing the lattice results with our framework's outcomes at high imaginary chemical potential and taking it as a rough estimate of the corresponding systematic error at real chemical-potential values, we infer a systematic error of approximately five to ten per cent for the CEP's location. In view of potential future work that can build on the results and methods in this chapter, we closed with an introduction of the theoretical basis behind Lee–Yang zeroes.

The Columbia Plot

In the final chapter, we treated the quark mass dependence of the QCD phase diagram. To this end, we studied the order of the phase transition in the limit of massless up/down quarks as a function of the mass of the strange quark. In this context, we investigated both the two- and the three-dimensional Columbia plot, i.e., both vanishing as well as small nonzero values for the baryon chemical potential. To this end, we extended our set of Dyson–Schwinger equations specifically for the investigation of the chiral second-order transition. That is, in addition to the microscopic degrees of freedom already present, we also included potential long-range correlations with the quantum numbers of pseudoscalar and scalar mesons. We obtain a chiral crossover as long as the light-quark masses remain nonzero, while a second-order phase transition occurs in the light-quark chiral limit. This behaviour persists along the left-hand side of the Columbia plot, i.e., for all strange-quark masses in the range $0 \leq m_{\mathrm{s}} \leq \infty$ as well as also for (small) imaginary and real chemical potentials. These results remain unchanged irrespective of whether we include a massive η' meson (in case the axial $\mathrm{U}_A(1)$ remains anomalously broken at T_{c}) or a massless η' meson (in case the axial $\mathrm{U}_A(1)$ is restored at T_{c}). Our findings contradict the long-standing notion of a chiral first-order transition in the $N_f = 3$ corner in the Columbia plot but align with recent findings from lattice QCD and indications from effective models. Beyond that, we also performed an exploratory investigation of the behaviour of the strange-quark condensate at the bottom edge of the Columbia plot, i.e., for chiral strange quarks, and found a second-order transition there as well.

A long-term goal would be to not resort to approximations for the mesons but to calculate their masses and wavefunctions directly within the BSE framework instead. This way, one might be able to make more quantitative statements about the Columbia plot both at vanishing and at nonzero chemical potential. Even though it entails significant technical challenges to treat mesons at nonzero temperature, it is, in principle, achievable within our framework [356] and results at nonzero chemical potential have already been produced recently [80, 249]. A further extension of the meson-backcoupling approach in the future is to also consider baryon- and diquark-backcoupling diagrams. Baryonic effects are assumed to become important in the low-temperature and high-chemical-potential region of the QCD phase diagram in order to resolve the nuclear liquid–gas phase transition or to describe the equation of state for neutron stars. Backcoupling effects of these diagrams have already been investigated in the past using parametrizations for the baryon and diquark dressing functions [49, 247]. Work in this direction within our framework using a more proper treatment is in progress.

Concluding Remarks

In total, we have demonstrated that Dyson–Schwinger equations in general and our truncation in particular are a very versatile approach that can be applied reasonably and productively to a wide variety of topics both in the context of the QCD phase diagram and beyond. We highlighted many synergetic effects with lattice QCD by using its input for our quenched gluon propagator, assessing the strength of commonly used extrapolation techniques – thereby also estimating the error of our truncation – or calculating in regions where the lattice cannot. Furthermore, we have showcased the ability of our truncation to allow for systematic extensions tailored to the relevant degrees of freedom of the problem in question. This renders our approach very well suited for further investigations of various topics in the context of QCD and similar theories.

Appendix A
Definitions and Conventions

A.1. Units

We work in *natural units*, i.e.,

$$\hbar = c = k_\mathrm{B} = 1\,. \tag{A.1}$$

This implies that

$$[\text{energy}] = [\text{momentum}] = [\text{mass}] = [\text{temperature}] = [\text{length}]^{-1} = [\text{time}]^{-1}\,. \tag{A.2}$$

Energy units are given in electronvolts (eV) or multiples thereof (keV, MeV, GeV, etc.), while length units are given in femtometres (fm). Conversion is performed by means of the relation

$$\hbar c = 1 = 0.197\,326\,98\,\text{GeV fm}\,. \tag{A.3}$$

A.2. Relativistic Notation

Consider an arbitrary d-dimensional space with a *metric tensor* $g^{\nu\rho} = g^{\rho\nu} \in \mathbb{R}^{d\times d}$. A *vector* $x^\nu \coloneqq (x^0, x^1, \ldots, x^{d-1})$ in this space is denoted by a superscript index. The corresponding *covector* x_ν, which is denoted by a subscript, is given by

$$x_\nu = x^\rho g_{\rho\nu}\,, \tag{A.4}$$

where $g_{\nu\rho}$ indicates the inverse metric tensor. This inverse tensor fulfils

$$g^{\nu\lambda} g_{\lambda\rho} = g^\nu{}_\rho \equiv \delta^\nu{}_\rho\,, \tag{A.5}$$

with δ being the Kronecker delta. Therefore, one can always use the metric to raise or lower indices. A derivative with respect to a vector produces a covector:

$$\frac{\partial}{\partial x^\nu} =: \partial_\nu\,. \tag{A.6}$$

In all cases, we use *Einstein summation convention*. That is to say, if an index appears once as superscript and once as subscript in one single term, it is summed (or *contracted*) over:

$$A^\nu B_\nu \equiv \sum_\nu A^\nu B_\nu\,. \tag{A.7}$$

Whenever further abbreviation is needed and/or there is no risk of confusion, we spare the indices and write such a contraction simply as a dot product:

$$x \cdot y \coloneqq x^\nu y_\nu\,. \tag{A.8}$$

Moreover, we make use of the *Feynman slash notation*, i.e.,

$$\not{A} := \gamma^\nu A_\nu \,, \tag{A.9}$$

where γ^ν denotes the Dirac matrices.

We remark that "$a := b$" and "$b =: a$" mean "a is defined to be equal to b", whereas "$a \equiv b$" is to be understood as "a is identical/equivalent to b", e.g., $\sin^2 x + \cos^2 x \equiv 1$.

A.3. Minkowski and Euclidean Spacetime

Of course, nature takes place in four-dimensional *Minkowski spacetime*[1]. The metric tensor $g^{\nu\rho} = \eta^{\nu\rho}$ of a d-dimensional Minkowski spacetime with one temporal and $d-1$ spatial dimensions is given by

$$\eta^{\nu\rho} = \eta_{\nu\rho} = \mathrm{diag}\{1, -1, \ldots, -1\} \,, \tag{A.10}$$

where $\nu, \rho = 0, \ldots, d-1$ are Lorentz indices. Thus, a vector x^ν in Minkowski spacetime takes the form $x^\nu := (x^0, \boldsymbol{x})$ where $\boldsymbol{x} \in \mathbb{R}^{d-1}$ and the Minkowski scalar product between two vectors x^ν and y^ν reads

$$x^\nu y_\nu = x^\nu y^\rho \eta_{\nu\rho} = x^0 y^0 - \sum_{i=1}^{d-1} x^i y^i = x^0 y^0 - \langle \boldsymbol{x}, \boldsymbol{y} \rangle \,. \tag{A.11}$$

In this thesis, however, we exclusively consider *Euclidean spacetime* as is conventional for the non-perturbative treatment of QFTs due to computational advantages. The metric tensor of a general d-dimensional Euclidean spacetime reads

$$g^{\nu\rho} = \delta^{\nu\rho} = \delta_{\nu\rho} = \mathrm{diag}\{1, \ldots, 1\} = \mathbb{1}_d \,, \tag{A.12}$$

where $\mathbb{1}_d$ labels the d-dimensional unit matrix. Minkowski and Euclidean spacetime are connected via *Wick rotation*, i.e., a "rotation" of the spacetime vector's zeroth component from the real into the negative imaginary axis. Effectively, this corresponds to a substitution of the temporal component while the spatial components are unaffected:

$$x^0 \longrightarrow x^0_M =: \mathrm{i} x^0_E \,, \quad \boldsymbol{x}_M = \boldsymbol{x}_E \,. \tag{A.13}$$

Going away from the general case, we note that we exclusively consider a *four-dimensional spacetime* throughout this thesis, i.e., three spatial and one temporal dimension. To this end, we always indicate the zeroth Euclidean component with a '4' as an abbreviatory notation:

$$x^4 := x^0_E \,. \tag{A.14}$$

One can easily show that the Wick rotation in Equation (A.13) indeed turns (A.11) into a Euclidean scalar product:

$$x^\nu_M y^\rho_M \eta_{\nu\rho} = (-\mathrm{i})^2 x^4 y^4 - \langle \boldsymbol{x}, \boldsymbol{y} \rangle = -\big(x^4 y^4 + \langle \boldsymbol{x}, \boldsymbol{y} \rangle\big) = -x^\nu_E y^\rho_E \delta_{\nu\rho} \,. \tag{A.15}$$

By this definition, it follows directly that

$$\partial_4 = \mathrm{i}\partial_0 \quad \text{and} \quad p^4 = \mathrm{i} p^0 \,. \tag{A.16}$$

[1] Under the reasonable assumption that we can neglect effects of general relativity.

However, we note that whenever we refer to the fourth component of a Euclidean momentum p_4 somewhere throughout this thesis we imply a real-valued Euclidean energy variable.

When working with fermionic fields in Minkowski or Euclidean spacetime, one needs to clarify how the Dirac matrices in these cases look like. Consider a d-dimensional spacetime with the metric tensor $g^{\nu\rho} = \eta^{\nu\rho}$ or $g^{\nu\rho} = \delta^{\nu\rho}$. Then, the Dirac matrices γ^ν have to satisfy the *Clifford algebra* – which in the Euclidean case is also called *Dirac algebra*,

$$\{\gamma^\nu, \gamma^\rho\} = \gamma^\nu\gamma^\rho + \gamma^\rho\gamma^\nu = 2g^{\nu\rho}\mathbb{1}_d\,. \tag{A.17}$$

Since we do not need an explicit representation for the Dirac matrices, we merely demand

$$\gamma^4 = \gamma^0\,, \quad \boldsymbol{\gamma}_E = \mathrm{i}\boldsymbol{\gamma}_M\,. \tag{A.18}$$

As a consequence, the momentum-space Dirac equation in Minkowski and Euclidean spacetime reads

$$\big(\not{p}_M - m\big)\psi = 0\,, \quad \big(\mathrm{i}\not{p}_E + m\big)\psi = 0\,. \tag{A.19}$$

A.4. Representation and Algebra of SU(N) Generators

Consider an SU(N) gauge group with a set of $N-1$ infinitesimal generators t^a obeying

$$[t^a, t^b] = \mathrm{i}f^{ab}{}_c\, t^c\,. \tag{A.20}$$

Here, f^{abc} labels the $\mathfrak{su}(N)$ structure constants, $a, b, c = 1, \ldots, N^2-1$ are the SU(N) indices of the generators and $[\cdot,\cdot]$ denotes the respective Lie bracket, i.e., the commutator.

For actual calculations, we need a representation of these generators. As is convention, we choose traceless, Hermitean $N \times N$ matrices,

$$(t^a)^\dagger = t^a\,, \qquad \mathrm{tr}[t^a] = 0\,, \qquad t^a \in \mathbb{C}^{N\times N}\,. \tag{A.21}$$

Moreover, we are able to choose t^a in a way such that they fulfil an orthogonality relation,

$$\mathrm{tr}[t^a t^b] = C\cdot\delta^{ab}\,, \tag{A.22}$$

where C labels a constant depending on the chosen representation. Analogous to the usual representation of SU(2), where the generators are proportional to the Pauli matrices σ^i,

$$t^i \coloneqq \sigma^i/2\,, \qquad i = 1,2,3\,, \tag{A.23}$$

we have $C = 1/2$.

For every Lie group, there exists a Casimir operator $\hat{C}$ that commutes with all generators,

$$[\hat{C}, t^a] = 0\,. \tag{A.24}$$

The most-commonly used form – which is also easiest to define – is the quadratic form:

$$\hat{C} \coloneqq t^a t_a\,. \tag{A.25}$$

Since our generators are represented by matrices, the Casimir operator has to be proportional to the N-dimensional unit matrix:

$$t^a t_a = C_F\cdot\mathbb{1}_N\,. \tag{A.26}$$

The proportionality factor C_F can be determined straightforwardly by perfoming the trace:

$$\mathrm{tr}[t^a t_a] = C_F\cdot\mathrm{tr}[\mathbb{1}_N] \quad\Rightarrow\quad \frac{\mathrm{tr}[\delta^{ab}]}{2} = C_F\cdot N \quad\Rightarrow\quad C_F = \frac{N^2-1}{2N}\,. \tag{A.27}$$

A.5. Momentum Space Summations and Integrations

Throughout this thesis, we often encounter equations containing integrals over the whole momentum space. Depending on volume and temperature of the system, however, each component of the possible momentum vectors can either be continuous or discrete. Since the corresponding equations are otherwise identical, we always utilize the generalized symbol

$$\sum\!\!\!\!\!\!\int_q f(q)\,,$$

for the respective integrals, where f denotes some integrand and q the four-dimensional (momentum-)integration variable. In this section, we specify the explicit form of this symbol for all combinations of finite and infinite volume both in vacuum and at nonzero temperature. The following remarks are essentially a brief summary of Appendix B.1 and Section 4.1. To this end, we recall the (temporal) Matsubara frequencies ω_n^T and the (spatial) Matsubara modes ω_m^L, respectively:

$$\omega_n^T = \begin{cases} 2n\pi T & \text{for bosons} \\ (2n+1)\pi T & \text{for fermions} \end{cases}, \quad \omega_m^L = \begin{cases} 2m\pi/L & \text{for PBC} \\ (2m+1)\pi/L & \text{for ABC} \end{cases}, \quad n, m \in \mathbb{Z}\,. \tag{A.28}$$

Here and in the following, T denotes the system's temperature whereas L labels the edge length of the (hyper)cubic volume. Additionally, ABC and PBC again stand for (anti)periodic boundary conditions, respectively.

A.5.1. Vacuum

The vacuum state is characterized by O(4) invariance in the momentum four-vector. As a consequence, the temporal dimension can be treated identically as the spatial dimensions.

Infinite Volume

The description of QFTs in vacuum and infinite volume is the one most-commonly found in the literature. In this case, all four momentum components can assume continuous values and integrals over all momenta read

$$\sum\!\!\!\!\!\!\int_q f(q) \coloneqq \int \frac{\mathrm{d}^4 q}{(2\pi)^4} f(q)\,. \tag{A.29}$$

We evaluate these integrals using four-dimensional hyperspherical coordinates. Since none of the integrands investigated in this thesis ever depend on the angles θ and φ, the four-dimensional integrals reduce to

$$\int \mathrm{d}^4 q = \int_0^\infty q^3 \,\mathrm{d}q \int_0^\pi \sin^2\psi \,\mathrm{d}\psi \int_0^\pi \sin\theta \,\mathrm{d}\theta \int_0^{2\pi} \mathrm{d}\varphi = 2\pi \int_0^\infty q^2 \,\mathrm{d}q^2 \int_{-1}^1 \sqrt{1-z^2}\,\mathrm{d}z\,, \tag{A.30}$$

where $z \coloneqq \cos\psi$.

Finite Volume (Pure Torus)

When bounding each of the four position components to a finite interval, its corresponding momentum component can only assume values of discrete spatial Matsubara modes. As a consequence, momentum integrals become sums over discrete momentum vectors q_i:

$$\sum\!\!\!\!\!\!\int_q f(q) \coloneqq \frac{1}{L^4} \sum_{q_i \in \{\omega^L_{m_i}\}} f(q)\,, \quad m_i \in \mathbb{Z},\ i = 1, \ldots, 4\,. \tag{A.31}$$

Finite Volume (Improved Torus)

For the UV-improved torus in vacuum, we consider the discrete summation only up to some cutoff Λ_{vol} for the magnitude of the four-momentum vector $|q| < \Lambda_{\text{vol}}$ and perform the continuous integration for larger momenta $|q| > \Lambda_{\text{vol}}$:

$$\sum\!\!\!\!\!\!\int_q f(q) \coloneqq \frac{1}{L^4} \sum_{q_i \in \{\omega^L_{m_i}\}}^{|q|<\Lambda_{\text{vol}}} f(q) + \int_{|q|>\Lambda_{\text{vol}}} \frac{\mathrm{d}^4 q}{(2\pi)^4} f(q)\,, \quad m_i \in \mathbb{Z}, i = 1, \ldots, 4\,. \tag{A.32}$$

A.5.2. Medium

At nonzero temperature, the temporal component has to be treated separately from the spatial components due to the emergence of the discrete temporal Matsubara frequencies ω_n.

Infinite Volume

In an infinite volume, only the temporal dimension is discretized while the spatial dimensions remain continuous,

$$\sum\!\!\!\!\!\!\int_q f(q) \coloneqq T \sum_{q_4 \in \{\omega^T_n\}} \int \frac{\mathrm{d}^3 q}{(2\pi)^3} f(q_4, \boldsymbol{q})\,, \quad n \in \mathbb{Z}\,. \tag{A.33}$$

The integrations over the three-momentum are performed with the aid of three-dimensional spherical coordinates. Again, all of our considered integrals are independent of the angle φ. Therefore, we obtain

$$\int \mathrm{d}^3 q = \int_0^\infty q_r^2 \,\mathrm{d}q_r \int_0^\pi \sin\theta \,\mathrm{d}\theta \int_0^{2\pi} \mathrm{d}\varphi = 2\pi \int_0^\infty q_r^2 \,\mathrm{d}q_r \int_{-1}^1 \mathrm{d}z\,, \tag{A.34}$$

where now $z \coloneqq \cos\theta$ and $q_r \coloneqq |\boldsymbol{q}|$.

Finite Volume (Pure Torus)

For systems in a finite volume at nonzero temperature, the three spatial components get discretized as well. The discretization, however, is analogous to the vacuum case albeit in three dimensions:

$$\sum\!\!\!\!\!\!\int_q f(q) \coloneqq \frac{T}{L^3} \sum_{q_4 \in \{\omega^T_n\}} \sum_{q_i \in \{\omega^L_{m_i}\}} f(q_4, \boldsymbol{q})\,, \quad n, m_i \in \mathbb{Z},\ i = 1, \ldots, 3\,. \tag{A.35}$$

Since nonzero temperature breaks O(4) invariance, the temporal Matsubara frequencies and the spatial Matsubara modes no longer necessarily coincide.

Finite Volume (Improved Torus)

The conventions for the UV-improved torus at nonzero temperature are analogous to the one in vacuum, except that the improvement now, of course, only affects the three spatial components. Consequently, the cutoff Λ_{vol} is formulated with respect to the magnitude of the three-vector $|\boldsymbol{q}|$:

$$\sum\!\!\!\!\!\!\int_{q} f(q) \coloneqq T \sum_{q_4 \in \left\{\omega_n^T\right\}} \left(\frac{1}{L^3} \sum_{q_i \in \left\{\omega_{m_i}^L\right\}}^{|\boldsymbol{q}|<\Lambda_{\mathrm{vol}}} f(q_4, \boldsymbol{q}) + \int_{|\boldsymbol{q}|>\Lambda_{\mathrm{vol}}} \frac{\mathrm{d}^3 q}{(2\pi)^3} f(q_4, \boldsymbol{q}) \right), \; n, m_i \in \mathbb{Z}, \; i = 1, \ldots, 3\,. \tag{A.36}$$

Appendix B
More on QFT, QCD and DSEs

This appendix is a collection of generalities (or specifics) about QFT, QCD and functional methods that would interrupt the main text but should be included in this thesis for the sake of completeness. We start with common textbook knowledge about thermal field theory, generating functionals and gauge fixing in QCD. Thereafter, we sketch the derivations of both the quark propagator DSE as well quark-number density and quark condensate. Subsequently, we introduce some commonly used models of QCD before we close with a short overview of the FRG.

B.1. Thermal Field Theory

We start out with a description how to introduce temperature and chemical potential into the mathematical framework of QFT. To this end, we have to combine the associated theory for such problems – namely *statistical mechanics* – with QFT. An excellent textbook on this topic is Ref. [284], which also serves as the prime source for all following explanations, and we refer to it for further details.

B.1.1. Nonzero Temperature

We recall that the appropriate description for systems at nonzero temperature is a *canonical ensemble* which allows energy exchange between the system and some heat bath. In this ensemble, the inverse temperature $\beta = T^{-1}$ enters as a Lagrange multiplier. In a quantum canonical ensemble, the expectation value of any operator $\hat{A}$ is given by

$$\langle \hat{A} \rangle_\beta = \frac{1}{\mathcal{Z}} \sum_n \langle n | \hat{A} \mathrm{e}^{-\beta \hat{H}} | n \rangle = \frac{\mathrm{tr}\left(\hat{A} \mathrm{e}^{-\beta \hat{H}}\right)}{\mathrm{tr}\left(\mathrm{e}^{-\beta \hat{H}}\right)} \quad \text{with} \quad \mathcal{Z} = \sum_n \langle n | \mathrm{e}^{-\beta \hat{H}} | n \rangle \,, \tag{B.1}$$

where $\hat{H}$ labels the *Hamiltonian operator* of the system, $\mathcal{Z}$ denotes the canonical partition function and $|n\rangle$ forms a set of orthonormal basis states.

Equation (B.1) strongly resembles the quantum field theoretical expectation value in *Euclidean spacetime*, i.e., *imaginary time*. This connection is further reinforced by the fact that the Boltzmann factor $\mathrm{e}^{-\beta \hat{H}}$ may also be interpreted as a quantum mechanical time evolution operator with respect to an imaginary time $\tau := -\mathrm{i}\beta$. Together, these observations have rather interesting implications. On the one hand, it shows that for systems with nonzero temperature it is "natural" to work in an imaginary time framework, i.e., in Euclidean spacetime. On the other hand, the time integration for the action is bounded by the interval $\tau \in [0, \beta]$.

We can derive additional important consequences of thermal QFT if we take a look at a two-point correlation function of some field operators $\hat{\varphi}$ at nonzero temperature:

$$\begin{aligned}\left\langle \hat{\varphi}(\tau,\boldsymbol{x})\hat{\varphi}(\tau,\boldsymbol{y})\right\rangle_\beta &= \frac{1}{\mathcal{Z}}\operatorname{tr}\left[\mathrm{e}^{-\beta\hat{H}}\hat{\varphi}(\tau,\boldsymbol{x})\hat{\varphi}(\tau,\boldsymbol{y})\right] = \frac{1}{\mathcal{Z}}\operatorname{tr}\left[\hat{\varphi}(\tau,\boldsymbol{x})\mathrm{e}^{-\beta\hat{H}}\left(\mathrm{e}^{+\beta\hat{H}}\hat{\varphi}(\tau,\boldsymbol{y})\mathrm{e}^{-\beta\hat{H}}\right)\right] \\ &= \frac{1}{\mathcal{Z}}\operatorname{tr}\left[\mathrm{e}^{-\beta\hat{H}}\hat{\varphi}(\tau+\beta,\boldsymbol{y})\hat{\varphi}(\tau,\boldsymbol{x})\right] = \left\langle \hat{\varphi}(\tau+\beta,\boldsymbol{y})\hat{\varphi}(\tau,\boldsymbol{x})\right\rangle_\beta, \end{aligned} \tag{B.2}$$

where we employed cyclicity of the trace. This relation leads to the *Kubo–Martin–Schwinger* condition [368, 369],

$$\varphi(\tau,\boldsymbol{x}) = \pm\varphi(\tau+\beta,\boldsymbol{x}), \tag{B.3}$$

where the sign depends on whether the fields commute (+, bosons) or anticommute (−, fermions). Further, this shows that fields have to be either periodic (bosons) or antiperiodic (fermions) with respect to the imaginary time, i.e., the boundary conditions are dictated by the spin–statistics theorem [141, 142].

Due to these boundary conditions and the boundedness of imaginary time, we can expand our fields in terms of discrete Fourier modes:

$$\varphi(\tau,\boldsymbol{x}) = \frac{1}{\beta}\sum_{n=-\infty}^{\infty}\varphi\left(\omega_n^T,\boldsymbol{x}\right)\exp\left(\mathrm{i}\omega_n^T\tau\right), \tag{B.4}$$

which implies that the energy can only take the discrete values of *Matsubara frequencies*:

$$\omega_n^T := \begin{cases} 2n\pi T & \text{for bosons} \\ (2n+1)\pi T & \text{for fermions} \end{cases}, \quad n\in\mathbb{Z}. \tag{B.5}$$

As a result, the actual inclusion of a nonzero temperature into QFT calculations is rather straightforward. That is, one can find that for an arbitrary integrand f – fulfilling either of aforementioned boundary conditions with respect to imaginary time – the integration over the imaginary energy coordinate ω merely has to be replaced by the sum over the corresponding Matsubara frequencies:

$$\int_{-\infty}^{\infty}\frac{\mathrm{d}\omega}{2\pi}\,f(\omega) \to T\sum_{n=-\infty}^{\infty} f\left(\omega_n^T\right). \tag{B.6}$$

B.1.2. Nonzero Chemical Potential

Just as we have made use of the canonical ensemble to include temperature into QFT, we may employ the *grand-canonical ensemble* to do the same with chemical potential. While in a canonical ensemble only energy exchange was permitted, the grand-canonical ensemble allows for a variable particle number. This leads to the inclusion of the chemical potential μ as another Lagrange multiplier. A phenomenological interpretation of the chemical potential is the change of the system's inner energy if a single particle is added. We note that actually each particle species in a system has its own associated chemical potential. However, whenever we refer to a chemical potential in this thesis, we always imply quark chemical potentials. For the sake of readability, we therefore restrict our explanations below to a single spinor.

In a quantum grand-canonical ensemble, the Boltzmann factor is modified according to

$$\mathrm{e}^{-\beta\hat{H}} \to \mathrm{e}^{-\beta(\hat{H}-\mu\hat{N})} =: \mathrm{e}^{-\beta\tilde{H}}\,, \tag{B.7}$$

where $\hat{N}$ labels the particle-number operator. Here, we have absorbed the additional term including the chemical potential into a redefined Hamiltonian operator $\tilde{H}$. This was done in view of introducing the chemical potential into the Lagrangian formalism of QFT.

To this end, we consider the respective operator densities below. The fermionic particle-number density may renownedly be expressed in terms of the fermionic spinors ψ as $\hat{n} = \psi^\dagger\psi$. Since including μ does not add any time derivatives of the spinor, the Legendre transform of our redefined Hamiltonian density $\tilde{H}$ is not affected. Hence, the Lagrangian density is modified like

$$\mathcal{L} \to \tilde{\mathcal{L}} = \mathcal{L} + \mu\overline{\psi}\gamma^0\psi\,. \tag{B.8}$$

For a free fermion in Minkowski spacetime, this implies that introducing a chemical potential corresponds to a mere shift in energy, $\omega \to \tilde{\omega} \coloneqq \omega + \mu$. This becomes apparent by looking at the inverse Minkowski propagator which can be obtained directly from the term enclosed by the quark spinors in the Lagrangian density:

$$S_0^{-1}(\omega, \boldsymbol{p}; \mu) = \gamma_0(\omega + \mu) - \boldsymbol{\gamma}\cdot\boldsymbol{p} - m = S_0^{-1}(\omega + \mu, \boldsymbol{p}; \mu = 0)\,. \tag{B.9}$$

When extending above thoughts to imaginary time, we note that the chemical potential becomes an *imaginary* shift in energy, $p_4 \to \tilde{p}_4 \coloneqq p_4 + \mathrm{i}\mu$, which follows directly from

$$-\mathrm{i}\tilde{p}_4 \coloneqq \tilde{\omega} = \omega + \mu = -\mathrm{i}p_4 + \mu = -\mathrm{i}(p_4 + \mathrm{i}\mu)\,. \tag{B.10}$$

B.2. Generating Functionals (in Euclidean Spacetime)

In this section, we elucidate how one can calculate any desired n-point function by performing functional derivatives of different *generating functionals* – a special set of functionals derived from the path-integral representation of the partition function. We will introduce the most-commonly used ones, with each of them generating a different type of Feynman diagrams, and clarify how they are related. For the sake of brevity and clarity, we restrict ourselves in the following to a single bosonic field. The statements below are based on Refs. [34–38], which we also refer to for more detailed information.

B.2.1. All Diagrams: $\mathcal{Z}$

We start with the most-fundamental one, which also serves as the basis for all other generating functionals: *the* generating functional $\mathcal{Z}$, which generates all Feynman diagrams – connected and disconnected. It is a modification of the path-integral representation of the partition function constructed in a way to mimic an often-used trick from statistical mechanics. Namely, one introduces an auxiliary field J – called the *source field* – such that functional derivatives with respect to it yield the quantities one is interested in, i.e., n-point correlation functions. The generating functional reads:

$$\mathcal{Z}[J] \coloneqq \int \mathcal{D}\varphi\ \exp\bigl(-\mathcal{S}[\varphi] + \langle\varphi, J\rangle\bigr)\,, \tag{B.11}$$

where $\langle \cdot, \cdot \rangle$ denotes the L^2-scalar product of square-integrable functions.[1] As already mentioned, $\mathcal{Z}[J]$ is an extension of the partition function $\mathcal{Z}$, which is trivially recovered in the limit $J \to 0$, i.e., $\mathcal{Z} = \mathcal{Z}[0]$.

By construction, we are now able to obtain any n-point correlation function $G^{(n)}$ by performing n functional derivatives with respect to J such that

$$G^{(n)}(x_1, \ldots, x_n) \coloneqq \langle \varphi(x_1) \cdots \varphi(x_n) \rangle = \frac{1}{\mathcal{Z}[0]} \frac{\delta}{\delta J(x_1)} \cdots \frac{\delta}{\delta J(x_n)} \mathcal{Z}[J] \bigg|_{J=0} . \tag{B.12}$$

In an alternative notion that further highlights their importance, the generating functional can be expressed as a series expansion of correlation functions together with the source fields:

$$\mathcal{Z}[J] = \sum_{n=0}^{\infty} \frac{1}{n!} \int \mathrm{d}^4 x_1 \cdots \int \mathrm{d}^4 x_n \, J(x_1) \cdots J(x_n) G^{(n)}(x_1, \ldots, x_n) \, . \tag{B.13}$$

B.2.2. Connected Diagrams: $\mathcal{W}$

As stated earlier, functional derivatives of $\mathcal{Z}$ yield also disconnected diagrams. Yet, we know that disconnected diagrams can be expressed in terms of fully connected diagrams. Therefore, constructing a generating functional of only fully connected diagrams might be desirable. Employing the *linked-cluster theorem*, one can find that such a functional exists and is given by the natural logarithm of $\mathcal{Z}$. Thus, it reads

$$\mathcal{W}[J] \coloneqq \ln \mathcal{Z}[J] \, . \tag{B.14}$$

Analogously to $\mathcal{Z}$, the fully connected correlation functions are calculated from the functional derivatives of $\mathcal{W}$ with respect to J:

$$\langle \varphi(x_1) \cdots \varphi(x_n) \rangle_{\text{conn.}} = \frac{\delta}{\delta J(x_1)} \cdots \frac{\delta}{\delta J(x_n)} \mathcal{W}[J] \bigg|_{J=0} . \tag{B.15}$$

One can nicely see how $\mathcal{W}$ generates only the fully connected Green's functions with the aid of a two-point function, i.e., its second functional derivative,

$$\frac{\delta^2 \mathcal{W}[J]}{\delta J(x_1) \delta J(x_2)} \bigg|_{J=0} = \langle \varphi(x_1) \varphi(x_2) \rangle - \langle \varphi(x_1) \rangle \langle \varphi(x_2) \rangle \, . \tag{B.16}$$

Obviously, this is just the full two-point function with the disconnected contributions subtracted, which leaves only the fully connected part.

B.2.3. 1PI Diagrams: Effective Action Γ

Next, we cover the *one-particle irreducible* (1PI) correlation functions, an often-used subclass of the connected ones. These are defined as those graphs that cannot be made disconnected by cutting a single internal line. As a consequence, all connected diagrams can be constructed

[1] In the most general case of multiple fields and sources, $(\varphi_i) \in \varphi$ and $(J_i) \in J$, the scalar product is given by $\langle \varphi, J \rangle = \sum_i \int \mathrm{d}^4 x \, \varphi_i(x) \cdot J_i(x)$.

by connecting 1PI diagrams with propagators. The corresponding generating functional is the so-called *effective action* Γ. It is defined as the Legendre transform of $\mathcal{W}$ with respect to J:

$$\Gamma[\Phi] = \mathcal{W}[J] - \left\langle \frac{\delta \mathcal{W}[J]}{\delta J}, J \right\rangle =: \mathcal{W}[J] - \langle \Phi, J \rangle \,. \tag{B.17}$$

Here, we defined the *(semi-)classical* (or *mean*) field Φ, which is the vacuum expectation value of φ in the presence of the external source J, as the transformed field variable:

$$\Phi(x) \coloneqq \langle \varphi(x) \rangle_J = \frac{\delta \mathcal{W}[J]}{\delta J(x)} \,. \tag{B.18}$$

As a Legendre transform, the effective action is a convex functional. The name 'effective action' comes from the fact that in the limit $\hbar \to 0$ one recovers the classical action, $\lim_{\hbar \to 0} \Gamma[\Phi] = \mathcal{S}[\Phi]$. Therefore, it can be seen as a quantum generalization of the classical action.

Using above definitions, it is a straightforward exercise to show that Γ fulfils

$$\frac{\delta \Gamma[\Phi]}{\delta \Phi(x)} = -J(x) \quad \text{and} \quad \frac{\delta^2 \Gamma[\Phi]}{\delta \Phi(x) \delta \Phi(y)} = -\left(\frac{\delta^2 \mathcal{W}[J]}{\delta J(x) \delta J(y)} \right)^{-1} . \tag{B.19}$$

The former relation reinforces the connection between classical and effective action, i.e., the physical fields $\lim_{J \to 0} \Phi$ extremize Γ. The second relation allows us to express the connected propagator in terms of Γ which is useful in the context of Dyson–Schwinger equations.

B.2.4. *n*PI Diagrams

The diagrammatic idea of 1PI correlation functions can be generalized by demanding that the corresponding Feynman diagrams cannot be made disconnected by cutting n internal lines resulting in the *n-particle irreducible* (nPI) correlation functions. This was pioneered for the 2PI effective action by John M. Cornwall, Roman W. Jackiw and E. Terry Tomboulis [370] (see also Ref. [237] for an early review). The approach can be extended to arbitrary order and we will collect some general properties of nPI effective actions in the following. Our statements are based on the review in Ref. [219].

The starting point is to not only introduce sources $J^{(m)}$ for the fields but also for higher m-point functions into the generating functional (where $m \leq n$):

$$\mathcal{Z}[J^{(1)}, J^{(2)}, J^{(3)}, \dots] \coloneqq \int \mathcal{D}\varphi \;\; \exp\Big(-\mathcal{S}[\varphi] + \big\langle \varphi_i, J_i^{(1)} \big\rangle + \big\langle \varphi_i \varphi_j, J_{ij}^{(2)} \big\rangle + \big\langle \varphi_i \varphi_j \varphi_k, J_{ijk}^{(3)} \big\rangle + \dots \Big) . \tag{B.20}$$

The associated nPI effective action $\Gamma_{n\mathrm{PI}}$ is then obtained analogously by a Legendre transform of $\mathcal{W} = \ln \mathcal{Z}$ with respect to all source fields:

$$\Gamma_{n\mathrm{PI}}[\Phi^{(1)}, \Phi^{(2)}, \Phi^{(3)}, \dots] = \mathcal{W}[J^{(1)}, J^{(2)}, J^{(3)}, \dots] - \sum_{i=1}^{n} \big\langle \Phi^{(n)}, J^{(i)} \big\rangle \,. \tag{B.21}$$

Here, we introduced the dressed m-point functions $\Phi^{(m)}$ which are obtained as functional derivatives of $\mathcal{W}$ with respect to $J^{(m)}$ and fulfil stationary conditions of the nPI effective action:

$$\Phi^{(m)} = \frac{\delta \mathcal{W}[J^{(1)}, J^{(2)}, J^{(3)}, \dots]}{\delta J^{(m)}} , \quad \frac{\delta \Gamma_{n\mathrm{PI}}[\Phi^{(1)}, \Phi^{(2)}, \Phi^{(3)}, \dots]}{\delta \Phi^{(m)}} = 0 \,. \tag{B.22}$$

By construction, all nPI effective actions are identical for vanishing sources,

$$\Gamma_{1\mathrm{PI}}[\Phi^{(1)}] = \Gamma_{2\mathrm{PI}}[\Phi^{(1)}, \Phi^{(2)}] = \cdots = \Gamma_{n\mathrm{PI}}[\Phi^{(1)}, \Phi^{(2)}, \ldots, \Phi^{(n)}]\,, \tag{B.23}$$

while their expansions up to m-loop order $\Gamma_{n\mathrm{PI}}^{m-\mathrm{loop}}$ do so only if $m \leq n$:

$$\Gamma_{1\mathrm{PI}}^{1-\mathrm{loop}}[\Phi^{(1)}] = \Gamma_{2\mathrm{PI}}^{1-\mathrm{loop}}[\Phi^{(1)}, \Phi^{(2)}] = \ldots\,, \tag{B.24}$$

$$\Gamma_{1\mathrm{PI}}^{2-\mathrm{loop}}[\Phi^{(1)}] \neq \Gamma_{2\mathrm{PI}}^{2-\mathrm{loop}}[\Phi^{(1)}, \Phi^{(2)}] = \Gamma_{3\mathrm{PI}}^{2-\mathrm{loop}}[\Phi^{(1)}, \Phi^{(2)}, \Phi^{(3)}] = \ldots\,, \tag{B.25}$$

$$\Gamma_{1\mathrm{PI}}^{3-\mathrm{loop}}[\Phi^{(1)}] \neq \Gamma_{2\mathrm{PI}}^{3-\mathrm{loop}}[\Phi^{(1)}, \Phi^{(2)}] \neq \Gamma_{3\mathrm{PI}}^{3-\mathrm{loop}}[\Phi^{(1)}, \Phi^{(2)}, \Phi^{(3)}] = \Gamma_{4\mathrm{PI}}^{3-\mathrm{loop}}[\ldots] = \ldots\,. \tag{B.26}$$

This is due to the fact that $\Gamma_{n\mathrm{PI}}$ depends explicitly on all dressed m-point functions up to $\Phi^{(n)}$, i.e., higher-order correlation functions must be expressed in terms of these while bare lower-order ones no longer occur. A consequence of this loop-expansion hierarchy is that one can obtain a self-consistent description of the theory up to m-loop order with an nPI effective action where $m \leq n$.

B.3. Gauge Fixing of QCD

As an extension of Section 2.1, we briefly sketch the derivation of the gauge-fixed QCD Lagrangian using the Faddeev–Popov procedure below while also commenting on shortcomings of this approach. Again, the following line of action and statements are based on the standard textbooks in Refs. [33–37].

In advance, we elaborate on why the QCD Lagrangian without gauge fixing yields an ill-defined gluon propagator. This becomes apparent when looking at the pure-Yang–Mills part of the action in its quadratic form in momentum space:

$$\begin{aligned} \mathcal{S}_{\mathrm{QCD}}^{\mathrm{YM}}[A] &= -\frac{1}{4}\int \mathrm{d}^4x\; F_{\nu\rho}^a F_a^{\nu\rho} = -\frac{1}{2}\int \mathrm{d}^4x\; A_\nu(x)\big(\partial^2 g^{\nu\rho} - \partial^\nu\partial^\rho\big)A_\rho(x) + O\big(A^3\big) \\ &= -\frac{1}{2}\int \mathrm{d}^4k\; A_\nu(k)\big(-k^2 g^{\nu\rho} - k^\nu k^\rho\big)A_\rho(k) + O\big(A^3\big)\,. \end{aligned} \tag{B.27}$$

The operator between the gluon fields – which corresponds to the inverse gluon propagator – has zero modes, e.g., for $A_\nu(k) = k_\nu \vartheta(k)$. This troublesome field is the so-called *pure gauge* field since it corresponds to $A_\nu \equiv 0$.

In order to now perform gauge fixing, we first define a *gauge orbit* $[A_\nu]$ as the set of all fields $A_\nu^\vartheta \in [A_\nu]$ that are equivalent via gauge transformations $U = U(x) = \exp(\mathrm{i}\vartheta)$ (where $\vartheta = \vartheta(x) = \vartheta_a(x)t^a$ is the gauge parameter of Equation (2.2)):

$$[A_\nu] \coloneqq \left\{A'_\nu : \exists U \text{ such that } A'_\nu = UA_\nu U^{-1} + \mathrm{i}g^{-1}(\partial_\nu U)U^{-1}\right\}. \tag{B.28}$$

The idea of the Faddeev–Popov procedure is based on the fact one can single out one specific value of a function using the Dirac δ distribution. More specifically, for any function f that has exactly one solution of $f(x_0) = 0$ with $f'(x_0) \neq 0$, we may express unity as

$$1 = \int \mathrm{d}x\; \delta\big(f(x)\big)\,\big|f'(x_0)\big|\,. \tag{B.29}$$

This relation can be generalized to a functional framework by replacing the respective quantities with their functional equivalents. The idea is to choose a functional F in such a way that it fulfils the equation $F[A^\vartheta] = 0$ exactly once per gauge orbit. As a consequence, we express functional unity analogously as

$$\mathbb{1} = \int \mathcal{D}\vartheta\ \delta\big(F[A^\vartheta]\big) \left|\det\left(\frac{\delta F[A^\vartheta]}{\delta\vartheta}\right)\right| =: \int \mathcal{D}\vartheta\ \delta\big(F[A^\vartheta]\big)\ \Delta_F[A^\vartheta]\,, \tag{B.30}$$

where Δ_F labels the so-called *Faddeev–Popov determinant* [139]. In order to single out one field configuration per gauge orbit, we insert Equation (B.30) into the pure-Yang–Mills part of the generating functional:

$$\int \mathcal{D}A\ \exp\big(-\mathcal{S}^{\mathrm{YM}}_{\mathrm{QCD}}[A]\big) = \int \mathcal{D}\vartheta\ \int \mathcal{D}A\ \exp\big(-\mathcal{S}^{\mathrm{YM}}_{\mathrm{QCD}}[A]\big)\ \delta\big(F[A^\vartheta]\big)\ \Delta_F[A^\vartheta]\,. \tag{B.31}$$

Here, we employed the fact that both $\mathcal{D}A$ and $\mathcal{S}^{\mathrm{YM}}_{\mathrm{QCD}}[A]$ are gauge-invariant and therefore commute with quantities depending on ϑ. As a gauge-fixing condition, we choose the functional

$$F[A^\vartheta] = \partial^\nu A^\vartheta_\nu - \omega\,, \tag{B.32}$$

with some auxiliary function ω. Hence, its derivative is given by[2]

$$\frac{\delta F[A^\vartheta]}{\delta\vartheta} = \frac{\mathrm{i}}{g}\partial^\nu D^{ab}_\nu = \frac{\mathrm{i}}{g}\partial^\nu\big(\delta^{ab}\partial_\nu + g f^{ab}{}_c\, A^c_\nu\big)\,, \tag{B.33}$$

where D^{ab}_ν denotes the covariant derivative in the adjoint representation.

As a first means of simplification, we want to eliminate the δ distribution. To this end, we integrate over ω weighted with a Gaussian that introduces the gauge-fixing parameter ξ:

$$\int \mathcal{D}\vartheta\ \delta\big(F(A^\vartheta)\big) = \int \mathcal{D}\vartheta\ \int \mathcal{D}\omega\ \exp\left(-\int \mathrm{d}^4x\ \frac{\omega^2}{2\xi}\right)\delta\big(\partial^\nu A^\vartheta_\nu - \omega\big) = \mathcal{N}\exp\left(-\int \mathrm{d}^4x\ \frac{(\partial_\nu A^\nu)^2}{2\xi}\right), \tag{B.34}$$

where $\mathcal{N}$ labels a normalization factor that stems from the integration over ϑ.

Up to this point, the chain of reasoning was identical to QED. There, however, the derivative of the gauge-fixing functional in Equation (B.33) does not depend on the gauge fields since the structure constants vanish. As a consequence, the Faddeev–Popov determinant is just a constant that can be absorbed in the normalization. In QCD, though, this is no longer the case. To this end, we introduce the auxiliary Grassmann-valued ghost fields $\bar{c}$, c.[3] This way, we can rewrite the Faddeev–Popov determinant as a Gaussian over these fields:

$$\Delta_F[A^\vartheta] = \int \mathcal{D}[c\bar{c}]\ \exp\left(-\mathrm{i}\int \mathrm{d}^4x\ \bar{c}_a\partial^\nu D^{ab}_\nu c_b\right). \tag{B.35}$$

Here, a factor of g^{-1} has been absorbed in the normalization of the ghost fields.

[2] For this functional derivative, it is more convenient to work with the *infinitesimal* gauge transformation: $A_\nu \to A'_\nu = A_\nu + \mathrm{i}g^{-1}D_\nu\vartheta$.

[3] To be more specific, c and $\bar{c}$ are conventionally labelled *ghost* and *antighost field*, respectively.

The integrals in Equations (B.34) and (B.35) can be combined to an effective Lagrangian that – when added to the one in Equation (2.6) – leads to a gauge-fixed description of QCD:

$$\mathcal{L}_{\mathrm{GF}} = -\frac{(\partial_\nu A^\nu)^2}{2\xi} + \mathrm{i}(\partial^\nu \overline{c})(D_\nu c)\,. \tag{B.36}$$

At this point, we remark that two of our assumptions made in the course of the derivation of the gauge-fixed Lagrangian are actually not quite correct. First, the functional F in Equation (B.32) does not fulfil the condition $F[A^\vartheta] = 0$ exactly once per gauge orbit but actually infinitely many times in QCD. This way, even the gauge-fixed partition function entails an integration over gauge-equivalent fields. These are the so-called *Gribov copies* that still lead to an overcounting of gauge-equivalent fields [181]. Second, the Fadeev–Popov determinant in Equation (B.32) is not really positive definite.

An attempt to circumvent these issues is to restrict the domain of functional integration to the *Gribov region* Ω, which is defined as follows:[4]

$$\Omega \coloneqq \left\{A_\nu : \partial^\nu A^\vartheta_\nu = 0 \ \wedge\ \det\left(-\partial^\nu D_\nu\right) \geq 0\right\}. \tag{B.37}$$

As it turns out, however, there are still Gribov copies inside the Gribov region. To this end, one defines the *fundamental modular region* (FMR) as the subspace of the Gribov region that one and only one solution for the gauge condition. Even though a restriction of the path integral to the FMR gets rid of Gribov copies in theory, it is extremely hard to implement for practical calculations. Fortunately, it was found from lattice calculations that Gribov copies inside the first Gribov region only affect the gluon propagator mildly in the deep infrared (see, e.g., Refs. [371–373]), while it has been argued that the continuum theory remains unaffected [374].

B.4. Sketched Derivation of the Quark Propagator DSE

Below, we sketch the derivation of the quark-propagator DSE, i.e., we convey the general idea and use some shortcuts rather than being completely rigorous. Let $\mathcal{S}$ be the gauge-fixed QCD action and $J = (j, \overline{\eta}, \eta)$ be the source fields for $(A, \psi, \overline{\psi})$, respectively. Let further a, b be some colour indices in the adjoint representation, while i, l, n, r, s label colour indices in the fundamental representation. Moreover, x, y, z, v, w denote positions in configuration space, ν and ρ are Lorentz indices, while all Dirac indices are suppressed.

In advance, we comment on the convention of *directional derivatives*. Since Grassmann-valued derivatives also anticommute, one sometimes introduces derivatives that act on either their left- or their right-hand side, respectively, in order to avoid some minuses:

$$\frac{\overrightarrow{\delta}}{\delta\eta_l(y)}\eta_i(x) = \delta(x-y)\delta_{il} = \eta_i(x)\frac{\overleftarrow{\delta}}{\delta\eta_l(y)}\,. \tag{B.38}$$

[4] Actually, the condition $\partial^\nu A^\vartheta_\nu = 0 \ \wedge\ \det\left(-\partial^\nu D_\nu\right) = 0$ is fulfilled infinitely often per gauge orbit and describes the so-called *Gribov horizons* which bound an infinite number of Gribov regions. Therefore, the region implied here is actually the *first* Gribov region where we impose the additional condition that $||A||^2$ be minimized.

We begin with the functional derivative of $\mathcal{S}$ with respect to $\overline{\psi}$ in configuration space:

$$\frac{\overrightarrow{\delta}}{\delta\overline{\psi}_i(x)}\mathcal{S}[\psi,\overline{\psi},A] = (-\not{\partial}+m)\psi_i(x) + \mathrm{i}gt_a\gamma^\nu A^a_\nu(x)\psi_i(x)\,. \tag{B.39}$$

Now, we apply Equation (3.3):

$$\eta_i(x) = (-\not{\partial}+m)\left(\frac{\overrightarrow{\delta}\mathcal{W}}{\delta\overline{\eta}_i(x)} + \frac{\overrightarrow{\delta}}{\delta\overline{\eta}_i(x)}\right)\cdot 1 + \mathrm{i}gt_a\gamma^\nu\left(\frac{\delta\mathcal{W}}{\delta j^\nu_a(x)} + \frac{\delta}{\delta j^\nu_a(x)}\right)\left(\frac{\overrightarrow{\delta}\mathcal{W}}{\delta\overline{\eta}_i(x)} + \frac{\overrightarrow{\delta}}{\delta\overline{\eta}_i(x)}\right)\cdot 1 \tag{B.40}$$

$$= (-\not{\partial}+m)\frac{\overrightarrow{\delta}\mathcal{W}}{\delta\overline{\eta}_i(x)} + \mathrm{i}gt_a\gamma^\nu\left(\frac{\delta\mathcal{W}}{\delta j^\nu_a(x)}\frac{\overrightarrow{\delta}\mathcal{W}}{\delta\overline{\eta}_i(x)} + \frac{\delta}{\delta j^\nu_a(x)}\frac{\overrightarrow{\delta}\mathcal{W}}{\delta\overline{\eta}_i(x)}\right) \tag{B.41}$$

and consequently differentiate with respect to $\eta_l(y)$ from the right while setting $J \to 0$:

$$\delta(x-y)\delta_{il} = (-\not{\partial}+m)\left(\frac{\overrightarrow{\delta}}{\delta\overline{\eta}_i(x)}\mathcal{W}\frac{\overleftarrow{\delta}}{\delta\eta_l(y)}\right) + \mathrm{i}gt_a\gamma^\nu\left(\frac{\delta}{\delta j^\nu_a(x)}\frac{\overrightarrow{\delta}}{\delta\overline{\eta}_i(x)}\mathcal{W}\frac{\overleftarrow{\delta}}{\delta\eta_l(y)}\right). \tag{B.42}$$

Here, we already spared the terms that drop out due to the vanishing one-point functions:[5]

$$\left(\frac{\delta\mathcal{W}}{\delta j^\nu_a(x)}\frac{\overrightarrow{\delta}\mathcal{W}}{\delta\overline{\eta}_i(x)}\right)\frac{\overleftarrow{\delta}}{\delta\eta_l(y)}\bigg|_{J\to 0} = \left\langle A^a_\nu(x)\psi_l(y)\right\rangle\left\langle\overline{\psi}_i(x)\right\rangle + \left\langle A^a_\nu(x)\right\rangle\left\langle\overline{\psi}_i(x)\psi_l(y)\right\rangle = 0\,. \tag{B.43}$$

Utilizing the following relation for the derivative of an inverse operator $M : \mathbb{R}^d \times \mathbb{R}^d \to \mathbb{K}^{n\times n}$:

$$\delta M^{-1}_{il}(x,y) = -\int \mathrm{d}^d v \int \mathrm{d}^d w\; M^{-1}_{in}(x,v)\big(\delta M^{nr}(v,w)\big)M^{-1}_{rl}(w,y)\,, \tag{B.44}$$

we can furthermore re-express the third functional derivative of $\mathcal{W}$, i.e., the connected three-point function, in terms of QCD propagators and vertices:

$$\frac{\delta}{\delta j^\nu_a(x)}\frac{\overrightarrow{\delta}}{\delta\overline{\eta}_i(x)}\mathcal{W}\frac{\overleftarrow{\delta}}{\delta\eta_l(y)} = \int \mathrm{d}^4 z\;\frac{\delta A^b_\rho(z)}{\delta j^\nu_a(x)}\frac{\delta}{\delta A^b_\rho(z)}\left(\frac{\overrightarrow{\delta}}{\delta\Psi_i(x)}\Gamma\frac{\overleftarrow{\delta}}{\delta\overline{\Psi}_l(y)}\right)^{-1} \tag{B.45}$$

$$= -\iiint \frac{\delta^2\mathcal{W}}{\delta j^\nu_a\delta j^\rho_b}\left(\frac{\overrightarrow{\delta}}{\delta\Psi_i}\Gamma\frac{\overleftarrow{\delta}}{\delta\overline{\Psi}_n}\right)^{-1}\left(\frac{\delta}{\delta A^b_\rho}\frac{\overrightarrow{\delta}}{\delta\Psi_n}\Gamma\frac{\overleftarrow{\delta}}{\delta\overline{\Psi}_r}\right)\left(\frac{\overrightarrow{\delta}}{\delta\Psi_r}\Gamma\frac{\overleftarrow{\delta}}{\delta\overline{\Psi}_l}\right)^{-1} \tag{B.46}$$

$$= -\int \mathrm{d}^4 z \int \mathrm{d}^4 v \int \mathrm{d}^4 w\; D^{ab}_{\nu\rho}(x,z)S_{in}(x,v)\Gamma^{\rho,nr}_b(z,v,w)S_{rl}(w,y)\,. \tag{B.47}$$

Above, we dropped the positional arguments in Line (B.46) for the sake of readability. As the last step, we want to bring one quark propagator in Equation (B.42) to the other side by applying

$$\sum_l \int \mathrm{d}^4 y\; S^{-1}_{ls}(x,y)$$

[5] This is generally true for non-scalar fields Φ due to Lorentz invariance of the vacuum: $\langle\Phi\rangle = \langle 0|\Phi|0\rangle = \langle 0|\Lambda^{-1}\Lambda\Phi\Lambda^{-1}\Lambda|0\rangle = \langle 0|\Lambda\Phi\Lambda^{-1}|0\rangle$, where Λ is a Lorentz transformation.

to both sides of the equation. Renaming some indices and pulling a factor of ig out of $\Gamma^{\rho,n}_{b,l}$ then yields

$$S^{-1}_{il}(x,y) = (-\not{\partial} + m)\delta(x-y)\delta_{il} + g^2 \int \mathrm{d}^4 z \int \mathrm{d}^4 v \; t_a \gamma^\nu D^{ab}_{\nu\rho}(x,z) S_{in}(x,v) \Gamma^{\rho,n}_{b,l}(z,v,y)\,, \quad \text{(B.48)}$$

where we can identify the bare quark propagator $S^{-1}_{0,il}(x,y) = (-\not{\partial} + m)\delta(x-y)\delta_{il}$. In order to transition to momentum space, we perform a Fourier transform and finally arrive at:

$$S^{-1}_{il}(p) = S^{-1}_{0,il}(p) + g^2 \int \frac{\mathrm{d}^4 q}{(2\pi)^4} t_a \gamma^\nu D^{ab}_{\nu\rho}(k) S_{in}(q) \Gamma^{\rho,n}_{b,l}(p,q)\,. \quad \text{(B.49)}$$

B.5. Derivations of Quark Condensate and Number Density

Both the quark condensate and the quark-number density are defined as partial derivatives of the QCD grand potential Ω. In the 2PI formalism, it can be related to the 2PI effective action Γ_{2PI} via the relation

$$\Omega = -\frac{T}{V} \ln \mathcal{Z} = -\frac{T}{V} \Gamma_{\mathrm{2PI}}\Big|_{J\to 0}\,. \quad \text{(B.50)}$$

Setting the sources to zero, $J \to 0$, implies evaluating Γ_{2PI} at the physical values of the fields and propagators:

$$\Gamma_{\mathrm{2PI}}\Big|_{J\to 0} = \Gamma_{\mathrm{2PI}}[A, \Psi, \overline{\Psi}, c, \bar{c}, S, D, G] = \Gamma_{\mathrm{2PI}}[S, D, G]\,. \quad \text{(B.51)}$$

Above, $A, \Psi, \overline{\Psi}, c, \bar{c}$ label the gluon, quark and ghost fields, respectively, whose vacuum expectation values vanish due to Lorentz invariance (see Appendix B.4). In addition, S, D, G denote the quark, gluon and ghost propagators, respectively. We recall that the propagators (and fields) fulfil stationary conditions at their physical values:

$$\frac{\delta\Gamma_{\mathrm{2PI}}[S,D,G]}{\delta S} = 0\,, \quad \frac{\delta\Gamma_{\mathrm{2PI}}[S,D,G]}{\delta D} = 0\,, \quad \frac{\delta\Gamma_{\mathrm{2PI}}[S,D,G]}{\delta G} = 0\,. \quad \text{(B.52)}$$

Furthermore, utilizing a loop expansion, the 2PI effective action can be written as [370]

$$\Gamma_{\mathrm{2PI}}[S,D,G] = \mathrm{tr}\ln S^{-1} - \mathrm{tr}\left[\mathbb{1} - S_0^{-1} S\right] + \Xi_{\mathrm{int}}[S,D] + \Gamma^{\mathrm{YM}}_{\mathrm{2PI}}[D,G]\,. \quad \text{(B.53)}$$

Here, $\Xi_{\mathrm{int}}[S,D]$ labels the interaction functional that contains all 2PI diagrams whose internal lines are dressed quark or gluon propagators. In addition, we collect all pure-Yang–Mills terms in $\Gamma^{\mathrm{YM}}_{\mathrm{2PI}}[D,G]$ since they are irrelevant for our derivation.

This form enables us now to (more or less) straightforwardly perform the partial derivatives with respect to $y_f \in \{m_f, \mu_f\}$. Specifically, we find that

$$-\frac{V}{T}\frac{\partial\Omega}{\partial y_f} = \sum_{X\in\{S,D,G\}} \frac{\delta\Gamma_{\mathrm{2PI}}[S,D,G]}{\delta X}\frac{\partial X}{\partial y_f} + \frac{\partial\Gamma_{\mathrm{2PI}}[S,D]}{\partial y_f}\,. \quad \text{(B.54)}$$

The derivatives with respect to the propagators vanish due to the stationary condition in Equation (B.52). For the explicit derivative, we employ the following consideration that follows

from generalities of the nPI formalism: By construction, the only quantities that can appear explicitly inside the 2PI effective action of QCD are dressed one- and two-point functions and the bare, primitively divergent three- and four-point functions. Since the former have already been accounted for in Equation (B.54) and the latter carry no explicit dependence on either m_f or μ_f, the derivative reduces to

$$\frac{\partial \Gamma_{\mathrm{2PI}}[S,D,G]}{\partial y_f} = \mathrm{tr}\left[\frac{\partial S_0^{-1}}{\partial y_f} S\right]. \tag{B.55}$$

The derivatives of the bare propagator trivially evaluate to

$$\frac{\partial S_0^{-1}}{\partial m_f} = Z_2^f Z_m^f \mathbb{1}_D\,, \quad \frac{\partial S_0^{-1}}{\partial \mu_f} = -Z_2^f \gamma_4\,. \tag{B.56}$$

This leads us directly to Equations (3.6) and (4.22):

$$\frac{\partial \Omega}{\partial m_f} = -N_c Z_2^f Z_m^f \sum\!\!\!\!\!\!\int_q \mathrm{tr}\big[S_f(q)\big]\,, \quad -\frac{\partial \Omega}{\partial \mu_f} = -N_c Z_2^f \sum\!\!\!\!\!\!\int_q \mathrm{tr}\big[\gamma_4 S_f(q)\big]\,, \tag{B.57}$$

where the traces over colour space result in a factor of N_c, the trace over momentum/position space can be (partially) evaluated to V/T (due to symmetries of the propagator) and the remaining traces only involve Dirac space. Since they have been derived directly from the 2PI effective action without approximations, these expressions are exact.

B.6. Models for QCD

In the following, we briefly introduce some commonly used effective models of (low-energy) QCD that are employed both in the context of mean-field approximations or functional approaches. On the one hand, these are sometimes referred to in this thesis and, on the other hand, they also used for calculations in Section 4.2.5.

B.6.1. Nambu–Jona-Lasinio and Quark–Meson Models

An often-used first approach for the description of dynamical chiral symmetry breaking in the low-energy regime of QCD is the *Nambu–Jona-Lasinio* (NJL) model (after Yoichiro Nambu and Giovanni Jona-Lasinio) [43, 44]. It dates back to 1961 – before QCD as the theory of quarks and gluons even existed – as an effective theory of nucleons featuring a mechanism for dynamical mass generation in analogy with the gap in the microscopic theory of superconductivity. In the follwing, we only want to give a brief overview and refer to the reviews in Refs. [61, 375] for more details.

In a two-flavour setup, its Lagrangian density is given by

$$\mathcal{L}_{\mathrm{NJL}} = \overline{\psi}(\mathrm{i}\partial\!\!\!/ - m)\psi + G\Big[\big(\overline{\psi}\psi\big)^2 - \big(\overline{\psi}\mathrm{i}\gamma^5\boldsymbol{\tau}\psi\big)^2\Big], \tag{B.58}$$

where $\boldsymbol{\tau} = (\tau_i)_{i=1,2,3}$ labels a vector containing the $\mathrm{SU}(N_f = 2)$ Pauli matrices, G indicates a (dimensionful) coupling constant and m denotes the bare-quark mass. This Lagrangian is invariant under $\mathrm{SU}_L(2) \times \mathrm{SU}_R(2)$ chiral symmetry transformations just as is QCD, which gets explicitly broken for $m \neq 0$ and spontaneously by the occurrence a non-vanishing condensates $\langle\overline{\psi}\psi\rangle$. However, in contrast to QCD, the interaction is mediated by a four-quark interaction and not by gluons so the NJL model does not feature a running coupling or confinement (in order to remedy the latter, there are *Polyakov-loop-enhanced* NJL models, see, e.g., Ref. [376]). Due to this four-quark interaction, it is also *non-renormalizable*, which implies that any regularization parameter also enters as another model parameter.

In a mean-field approximation, the NJL Lagrangian becomes [221]

$$\mathcal{L}_{\mathrm{NJL}}^{\mathrm{MF}} = \overline{\psi}(\mathrm{i}\partial\!\!\!/ - M)\psi - \frac{(M-m)^2}{4G}, \quad \text{with} \quad \langle\overline{\psi}\psi\rangle = -\frac{M-m}{2G}. \tag{B.59}$$

Here, M labels the dynamically generated constituent-quark mass. Mean-field approximations have the beneficial property that the grand potential is directly accessible:

$$\Omega_{\mathrm{NJL}}^{\mathrm{MF}}(T,\mu) = \frac{(M-m)^2}{4G} - 2N_c N_f \int \frac{\mathrm{d}^3k}{(2\pi)^3}\left[E_{\boldsymbol{k}}\cdot\Theta(\Lambda-|\boldsymbol{k}|) + T\sum_{z=\pm1}\log\left(1+\mathrm{e}^{-(E_{\boldsymbol{k}}+z\mu)/T}\right)\right]. \tag{B.60}$$

Here, $E_{\boldsymbol{k}} = \sqrt{\boldsymbol{k}^2 + M^2}$ denotes the energy, while we regularize the UV-divergent vacuum contribution with a hard UV cutoff Λ ensured by the Heaviside step function Θ. The physical constituent-quark mass is the one that minimizes the grand potential: $\partial\Omega/\partial M = 0$. For the calculations in Section 4.2.5, we utilize the model parameters from Ref. [221], i.e., $m = 5.6\,\mathrm{MeV}$, $\Lambda = 587.9\,\mathrm{MeV}$ and $G = 2.44/\Lambda^2$. The NJL model can also be described in the framework of DSEs (where it is sometimes known as the *contact model*) by setting [207]

$$\frac{g^2 C_F}{(2\pi)^2} D^{\nu\rho}(k) = \delta^{\nu\rho}\frac{G}{\Lambda^2}. \tag{B.61}$$

A renormalizable version of the NJL model is the *quark–meson* (QM) model, which is sometimes also called *linear σ model* with quarks or *Gell-Mann–Lévy model* [14]. See Ref. [377] for a review. Here, the four-quark interaction is eliminated by bosonizing the quark bilinears into an isosinglet scalar meson $\sigma = \overline{\psi}\psi$ and an isotriplet of pseudoscalar mesons $\boldsymbol{\pi} = \mathrm{i}\overline{\psi}\gamma^5\boldsymbol{\tau}\psi$. Adding kinetic terms for the new meson fields and introducing a generalized meson potential U, a commonly used form of the QM Lagrangian reads

$$\mathcal{L}_{\mathrm{QM}} = \overline{\psi}\left(\mathrm{i}\partial\!\!\!/ - g(\sigma + \mathrm{i}\gamma^5\boldsymbol{\tau}\cdot\boldsymbol{\pi})\right)\psi + \frac{1}{2}\left[(\partial_\nu\sigma)(\partial^\nu\sigma) + (\partial_\nu\boldsymbol{\pi})(\partial^\nu\boldsymbol{\pi})\right] - U\left(\sigma^2 + \boldsymbol{\pi}^2\right). \tag{B.62}$$

Here, the explicit symmetry breaking term $m\overline{\psi}\psi = m\sigma$ can be absorbed in the potential U. The QM model is treated very frequently in an FRG approach [50, 290, 340].

B.6.2. Maris–Tandy Model

Many of the successes and results of the rainbow–ladder truncation outlined in Section 3.5.1 were actually obtained using the *Maris–Tandy model* first proposed in [280]. Its parametrization

of the interaction strength α is based on both the well-known perturbative behaviour in the ultraviolet sector as well as phenomenologically required features in the infrared momentum region, such as a sufficient interaction-strength enhancement to trigger DCSB, and reads

$$\alpha(k^2) \coloneqq \pi \frac{\eta^7}{\Lambda^4} k^4 \exp\left(-\frac{\eta^2}{\Lambda^2} k^2\right) + \frac{2\pi\gamma_m \left(1 - \exp\left(k^2/\Lambda_t^2\right)\right)}{\ln\left(\mathrm{e}^2 - 1 + \left(1 + k^2/\Lambda_{\mathrm{QCD}}^2\right)^2\right)} \,. \tag{B.63}$$

Here, $\Lambda_{\mathrm{QCD}} = 0.234\,\mathrm{GeV}$ denotes the QCD scale for $N_f = 4$ quark flavours,[6] $N_c = 3$ is the number of colours, while $\gamma_m = 12/(11N_c - 2N_f)$ labels the anomalous dimension of the quark mass function. The model parameters – a dimensionless quantity $\eta = 1.8$, a UV parameter $\Lambda_t = 1\,\mathrm{GeV}$ and an infrared scale $\Lambda = 0.72\,\mathrm{GeV}$ – are fitted to comply with physical quantities such as the pion decay constant f_π and the pion mass m_π obtained by Bethe–Salpeter calculations for mesons. Sometimes, it is alternatively expressed in terms of the parameters $\omega = \Lambda/\eta$ and $D = \eta\Lambda^2$ [207].

When applied to systems at nonzero temperature, the gluon's splitting into transverse and longitudinal parts may be accounted for by introducing corresponding *screening masses*, $m_{\mathrm{th}}^{T/L}$, that depend on T and μ [283]. An overview of different versions can be found in Ref. [84]. For instance, the screening masses are parametrized in accordance with leading-order hard-thermal-loop perturbation theory [378]. As a consequence, the split interaction-strength functions may be defined as

$$\alpha_{T/L}(k^2) \coloneqq \alpha\left(k^2 + \left(m_{\mathrm{th}}^{T/L}\right)^2\right), \quad \left(m_{\mathrm{th}}^{T}\right)^2 = 0\,, \quad \left(m_{\mathrm{th}}^{L}\right)^2 = \frac{16}{5}\left(T^2 + \frac{6}{5\pi^2}\mu^2\right). \tag{B.64}$$

B.7. Functional Renormalization Group

Finally, we elucidate some details about the third non-perturbative (and second functional) method that has often been referenced throughout this thesis, namely the *functional renormalization group* (FRG). It is an implementation of the renormalization-group approach of Kenneth Wilson [379, 380] into the functional framework of quantum field theory, i.e., the path integral, introduced by Christof Wetterich [381]. In the following, we only give a very brief introduction and overview. For more a extensive treatment, we refer, e.g., to the reviews in Refs. [364, 382, 383].

The general idea behind the FRG is to include a momentum (or RG) scale k into the effective action Γ that enables to interpolate smoothly between the microscopic physical laws at high k and the macroscopic long-range effects at low k. Quite pictorially, the RG scale can be thought of as somewhat analogous to the resolution of a microscope: At a high resolution (large k), we get a precise view of a very limited region – the microscopic laws – while at decreasing resolution the view becomes more coarse grained but extends to more space [384].

Usually, one starts at some cutoff scale $k = \Lambda$ where the underlying physics is known, which often corresponds to a UV fixed point. Then, one lowers k to include quantum fluctuations between Λ and the current scale, $0 \lesssim k \lesssim \Lambda$, such that all fluctuations are included at $k \to 0$

[6] Since different quark flavours do not backcouple onto each other in the Maris–Tandy model, N_f is a model parameter to comply with Λ_{QCD} and does not reflect the actual number of considered quark flavours.

where one recovers the full macroscopic physics. In a QFT framework, we start at the known classical action $\mathcal{S} = \Gamma_{k\to\Lambda}$ and successively integrate out quantum fluctuations at certain momenta $q^2 \gtrsim k^2$ until we arrive at the full 1PI effective action $\Gamma = \Gamma_{k\to 0}$.

To include a scale dependence into the generating functional, one adds a scale-dependent regulator term $\Delta\mathcal{S}_k$ to the classical action, $\mathcal{S} \to \mathcal{S}_k = \mathcal{S} + \Delta\mathcal{S}_k$. The regulator term is chosen to be a quadratic functional of the fields φ, i.e., a mass-like term, with some regulator (or cutoff) function R_k:

$$\Delta\mathcal{S}_k[\varphi] \sim \langle \varphi R_k \varphi \rangle \,. \tag{B.65}$$

This function R_k can in general be chosen rather freely as long as it obeys certain restrictions to effectively regulate the theory. First, the full, unregulated theory shall be recovered for all momenta in the limit $k \to 0$, i.e., ΔS_k must vanish. Second, the theory shall be regularized in the IR. This is the case if $R_k(q)$ stays positive for small q^2 (compared to k^2). Third, one wants to ensure that the effective action becomes the classical action at the UV cutoff, i.e., $\Gamma_{k\to\Lambda} = \mathcal{S}$. In total, this is the case if

$$\lim_{k\to 0} R_k(q) = 0\,, \quad \lim_{q\to 0} R_k(q) > 0\,, \quad \lim_{k\to\Lambda} R_k(q) \to \infty\,. \tag{B.66}$$

Using these conditions, one can derive an exact renormalization-group flow equation for the (scale-dependent) effective action Γ_k without any approximations, also known as the *Wetterich equation* [381]:

$$\partial_k \Gamma_k[\Phi] = \mathrm{STr}\Big(\partial_k R_k[\Phi] \cdot \big(\Gamma_k^{(2)}[\Phi] + R_k[\Phi]\big)^{-1}\Big)\,. \tag{B.67}$$

The occurring *super trace* (STr) incorporates the summation over all inner indices and integration over all momenta in both all bosonic and fermionic degrees of freedom while providing a negative sign in the purely fermionic parts.

Even though it is based on entirely different principles, the FRG has several similarities with DSEs. That is, Equation (B.67) contains both Γ and its second functional derivative $\Gamma^{(2)}$ so it implies an infinite tower of equations and thus necessitates truncations as well. Also, these can be solved analytically without truncations in the deep infrared [225, 226, 382]. In other respects, it has both advantages and disadvantages over DSEs. On the one hand, the FRG works directly with Γ which makes the grand potential immediately accessible. Moreover, the regulator (by construction) renders all occuring integrals finite. On the other hand, as can be seen in Equation (B.67), each n-point function implies at least also dressed $n+2$-point functions which is not the case for DSEs. In addition, the Wetterich equation is a differential equation with respect to the RG scale k but also contains integrals over momentum space. DSEs, in turn, are integral equations only.

Appendix C
Projected DSEs

In this appendix, we specify the *projected DSEs* that are actually used in our calculations, i.e., the DSEs for the scalar dressing functions. They can be obtained straightforwardly by projecting the propagator DSEs onto their respective tensor structures. We will derive and discuss the projected DSEs for both quark and unquenched gluon propagator by reference to the truncations and models introduced in Section 3.5.

Up front, we clarify some notational details that will enable us to describe all of these truncations in a unified framework. First, inspired by the rainbow–ladder truncation, we always combine both the coupling constant and the dressing functions of gluon and vertex into a scalar interaction-strength function α which depends solely on the gluon momentum k. In vacuum, it is defined by the relation

$$\frac{1}{\tilde{Z}_3}\frac{g^2}{4\pi}D_{\nu\rho}(k)\Gamma^{\rho}(p,q,k) =: P^{\mathcal{T}}_{\nu\rho}\frac{\alpha(k)}{k^2}\Gamma^{\rho}_{\mathrm{BC}}(p,q)\,, \tag{C.1}$$

where $\tilde{Z}_3$ denotes the ghost renormalization constant, g is the coupling constant, $D_{\nu\rho}$ names the dressed gluon propagator, Γ^{ρ} the dressed quark–gluon vertex and $P^{\mathcal{T}}_{\nu\rho}$ labels the transversal projector since we are working in Landau gauge exclusively.

In medium, we have to account for the gluon's splitting into parts transversal and longitudinal to the heat bath. As a consequence, the interaction-strength function also splits into such parts, α_T and α_L, which are defined analogously,

$$\frac{1}{\tilde{Z}_3}\frac{g^2}{4\pi}D_{\nu\rho}(k)\Gamma^{\rho}(p,q,k) =: \left(P^{T}_{\nu\rho}\frac{\alpha_T(k)}{k^2} + P^{L}_{\nu\rho}\frac{\alpha_L(k)}{k^2}\right)\Gamma^{\rho}_{\mathrm{BC}}(p,q)\,, \tag{C.2}$$

where $P^{T/L}_{\nu\rho}$ are the transversal and longitudinal three-dimensional projectors, respectively.

Second, we always employ the vertex decomposition of Equation (3.28), regardless of whether we actually use the Ball–Chiu vertex or not. In case of the rainbow–ladder truncation, we simply have to set $\Gamma_4(p,q) \equiv \Gamma_s(p,q) \equiv Z_2$. Here and above, we already inserted the renormalization constants. Throughout the derivations below, these will be initially set to 1 but inserted in the end according to Equations (2.14) and (2.15). For the sake of readability, we will also mostly spare the flavour indices f and assume them to be present implicitly if they are not.

C.1. Quark Propagator

C.1.1. Vacuum

We recall the parametrization of the inverse quark propagator in vacuum in terms of dressing functions in Equation (3.11). Utilizing well-known γ trace relations, one can easily derive

projections onto A and B from Equation (3.7) (with $\mathbb{1} = \mathbb{1}_D = \mathbb{1}_4$):

$$A(p) = 1 - \frac{\mathrm{tr}[\mathrm{i}\not{p}\Sigma(p)]}{p^2\,\mathrm{tr}[\mathbb{1}]}\,, \quad B(p) = m_0 + \frac{\mathrm{tr}[\Sigma(p)]}{\mathrm{tr}[\mathbb{1}]}\,. \tag{C.3}$$

The quark self-energy in vacuum after inserting the dressing functions reads

$$\Sigma(p) = 4\pi C_F \sum\!\!\!\!\!\!\int_q \gamma^\nu \frac{-\mathrm{i}\not{q}A(q) + B(q)}{q^2A^2(q) + B^2(q)} P_{\nu\rho}(k)\gamma^\rho \frac{\alpha(k)}{k^2}\Gamma_s(p,q)\,. \tag{C.4}$$

Evaluating the traces and inserting the renormalization constants then yields the projected quark DSEs in vacuum:

$$A(p) = Z_2 + \frac{Z_2 4\pi C_F}{p^2} \sum\!\!\!\!\!\!\int_q \frac{A(q)}{q^2A^2(q) + B^2(q)} \left(p\cdot q + 2\frac{(p\cdot k)(q\cdot k)}{k^2}\right) \frac{\alpha(k)}{k^2}\Gamma_s(p,q)\,, \tag{C.5}$$

$$B(p) = Z_2 Z_m m_0 + Z_2 4\pi C_F \sum\!\!\!\!\!\!\int_q \frac{3B(q)}{q^2A^2(q) + B^2(q)} \frac{\alpha(k)}{k^2}\Gamma_s(p,q)\,. \tag{C.6}$$

C.1.2. Medium

Apart from dealing with one more dressing function and slightly different Dirac structures, the modus operandi in medium is completely analogous to the one in vacuum. That is, we take the nonzero-temperature representation of the quark propagator in Equation (3.15) and project out each of the three dressing functions with the aid of traces,

$$A(p) = 1 - \frac{\mathrm{tr}[\mathrm{i}\boldsymbol{\gamma}\cdot\boldsymbol{p}\Sigma(p)]}{\boldsymbol{p}^2\,\mathrm{tr}[\mathbb{1}]}\,, \quad B(p) = m_0 + \frac{\mathrm{tr}[\Sigma(p)]}{\mathrm{tr}[\mathbb{1}]}\,, \quad C(p) = 1 - \frac{\mathrm{tr}[\mathrm{i}\gamma_4\Sigma(p)]}{p_4\,\mathrm{tr}[\mathbb{1}]}\,. \tag{C.7}$$

After applying these once more to Equation (3.8), evaluating the traces and inserting the renormalization constants, we end up with the following projected DSEs for the quark dressing functions at nonzero temperature (where now $\Gamma_s = \Gamma_s(p,q)$ and $\Gamma_4 = \Gamma_4(p,q)$):

$$A(p_4,\boldsymbol{p}) = Z_2 + Z_2\frac{4\pi C_F}{\boldsymbol{p}^2} \sum\!\!\!\!\!\!\int_q \frac{A(q_4,\boldsymbol{q})(\Gamma_s K_{AAs} + \Gamma_4 K_{AA4}) + q_4 C(q_4,\boldsymbol{q})(\Gamma_s+\Gamma_4)K_{AC}}{q_4^2C^2(q_4,\boldsymbol{q}) + \boldsymbol{q}^2A^2(q_4,\boldsymbol{q}) + B^2(q_4,\boldsymbol{q})}\,, \tag{C.8}$$

$$B(p_4,\boldsymbol{p}) = Z_2 Z_m m_0 + Z_2 4\pi C_F \sum\!\!\!\!\!\!\int_q \frac{B(q_4,\boldsymbol{q})(\Gamma_s K_{BBs} + \Gamma_4 K_{BB4})}{q_4^2C^2(q_4,\boldsymbol{q}) + \boldsymbol{q}^2A^2(q_4,\boldsymbol{q}) + B^2(q_4,\boldsymbol{q})}\,, \tag{C.9}$$

$$C(p_4,\boldsymbol{p}) = Z_2 + Z_2\frac{4\pi C_F}{p_4} \sum\!\!\!\!\!\!\int_q \frac{A(q_4,\boldsymbol{q})(\Gamma_s+\Gamma_4)K_{CA} + q_4 C(q_4,\boldsymbol{q})(\Gamma_s K_{CCs} + \Gamma_4 K_{CC4})}{q_4^2C^2(q_4,\boldsymbol{q}) + \boldsymbol{q}^2A^2(q_4,\boldsymbol{q}) + B^2(q_4,\boldsymbol{q})}\,. \tag{C.10}$$

Here, we used the shorthand notation $K_{xyz} = K_{xyz}(p,q)$ for the integral kernels:

$$K_{AAs} = (\boldsymbol{p}\cdot\boldsymbol{q})\frac{k_4^2}{k^2}\frac{\alpha_L}{k^2} + 2\left(\frac{\alpha_T}{k^2} - \frac{k_4^2}{k^2}\frac{\alpha_L}{k^2}\right)\frac{(\boldsymbol{p}\cdot\boldsymbol{k})(\boldsymbol{q}\cdot\boldsymbol{k})}{\boldsymbol{k}^2}\,, \quad K_{AA4} = (\boldsymbol{p}\cdot\boldsymbol{q})\frac{k_4^2}{k^2}\frac{\alpha_L}{k^2}\,, \tag{C.11}$$

$$K_{AC} = (\boldsymbol{p}\cdot\boldsymbol{k})\frac{k_4}{k^2}\frac{\alpha_L}{k^2}\,, \quad K_{BBs} = 2\frac{\alpha_T}{k^2} + \frac{k_4^2}{k^2}\frac{\alpha_L}{k^2}\,, \quad K_{BB4} = \frac{\boldsymbol{k}^2}{k^2}\frac{\alpha_L}{k^2}\,, \tag{C.12}$$

$$K_{CA} = (\boldsymbol{q}\cdot\boldsymbol{k})\frac{k_4}{k^2}\frac{\alpha_L}{k^2}\,, \quad K_{CCs} = 2\frac{\alpha_T}{k^2} + \frac{k_4^2}{k^2}\frac{\alpha_L}{k^2} = K_{BBs}\,, \quad K_{CC4} = -\frac{\boldsymbol{k}^2}{k^2}\frac{\alpha_L}{k^2} = -K_{BB4}\,. \tag{C.13}$$

By contrast, the introduction of a quark chemical potential is quite trivial. As explained in Appendix B.1.2, a finite chemical potential leads to an imaginary shift in p_4 and thus also in q_4. Therefore, we merely have to replace

$$p_4 \to \tilde{p}_4 \coloneqq p_4 + \mathrm{i}\mu\,, \quad q_4 \to \tilde{q}_4 \coloneqq q_4 + \mathrm{i}\mu \tag{C.14}$$

in the projected quark DSEs.

C.1.3. Regularization and Renormalization

We always use a Pauli–Villars regulator for the quark self-energy as introduced in Section 2.1.1, except for finite-volume calculations on a pure torus (see below). This is due to the fact that PV regularization ensures the correct UV behaviour of the imaginary part of the C dressing function, which is vital for quark-number densities.

For renormalization, we employ a momentum-subtraction scheme in vacuum, i.e., we subtract the quadratically divergent contribution of the quark self-energy at some renormalization point ζ deep in the perturbative regime in the UV:

$$\Sigma(p) \to \Sigma^{\mathrm{ren}}(p) = \Sigma(p) - \Sigma(\zeta)\,. \tag{C.15}$$

Equivalently, we demand that the inverse dressed and bare quark propagators have to be equal at $p^2 = \zeta^2$, which yields the following conditions in terms of the dressing functions:

$$A_f(\zeta) \stackrel{!}{=} 1\,, \quad B_f(\zeta) \stackrel{!}{=} m_f\,. \tag{C.16}$$

From these, we can derive prescriptions how to calculate the renormalization constants:

$$Z_2^f = \left(1 + \Sigma_A^f(\zeta)\right)^{-1}, \quad Z_2^m = \left(Z_2^f\right)^{-1} - \Sigma_B^f(\zeta)/m_f\,. \tag{C.17}$$

In fact, the mass renormalization constant Z_m^f is largely independent of m_f, so we use a single Z_m for all quark flavours and calculate it with the aid of an auxiliary "heavy" quark whose mass reads $m_{\mathrm{h}} = 1\,\mathrm{GeV}$. This is especially important for the chiral limit $m_f \to 0$ where Z_m is needed for the calculation of the renormalized quark condensate but where it cannot be determined from Equation (C.17).

For the quarks, we always choose a renormalization point of $\zeta_Q = 80\,\mathrm{GeV}$ which is far larger than all other scales in the system. As a consequence, medium effects have a negligible influence at ζ_Q. Since the medium introduces no further divergences [385], we therefore fix the renormalization constants in vacuum and leave them unchanged for the calculations at nonzero temperature and chemical potential.

Pure Torus

As outlined in Section 4.1.4, calculations on a pure torus are restricted to quite small momentum cutoffs, $\Lambda = 10\,\mathrm{GeV}$. As a consequence, we have to choose a renormalization point smaller than that: $\zeta_{\mathrm{PT}} = 8\,\mathrm{GeV}$. This is so small, in fact, that we are not deep enough in the perturbative region to neglect any dynamical effects. As a consequence, we have to adjust our renormalization scheme based on observations of our pure-torus setup.

First, we demand that our quark propagator for $L = 8\,\mathrm{fm}$ be identical to the infinite-volume one. This is due to the fact that the behaviour within finite-volume calculations is consistent, so we want to fix the "almost" infinite-volume $L = 8\,\mathrm{fm}$ to the properly renormalized $L \to \infty$ result. Second, because of the different torus dimensionality, the limit $T \to 0$ is also not perfectly realized, so we now renormalize in medium at a temperature that is "almost" vacuum, i.e., $T = 50\,\mathrm{MeV}$. In total, our renormalization conditions on a pure torus read

$$A_f^{L=8\,\mathrm{fm}}(\omega_0^T, \zeta) \stackrel{!}{=} A_f^{L\to\infty}(\omega_0^T, \zeta)\Big|_{T=50\,\mathrm{MeV}}, \quad B_f^{L=8\,\mathrm{fm}}(\omega_0^T, \zeta) \stackrel{!}{=} B_f^{L\to\infty}(\omega_0^T, \zeta)\Big|_{T=50\,\mathrm{MeV}}. \tag{C.18}$$

C.1.4. Quark Condensate and Quark-Number Density

The traces in Equations (3.6) and (4.22) can be carried out straightforwardly and yield (with again $\mu_f \in \mu$)

$$\langle\overline{\psi}\psi\rangle_f(T,\mu) = -N_c Z_2^f Z_m^f \sum\!\!\!\!\!\!\int_q \frac{4B_f(q_4,\boldsymbol{q})}{(q_4+\mathrm{i}\mu_f)^2 C_f^2(q_4,\boldsymbol{q}) + \boldsymbol{q}^2 A_f^2(q_4,\boldsymbol{q}) + B_f^2(q_4,\boldsymbol{q})}, \tag{C.19}$$

$$n_f(T,\mu) = N_c Z_2^f \sum\!\!\!\!\!\!\int_q \frac{4\mathrm{i}(q_4+\mathrm{i}\mu_f) C_f(q_4,\boldsymbol{q})}{(q_4+\mathrm{i}\mu_f)^2 C_f^2(q_4,\boldsymbol{q}) + \boldsymbol{q}^2 A_f^2(q_4,\boldsymbol{q}) + B_f^2(q_4,\boldsymbol{q})}. \tag{C.20}$$

C.2. Unquenched Gluon Propagator

C.2.1. Projections in Vacuum and in Medium

In vacuum, the Landau-gauge gluon propagator and its inverse are parametrized as follows:

$$D_{\nu\rho}(k) = P^{\mathcal{T}}_{\nu\rho}\frac{Z(k^2)}{k^2}, \quad D^{-1}_{\nu\rho}(k) = P^{\mathcal{T}}_{\nu\rho}\frac{k^2}{Z(k^2)}. \tag{C.21}$$

Here and in the following, we always assume the quenched gluon propagator to be of the same form as the full one, except that the full gluon dressing function Z is replaced by the quenched one Z_{que}. In order to now project out the gluon dressing function, we have to insert Equation (3.18) and contract with $P^{\mathcal{T}}_{\nu\rho}$:

$$\big(Z(k)\big)^{-1} = \big(Z_{\mathrm{que}}(k)\big)^{-1} + \frac{P^{\mathcal{T}}_{\nu\rho}\Pi^{\nu\rho}}{\mathrm{tr}\big[P^{\mathcal{T}}_{\nu\rho}\big]k^2}. \tag{C.22}$$

In medium, due to the gluon propagator splitting into parts transversal and longitudinal to the heat bath, the parametrizations change to

$$D_{\nu\rho}(k) = P^T_{\nu\rho}\frac{Z^T(k)}{k^2} + P^L_{\nu\rho}\frac{Z^L(k)}{k^2}, \quad D^{-1}_{\nu\rho}(k) = P^T_{\nu\rho}\frac{k^2}{Z^T(k)} + P^L_{\nu\rho}\frac{k^2}{Z^L(k)}. \tag{C.23}$$

With a completely analogous rationale as in vacuum, this implies the following projected DSEs for the transversal and longitudinal dressing functions:

$$\big(Z^{T/L}(k)\big)^{-1} = \big(Z^{T/L}_{\mathrm{que}}(k)\big)^{-1} + \frac{P^{T/L}_{\nu\rho}\Pi^{\nu\rho}}{\mathrm{tr}\big[P^{T/L}_{\nu\rho}\big]k^2}. \tag{C.24}$$

C.2.2. Regularization and Renormalization

Before we proceed with the actual expressions, we need to regularize and renormalize the quark loop. To this end, we first provide the full gluon DSE in an abbreviated form:

$$D^{-1}_{\nu\rho}(k) = Z_3 \cdot \left(D^0_{\nu\rho}(k)\right)^{-1} + \Pi^{\mathrm{YM}}_{\nu\rho}(k) + \Pi_{\nu\rho}(k)\,. \tag{C.25}$$

In addition to the quark loop $\Pi_{\nu\rho}(k)$, both the bare gluon propagator $D^0_{\nu\rho}(k)$ (obtained by setting $Z(k) = 1$) as well as the pure-Yang–Mills self-energy $\Pi^{\mathrm{YM}}_{\nu\rho}(k)$ appear, i.e., all loop diagrams without quarks. In spite of being formulated in Landau gauge, the quark loop not only contains a transversal but also a longitudinal component, both of which have the same quadratic divergence. Since the gluon propagator must be transversal, the longitudinal contributions from $\Pi_{\nu\rho}$ and $\Pi^{\mathrm{YM}}_{\nu\rho}$ have to cancel. In our truncation, however, $\Pi^{\mathrm{YM}}_{\nu\rho}$ is absorbed in the lattice fit, so we need to remove the longitudinal component of the quark loop by hand. To this end, we regularize the transversal component of the quark loop by subtracting the longitudinal one:

$$\Pi^{\mathrm{reg}}_{\mathcal{T}} = \Pi_{\mathcal{T}} - \Pi_{\mathcal{L}}\,. \tag{C.26}$$

We can get access to these components with simple projections:

$$\Pi_{\mathcal{T}} = \mathrm{tr}\left[P^{\mathcal{T}}_{\nu\rho}\right]^{-1} \cdot P^{\mathcal{T}}_{\nu\rho}\Pi^{\nu\rho} = \frac{1}{3}P^{\mathcal{T}}_{\nu\rho}\Pi^{\nu\rho}\,, \quad \Pi_{\mathcal{L}} = \mathrm{tr}\left[P^{\mathcal{L}}_{\nu\rho}\right]^{-1} \cdot P^{\mathcal{L}}_{\nu\rho}\Pi^{\nu\rho} = P^{\mathcal{L}}_{\nu\rho}\Pi^{\nu\rho}\,, \tag{C.27}$$

with $P^{\mathcal{T}}_{\nu\rho}$ and $P^{\mathcal{L}}_{\nu\rho}$ being again the four-dimensional longitudinal and transversal projectors, respectively. At the same time, we also find that

$$3\Pi^{\mathrm{reg}}_{\mathcal{T}} = \left(P^{\mathcal{T}}_{\lambda\sigma} - 3P^{\mathcal{L}}_{\lambda\sigma}\right)\Pi^{\lambda\sigma} = \left(P^{\mathcal{T}}_{\lambda\sigma} - \delta^{\nu\rho}P^{\mathcal{T}}_{\nu\rho}P^{\mathcal{L}}_{\lambda\sigma}\right)\Pi^{\lambda\sigma} = P^{\mathcal{T}}_{\nu\rho}\left(\delta^{\nu}{}_{\lambda}\delta^{\rho}{}_{\sigma} - \delta^{\nu\rho}P^{\mathcal{L}}_{\lambda\sigma}\right)\Pi^{\lambda\sigma} \tag{C.28}$$

$$= P^{\mathcal{T}}_{\nu\rho}\left(\Pi^{\nu\rho} - \delta^{\nu\rho}\Pi_{\mathcal{L}}\right) =: P^{\mathcal{T}}_{\nu\rho}\Pi^{\nu\rho}_{\mathrm{reg}}\,, \tag{C.29}$$

where we define the regularized quark loop:

$$\Pi^{\mathrm{reg}}_{\nu\rho} = \Pi_{\nu\rho} - \delta_{\nu\rho}\Pi_{\mathcal{L}}\,. \tag{C.30}$$

By construction, this regularized quark loop is transversal and does not exhibit any quadratic divergences [222]. Alternatively, we can introduce the *Brown–Pennington projector* $P^{\mathrm{BP}}_{\nu\rho}$ to find

$$P^{\mathcal{T}}_{\nu\rho}\Pi^{\nu\rho}_{\mathrm{reg}} = P^{\mathrm{BP}}_{\nu\rho}\Pi^{\nu\rho}\,, \quad P^{\mathrm{BP}}_{\nu\rho} \coloneqq \delta_{\nu\rho} - 4\frac{k_\nu k_\rho}{k^2} = P^{\mathcal{T}}_{\nu\rho} - 3P^{\mathcal{L}}_{\nu\rho}\,. \tag{C.31}$$

In order to remove the remaining logarithmic divergence and as a renormalization condition, we employ a momentum-subtraction scheme analogous to the quark:

$$\Pi^{\mathrm{ren}}_{\nu\rho}(k) \coloneqq \Pi^{\mathrm{reg}}_{\nu\rho}(k) - \Pi^{\mathrm{reg}}_{\nu\rho}(\zeta)\,. \tag{C.32}$$

As a means of simplification, we again assume medium effects on $\Pi_{\nu\rho}(\zeta)$ to be negligible. Thus, we always approximate $\Pi_{\nu\rho}(\zeta)$ by the vacuum quark loop $\Pi^{\mathrm{vac}}_{\nu\rho}(\zeta)$ which is the same for the transversal and longitudinal parts of the gluon propagator. In vacuum, the renormalized gluon DSE reads

$$Z^{-1}(k) = Z^{-1}_{\mathrm{que}}(k) - \frac{P^{\mathcal{T}}_{\nu\rho}\Pi^{\nu\rho}_{\mathrm{ren}}(k)}{\mathrm{tr}\left[P^{\mathcal{T}}_{\nu\rho}\right]k^2}\,. \tag{C.33}$$

In contrast to the quark DSE, we do not need to fix the gluon renormalization constant Z_3. This is due to the fact that the momentum subtraction of Equation (C.32) removes it from Equation (C.25). In turn, the renormalization of the pure-Yang–Mills part is implicitly taken care of by the parametrization of the quenched gluon dressing function. For this reason, we also inherit the renormalization point of $\zeta_G = 10\,\mathrm{GeV}$ from the lattice calculations.

Pure Torus

Renormalization of the gluon DSE on a pure torus is performed absolutely analogous to the quark DSE. That is, we demand

$$Z_T^{L=8\,\mathrm{fm}}(\zeta) \stackrel{!}{=} Z_T^{L\to\infty}(\zeta)\Big|_{T=50\,\mathrm{MeV}}, \quad Z_L^{L=8\,\mathrm{fm}}(\zeta) \stackrel{!}{=} Z_L^{L\to\infty}(\zeta)\Big|_{T=50\,\mathrm{MeV}}, \tag{C.34}$$

for a renormalization point of $\zeta_{\mathrm{PT}} = 8\,\mathrm{GeV}$.

C.2.3. Projected Equations

Before showing the projected gluon DSEs, we make some remarks. First, due to approximate restoration of O(4) symmetry of the gluon dressing function already at the zeroth Matsubara frequency, we perform the following simplification:

$$Z_{T/L}\big(k_4, \boldsymbol{k}^2\big) = Z_{T/L}\big(0, k_4^2 + \boldsymbol{k}^2\big) =: Z_{T/L}\big(k^2\big)\,, \tag{C.35}$$

which implicitly sets $k_4 = 0$ and $\boldsymbol{k}^2 = k^2$ inside the quark loop. In order to preserve multiplicative renormalizability, the argument for the vertex model function Γ is $p^2 + q^2$. Since we assume $\Gamma(x)$ to be independent of temperature and chemical potential [78], the momentum argument inside the quark loop is given by $x = p_4^2 + \boldsymbol{p}^2 + q_4^2 + \boldsymbol{q}^2$ even at nonzero chemical potential. This way, $\Gamma(x)$ also always stays real. Thus, the Ball–Chiu vertex actually reads

$$\frac{1}{\tilde{Z}_3}\Gamma_f^\nu(\tilde{p}, \tilde{q}) = \Gamma\left(p_4^2 + \boldsymbol{p}^2 + q_4^2 + \boldsymbol{q}^2\right) \cdot \Gamma_{\mathrm{BC}}^\nu(\tilde{p}, \tilde{q})\,, \tag{C.36}$$

where again $\tilde{p} = (p_4 + \mathrm{i}\mu, \boldsymbol{p})$ and $\tilde{q} = (q_4 + \mathrm{i}\mu, \boldsymbol{q})$.

Now, one only needs to calculate the aforementioned traces. Doing so and bringing the resulting gluon DSEs into a more convenient and consistent form, we end up with the following equations. Starting with the vacuum case, we obtain

$$Z^{-1}(k) = Z_{\mathrm{que}}^{-1}(k) - \frac{8\pi\alpha}{3k^2}\sum\!\!\!\!\!\!\int_q \frac{K_Z(k,q)}{q^2A^2(q) + B^2(q)}\,, \tag{C.37}$$

where the kernel K_Z containing all angular dependences reads

$$K_Z(k,q) \coloneqq 2\left(p\cdot q - 4\frac{(p\cdot k)(q\cdot k)}{k^2}\right)\frac{A(p)A(q)}{p^2A^2(p) + B^2(p)}\Gamma_s(p,q)\Gamma\big(p^2 + q^2\big)\,. \tag{C.38}$$

In medium, we obtain the transversal dressing function

$$\big(Z^T(k)\big)^{-1} = \big(Z_{\mathrm{que}}^T(k)\big)^{-1} - \frac{8\pi\alpha}{2k^2}\sum\!\!\!\!\!\!\int_q \frac{K_{ZT}(k,q)}{q_4^2C^2(q) + \boldsymbol{q}^2A^2(q) + B^2(q)}\,, \tag{C.39}$$

with the kernel:

$$K_{ZT}(k,q) \coloneqq 2\left(\boldsymbol{p}\cdot\boldsymbol{q} - 3\frac{(\boldsymbol{k}\cdot\boldsymbol{p})(\boldsymbol{k}\cdot\boldsymbol{q})}{\boldsymbol{k}^2}\right)\frac{A(p)A(q)}{p_4^2C^2(p)+\boldsymbol{p}^2A^2(p)+B^2(p)}\Gamma_s(p,q)\Gamma\left(p^2+q^2\right). \tag{C.40}$$

The transversal dressing function reads

$$\left(Z^L(k)\right)^{-1} = \left(Z^L_{\text{que}}(k)\right)^{-1} - \frac{8\pi\alpha}{k^2}\sum\!\!\!\!\!\!\int_q \frac{K_{ZL}(k,q)}{q_4^2C^2(q)+\boldsymbol{q}^2A^2(q)+B^2(q)}, \tag{C.41}$$

where

$$\begin{aligned} K_{ZL}(k,q) \coloneqq \Big[&\left(p_4q_4C(p)C(q) - \boldsymbol{p}\cdot\boldsymbol{q}A(p)A(q) - B(p)B(q)\right)\Gamma_4(p,q) + \\ &+\left(p_4q_4C(p)C(q) + \left(\boldsymbol{p}\cdot\boldsymbol{q} - 2\frac{(\boldsymbol{k}\cdot\boldsymbol{p})(\boldsymbol{k}\cdot\boldsymbol{q})}{\boldsymbol{k}^2}\right)A(p)A(q) + B(p)B(q)\right)\Gamma_s(p,q)\Big]\times \\ &\times\frac{\Gamma\left(p^2+q^2\right)}{p_4^2C^2(p)+\boldsymbol{p}^2A^2(p)+B^2(p)}. \end{aligned} \tag{C.42}$$

C.2.4. Screening Mass

Looking at the kernels of the quark loop, we notice that they do not vanish in the limit $k \to 0$. While this problem is resolved by the angular integration over z both for the vacuum and transversal finite-temperature kernel,

$$\lim_{k\to 0}\int_{-1}^{1}\mathrm{d}z\; K_Z(k,q) = 0 = \lim_{k\to 0}\int_{-1}^{1}\mathrm{d}z\; K_{ZT}(k,q), \tag{C.43}$$

the longitudinal kernel stays nonzero in the deep infrared:

$$\begin{aligned} \lim_{k\to 0}K_{ZL}(k,q) = \Big[&q_4^2C^2(q)\left(\Gamma_s(q,q)+\Gamma_4(q,q)\right) + \boldsymbol{q}^2A^2(q)\left((2z^2-1)\Gamma_s(q,q) - \Gamma_4(q,q)\right) + \\ &+B^2(q)\left(\Gamma_s(q,q)-\Gamma_4(q,q)\right)\Big]\frac{\Gamma\left(2q^2\right)}{q_4^2C^2(q)+\boldsymbol{q}^2A^2(q)+B^2(q)}. \end{aligned} \tag{C.44}$$

This implies that the IR behaviour of the longitudinal quark loop can be parametrized as

$$\frac{\Pi^L_{\mu\nu}(k)}{k^2} \simeq \frac{2m_L^2}{k^2}. \tag{C.45}$$

Consequently, the longitudinal part of the gluon develops an effective mass at nonzero temperature, the longitudinal (or magnetic) *screening mass* m_L, which has to be taken care of in the numerical treatment (see Appendix D.1.4).

C.3. Colour Space of Quark Self-Energy and Quark Loop

Below, we calculate the colour prefactors of the (non-hadronic) quark self-energy and the quark loop. In advance, we briefly revise the colour-space structure of quark propagator, gluon propagator and quark–gluon vertex. In the following, let $a, b \in (3)$ and $i, j, l, o \in (\overline{8})$ be colour indices, where (3) denotes the three-dimensional representation of the SU(3) and $(\overline{8})$ labels the eight-dimensional adjoint representation. Moreover, let ν and ρ be Lorentz indices of the gauge boson. All other indices (e.g., Dirac, flavour, etc.) will be spared. Then, one obtains

$$S_{ij} \sim \delta_{ij}\,, \quad D^{\nu\rho}_{ab} \sim \delta_{ab}\,, \quad \left(\Gamma^a_\nu\right)_{ij} \sim \left(t^a\right)_{ij}\,. \tag{C.46}$$

Now, we apply these identities to the colour indices of the quark self-energy in Equation (3.8) and the quark loop in Equation (3.19). Since we are interested in colour space only, we solely consider the relevant tensor structures and their indices while neglecting everything else. For the quark self-energy, we can find

$$\Sigma^{ij} \sim (t^a)^{il}\delta_{lo}(t^b)^{oj}\delta_{ab} = (t^a)^{il}(t_a)_l{}^j = (t^a t_a)^{ij} = \delta^{ij}\cdot C_F\,, \tag{C.47}$$

which indeed yields a colour factor of $C_F = 4/3$ for $N_c = 3$ (see Appendix A.4). Analogously, the quark loop evaluates to

$$\Pi^{ab}_{\mu\nu} \sim (t^a)^{il}\delta_{lo}(t^b)^{oj}\delta_{ij} = (t^a)^{il}(t^b)_{li} = \mathrm{tr}[t^a t^b] = \delta^{ab}/2\,, \tag{C.48}$$

which corresponds to a prefactor of $1/2$.

C.4. Meson-Backcoupling Self-Energies

In this last section, we elucidate several aspects of the meson-backcoupling diagrams in the quark self-energy. First, we provide explicit expressions for the backcoupling diagrams inside the quark self-energy. Second, we briefly justify the non-trivial sign of the two-loop diagram. Third, we derive their multiplicities from flavour traces. Fourth, we specify how the meson decay constants are precisely calculated.

C.4.1. Projected Quark Self-Energies

Projecting onto the contributions for the different dressing functions, i.e., employing Equations (6.3) and (C.7), yields the following expressions for the meson-backoupling diagrams in the quark self-energy:

$$\Sigma_f^{\mathrm{M},A}(p_4,\boldsymbol{p}) = \frac{T}{\boldsymbol{p}^2}\sum_X F_X^f \frac{B_f^r(p_4,\boldsymbol{p})}{\left(f_X^s\right)^2}\int\frac{\mathrm{d}^3q}{(2\pi)^3}\frac{A_X^f(p_4,\boldsymbol{q})\,K_X^A(p,q)\,B_f^r(p_4,\boldsymbol{q})}{p_4^2\left(C_X^f\right)^2(p_4,\boldsymbol{q}) + \boldsymbol{q}^2\left(A_X^f\right)^2(p_4,\boldsymbol{q}) + \left(B_X^f\right)^2(p_4,\boldsymbol{q})}\,, \tag{C.49}$$

$$\Sigma_f^{\mathrm{M},B}(p_4,\boldsymbol{p}) = T\sum_X F_X^f \frac{B_f^r(p_4,\boldsymbol{p})}{\left(f_X^s\right)^2}\int\frac{\mathrm{d}^3q}{(2\pi)^3}\frac{B_X^f(p_4,\boldsymbol{q})\,K_X^B(p,q)\,B_f^r(p_4,\boldsymbol{q})}{p_4^2\left(C_X^f\right)^2(p_4,\boldsymbol{q}) + \boldsymbol{q}^2\left(A_X^f\right)^2(p_4,\boldsymbol{q}) + \left(B_X^f\right)^2(p_4,\boldsymbol{q})}\,, \tag{C.50}$$

$$\Sigma_f^{\mathrm{M},C}(p_4,\boldsymbol{p}) = \frac{T}{p_4}\sum_X F_X^f \frac{B_f^r(p_4,\boldsymbol{p})}{\left(f_X^s\right)^2}\int\frac{\mathrm{d}^3q}{(2\pi)^3}\frac{C_X^f(p_4,\boldsymbol{q})\,K_X^C(p,q)\,B_f^r(p_4,\boldsymbol{q})}{p_4^2\left(C_X^f\right)^2(p_4,\boldsymbol{q})+\boldsymbol{q}^2\left(A_X^f\right)^2(p_4,\boldsymbol{q})+\left(B_X^f\right)^2(p_4,\boldsymbol{q})}\,. \tag{C.51}$$

Here, K_X^A, K_X^B and K_X^C label the integral kernels encoding the angular dependence:

$$K_X^A(p,q) = \frac{\boldsymbol{p}\cdot\boldsymbol{q}}{\boldsymbol{k}^2+m_X^2}\,,\quad K_X^B(p,q) = \frac{(-1)^X}{\boldsymbol{k}^2+m_X^2}\,,\quad K_X^C(p,q) = \frac{p_4}{\boldsymbol{k}^2+m_X^2}\,. \tag{C.52}$$

Above, we did not employ the $\oint\!\!\!\!\!\!\sum$ notation from Appendix A.5 since the Matsubara sum is cancelled by setting $q_4 = p_4$. For finite-volume calculations, though, the three-dimensional spatial momentum integration has to be replaced as usual.

C.4.2. Non-Trivial Sign of the Two-Loop Diagram

From Figures 6.4 and 6.5, we find that the quantity $\tilde{\Gamma}_X^f(l,P)$ can be expressed as

$$\tilde{\Gamma}_X^f(l,P) \sim \oint\!\!\!\!\!\!\sum_q (\mathrm{i}g)^2\gamma_\nu D^{\nu\rho}(l-q)\gamma_\rho\, S_f(q_+)\,\hat{\Gamma}_X^f(q,P)\,S_X^f(q_-)\,, \tag{C.53}$$

where q_+ and q_- are internal momenta. It turns out that the signs are only relevant close to T_c, i.e., if the mass (and thus the scalar dressing) function of the external quark, B_f, is small. Therefore, we consider the limit $B_f \to 0$. In this case, we find

$$S_f(q_+)\gamma_X = (-1)^X\gamma_X S_f(q_+)\,, \tag{C.54}$$

where $(-1)^X = -1$ for the pseudoscalar mesons and $(-1)^X = +1$ for the scalar mesons. Next, we pull the matrix γ_X before the integral and (approximately) identify it with the homogeneous BSE. As a consequence, the integral becomes the "ordinary" BSA $\hat{\Gamma}_X^f(l,P)$ and we end up with

$$\tilde{\Gamma}_X^f(l,P) = (-1)^X\hat{\Gamma}_X^f(l,P)\,. \tag{C.55}$$

C.4.3. Flavour Traces

In order to properly calculate the flavour traces for our meson-backcoupling diagrams, we first define the following basis in flavour space:

$$\mathrm{u} = \hat{e}_1\,,\quad \mathrm{d} = \hat{e}_2\,,\quad \mathrm{s} = \hat{e}_3\,. \tag{C.56}$$

Next, we construct the flavour matrices of the Bethe–Salpeter amplitudes. To this end, we also need the following vectors:

$$\overline{\mathrm{u}} = \hat{e}_1^T\,,\quad \overline{\mathrm{d}} = \hat{e}_2^T\,,\quad \overline{\mathrm{s}} = \hat{e}_3^T\,. \tag{C.57}$$

Using these definitions, we can now build the flavour matrix τ_X of meson X from its quark content. Starting with the pseudoscalar octet and singlet, we obtain

$$\tau_{\pi^+} = \mathrm{u}\overline{\mathrm{d}}\,,\quad \tau_{\pi^-} = \mathrm{d}\overline{\mathrm{u}}\,,\quad \tau_{\pi^0} = \left(\mathrm{u}\overline{\mathrm{u}} - \mathrm{d}\overline{\mathrm{d}}\right)/\sqrt{2}\,, \tag{C.58}$$

$$\tau_{K^+} = \mathrm{u}\bar{\mathrm{s}}\,, \quad \tau_{K^0} = \mathrm{d}\bar{\mathrm{s}}\,, \quad \tau_{K^-} = \mathrm{s}\bar{\mathrm{u}}\,, \quad \tau_{\overline{K}^0} = \mathrm{s}\bar{\mathrm{d}}\,, \tag{C.59}$$

$$\tau_{\eta_8} = \left(\mathrm{u}\bar{\mathrm{u}} + \mathrm{d}\bar{\mathrm{d}} - 2\mathrm{s}\bar{\mathrm{s}}\right)/\sqrt{6}\,, \quad \tau_{\eta_0} = \left(\mathrm{u}\bar{\mathrm{u}} + \mathrm{d}\bar{\mathrm{d}} + \mathrm{s}\bar{\mathrm{s}}\right)/\sqrt{3}\,. \tag{C.60}$$

Additionally, we consider the following part of the scalar nonet:

$$\tau_{f_0(500)} = \tau_\sigma = \left(\mathrm{u}\bar{\mathrm{u}} + \mathrm{d}\bar{\mathrm{d}}\right)/\sqrt{2}\,, \quad \tau_{f_0(980)} = \mathrm{s}\bar{\mathrm{s}}\,. \tag{C.61}$$

As a consequence, we neglect both the $a_0(980)$ (the scalar partners of the pions) and the $\kappa(700)$ (the scalar partners of the kaons). To account for this, we modify the prefactor of the $f_0(980)$ and do not use its flavour trace in contrast to all other considered mesons (see below).

$N_f = 2 + 1$ Flavours:

First, we cover the case of $N_f = 2 + 1$ quark flavours, i.e., mass-degenerate up and down quarks and distinct strange quarks. To this end, we define the projectors onto the respective subspaces:

$$P_{\mathrm{ud}} \coloneqq \left(\begin{smallmatrix} 1 & 0 & 0 \\ 0 & 1 & 0 \\ 0 & 0 & 0 \end{smallmatrix}\right), \quad P_{\mathrm{s}} \coloneqq \left(\begin{smallmatrix} 0 & 0 & 0 \\ 0 & 0 & 0 \\ 0 & 0 & 1 \end{smallmatrix}\right). \tag{C.62}$$

Using these, the flavour degeneracy factors of the respective meson-backcoupling diagrams can be obtained in the following way. The flavour part of each diagram is given by

$$\Sigma_X^f = (\tau_X)^T P_f \tau_X\,. \tag{C.63}$$

Here, we expressed the flavour part of the meson propagator by the projector of the external quark f in order to eliminate vanishing diagrams. For instance, the σ meson does not couple to the strange quarks, hence one would have

$$\Sigma_\sigma^{\mathrm{s}} = (\tau_\sigma)^T P_{\mathrm{s}} \tau_\sigma = 0\,. \tag{C.64}$$

Since the meson-backcoupling diagrams in the quark self-energy must not change the flavour of the external quark, their flavour part in total has to be proportional to the associated projector. This way, we are able to read of the multiplicity of the diagram F_X^f as the proportionality factor:

$$\Sigma_X^f = F_X^f P_f\,. \tag{C.65}$$

Below, we only consider non-vanishing contributions. We start with the pions in the up-quark DSE:

$$\Sigma_{\pi^+}^{\mathrm{ud}} = (\tau_{\pi^+})^T P_{\mathrm{ud}} \tau_{\pi^+} = \left(\begin{smallmatrix} 0 & 0 & 0 \\ 1 & 0 & 0 \\ 0 & 0 & 0 \end{smallmatrix}\right)\left(\begin{smallmatrix} 1 & 0 & 0 \\ 0 & 1 & 0 \\ 0 & 0 & 0 \end{smallmatrix}\right)\left(\begin{smallmatrix} 0 & 1 & 0 \\ 0 & 0 & 0 \\ 0 & 0 & 0 \end{smallmatrix}\right) = \left(\begin{smallmatrix} 0 & 0 & 0 \\ 0 & 1 & 0 \\ 0 & 0 & 0 \end{smallmatrix}\right), \tag{C.66}$$

$$\Sigma_{\pi^-}^{\mathrm{ud}} = (\tau_{\pi^-})^T P_{\mathrm{ud}} \tau_{\pi^-} = \left(\begin{smallmatrix} 0 & 1 & 0 \\ 0 & 0 & 0 \\ 0 & 0 & 0 \end{smallmatrix}\right)\left(\begin{smallmatrix} 1 & 0 & 0 \\ 0 & 1 & 0 \\ 0 & 0 & 0 \end{smallmatrix}\right)\left(\begin{smallmatrix} 0 & 0 & 0 \\ 1 & 0 & 0 \\ 0 & 0 & 0 \end{smallmatrix}\right) = \left(\begin{smallmatrix} 1 & 0 & 0 \\ 0 & 0 & 0 \\ 0 & 0 & 0 \end{smallmatrix}\right), \tag{C.67}$$

$$\Sigma_{\pi^0}^{\mathrm{ud}} = (\tau_{\pi^0})^T P_{\mathrm{ud}} \tau_{\pi^0} = \frac{1}{2}\left(\begin{smallmatrix} 1 & 0 & 0 \\ 0 & -1 & 0 \\ 0 & 0 & 0 \end{smallmatrix}\right)\left(\begin{smallmatrix} 1 & 0 & 0 \\ 0 & 1 & 0 \\ 0 & 0 & 0 \end{smallmatrix}\right)\left(\begin{smallmatrix} 1 & 0 & 0 \\ 0 & -1 & 0 \\ 0 & 0 & 0 \end{smallmatrix}\right) = \frac{1}{2}\left(\begin{smallmatrix} 1 & 0 & 0 \\ 0 & 1 & 0 \\ 0 & 0 & 0 \end{smallmatrix}\right), \tag{C.68}$$

$$\Sigma_\pi^{\mathrm{ud}} = \Sigma_{\pi^+}^{\mathrm{ud}} + \Sigma_{\pi^-}^{\mathrm{ud}} + \Sigma_{\pi^0}^{\mathrm{ud}} = \frac{3}{2}\left(\begin{smallmatrix} 1 & 0 & 0 \\ 0 & 1 & 0 \\ 0 & 0 & 0 \end{smallmatrix}\right) = \frac{3}{2} P_{\mathrm{ud}}\,. \tag{C.69}$$

Analogously, we find for the kaons in the up-quark DSE:

$$\Sigma_{K^-}^{\mathrm{ud}} = (\tau_{K^-})^T P_{\mathrm{ud}} \tau_{K^-} = \left(\begin{smallmatrix} 0 & 0 & 1 \\ 0 & 0 & 0 \\ 0 & 0 & 0 \end{smallmatrix}\right)\left(\begin{smallmatrix} 1 & 0 & 0 \\ 0 & 1 & 0 \\ 0 & 0 & 0 \end{smallmatrix}\right)\left(\begin{smallmatrix} 0 & 0 & 0 \\ 0 & 0 & 0 \\ 1 & 0 & 0 \end{smallmatrix}\right) = \left(\begin{smallmatrix} 1 & 0 & 0 \\ 0 & 0 & 0 \\ 0 & 0 & 0 \end{smallmatrix}\right), \tag{C.70}$$

$$\Sigma^{\mathrm{ud}}_{\overline{K}^0} = \left(\tau_{\overline{K}^0}\right)^T P_{\mathrm{ud}} \tau_{\overline{K}^0} = \begin{pmatrix} 0&0&0\\0&0&1\\0&0&0 \end{pmatrix}\begin{pmatrix} 1&0&0\\0&1&0\\0&0&0 \end{pmatrix}\begin{pmatrix} 0&0&0\\1&0&0\\0&0&0 \end{pmatrix} = \begin{pmatrix} 0&0&0\\0&1&0\\0&0&0 \end{pmatrix}, \tag{C.71}$$

$$\Sigma^{\mathrm{ud}}_{K} = \Sigma^{\mathrm{ud}}_{K^-} + \Sigma^{\mathrm{ud}}_{\overline{K}^0} = \begin{pmatrix} 1&0&0\\0&1&0\\0&0&0 \end{pmatrix} = P_{\mathrm{ud}}\,, \tag{C.72}$$

and for the kaons in the strange-quark DSE:

$$\Sigma^{\mathrm{s}}_{K^+} = \left(\tau_{K^+}\right)^T P_{\mathrm{s}} \tau_{K^+} = \begin{pmatrix} 0&0&0\\0&0&0\\1&0&0 \end{pmatrix}\begin{pmatrix} 0&0&0\\0&0&0\\0&0&1 \end{pmatrix}\begin{pmatrix} 0&0&1\\0&0&0\\0&0&0 \end{pmatrix} = \begin{pmatrix} 0&0&0\\0&0&0\\0&0&1 \end{pmatrix}, \tag{C.73}$$

$$\Sigma^{\mathrm{s}}_{K^0} = \left(\tau_{K^0}\right)^T P_{\mathrm{s}} \tau_{K^0} = \begin{pmatrix} 0&0&0\\0&0&0\\0&1&0 \end{pmatrix}\begin{pmatrix} 0&0&0\\0&0&0\\0&0&1 \end{pmatrix}\begin{pmatrix} 0&0&0\\0&0&1\\0&0&0 \end{pmatrix} = \begin{pmatrix} 0&0&0\\0&0&0\\0&0&1 \end{pmatrix}, \tag{C.74}$$

$$\Sigma^{\mathrm{s}}_{K} = \Sigma^{\mathrm{s}}_{K^+} + \Sigma^{\mathrm{s}}_{K^0} = \begin{pmatrix} 0&0&0\\0&0&0\\0&0&2 \end{pmatrix} = 2P_{\mathrm{s}}\,, \tag{C.75}$$

The remaining flavour matrices are diagonal so we trivially find for the pseudoscalar mesons:

$$\Sigma^{\mathrm{ud}}_{\eta_8} = \left(\tau_{\eta_8}\right)^T P_{\mathrm{ud}} \tau_{\eta_8} = \frac{1}{6} P_{\mathrm{ud}}\,, \quad \Sigma^{\mathrm{s}}_{\eta_8} = \left(\tau_{\eta_8}\right)^T P_{\mathrm{s}} \tau_{\eta_8} = \frac{2}{3} P_{\mathrm{s}}\,, \tag{C.76}$$

$$\Sigma^{\mathrm{ud}}_{\eta_0} = \left(\tau_{\eta_0}\right)^T P_{\mathrm{ud}} \tau_{\eta_0} = \frac{1}{3} P_{\mathrm{ud}}\,, \quad \Sigma^{\mathrm{s}}_{\eta_0} = \left(\tau_{\eta_0}\right)^T P_{\mathrm{s}} \tau_{\eta_0} = \frac{1}{3} P_{\mathrm{s}}\,, \tag{C.77}$$

and for the scalar mesons:

$$\Sigma^{\mathrm{ud}}_{\sigma} = \left(\tau_{\sigma}\right)^T P_{\mathrm{ud}} \tau_{\sigma} = \frac{1}{2} P_{\mathrm{ud}}\,, \quad \Sigma^{\mathrm{s}}_{f_0} = \left(\tau_{f_0}\right)^T P_{\mathrm{s}} \tau_{f_0} = P_{\mathrm{s}}\,. \tag{C.78}$$

To get a consistent $N_f = 3$ limit, we account for the missing contributions of the $a_0(980)$ by choosing identical prefactors for both $f_0(980)$ and σ, i.e., $F^{\mathrm{s}}_{f_0} = F^{\mathrm{ud}}_{\sigma} = 1/2$.

$N_f = 3$ Flavours:

In the case of three degenerate quark flavours, the need for projectors disappears as they may be replaced by the unit matrix. Additionally, all mesons in the pseudoscalar octet become degenerate. As a consequence, the flavour matrix of this meson (π for simplicity) is given by the sum over all pseudoscalar $N_f = 2 + 1$ flavour matrices:

$$\Sigma^{\mathrm{uds}}_{\pi} = \Sigma^{\mathrm{ud}}_{\pi} + \Sigma^{\mathrm{ud}}_{K} + \Sigma^{\mathrm{s}}_{K} + \Sigma^{\mathrm{ud}}_{\eta_8} + \Sigma^{\mathrm{s}}_{\eta_8} = \frac{8}{3}\mathbb{1}_3\,, \quad \Sigma^{\mathrm{uds}}_{\eta_0} = \Sigma^{\mathrm{ud}}_{\eta_0} + \Sigma^{\mathrm{s}}_{\eta_0} = \frac{1}{3}\mathbb{1}_3\,. \tag{C.79}$$

By construction, the scalar mesons in the three-flavour case keep the flavour factor of the $N_f = 2 + 1$ σ meson, i.e., $F^{\mathrm{uds}}_{\sigma} = F^{\mathrm{uds}}_{f_0} = 1/2$.

C.4.4. Bottom Edge of the Columbia Plot: $N_f = 1 + 2$ Flavour Setup

In the $N_f = 1+2$ setup of Section 6.3.5 with a chiral strange quark and varying up/down-quark mass, we work with two assumptions. First, we assume that the axial anomaly is restored at the chiral transition temperature such that no anomalous mass contributions arise. Second, under this assumption, it is natural to assume that mixing between the isoscalar, pseudoscalar octet and singlet states results in a massless Goldstone boson with pure $\mathrm{s\bar{s}}$ content and a massive meson with up/down-quark content, i.e., $(\eta_8, \eta_0) \to (\eta_\ell, \eta_{\mathrm{s}})$, in the following way:

$$\tau_{\eta_\ell} = \left(\mathrm{u\bar{u}} + \mathrm{d\bar{d}}\right)/\sqrt{2}\,, \quad \tau_{\eta_{\mathrm{s}}} = \mathrm{s\bar{s}}\,. \tag{C.80}$$

$N_f = 1 + 2$:

	$f = \ell$			$f = \mathrm{s}$		
X	F_X^f	S_X^f	f_X^f	F_X^f	S_X^f	f_X^f
π	$3/2$	S_ℓ	$f_{\ell\ell}^{\mathrm{ps}}$	–	–	–
K	1	S_s	$f_{\ell\mathrm{s}}^{\mathrm{ps}}$	2	S_ℓ	$f_{\mathrm{s}\ell}^{\mathrm{ps}}$
η_ℓ	$1/2$	S_ℓ	$f_{\ell\ell}^{\mathrm{ps}}$	–	–	–
η_s	–	–	–	1	S_s	$f_{\mathrm{ss}}^{\mathrm{ps}}$
σ	$1/2$	S_ℓ	$f_{\ell\ell}^{\mathrm{sc}}$	–	–	–
f_0	–	–	–	$1/2$	S_s	$f_{\mathrm{ss}}^{\mathrm{sc}}$

$N_f = 1 + 2 \to 3$:

	$f = \ell$		
X	F_X^f	S_X^f	f_X^f
$\pi, K, \eta_\ell, \eta_\mathrm{s}$	3	S_ℓ	$f_{\ell\ell}^{\mathrm{ps}}$
σ, f_0	$1/2$	S_ℓ	$f_{\ell\ell}^{\mathrm{sc}}$

Table C.1.: Information of multiplicities, internal quark propagators and decay constants for all considered meson-backcoupling diagrams the $N_f = 1 + 2$ setup.

The resulting multiplicities can be obtained analogously to Appendix C.4.3 and are displayed in Table C.1. In case of a restored $\mathrm{U}_A(1)$, i.e., a massless η_0, the limit $N_f = 1 + 2 \to 3$ is consistent with the corresponding limit $N_f = 2 + 1 \to 3$ in Table 6.1.

Additionally, the kaons are massive away from the $N_f = 3$ limit, similar to the $N_f = 2{+}1$ case, but this time due to the non-chiral up/down quarks. In total, we reuse the parametrizations of Equation (6.5) but adjust the quark masses in the kaon argument and set the η_s and f_0 masses to zero:[1]

$$\begin{aligned} &m_\pi = 156.525\,\mathrm{MeV}^{1/2} \cdot \sqrt{m_\ell}\,, \quad m_K = 74.2\,\mathrm{MeV}^{1/2} \cdot \sqrt{m_\ell} + 1.54 \cdot m_\ell\,, \\ &m_{\eta_\mathrm{s}} = m_{f_0} = 0\,, \quad m_\sigma = 2m_\pi\,, \quad m_{\eta_\ell} = 2m_K\,. \end{aligned} \tag{C.81}$$

C.4.5. Meson Decay Constants: Generalized Pagels–Stokar Relation

We recall the definition of the meson decay constants in Equation (6.9),

$$\mathrm{i}\tilde{P}_\nu \left(f_{xyz}^{Y,t}\right)^2 = 3 \sum_q \int \mathrm{tr}\Big[S_x(q+P)\gamma_Y\gamma_\nu S_y(q)\gamma_Y B_z^r(q)\Big]\,, \quad \tilde{P}_\nu = (P_4, u_Y \boldsymbol{P})\,, \tag{C.82}$$

which has to be evaluated in the limit $P_\nu \to 0$. In advance, we introduce the following decomposition of the quark propagator:

$$S(q_4, \boldsymbol{q}) =: -\mathrm{i}\gamma_4 q_4 \sigma^C(q_4, \boldsymbol{q}) - \mathrm{i}\boldsymbol{\gamma}\cdot\boldsymbol{q}\,\sigma^A(q_4, \boldsymbol{q}) + \sigma^B(q_4, \boldsymbol{q})\,, \tag{C.83}$$

where σ^A, σ^B, σ^C are some scalar functions. First, we generally evaluate the trace in Equation (C.82). For the sake of readability, we spare the momentum arguments for now and define

$$\tilde{S}_x \coloneqq -\mathrm{i}\gamma_4 g^C - \mathrm{i}\gamma^i g_i^A + g^B\,, \quad \tilde{S}_y \coloneqq -\mathrm{i}\gamma_4 h^C - \mathrm{i}\gamma^i h_i^A + h^B\,, \tag{C.84}$$

[1] Formally, we again express the η_s and f_0 masses via the kaon mass but now with m_s as an argument, i.e., we set $m_{\eta_\mathrm{s}} = m_{f_0} = 2m_K(m_\mathrm{s})$ which, of course, evaluates to zero if $m_\mathrm{s} \to 0$.

with some scalar functions g_i^A, g^B, g^C and h_i^A, h^B, h^C. We can immediately discard all terms with an odd number of γ matrices. Using the usual anticommutation relations, we find

$$\begin{aligned}&\operatorname{tr}\left[\tilde{S}_x\gamma_Y\gamma_\nu\tilde{S}_y\gamma_Y\right]\\&= -\mathrm{i}\left(g^C h^B \operatorname{tr}\left[\gamma_4\gamma_Y\gamma_\nu\gamma_Y\right] + g_i^A h^B \operatorname{tr}\left[\gamma_i\gamma_Y\gamma_\nu\gamma_Y\right] + g^B h^C \operatorname{tr}\left[\gamma_Y\gamma_\nu\gamma_4\gamma_Y\right] + g^B h_j^A \operatorname{tr}\left[\gamma_Y\gamma_\nu\gamma_j\gamma_Y\right]\right)\end{aligned} \tag{C.85}$$

$$= \mathrm{i}\operatorname{tr}[\mathbb{1}]\left((g^C h^B + (-1)^Y g^B h^C)\delta_{4\nu} + (g_i^A h^B + (-1)^Y g^B h_i^A)\delta^i{}_\nu\right). \tag{C.86}$$

This trace tells us that the integral in Equation (C.82) vanishes for $P_\nu \to 0$ so the expression is well-defined. This is due to the fact that g^B and h^B are even with respect to q_ν whereas g_i^A, h_i^A, g^C and h^C are odd which in total renders the integrand odd.

Temporal Part

First, we derive an explicit expression for the temporal part of Equation (C.82). Looking at the fourth momentum component, we find

$$\mathrm{i}\left(f_{xyz}^{Y,t}\right)^2 = 3\sum\!\!\!\!\!\!\int_q \operatorname{tr}\left[\left(\lim_{P_4\to 0}\frac{S_x(q_4+P_4,\boldsymbol{q})}{P_4}\right)\gamma_Y\gamma_4 S_y(q)\gamma_Y B_z^r(q)\right] \tag{C.87}$$

$$= 3\sum\!\!\!\!\!\!\int_q \operatorname{tr}\left[\left(\frac{\partial}{\partial q_4}S_x(q)\right)\gamma_Y\gamma_4 S_y(q)\gamma_Y B_z^r(q)\right]. \tag{C.88}$$

In order to evaluate the trace, we now only have to identify the correct functions g^B, g^C, h^B, h^C and insert them into Equation (C.86). We find:

$$\frac{\partial}{\partial q_4}S_x(q) = -\mathrm{i}\gamma_4\left(1 + q_4\frac{\partial}{\partial q_4}\right)\sigma_x^C(q) - \mathrm{i}\boldsymbol{\gamma}\cdot\boldsymbol{q}\frac{\partial}{\partial q_4}\sigma_x^A(q) + \frac{\partial}{\partial q_4}\sigma_x^B(q), \tag{C.89}$$

which yields

$$\frac{\left(f_{xyz}^{Y,t}\right)^2}{3\operatorname{tr}[\mathbb{1}]} = \sum\!\!\!\!\!\!\int_q \left[\sigma_x^C(q)\sigma_y^B(q) + q_4\left(\left(\frac{\partial}{\partial q_4}\sigma_x^C(q)\right)\sigma_y^B(q) + (-1)^Y\left(\frac{\partial}{\partial q_4}\sigma_x^B(q)\right)\sigma_y^C(q)\right)\right]\cdot B_z^r(q). \tag{C.90}$$

Spatial Part

We proceed analogously with the spatial part. Defining $P_r := |\boldsymbol{P}|$, we obtain

$$\mathrm{i}f_{xyz}^{Y,s}f_{xyz}^{Y,t} = 3\sum\!\!\!\!\!\!\int_q \operatorname{tr}\left[\left(\lim_{P_r\to 0}\frac{S_x(q_4,\boldsymbol{q}+\boldsymbol{P})}{P_r^2}\gamma_Y(\boldsymbol{P}\cdot\boldsymbol{\gamma})\right)S_y(q)\gamma_Y B_z^r(q)\right], \tag{C.91}$$

$$3\mathrm{i}f_{xyz}^{Y,s}f_{xyz}^{Y,t} = 3\sum\!\!\!\!\!\!\int_q \operatorname{tr}\left[\sum_{j=1}^3\left(\lim_{P_r\to 0}\frac{S_x(q_4,\boldsymbol{q}+P_r\boldsymbol{e}_j)}{P_r}\right)\gamma_Y\gamma_j S_y(q)\gamma_Y B_z^r(q)\right] \tag{C.92}$$

$$= 3\sum\!\!\!\!\!\!\int_q \operatorname{tr}\left[\sum_{j=1}^3\left(\frac{\partial}{\partial q_j}S_x(q)\right)\gamma_Y\gamma_j S_y(q)\gamma_Y B_z^r(q)\right]. \tag{C.93}$$

In the second step, we used that S is O(3) invariant. Thus, we can set $\boldsymbol{P} = P_r \boldsymbol{e}_j$ and sum over each direction in order to reformulate the scalar product as the defintion of the directional derivative. Consequently, we obtain this time:

$$\frac{\partial}{\partial q_j} S_x(q) = -\mathrm{i}\gamma_4 \frac{\partial}{\partial q_j} \sigma_x^C(q) - \mathrm{i}\gamma^i \left(\delta_{ij} + q_i \frac{\partial}{\partial q_j}\right) \sigma_x^A(q) + \frac{\partial}{\partial q_j} \sigma_x^B(q) \,. \tag{C.94}$$

Additionally, we use the chain rule in order to re-express the spatial derivatives in terms of $q_r \coloneqq |\boldsymbol{q}|$:

$$\frac{\partial}{\partial q_j} = \frac{\partial q_r^2}{\partial q_j} \frac{\partial}{\partial q_r^2} = \frac{2q^j}{2q_r} \frac{\partial}{\partial q_r} = \frac{q^j}{q_r} \frac{\partial}{\partial q_r} \,. \tag{C.95}$$

Finally, we arrive at the following expression for the spatial part:

$$\frac{f_{xyz}^{Y,s} f_{xyz}^{Y,t}}{3\,\mathrm{tr}[\mathbb{1}]} = \sum\!\!\!\!\!\!\int_q \left[\sigma_x^A(q)\sigma_y^B(q) + \frac{q_r}{3}\left(\left(\frac{\partial}{\partial q_r}\sigma_x^A(q)\right)\sigma_y^B(q) + (-1)^Y \left(\frac{\partial}{\partial q_r}\sigma_x^B(q)\right)\sigma_y^A(q)\right)\right] \cdot B_z^r(q) \,. \tag{C.96}$$

Unequal Quark Flavours and Summary

In almost all of the mesons we consider, both contributing quark flavours are identical with the lone exception of the kaons. Different quark flavours, however, pose an inconvenience since the expressions in Equations (C.90) and (C.96) are not symmetric under an exchange of the quark propagators. We can solve this problem with the observation that the integral in Equation (C.82) is invariant under a shift of the integration variable,

$$\sum\!\!\!\!\!\!\int_q \mathrm{tr}\left[S_x(q+P)\gamma_Y\gamma_\nu S_y(q)\Gamma_Y(q,P)\right] = \sum\!\!\!\!\!\!\int_q \mathrm{tr}\left[S_x(q)\gamma_Y\gamma_\nu S_y(q-P)\Gamma_Y(q,P)\right] . \tag{C.97}$$

We remark that the q argument of the BSA does not change since we are able to account for this shift with a different momentum routing. Therefore, we may symmetrize the expressions in Equations (C.90) and (C.96) with the arithmetic mean of the exchanged quark flavours.

In total, we obtain the meson decay constants from the following relations:

$$f_{xy}^Y = \frac{f_{xy}^{Y,s} f_{xy}^{Y,t}}{\sqrt{\left(f_{xy}^{Y,t}\right)^2}} \,, \quad f_{xy}^{Y,s} f_{xy}^{Y,t} = \frac{f_{xyx}^{Y,s} f_{xyx}^{Y,t} + f_{yxx}^{Y,s} f_{yxx}^{Y,t}}{2} \,, \quad \left(f_{xy}^{Y,t}\right)^2 = \frac{\left(f_{xyx}^{Y,t}\right)^2 + \left(f_{yxx}^{Y,t}\right)^2}{2} \,. \tag{C.98}$$

Appendix D
Numerical Details and Setup

For the sake of both transparency and reproducibility, we cover a number of technical subtleties regarding the actual numerical implementation of our calculations in this appendix. Some of them are crucial for numerical stability while others mainly enhance performance. Additionally, we comment on the specifics of the setup this thesis was created in. Preferably, the information provided below in combination with the previos statements should suffice to recalculate all results in this thesis.

D.1. Solving the Set of DSEs

In this section, we detail how we solve the system of DSEs introduced in Chapter 3 and outlined in Appendix C for all setups that were presented in this thesis. This includes all numerical parameters.

D.1.1. Interpolation

One-dimensional interpolation is performed by means of *cubic splines* with natural boundary conditions, i.e., their second derivative is zero at the bounds of the interpolation interval. Sometimes, we also employ *linear interpolations*. Rarely, we need to interpolate *two-dimensional functions* which is handled by a *bicubic interpolation*. For all of the aforementioned methods, we use implementations of the GSL (see Appendix D.3).

D.1.2. Integration

In the most general case, we subdivide any ocurring integral into $N-1$ subintervals:

$$\int_a^b f(x)\,\mathrm{d}x = \sum_{i=1}^{N-1} \int_{x_i}^{x_{i+1}} f(x)\,\mathrm{d}x\,, \quad x_1 = a\,, \quad x_N = b\,, \quad N \in \mathbb{N}^+\,. \tag{D.1}$$

The integrations in the subintervals are then performed by means of a *Gaussian quadrature*. That is, we decompose the integrand into some function g and a *weight function* w best suited for the problem. The integral is then approximated by a sum over some nodes x_j and weights α_j that depend on both the weight function and the number of quadrature points N_{quad}:

$$\int_{x_i}^{x_{i+1}} f(x)\,\mathrm{d}x = \int_{x_i}^{x_{i+1}} g(x)w(x)\,\mathrm{d}x \approx \sum_{j=1}^{N_{\text{quad}}} g(x_j)\alpha_j\,, \quad x_j \in [x_i, x_{i+1}]\,, \quad N_{\text{quad}} \in \mathbb{N}^+\,. \tag{D.2}$$

We employ either a Gauss–Legendre quadrature, $w(x) = 1$, or a Gauss–Chebyshev quadrature (of the second kind), $w(x) = \sqrt{x^2-1}$. For both, we again use implementations of the GSL (see Appendix D.3).

Radial

In general, all radial integrations are mapped logarithmically. In an **infinite volume**, our radial grid comprises N_r (logarithmically) equidistant points between an infrared cutoff Λ_{IR} and an ultraviolet cutoff Λ_3 with N_r^{quad} Gauss–Legendre points in between each interval. We only calculate the dressing functions for the N_r equidistant points explicitly whereas the values for the intermediate points are obtained with a cubic spline interpolation.

On the **pure torus**, the grid points are predetermined by the possible momentum shells according to the boundary conditions. To these, we apply a numerical speedup: Only the 20 innermost shells are calculated explicitly while thereafter we just consider radial points that are separated by a certain ratio, $p_{i+1}/p_i > 1.2$, and interpolate the dressing functions for the remaining shells in between. This is justified since the shells become increasingly dense for larger radii.

The **improved-torus** setup is basically a combination of the pure torus and the infinite volume. In the infrared, we always generate a torus with a fixed size of N_{tor} points in each direction to which we also apply the speedup described above. Its outermost shell then defines the torus cutoff Λ_{vol} which serves as the infrared cutoff for the infinite-volume grid.

Angular

In an **infinite volume**, the angular integral depends on whether we consider the vacuum or medium case (see Appendix A.5). In vacuum, the measure $\sqrt{x^2-1}$ of the angular integration is transformed into the weight of the quadrature rule, i.e., we use a Gauss–Chebyshev quadrature (of the second kind). At nonzero temperature, the angular integration is split into two subintervals, $[-1,0]$ and $[0,1]$, with N_z^{quad} Gauss–Legendre-quadrature points each.

On the **pure Torus**, the angular integration – or rather summation – is dictated by the distribution of the torus points. The only intricacy arises when considering zero modes, which was already described in the main text in Section 4.1.3: We set the zero-mode momentum to a small but nonzero value ε, all angles of an internal zero mode are considered to be $z = 0$, whereas we use the angular information of the first nonzero momentum shell for an external zero mode.

For the **improved torus**, we again have to combine the pure-torus and the infinite-volume setups. Therefore, the angles are determined as follows: If both the external and the internal momentum are located on the torus part, we perform a scalar product like for the pure torus. If the internal momentum is in the continuum regardless of the external momentum, we perform a continuous integration as in infinite volume. If the internal momentum is on the torus and the external momentum is in continuum, we pick an arbitrary point on the outermost shell and use the angular information of this point for scalar products on the torus.

Matsubara Summation

In an **infinite volume**, only a certain number of Matsubara frequencies N_4 in the IR is calculated explicitly. Higher ones are approximated utilizing the restored O(4) invariance in the ultraviolet. That is to say, the dressing functions only depend on the square four-

momentum in this region:

$$D_f(p_4, \boldsymbol{p}) = D_f\left(p_4^2 + \boldsymbol{p}^2\right), \quad D \in \{A, B, C\}. \tag{D.3}$$

As a consequence, we may obtain values of the dressing functions at energies p_4 whose absolute value is larger than the one of the outermost Matsubara frequencies, $\omega^T_{N_4-1} = -\omega^T_{-N_4}$, via

$$D_f(p_4, \boldsymbol{p}) = \begin{cases} D_f\left(\omega^T_{N_4-1}, \sqrt{p_4^2 - \left(\omega^T_{N_4-1}\right)^2 + \boldsymbol{p}^2}\right) & \text{for } p_4 > \omega^T_{N_4-1}, \\ D_f\left(\omega^T_{-N_4}, \sqrt{p_4^2 - \left(\omega^T_{-N_4}\right)^2 + \boldsymbol{p}^2}\right) & \text{for } p_4 < \omega^T_{-N_4}. \end{cases} \tag{D.4}$$

For this reason, we always use an O(4)-invariant, four-dimensional cutoff Λ_4 for calculations at nonzero temperature. This way, the UV cutoff of the radial grid Λ_3 depends on the energy:

$$\Lambda_3^2 = \Lambda_3^2(p_4) = \Lambda_4^2 - p_4^2. \tag{D.5}$$

In addition, we simplify the sum over larger Matsubara frequencies (which served as the inspiration of the improved-torus setup). Namely, on a logarithmic grid, the Matsubara frequencies become increasingly dense in the UV and the integrand f does not change much from frequency to frequency. Therefore, we approximate the sum over the outermost Matsubara frequencies, $|p_4| > \left|\omega^T_{N_4-1}\right|$, by a continuous integration:

$$T \sum_{q_4 \in \left\{\omega_n^T\right\}}^{|q_4|<\Lambda_4} f(q_4) = \int_{-\Lambda_4}^{\omega_{-N_4}-\pi T} \frac{\mathrm{d}q_4}{2\pi} f(q_4) + T \sum_{n=-N_4}^{N_4-1} f\left(\omega_n^T\right) + \int_{\omega_{N_4-1}+\pi T}^{\Lambda_4} \frac{\mathrm{d}q_4}{2\pi} f(q_4). \tag{D.6}$$

The UV integrals are performed by means of a Gauss–Legendre quadrature with N_4^{quad} points. The shift of πT inside the integral bounds is due to the fact that every Matsubara frequency "covers" an interval of $2\pi T$ and the results react quite sensitively to its omission.

On the **pure torus**, due to the small UV cutoff, we perform the full Matsubara summation up to the cutoff Λ_4 without Gauss–Legendre quadrature. Nevertheless, we only explicitly calculate the $N_4 = 5$ innermost frequencies while the values at the remaining ones are calculated using O(4) invariance. Analogously to the infinite volume, however, we cut the torus summation in an O(4)-invariant way (which is necessary to obtain a proper longitudinal part of the gluon).

Yet another time, the **improved torus** is a combination of the infinite-volume and the pure-torus setups. That is, we utilize an O(4)-invariant torus in the IR, while the number of Matsubara frequencies and Gauss–Legendre points is chosen identically as in infinite volume. The radii $\Lambda^2_{\text{vol}} < p^2 < \Lambda_4^2$ are treated according to the infinite-volume procedure.

D.1.3. Quark DSE

The external momentum grid of the quark is determined by the distribution of the equidistant radial points in the quark self-energy.

(Non-Hadronic) Quark Self-Energy

Except for the pure torus (where we always use a hard cutoff of $\Lambda_4^{\mathrm{PT}} = 10\,\mathrm{GeV}$), the (four-dimensional) UV cutoff depends on whether we employ a Pauli–Villars regulator or a hard cutoff. In the former case, the (formally infinite) cutoff of $\Lambda_4^{\mathrm{PV}} = 1.2\,\mathrm{TeV}$ has to be significantly larger than the Pauli–Villars scale, $\Lambda_{\mathrm{PV}} = 200\,\mathrm{GeV}$. In the latter case, we set $\Lambda_4^{\mathrm{HC}} = 300\,\mathrm{GeV}$.

For the **temporal summation/integration**, we use $N_4 = 8$ explicit Matsubara frequencies and $N_4^{\mathrm{quad}} = 16$ implicit Gauss–Legendre points each for both positive and negative energies, respectively. In the **radial integration**, we use $N_r^{\mathrm{quad}} = 5$ Gauss–Legendre points in between each of the $N_r = 32$ equidistant points. In case of an improved torus, we utilize $N_{\mathrm{tor}} = 25$ torus points in each direction. As an IR cutoff, we consistently choose $\Lambda_{\mathrm{IR}} = 1\,\mathrm{MeV}$. For the **angular integration**, we use either $N_z^{\mathrm{quad}} = 160$ points on a single interval $[-1, 1]$ (vacuum) or $N_z^{\mathrm{quad}} = 80$ points (medium) on each of the two subintervals, $[-1, 0]$ and $[0, 1]$, respectively.

Quark Condensate

The quark condensate is calculated with the same parameters as the quark self-energy. However, the integral is not regularized using a potential Pauli–Villars regulator but always by means of the different subtraction procedures described in the main text.

Quark-Number Density

The quark-number density requires an especially sensitive treatment and is handled very differently from all other quantities. First, the Matsubara summation/integration is executed before the three-momentum integration. In addition, the four-dimensional summations/integrations are *not* performed in an $\mathrm{O}(4)$-invariant way and we have different cutoffs in temporal, $\Lambda_4 = \Lambda_4^{\mathrm{PV}} = 1.2\,\mathrm{TeV}$, and spatial, $\Lambda_3 = 90\,\mathrm{GeV}$, directions, respectively. Moreover, we utilize $N_r = 64$ equidistant points on the interval $[\Lambda_{\mathrm{IR}}, \Lambda_3]$ with $N_r^{\mathrm{quad}} = 10$ Gauss–Legendre points in between for the radial integration. For the continuous integration inside the vacuum contribution, we employ $N_4^{\mathrm{quad}} = 64$ Gauss–Legendre points *between* the Matsubara frequencies and use a linear interpolation to obtain these values.

Meson-Backcoupling Diagrams and Meson Decay Constants

By and large, the meson-backcoupling diagrams inherit the numerical parameters from the non-hadronic self-energy diagram. However, the diagrams do not need to be regularized as this is already accounted for by the Pauli–Villars-like term inside the approximated BSAs. In the $(2+1)$-flavour setup, however, the meson-backcoupling diagrams introduce a complication when it comes to updating the quarks after an iteration (see below). Due to the mesons, the quarks are now coupled directly (and not only indirectly through the quark loop). Therefore, they have to be iterated alternatingly and updated at the same time after an iteration. Otherwise, different quark flavours get different input which spoils a consistent $N_f = 3$ limit.

The Pagels–Stokar integral for the decay constants is treated analogously to the meson-backcoupling diagrams and the non-hadronic self-energy. The only subtlety are the partial derivatives of the dressing functions. These are calculated using a bicubic interpolation (see above).

D.1.4. Gluon DSE

The external momentum grid of the gluon is determined by the distribution of the equidistant radial points in the quark loop.

Longitudinal Quark Loop

Most of the parameters of the quark-loop integrations are chosen identically as the ones of the quark-self energy. For this reason, we will only mention the differences below.

First, we slightly adjust the UV cutoffs. The quark loop is regularized explicitly by the Brown–Pennington projection (see Appendix C.2.2), so we do not add an explicit regulator inside the integral. As a consequence, in case of a Pauli–Villars regulator in the quark self-energy, the UV cutoff is only increased mildly to $\Lambda_4^{\mathrm{PV}} = 400\,\mathrm{GeV}$ whereas the other cutoffs remain unchanged, i.e., $\Lambda_4^{\mathrm{HC}} = 300\,\mathrm{GeV}$ and $\Lambda_4^{\mathrm{PT}} = 10\,\mathrm{GeV}$. For the **temporal summation**, we do not use a Gauss–Legendre integration but rather execute the Matsubara sum explicitly up to the UV cutoff Λ_4 for stability reasons.

Also for reasons of numerical stability, we manually subtract the *screening mass part* (i.e., the analytical $k \to 0$ limit in Appendix C.2.4) inside the kernels of the quark loop and explicitly add it again later with some adjustments (see below). This is done both in infinite volume and on the improved torus. For the pure torus, we do not subtract the screening-mass contribution.

Screening Mass

In an **infinite volume**, the screening-mass contribution is calculated very similarly to the longitudinal quark loop with two major exceptions. First, the angular integration is performed analytically. Second, we use a mixing between the C and A dressing functions to ensure O(4) invariance for large momenta:

$$C_f(q) \to \tilde{C}_f(q) = \exp\!\left(-q^2/\Lambda_{AC}\right) C_f(q) + \left(1 - \exp\!\left(-q^2/\Lambda_{AC}\right)\right) A_f(q)\,, \quad \Lambda_{AC} = 40\,\mathrm{GeV}^2\,. \tag{D.7}$$

In the **improved-torus** setup, we have to use quite a large torus of $N_{\mathrm{tor}} = 1000$ points to render the results stable. In case of a **pure torus**, as stated above, we do not calculate a screening mass.

D.1.5. Iterating the Set of DSEs

Finally, we put all of the aforementioned pieces together and elucidate how the DSE system is solved in its entirety. Before the calculation, we initialize the dressing functions with some values. In the most general case, we choose $A_f \equiv B_f \equiv C_f \equiv Z_T \equiv Z_L \equiv 1$. In the vicinity of a second-order phase transition, however, it may be beneficial to start with the result for a nearby temperature or chemical potential as an input, either to reduce runtime or to enhance numerical stability.

The iteration procedure then advances as follows. First, we calculate the gluon (and thus the quark loop) with the initial input. This gluon consequently serves as input for the iteration of the quark system. If the quark system does not converge within one iteration, we repeat this process until it does.

As the convergence criterion of the quark system at some iteration $k = k_{\max} \geq 1$, we demand that the relative difference for all dressing functions $D \in \{A, B, C\}$ of all quark flavours f at all temporal points $p_4^i, 0 \leq i \leq N_4 - 1$, and all radial points $\boldsymbol{p}^j, 0 \leq j \leq N_r - 1$, no longer exceed 10^{-6} (where $k = 0$ indicates the initial values before the first iteration), i.e.,

$$\max_{\left(p_4^i, \boldsymbol{p}^j, D, f\right)} \left| \frac{D_f^k\left(p_4^i, \boldsymbol{p}^j\right) - D_f^{k-1}\left(p_4^i, \boldsymbol{p}^j\right)}{D_f^k\left(p_4^i, \boldsymbol{p}^j\right) + D_f^{k-1}\left(p_4^i, \boldsymbol{p}^j\right)} \right| < 10^{-6} \,. \tag{D.8}$$

Relaxation

Sometimes, i.e., in the vicinity of a second-order phase transition or for very small volumes, the iteration jumps between two possible solutions or becomes otherwise numerically unstable. This either leads to non-convergence of the system or to discontinuities of the condensate with respect to temperature, chemical potential and/or volume. In this case, *relaxation* can render the iteration more stable. That is, we do not fully accept the newly calculated value of a dressing function for the next iteration but rather mix in a certain percentage of the previous value, expressed in terms of a relaxation parameter $r \in [0, 1)$. The replacement rule then reads

$$D_f^k \to \tilde{D}_f^k = (1 - r) D_f^k + r D_f^{k-1} \,. \tag{D.9}$$

Typical values are $r = 0.5$ or (in severe cases) $r = 0.95$. We note that the results are identical for all choices of r that lead to converging iterations.

D.2. Finite-Difference Formulae

At some points, we necessitate derivatives of the quark condensate or quark-number density with respect to quark mass or chemical potential, respectively. While these could be calculated directly by performing analytical derivatives, this requires knowledge of the derivatives of the dressing functions. Instead of concurrently solving these as well, which adds on order of magnitude more complexity to the system, we resort to well-known *finite-difference* formulae. The quality of those was tested in similar cases and was found to be consistent on the sub-per-cent level [137].

D.2.1. Baryon Number Fluctuations

We calculate all baryon-number fluctuations using the central finite-difference quotients with a second-order accuracy. For some function f at some point x_0 and up to the third derivative, these read

$$f'(x_0) = \frac{f(x_0 + h) - f(x_0 - h)}{2h} + O(h^2) \,, \tag{D.10}$$

$$f''(x_0) = \frac{f(x_0 + h) + 2f(x_0) - f(x_0 - h)}{h^2} + O(h^2) \,, \tag{D.11}$$

$$f'''(x_0) = \frac{f(x_0 + 2h) - 2f(x_0 + h) + 2f(x_0 - h) - f(x_0 - 2h)}{2h^3} + O(h^2) \,, \tag{D.12}$$

where $h = \Delta x$ labels the finite difference between the discrete input points. In principle, one could also use formulae with higher orders of accuracy. In practice, however, the results become numerically increasingly unstable when going beyond second order – especially for finite-volume calculations. For the sake of consistency, we thus use second-order accuracy also for the lower derivatives.

As stated in Section 4.3, we neglect off-diagonal derivatives for the calculation of baryon-number fluctuations. If we now, for example, want to calculate the second-order baryon-number fluctuation,

$$\chi_2^{\mathrm{B}} = \frac{1}{9}\left(2\chi_2^{\mathrm{u}} + \chi_2^{\mathrm{s}}\right) , \tag{D.13}$$

we find for the second-order up-quark-number fluctuation,

$$T^2\chi_2^{\mathrm{u}} = \frac{\partial n_{\mathrm{u}}}{\partial \mu_{\mathrm{u}}} = \frac{n_{\mathrm{u}}(T, \mu_{\mathrm{u}} - \Delta\mu_{\mathrm{u}}, \mu_{\mathrm{s}} = 0) - n_{\mathrm{u}}(T, \mu_{\mathrm{u}} + \Delta\mu_{\mathrm{u}}, \mu_{\mathrm{s}} = 0)}{2\Delta\mu_{\mathrm{u}}} + O(\Delta\mu_{\mathrm{u}}^2) , \tag{D.14}$$

and analogously for the strange quark:

$$T^2\chi_2^{\mathrm{s}} = \frac{\partial n_{\mathrm{s}}}{\partial \mu_{\mathrm{s}}} = \frac{n_{\mathrm{s}}(T, \mu_{\mathrm{u}}, \mu_{\mathrm{s}} = -\Delta\mu_{\mathrm{s}}) - n_{\mathrm{s}}(T, \mu_{\mathrm{u}}, \mu_{\mathrm{s}} = \Delta\mu_{\mathrm{s}})}{2\Delta\mu_{\mathrm{s}}} + O(\Delta\mu_{\mathrm{s}}^2) \tag{D.15}$$

$$= \frac{n_{\mathrm{s}}(T, \mu_{\mathrm{u}}, \mu_{\mathrm{s}} = \Delta\mu_{\mathrm{s}})}{\Delta\mu_{\mathrm{s}}} + O(\Delta\mu_{\mathrm{s}}^2) . \tag{D.16}$$

In the latter equation, we employed antisymmetry of the quark-number density for negative chemical potentials, $n_f(-\mu_f) = -n_f(\mu_f)$.[1] We always use $\Delta\mu_f = 1\,\mathrm{MeV}$.

D.2.2. Chiral Susceptibility

The chiral susceptibilities as the derivatives of the (regularized) quark condensate with respect to the up-quark mass are calculated with central finite-difference quotients as well. We again resort to Equation (D.10) and always take $\Delta m_{\mathrm{u}} = 1\,\mathrm{keV}$.

D.3. Technical Setup

For the sake of transparency, both software – which was always used in its latest stable versions, respectively – and hardware that was utilized making this thesis is listed below.

Numerical Calculations

- For the computationally expensive calculations – i.e., solution of the projected DSEs and determination of the quark condensate and quark-number densities – a self-developed code written in the *C programming language* using its 1999 standard [386] without compiler extensions was employed.
- The C compiler of the *GNU Compiler Collection* (GCC) [387] was used for compilation.

[1] This is easily verified. Since the QCD action $\mathcal{S}$ is C-, P- and T-invariant, it is symmetric with respect to particle–antiparticle exchange: $\mathcal{S}(\mu) = \mathcal{S}(-\mu)$. This is handed down to the QCD grand potential Ω. Therefore, the particle-number density as its derivative must be antisymmetric: $\partial\Omega(-\mu)/\partial\mu = -\partial\Omega(\mu)/\partial\mu$.

- The sole external library that was included in this code is the *GNU Scientific Library* (GSL) [388] for its implementations of cubic splines, bicubic and linear interpolations and quadratures.
- *CMake* [389] was used for build automation.
- Some (minor) data analysis – like the calculation of regularized condensates and numerical derivatives as well as preparation of plots – was performed by self-developed scripts written in *Python 3* [390] using the libraries *SciPy* [391] and *NumPy* [392].

Typesetting, Figures and Plots

- Typesetting was performed, of course, with LaTeX (in combination with a peculiar mixture of *pdfTeX* for the main document and *LuaTeX* for TikZ figures) all of which are included in the *TeX Live* distribution [393] for *Arch Linux*.
- Plots of the produced data were created with the Python library *Matplotlib* [394] utilizing its TeX backend.
- All other figures were self-made using *PGF/TikZ* [395].
- Out of these, the Feynman diagrams were drawn with the package *TikZ-Feynman* [396].

Machines and OSs

- Most calculations with a high demand on CPU performance and/or RAM capacity were performed on the local *Tiger* cluster of the Institute for Theoretical Physics at the JLU Gießen running Ubuntu [397] (first 16.04 LTS, later 20.04 LTS).
- Everything else was done on several ordinary machines running Arch Linux [398].

Appendix E
Bibliography

[1] S. Borsanyi et al., *QCD Crossover at Finite Chemical Potential from Lattice Simulations*, Phys. Rev. Lett. **125**, 052001 (2020), arXiv:2002.02821 [hep-lat].

[2] S. Tomonaga, *On a relativistically invariant formulation of the quantum theory of wave fields*, Prog. Theor. Phys. **1**, 27 (1946).

[3] J. S. Schwinger, *On Quantum electrodynamics and the magnetic moment of the electron*, Phys. Rev. **73**, 416 (1948).

[4] R. P. Feynman, *Space-time approach to nonrelativistic quantum mechanics*, Rev. Mod. Phys. **20**, 367 (1948).

[5] F. J. Dyson, *The Radiation theories of Tomonaga, Schwinger, and Feynman*, Phys. Rev. **75**, 486 (1949).

[6] X. Fan, T. G. Myers, B. A. D. Sukra and G. Gabrielse, *Measurement of the Electron Magnetic Moment*, Phys. Rev. Lett. **130**, 071801 (2023), arXiv:2209.13084 [physics.atom-ph].

[7] S. L. Glashow, *Partial Symmetries of Weak Interactions*, Nucl. Phys. **22**, 579 (1961).

[8] S. Weinberg, *A Model of Leptons*, Phys. Rev. Lett. **19**, 1264 (1967).

[9] A. Salam, *Weak and Electromagnetic Interactions*, Conf. Proc. C **680519**, 367 (1968).

[10] P. W. Higgs, *Broken Symmetries and the Masses of Gauge Bosons*, Phys. Rev. Lett. **13**, 508 (1964).

[11] F. Englert and R. Brout, *Broken Symmetry and the Mass of Gauge Vector Mesons*, Phys. Rev. Lett. **13**, 321 (1964).

[12] G. S. Guralnik, C. R. Hagen and T. W. B. Kibble, *Global Conservation Laws and Massless Particles*, Phys. Rev. Lett. **13**, 585 (1964).

[13] G. Aad et al. (ATLAS), *Observation of a new particle in the search for the Standard Model Higgs boson with the ATLAS detector at the LHC*, Phys. Lett. B **716**, 1 (2012), arXiv:1207.7214 [hep-ex].

[14] M. Gell-Mann, *A Schematic Model of Baryons and Mesons*, Phys. Lett. **8**, 214 (1964).

[15] G. Zweig, *An SU(3) model for strong interaction symmetry and its breaking. Version 1*, 10.17181/CERN-TH-401 (1964).

[16] G. Zweig, *An SU(3) model for strong interaction symmetry and its breaking. Version 2*, 10.17181/CERN-TH-412 (1964).

[17] F. Abe et al. (CDF), *Observation of top quark production in $\overline{p}p$ collisions*, Phys. Rev. Lett. **74**, 2626 (1995), arXiv:hep-ex/9503002.

[18] S. Abachi et al. (D0), *Observation of the top quark*, Phys. Rev. Lett. **74**, 2632 (1995), arXiv:hep-ex/9503003.

[19] R. L. Workman et al. (Particle Data Group), *Review of Particle Physics*, Prog. Theor. Exp. Phys. **2022**, 083C01 (2022).

[20] O. W. Greenberg, *Spin and Unitary Spin Independence in a Paraquark Model of Baryons and Mesons*, Phys. Rev. Lett. **13**, 598 (1964).

[21] M. Y. Han and Y. Nambu, *Three Triplet Model with Double SU(3) Symmetry*, Phys. Rev. **139**, B1006 (1965).

[22] J. Greensite, *An Introduction to the Confinement Problem*, Vol. 821, Lecture Notes in Physics (2011).

[23] E. D. Bloom et al., *High-Energy Inelastic e p Scattering at 6-Degrees and 10-Degrees*, Phys. Rev. Lett. **23**, 930 (1969).

[24] C.-N. Yang and R. L. Mills, *Conservation of Isotopic Spin and Isotopic Gauge Invariance*, Phys. Rev. **96**, 191 (1954).

[25] D. J. Gross and F. Wilczek, *Ultraviolet Behavior of Nonabelian Gauge Theories*, Phys. Rev. Lett. **30**, 1343 (1973).

[26] H. D. Politzer, *Reliable Perturbative Results for Strong Interactions?*, Phys. Rev. Lett. **30**, 1346 (1973).

[27] H. Fritzsch, M. Gell-Mann and H. Leutwyler, *Advantages of the Color Octet Gluon Picture*, Phys. Lett. B **47**, 365 (1973).

[28] A. Ali and G. Kramer, *Jets and QCD: A Historical Review of the Discovery of the Quark and Gluon Jets and its Impact on QCD*, Eur. Phys. J. H **36**, 245 (2011), arXiv:1012.2288 [hep-ph].

[29] S. Bethke, *Experimental tests of asymptotic freedom*, Prog. Part. Nucl. Phys. **58**, 351 (2007), arXiv:hep-ex/0606035.

[30] R. P. Feynman, *The principle of least action in quantum mechanics*, PhD thesis (Princeton University, 1942).

[31] P. A. M. Dirac, *The Lagrangian in quantum mechanics*, Phys. Z. Sowjetunion **3**, 64 (1933).

[32] M. Chaichian and A. Demichev, *Path Integrals in Physics* (CRC Press, Oct. 2018).

[33] S. Weinberg, *The Quantum Theory of Fields, Volume 1: Foundations* (Cambridge University Press, June 2005).

[34] S. Weinberg, *The Quantum Theory of Fields, Volume 2: Modern Applications* (Cambridge University Press, Aug. 2013).

[35] C. Itzykson and J. B. Zuber, *Quantum Field Theory*, International Series In Pure and Applied Physics (McGraw-Hill, New York, 1980).

[36] J. Zinn-Justin, *Quantum Field Theory and Critical Phenomena*, Vol. 77, International Series of Monographs on Physics (Oxford University Press, Apr. 2021).

[37] M. E. Peskin and D. V. Schroeder, *An Introduction To Quantum Field Theory* (Addison-Wesley, Reading, USA, 1995).

[38] R. J. Rivers, *Path Integral Methods in Quantum Field Theory*, Cambridge Monographs on Mathematical Physics (Cambridge University Press, Oct. 1988).

[39] Z. Fodor and C. Hoelbling, *Light Hadron Masses from Lattice QCD*, Rev. Mod. Phys. **84**, 449 (2012), arXiv:1203.4789 [hep-lat].

[40] G. Colangelo et al., *Review of lattice results concerning low energy particle physics*, Eur. Phys. J. C **71**, 1695 (2011), arXiv:1011.4408 [hep-lat].

[41] F. J. Dyson, *The S matrix in quantum electrodynamics*, Phys. Rev. **75**, 1736 (1949).

[42] J. S. Schwinger, *On the Green's functions of quantized fields. 1.* Proc. Nat. Acad. Sci. **37**, 452 (1951).

[43] Y. Nambu and G. Jona-Lasinio, *Dynamical Model of Elementary Particles Based on an Analogy with Superconductivity. 1.* Phys. Rev. **122**, 345 (1961).

[44] Y. Nambu and G. Jona-Lasinio, *Dynamical model of elementary particles based on an analogy with superconductivity. II.* Phys. Rev. **124**, 246 (1961).

[45] M. Gell-Mann and M. Levy, *The axial vector current in beta decay*, Nuovo Cim. **16**, 705 (1960).

[46] D. U. Jungnickel and C. Wetterich, *Effective action for the chiral quark-meson model*, Phys. Rev. D **53**, 5142 (1996), arXiv:hep-ph/9505267.

[47] D. U. Jungnickel and C. Wetterich, *Effective linear meson model*, Eur. Phys. J. C **1**, 669 (1998), arXiv:hep-ph/9606483.

[48] P. Isserstedt, *Thermodynamics of strong-interaction matter: On the phase structure and thermodynamics of quantum chromodynamics with Dyson–Schwinger equations*, PhD thesis (Justus-Liebig-Universität Gießen, 2021).

[49] P. J. Gunkel, *Hadronic effects in the QCD phase diagram*, PhD thesis (Justus-Liebig-Universität Gießen, 2021).

[50] B.-J. Schaefer and M. Wagner, *On the QCD phase structure from effective models*, Prog. Part. Nucl. Phys. **62**, 381 (2009), arXiv:0812.2855 [hep-ph].

[51] D. J. Gross, R. D. Pisarski and L. G. Yaffe, *QCD and Instantons at Finite Temperature*, Rev. Mod. Phys. **53**, 43 (1981).

[52] L. Y. Glozman, O. Philipsen and R. D. Pisarski, *Chiral spin symmetry and the QCD phase diagram*, Eur. Phys. J. A **58**, 247 (2022), arXiv:2204.05083 [hep-ph].

[53] A. Rothkopf, *Heavy Quarkonium in Extreme Conditions*, Phys. Rep. **858**, 1 (2020), arXiv:1912.02253 [hep-ph].

[54] K. Yagi, T. Hatsuda and Y. Miake, *Quark-gluon plasma: From big bang to little bang*, Vol. 23, Cambridge Monographs on Particle Physics, Nuclear Physics and Cosmology (2005).

[55] S. Borsanyi et al. (Wuppertal-Budapest), *Is there still any T_c mystery in lattice QCD? Results with physical masses in the continuum limit III*, J. High. Energy Phys. **09**, 073 (2010), arXiv:1005.3508 [hep-lat].

[56] A. Bazavov et al., *The chiral and deconfinement aspects of the QCD transition*, Phys. Rev. D **85**, 054503 (2012), arXiv:1111.1710 [hep-lat].

[57] J. C. Collins and M. J. Perry, *Superdense Matter: Neutrons Or Asymptotically Free Quarks?*, Phys. Rev. Lett. **34**, 1353 (1975).

[58] N. Cabibbo and G. Parisi, *Exponential Hadronic Spectrum and Quark Liberation*, Phys. Lett. B **59**, 67 (1975).

[59] A. M. Halasz et al., *On the phase diagram of QCD*, Phys. Rev. D **58**, 096007 (1998), arXiv:hep-ph/9804290.

[60] S. Das Gupta, A. Z. Mekjian and M. B. Tsang, *Liquid-gas phase transition in nuclear multifragmentation*, Avd. Nucl. Phys. **26**, 89 (2001), arXiv:nucl-th/0009033.

[61] M. Buballa, *NJL model analysis of quark matter at large density*, Phys. Rep. **407**, 205 (2005), arXiv:hep-ph/0402234.

[62] B.-J. Schaefer and J. Wambach, *The phase diagram of the quark meson model*, Nucl. Phys. A **757**, 479 (2005), arXiv:nucl-th/0403039.

[63] R.-A. Tripolt, B.-J. Schaefer, L. von Smekal and J. Wambach, *Low-temperature behavior of the quark-meson model*, Phys. Rev. D **97**, 034022 (2018), arXiv:1709.05991 [hep-ph].

[64] M. G. Alford, K. Rajagopal and F. Wilczek, *Color flavor locking and chiral symmetry breaking in high density QCD*, Nucl. Phys. B **537**, 443 (1999), arXiv:hep-ph/9804403.

[65] D. Bailin and A. Love, *Superfluidity and Superconductivity in Relativistic Fermion Systems*, Phys. Rep. **107**, 325 (1984).

[66] B. Friman, F. Karsch, K. Redlich and V. Skokov, *Fluctuations as probe of the QCD phase transition and freeze-out in heavy ion collisions at LHC and RHIC*, Eur. Phys. J. C **71**, 1694 (2011), arXiv:1103.3511 [hep-ph].

[67] M. Buballa and S. Carignano, *Inhomogeneous chiral condensates*, Prog. Part. Nucl. Phys. **81**, 39 (2015), arXiv:1406.1367 [hep-ph].

[68] A. Bazavov et al., *Skewness, kurtosis, and the fifth and sixth order cumulants of net baryon-number distributions from lattice QCD confront high-statistics STAR data*, Phys. Rev. D **101**, 074502 (2020), arXiv:2001.08530 [hep-lat].

[69] S. Borsányi et al., *Lattice QCD Equation of State at Finite Chemical Potential from an Alternative Expansion Scheme*, Phys. Rev. Lett. **126**, 232001 (2021), arXiv:2102.06660 [hep-lat].

[70] J. N. Guenther, *Overview of the QCD phase diagram: Recent progress from the lattice*, Eur. Phys. J. A **57**, 136 (2021), arXiv:2010.15503 [hep-lat].

[71] S. Borsanyi et al., *The QCD equation of state with dynamical quarks*, J. High. Energy Phys. **11**, 077 (2010), arXiv:1007.2580 [hep-lat].

[72] S. Borsanyi et al., *Full result for the QCD equation of state with 2+1 flavors*, Phys. Lett. B **730**, 99 (2014), arXiv:1309.5258 [hep-lat].

[73] A. Bazavov et al. (HotQCD), *Equation of state in (2+1)-flavor QCD*, Phys. Rev. D **90**, 094503 (2014), arXiv:1407.6387 [hep-lat].

[74] H.-T. Ding, F. Karsch and S. Mukherjee, *Thermodynamics of strong-interaction matter from Lattice QCD*, Int. J. Mod. Phys. E **24**, 1530007 (2015), arXiv:1504.05274 [hep-lat].

[75] A. Bazavov et al., *The QCD Equation of State to $O(\mu_B^6)$ from Lattice QCD*, Phys. Rev. D **95**, 054504 (2017), arXiv:1701.04325 [hep-lat].

[76] K. Nagata, *Finite-density lattice QCD and sign problem: Current status and open problems*, Prog. Part. Nucl. Phys. **127**, 103991 (2022), arXiv:2108.12423 [hep-lat].

[77] A. Bazavov et al. (HotQCD), *Chiral crossover in QCD at zero and non-zero chemical potentials*, Phys. Lett. B **795**, 15 (2019), arXiv:1812.08235 [hep-lat].

[78] C. S. Fischer, J. Luecker and C. A. Welzbacher, *Phase structure of three and four flavor QCD*, Phys. Rev. D **90**, 034022 (2014), arXiv:1405.4762 [hep-ph].

[79] P. Isserstedt, M. Buballa, C. S. Fischer and P. J. Gunkel, *Baryon number fluctuations in the QCD phase diagram from Dyson-Schwinger equations*, Phys. Rev. D **100**, 074011 (2019), arXiv:1906.11644 [hep-ph].

[80] P. J. Gunkel and C. S. Fischer, *Locating the critical endpoint of QCD: Mesonic backcoupling effects*, Phys. Rev. D **104**, 054022 (2021), arXiv:2106.08356 [hep-ph].

[81] W.-j. Fu, J. M. Pawlowski and F. Rennecke, *QCD phase structure at finite temperature and density*, Phys. Rev. D **101**, 054032 (2020), arXiv:1909.02991 [hep-ph].

[82] F. Gao and J. M. Pawlowski, *QCD phase structure from functional methods*, Phys. Rev. D **102**, 034027 (2020), arXiv:2002.07500 [hep-ph].

[83] F. Gao and J. M. Pawlowski, *Chiral phase structure and critical end point in QCD*, Phys. Lett. B **820**, 136584 (2021), arXiv:2010.13705 [hep-ph].

[84] C. S. Fischer, *QCD at finite temperature and chemical potential from Dyson–Schwinger equations*, Prog. Part. Nucl. Phys. **105**, 1 (2019), arXiv:1810.12938 [hep-ph].

[85] W.-j. Fu, *QCD at finite temperature and density within the fRG approach: an overview*, Commun. Theor. Phys. **74**, 097304 (2022), arXiv:2205.00468 [hep-ph].

[86] A. Bzdak et al., *Mapping the phases of quantum chromodynamics with beam energy scan*, Phys. Rep. **853**, 1 (2020), arXiv:1906.00936 [nucl-th].

[87] *The CBM Physics Book: Compressed Baryonic Matter in Laboratory Experiments*, Lecture Notes in Physics 814 (Springer, 2011).

[88] P. Salabura and J. Stroth, *Dilepton radiation from strongly interacting systems*, Prog. Part. Nucl. Phys. **120**, 103869 (2021), arXiv:2005.14589 [nucl-ex].

[89] D. Almaalol et al., *QCD Phase Structure and Interactions at High Baryon Density: Continuation of BES Physics Program with CBM at FAIR*, arXiv:2209.05009 [nucl-ex].

[90] P. Braun-Munzinger, V. Koch, T. Schäfer and J. Stachel, *Properties of hot and dense matter from relativistic heavy ion collisions*, Phys. Rep. **621**, 76 (2016), arXiv:1510.00442 [nucl-th].

[91] X. Luo and N. Xu, *Search for the QCD critical point with fluctuations of conserved quantities in relativistic heavy-ion collisions at RHIC: an overview*, Nucl. Sci. Tech. **28**, 112 (2017), arXiv:1701.02105 [nucl-ex].

[92] W. Busza, K. Rajagopal and W. van der Schee, *Heavy Ion Collisions: The Big Picture, and the Big Questions*, Ann. Rev. Nucl. Part. Sci. **68**, 339 (2018), arXiv:1802.04801 [hep-ph].

[93] M. A. Stephanov, K. Rajagopal and E. V. Shuryak, *Signatures of the Tricritical Point in QCD*, Phys. Rev. Lett. **81**, 4816 (1998), arXiv:hep-ph/9806219.

[94] M. A. Stephanov, K. Rajagopal and E. V. Shuryak, *Event-by-event fluctuations in heavy ion collisions and the QCD critical point*, Phys. Rev. D **60**, 114028 (1999), arXiv:hep-ph/9903292.

[95] M. Asakawa, S. Ejiri and M. Kitazawa, *Third Moments of Conserved Charges as Probes of QCD Phase Structure*, Phys. Rev. Lett. **103**, 262301 (2009), arXiv:0904.2089 [nucl-th].

[96] M. A. Stephanov, *Sign of Kurtosis near the QCD Critical Point*, Phys. Rev. Lett. **107**, 052301 (2011), arXiv:1104.1627 [hep-ph].

[97] V. Skokov, B. Friman and K. Redlich, *Volume fluctuations and higher-order cumulants of the net baryon number*, Phys. Rev. C **88**, 034911 (2013), arXiv:1205.4756 [hep-ph].

[98] A. Bzdak, V. Koch and N. Strodthoff, *Cumulants and correlation functions versus the QCD phase diagram*, Phys. Rev. C **95**, 054906 (2017), arXiv:1607.07375 [nucl-th].

[99] G. A. Almási, R. D. Pisarski and V. V. Skokov, *Volume dependence of baryon number cumulants and their ratios*, Phys. Rev. D **95**, 056015 (2017), arXiv:1612.04416 [hep-ph].

[100] A. Bhattacharyya et al., *Thermodynamic properties of strongly interacting matter in finite volume using the Polyakov–Nambu–Jona-Lasinio model*, Phys. Rev. D **87**, 054009 (2013), arXiv:1212.5893 [hep-ph].

[101] A. Bhattacharyya, R. Ray and S. Sur, *Fluctuation of strongly interacting matter in the Polyakov–Nambu–Jona-Lasinio model in a finite volume*, Phys. Rev. D **91**, 051501(R) (2015), arXiv:1412.8316 [hep-ph].

[102] J. Braun, B. Klein and B.-J. Schaefer, *On the phase structure of QCD in a finite volume*, Phys. Lett. B **713**, 216 (2012), arXiv:1110.0849 [hep-ph].

[103] R.-A. Tripolt, J. Braun, B. Klein and B.-J. Schaefer, *Effect of fluctuations on the QCD critical point in a finite volume*, Phys. Rev. D **90**, 054012 (2014), arXiv:1308.0164 [hep-ph].

[104] L. Fister and J. M. Pawlowski, *Functional renormalization group in a finite volume*, Phys. Rev. D **92**, 076009 (2015), arXiv:1504.05166 [hep-ph].

[105] A. Juričić and B.-J. Schaefer, *Chiral Thermodynamics in a Finite Box*, Acta Phys. Polon. B Proc. Supp. **10**, 609 (2017), arXiv:1611.03653 [hep-ph].

[106] B. Klein, *Modeling finite-volume effects and chiral symmetry breaking in two-flavor QCD thermodynamics*, Phys. Rep. **707–708**, 1 (2017), arXiv:1710.05357 [hep-ph].

[107] C. S. Fischer, R. Alkofer and H. Reinhardt, *The elusiveness of infrared critical exponents in Landau gauge Yang–Mills theories*, Phys. Rev. D **65**, 094008 (2002), arXiv:hep-ph/0202195.

[108] C. S. Fischer, B. Gruter and R. Alkofer, *Solving coupled Dyson-Schwinger equations on a compact manifold*, Ann. Phys. **321**, 1918 (2006), arXiv:hep-ph/0506053.

[109] C. S. Fischer and M. R. Pennington, *Finite volume effects in a quenched lattice-QCD quark propagator*, Phys. Rev. D **73**, 034029 (2006), arXiv:hep-ph/0512233.

[110] C. S. Fischer, A. Maas, J. M. Pawlowski and L. von Smekal, *Large volume behaviour of Yang–Mills propagators*, Ann. Phys. **322**, 2916 (2007), arXiv:hep-ph/0701050.

[111] C. S. Fischer, *Deconfinement phase transition and the quark condensate*, Phys. Rev. Lett. **103**, 052003 (2009), arXiv:0904.2700 [hep-ph].

[112] C. S. Fischer and J. A. Mueller, *Chiral and deconfinement transition from Dyson-Schwinger equations*, Phys. Rev. D **80**, 074029 (2009), arXiv:0908.0007 [hep-ph].

[113] J. Luecker, C. S. Fischer and R. Williams, *Volume behaviour of quark condensate, pion mass and decay constant from Dyson-Schwinger equations*, Phys. Rev. D **81**, 094005 (2010), arXiv:0912.3686 [hep-ph].

[114] T. Goecke, C. S. Fischer and R. Williams, *Finite volume effects and dynamical chiral symmetry breaking in QED3*, Phys. Rev. B **79**, 064513 (2009), arXiv:0811.1887 [hep-ph].

[115] J. A. Bonnet, C. S. Fischer and R. Williams, *Effects of Anisotropy in QED_3 from Dyson-Schwinger equations in a box*, Phys. Rev. B **84**, 024520 (2011), arXiv:1103.1578 [hep-ph].

[116] B.-L. Li et al., *Finite volume effects on the chiral phase transition from Dyson–Schwinger equations of QCD*, Nucl. Phys. B **938**, 298 (2019), arXiv:1711.04914 [hep-ph].

[117] Y.-P. Zhao, R.-R. Zhang, H. Zhang and H.-S. Zong, *Chiral phase transition from the Dyson-Schwinger equations in a finite spherical volume*, Chin. Phys. C **43**, 063101 (2019), arXiv:1903.11243 [hep-ph].

[118] Y.-Z. Xu, C. Shi, X.-T. He and H.-S. Zong, *Chiral crossover transition from the Dyson-Schwinger equations in a sphere*, Phys. Rev. D **102**, 114011 (2020), arXiv:2009.12035 [nucl-th].

[119] C. R. Allton et al., *The QCD thermal phase transition in the presence of a small chemical potential*, Phys. Rev. D **66**, 074507 (2002), arXiv:hep-lat/0204010.

[120] R. V. Gavai and S. Gupta, *QCD at finite chemical potential with six time slices*, Phys. Rev. D **78**, 114503 (2008), arXiv:0806.2233 [hep-lat].

[121] S. Borsanyi et al., *QCD equation of state at nonzero chemical potential: continuum results with physical quark masses at order μ^2*, J. High. Energy Phys. **08**, 053 (2012), arXiv:1204.6710 [hep-lat].

[122] M. Giordano et al., *Radius of convergence in lattice QCD at finite μ_B with rooted staggered fermions*, Phys. Rev. D **101**, 074511 (2020), arXiv:1911.00043 [hep-lat].

[123] D. Bollweg et al. (HotQCD), *Taylor expansions and Padé approximants for cumulants of conserved charge fluctuations at nonvanishing chemical potentials*, Phys. Rev. D **105**, 074511 (2022), arXiv:2202.09184 [hep-lat].

[124] A. Hasenfratz and D. Toussaint, *Canonical ensembles and nonzero density quantum chromodynamics*, Nucl. Phys. B **371**, 539 (1992).

[125] Z. Fodor and S. D. Katz, *A New method to study lattice QCD at finite temperature and chemical potential*, Phys. Lett. B **534**, 87 (2002), arXiv:hep-lat/0104001.

[126] Z. Fodor and S. D. Katz, *Lattice determination of the critical point of QCD at finite T and mu*, J. High. Energy Phys. **03**, 014 (2002), arXiv:hep-lat/0106002.

[127] M. Giordano et al., *New approach to lattice QCD at finite density; results for the critical end point on coarse lattices*, J. High. Energy Phys. **05**, 088 (2020), arXiv:2004.10800 [hep-lat].

[128] C. Ratti, *Equation of state for QCD from lattice simulations*, Prog. Part. Nucl. Phys. **129**, 104007 (2023).

[129] P. de Forcrand and O. Philipsen, *The QCD phase diagram for small densities from imaginary chemical potential*, Nucl. Phys. B **642**, 290 (2002), arXiv:hep-lat/0205016.

[130] P. Dimopoulos et al., *Contribution to understanding the phase structure of strong interaction matter: Lee-Yang edge singularities from lattice QCD*, Phys. Rev. D **105**, 034513 (2022), arXiv:2110.15933 [hep-lat].

[131] S. Borsanyi et al., *Equation of state of a hot-and-dense quark gluon plasma: lattice simulations at real μ_B vs. extrapolations*, Phys. Rev. D **107**, L091503 (2022), arXiv:2208.05398 [hep-lat].

[132] S. Borsanyi et al., *Resummed lattice QCD equation of state at finite baryon density: Strangeness neutrality and beyond*, Phys. Rev. D **105**, 114504 (2022), arXiv:2202.05574 [hep-lat].

[133] R. D. Pisarski and F. Wilczek, *Remarks on the Chiral Phase Transition in Chromodynamics*, Phys. Rev. D **29**, 338 (1984).

[134] F. R. Brown et al., *On the existence of a phase transition for QCD with three light quarks*, Phys. Rev. Lett. **65**, 2491 (1990).

[135] J. Bernhardt, C. S. Fischer, P. Isserstedt and B.-J. Schaefer, *Critical endpoint of QCD in a finite volume*, Phys. Rev. D **104**, 074035 (2021), arXiv:2107.05504 [hep-ph].

[136] J. Bernhardt, C. S. Fischer and P. Isserstedt, *Finite-volume effects in baryon number fluctuations around the QCD critical endpoint*, Phys. Lett. B **841**, 137908 (2023), arXiv:2208.01981 [hep-ph].

[137] J. Bernhardt and C. S. Fischer, *From imaginary to real chemical potential QCD with functional methods*, Eur. Phys. J. A **59**, 181 (2023), arXiv:2305.01434 [hep-ph].

[138] J. Bernhardt and C. S. Fischer, *QCD phase transitions in the light quark chiral limit*, arXiv:2309.06737 [hep-ph].

[139] L. D. Faddeev and V. N. Popov, *Feynman Diagrams for the Yang-Mills Field*, Phys. Lett. B **25**, 29 (1967).

[140] L. D. Faddeev, *Feynman integral for singular Lagrangians*, Theor. Math. Phys. **1**, 1 (1969).

[141] M. Fierz, *Über die relativistische Theorie kräftefreier Teilchen mit beliebigem Spin*, Helv. Phys. Acta **12**, 3 (1939).

[142] W. Pauli, *The Connection Between Spin and Statistics*, Phys. Rev. **58**, 716 (1940).

[143] J. C. Ward, *An Identity in Quantum Electrodynamics*, Phys. Rev. **78**, 182 (1950).

[144] Y. Takahashi, *On the generalized Ward identity*, Nuovo Cim. **6**, 371 (1957).

[145] W. Pauli and F. Villars, *On the Invariant regularization in relativistic quantum theory*, Rev. Mod. Phys. **21**, 434 (1949).

[146] G. 't Hooft, *Renormalization of Massless Yang-Mills Fields*, Nucl. Phys. B **33**, 173 (1971).

[147] G. 't Hooft and M. J. G. Veltman, *Regularization and Renormalization of Gauge Fields*, Nucl. Phys. B **44**, 189 (1972).

[148] B. W. Lee and J. Zinn-Justin, *Spontaneously Broken Gauge Symmetries Part 1: Preliminaries*, Phys. Rev. D **5**, 3121 (1972).

[149] B. W. Lee and J. Zinn-Justin, *Spontaneously Broken Gauge Symmetries Part 2: Perturbation Theory and Renormalization*, Phys. Rev. D **5**, 3137 (1972).

[150] B. W. Lee and J. Zinn-Justin, *Spontaneously Broken Gauge Symmetries Part 4: General Gauge Formulation*, Phys. Rev. D **7**, 1049 (1973).

[151] A. A. Slavnov, *Ward Identities in Gauge Theories*, Theor. Math. Phys. **10**, 99 (1972).

[152] J. C. Taylor, *Ward Identities and Charge Renormalization of the Yang-Mills Field*, Nucl. Phys. B **33**, 436 (1971).

[153] R. Alkofer and L. von Smekal, *The Infrared behavior of QCD Green's functions: Confinement dynamical symmetry breaking, and hadrons as relativistic bound states*, Phys. Rep. **353**, 281 (2001), arXiv:hep-ph/0007355.

[154] E. Noether, *Invariante Variationsprobleme*, Nachr. d. König. Gesellsch. d. Wiss. zu Göttingen, Math.-Phys. Klasse **1918**, 235 (1918), arXiv:physics/0503066.

[155] J. Goldstone, *Field Theories with Superconductor Solutions*, Nuovo Cim. **19**, 154 (1961).

[156] J. Goldstone, A. Salam and S. Weinberg, *Broken Symmetries*, Phys. Rev. **127**, 965 (1962).

[157] Y. Nambu, *Quasiparticles and Gauge Invariance in the Theory of Superconductivity*, Phys. Rev. **117**, 648 (1960).

[158] M. A. Shifman, *Anomalies and Low-Energy Theorems of Quantum Chromodynamics*, Sov. Phys. Usp. **32**, 289 (1989).

[159] S. L. Adler, *Anomalies*, arXiv:hep-th/0411038.

[160] C. Abel et al., *Measurement of the Permanent Electric Dipole Moment of the Neutron*, Phys. Rev. Lett. **124**, 081803 (2020), arXiv:2001.11966 [hep-ex].

[161] M. D. Schwartz, *Quantum Field Theory and the Standard Model* (Cambridge University Press, Mar. 2014).

[162] C. Becchi, A. Rouet and R. Stora, *The Abelian Higgs-Kibble Model. Unitarity of the S Operator*, Phys. Lett. B **52**, 344 (1974).

[163] C. Becchi, A. Rouet and R. Stora, *Renormalization of the Abelian Higgs-Kibble Model*, Commun. Math. Phys. **42**, 127 (1975).

[164] C. Becchi, A. Rouet and R. Stora, *Renormalization of Gauge Theories*, Ann. Phys. **98**, 287 (1976).

[165] I. V. Tyutin, *Gauge Invariance in Field Theory and Statistical Physics in Operator Formalism*, arXiv:0812.0580 [hep-th].

[166] M. Z. Iofa and I. V. Tyutin, *Gauge Invariance of Spontaneously Broken Nonabelian Theories in the Bogolyubov-Parasiuk-HEPP-Zimmerman Method*, Teor. Mat. Fiz. **27**, 38 (1976).

[167] N. Nakanishi and I. Ojima, *Covariant operator formalism of gauge theories and quantum gravity*, Vol. 27 (1990).

[168] S. L. Adler, *Axial vector vertex in spinor electrodynamics*, Phys. Rev. **177**, 2426 (1969).

[169] J. S. Bell and R. Jackiw, *A PCAC puzzle: $\pi^0 \to \gamma\gamma$ in the σ model*, Nuovo Cim. A **60**, 47 (1969).

[170] H. Fukuda and Y. Miyamoto, *On the γ-Decay of Neutral Meson*, Prog. Theor. Phys. **4**, 347 (1949).

[171] J. Steinberger, *On the Use of subtraction fields and the lifetimes of some types of meson decay*, Phys. Rev. **76**, 1180 (1949).

[172] J. S. Schwinger, *On gauge invariance and vacuum polarization*, Phys. Rev. **82**, 664 (1951).

[173] M. A. Shifman, A. I. Vainshtein and V. I. Zakharov, *Remarks on Higgs Boson Interactions with Nucleons*, Phys. Lett. B **78**, 443 (1978).

[174] N. K. Nielsen, *Gauge Invariance and Broken Conformal Symmetry*, Nucl. Phys. B **97**, 527 (1975).

[175] J. C. Collins, A. Duncan and S. D. Joglekar, *Trace and Dilatation Anomalies in Gauge Theories*, Phys. Rev. D **16**, 438 (1977).

[176] B. L. Ioffe, *Condensates in quantum chromodynamics*, Phys. Atom. Nucl. **66**, 30 (2003), arXiv:hep-ph/0207191.

[177] M. Gell-Mann, R. J. Oakes and B. Renner, *Behavior of current divergences under SU(3) x SU(3)*, Phys. Rev. **175**, 2195 (1968).

[178] H. Fukaya et al. (JLQCD), *Determination of the chiral condensate from 2+1-flavor lattice QCD*, Phys. Rev. Lett. **104**, 122002 (2010), arXiv:0911.5555 [hep-lat].

[179] T. Kugo and I. Ojima, *Local Covariant Operator Formalism of Nonabelian Gauge Theories and Quark Confinement Problem*, Prog. Theor. Phys. Suppl. **66**, 1 (1979).

[180] D. Zwanziger, *Nonperturbative Landau gauge and infrared critical exponents in QCD*, Phys. Rev. D **65**, 094039 (2002), arXiv:hep-th/0109224.

[181] V. N. Gribov, *Quantization of Nonabelian Gauge Theories*, Nucl. Phys. B **139**, 1 (1978).

[182] A. P. Szczepaniak and E. S. Swanson, *Coulomb gauge QCD, confinement, and the constituent representation*, Phys. Rev. D **65**, 025012 (2001), arXiv:hep-ph/0107078.

[183] J. Greensite and S. Olejnik, *Coulomb energy, vortices, and confinement*, Phys. Rev. D **67**, 094503 (2003), arXiv:hep-lat/0302018.

[184] D. Zwanziger, *Analytic calculation of color Coulomb potential*, Phys. Rev. D **70**, 094034 (2004), arXiv:hep-ph/0312254.

[185] C. Feuchter and H. Reinhardt, *Variational solution of the Yang-Mills Schrodinger equation in Coulomb gauge*, Phys. Rev. D **70**, 105021 (2004), arXiv:hep-th/0408236.

[186] D. Zwanziger, *Vanishing of zero momentum lattice gluon propagator and color confinement*, Nucl. Phys. B **364**, 127 (1991).

[187] D. Zwanziger, *Renormalizability of the critical limit of lattice gauge theory by BRS invariance*, Nucl. Phys. B **399**, 477 (1993).

[188] C. Gattringer and C. B. Lang, *Quantum Chromodynamics on the Lattice*, Vol. 788, Lecture Notes in Physics (Springer, Berlin, 2010).

[189] O. Philipsen, *Lattice Constraints on the QCD Chiral Phase Transition at Finite Temperature and Baryon Density*, Symmetry **13**, 2079 (2021), arXiv:2111.03590 [hep-lat].

[190] A. Haar, *Der Massbegriff in der Theorie der Kontinuierlichen Gruppen*, Ann. Math. **34**, 147 (1933).

[191] K. G. Wilson, *Confinement of Quarks*, Phys. Rev. D **10**, 2445 (1974).

[192] H. B. Nielsen and M. Ninomiya, *Absence of Neutrinos on a Lattice. 1. Proof by Homotopy Theory*, Nucl. Phys. B **185**, 20 (1981).

[193] H. B. Nielsen and M. Ninomiya, *Absence of Neutrinos on a Lattice. 2. Intuitive Topological Proof*, Nucl. Phys. B **193**, 173 (1981).

[194] H. B. Nielsen and M. Ninomiya, *No Go Theorem for Regularizing Chiral Fermions*, Phys. Lett. B **105**, 219 (1981).

[195] P. H. Ginsparg and K. G. Wilson, *A Remnant of Chiral Symmetry on the Lattice*, Phys. Rev. D **25**, 2649 (1982).

[196] H. Neuberger, *Exactly massless quarks on the lattice*, Phys. Lett. B **417**, 141 (1998), arXiv:hep-lat/9707022.

[197] H. Neuberger, *More about exactly massless quarks on the lattice*, Phys. Lett. B **427**, 353 (1998), arXiv:hep-lat/9801031.

[198] J. B. Kogut and L. Susskind, *Hamiltonian Formulation of Wilson's Lattice Gauge Theories*, Phys. Rev. D **11**, 395 (1975).

[199] D. B. Kaplan, *A Method for simulating chiral fermions on the lattice*, Phys. Lett. B **288**, 342 (1992), arXiv:hep-lat/9206013.

[200] Y. Shamir, *Chiral fermions from lattice boundaries*, Nucl. Phys. B **406**, 90 (1993), arXiv:hep-lat/9303005.

[201] R. Frezzotti, P. A. Grassi, S. Sint and P. Weisz (Alpha), *Lattice QCD with a chirally twisted mass term*, J. High. Energy Phys. **08**, 058 (2001), arXiv:hep-lat/0101001.

[202] H. Leutwyler and A. V. Smilga, *Spectrum of Dirac operator and role of winding number in QCD*, Phys. Rev. D **46**, 5607 (1992).

[203] P. Hasenfratz and F. Karsch, *Chemical Potential on the Lattice*, Phys. Lett. B **125**, 308 (1983).

[204] E. E. Salpeter and H. A. Bethe, *A Relativistic equation for bound state problems*, Phys. Rev. **84**, 1232 (1951).

[205] L. Faddeev and S. Merkuriev, *Quantum Scattering Theory for Several Particle Systems*, Mathematical Physics and Applied Mathematics (Springer Netherlands, 1993).

[206] C. S. Fischer, S. Kubrak and R. Williams, *Mass spectra and Regge trajectories of light mesons in the Bethe-Salpeter approach*, Eur. Phys. J. A **50**, 126 (2014), arXiv:1406.4370 [hep-ph].

[207] G. Eichmann et al., *Baryons as relativistic three-quark bound states*, Prog. Part. Nucl. Phys. **91**, 1 (2016), arXiv:1606.09602 [hep-ph].

[208] G. Eichmann et al., *Four-Quark States from Functional Methods*, Few Body Syst. **61**, 38 (2020), arXiv:2008.10240 [hep-ph].

[209] M. Q. Huber, C. S. Fischer and H. Sanchis-Alepuz, *Spectrum of scalar and pseudoscalar glueballs from functional methods*, Eur. Phys. J. C **80**, 1077 (2020), arXiv:2004.00415 [hep-ph].

[210] C. S. Fischer, R. Alkofer, T. Dahm and P. Maris, *Dynamical chiral symmetry breaking in unquenched QED(3)*, Phys. Rev. D **70**, 073007 (2004), arXiv:hep-ph/0407104.

[211] C. S. Fischer, T. Goecke and R. Williams, *A fresh look at hadronic light-by-light scattering in the muon g-2 with the Dyson-Schwinger approach*, Eur. Phys. J. A **47**, 28 (2011), arXiv:1009.5297 [hep-ph].

[212] G. Eichmann, C. S. Fischer, E. Weil and R. Williams, *Single pseudoscalar meson pole and pion box contributions to the anomalous magnetic moment of the muon*, Phys. Lett. B **797**, 134855 (2019), arXiv:1903.10844 [hep-ph].

[213] G. Eichmann, C. S. Fischer, E. Weil and R. Williams, *On the large-Q^2 behavior of the pion transition form factor*, Phys. Lett. B **774**, 425 (2017), arXiv:1704.05774 [hep-ph].

[214] E. Weil, G. Eichmann, C. S. Fischer and R. Williams, *Electromagnetic decays of the neutral pion investigated in the Dyson-Schwinger formalism*, J. Phys. Conf. Ser. **1024**, 012032 (2018), arXiv:1710.08169 [hep-ph].

[215] C. D. Roberts and A. G. Williams, *Dyson-Schwinger equations and their application to hadronic physics*, Prog. Part. Nucl. Phys. **33**, 477 (1994), arXiv:hep-ph/9403224.

[216] C. D. Roberts and S. M. Schmidt, *Dyson-Schwinger equations: Density, temperature and continuum strong QCD*, Prog. Part. Nucl. Phys. **45**, S1 (2000), arXiv:nucl-th/0005064.

[217] M. Q. Huber and M. Mitter, *CrasyDSE: A Framework for solving Dyson-Schwinger equations*, Comput. Phys. Commun. **183**, 2441 (2012), arXiv:1112.5622 [hep-th].

[218] M. Q. Huber, A. K. Cyrol and J. M. Pawlowski, *DoFun 3.0: Functional equations in Mathematica*, Comput. Phys. Commun. **248**, 107058 (2020), arXiv:1908.02760 [hep-ph].

[219] J. Berges, *N-particle irreducible effective action techniques for gauge theories*, Phys. Rev. D **70**, 105010 (2004), arXiv:hep-ph/0401172.

[220] M. E. Carrington and Y. Guo, *Techniques for n-Particle Irreducible Effective Theories*, Phys. Rev. D **83**, 016006 (2011), arXiv:1010.2978 [hep-ph].

[221] P. Isserstedt, C. S. Fischer and T. Steinert, *Thermodynamics from the quark condensate*, Phys. Rev. D **103**, 054012 (2021), arXiv:2012.04991 [hep-ph].

[222] C. S. Fischer and R. Alkofer, *Nonperturbative propagators, running coupling and dynamical quark mass of Landau gauge QCD*, Phys. Rev. D **67**, 094020 (2003), arXiv:hep-ph/0301094.

[223] C. Lerche and L. von Smekal, *On the infrared exponent for gluon and ghost propagation in Landau gauge QCD*, Phys. Rev. D **65**, 125006 (2002), arXiv:hep-ph/0202194.

[224] R. Alkofer, C. S. Fischer and F. J. Llanes-Estrada, *Vertex functions and infrared fixed point in Landau gauge SU(N) Yang-Mills theory*, Phys. Lett. B **611**, 279 (2005), arXiv:hep-th/0412330.

[225] C. S. Fischer and J. M. Pawlowski, *Uniqueness of infrared asymptotics in Landau gauge Yang-Mills theory*, Phys. Rev. D **75**, 025012 (2007), arXiv:hep-th/0609009.

[226] C. S. Fischer and J. M. Pawlowski, *Uniqueness of infrared asymptotics in Landau gauge Yang-Mills theory II*, Phys. Rev. D **80**, 025023 (2009), arXiv:0903.2193 [hep-th].

[227] R. Williams, *The quark-gluon vertex in Landau gauge bound-state studies*, Eur. Phys. J. A **51**, 57 (2015), arXiv:1404.2545 [hep-ph].

[228] R. Contant and M. Q. Huber, *Phase structure and propagators at nonvanishing temperature for QCD and QCD-like theories*, Phys. Rev. D **96**, 074002 (2017), arXiv:1706.00943 [hep-ph].

[229] M. Q. Huber, *Correlation functions of Landau gauge Yang-Mills theory*, Phys. Rev. D **101**, 114009 (2020), arXiv:2003.13703 [hep-ph].

[230] M. Q. Huber, *On non-primitively divergent vertices of Yang–Mills theory*, Eur. Phys. J. C **77**, 733 (2017), arXiv:1709.05848 [hep-ph].

[231] M. Q. Huber, C. S. Fischer and H. Sanchis-Alepuz, *Higher spin glueballs from functional methods*, Eur. Phys. J. C **81**, 1083 (2021), arXiv:2110.09180 [hep-ph].

[232] R. Williams, C. S. Fischer and W. Heupel, *Light mesons in QCD and unquenching effects from the 3PI effective action*, Phys. Rev. D **93**, 034026 (2016), arXiv:1512.00455 [hep-ph].

[233] O. Oliveira, W. de Paula, T. Frederico and J. P. B. C. de Melo, *The Quark-Gluon Vertex and the QCD Infrared Dynamics*, Eur. Phys. J. C **79**, 116 (2019), arXiv:1807.10348 [hep-ph].

[234] C. A. Welzbacher, *Quarks and gluons in the phase diagram of quantum chromodynamics*, PhD thesis (Justus-Liebig-Universität Gießen, 2016).

[235] R. Contant et al., *On the quark-gluon vertex at non-vanishing temperature*, Acta Phys. Polon. Supp. **11**, 483 (2018), arXiv:1805.05885 [hep-ph].

[236] M. Q. Huber and L. von Smekal, *On two- and three-point functions of Landau gauge Yang-Mills theory*, Proc. Sci. **LATTICE2013**, 364 (2014), arXiv:1311.0702 [hep-lat].

[237] R. W. Haymaker, *Variational methods for composite operators*, Riv. Nuovo Cim. **14N8**, 1 (1991).

[238] F. Gao et al., *Phase diagram and thermal properties of strong-interaction matter*, Phys. Rev. D **93**, 094019 (2016), arXiv:1507.00875 [nucl-th].

[239] T. F. Motta, J. Bernhardt, M. Buballa and C. S. Fischer, *Towards a Stability Analysis of Inhomogeneous Phases in QCD*, arXiv:2306.09749 [hep-ph].

[240] C. Shi et al., *Locate QCD Critical End Point in a Continuum Model Study*, J. High. Energy Phys. **07**, 014 (2014), arXiv:1403.3797 [hep-ph].

[241] J. S. Ball and T.-W. Chiu, *Analytic Properties of the Vertex Function in Gauge Theories. 1.* Phys. Rev. D **22**, 2542 (1980).

[242] A. Maas, *Gluons at finite temperature in Landau gauge Yang-Mills theory*, Mod. Phys. Lett. A **20**, 1797 (2005), arXiv:hep-ph/0506066.

[243] A. Maas, *Describing gauge bosons at zero and finite temperature*, Phys. Rep. **524**, 203 (2013), arXiv:1106.3942 [hep-ph].

[244] W. Heupel, T. Goecke and C. S. Fischer, *Beyond Rainbow-Ladder in bound state equations*, Eur. Phys. J. A **50**, 85 (2014), arXiv:1402.5042 [hep-ph].

[245] C. S. Fischer, A. Maas and J. A. Muller, *Chiral and deconfinement transition from correlation functions: SU(2) vs. SU(3)*, Eur. Phys. J. C **68**, 165 (2010), arXiv:1003.1960 [hep-ph].

[246] C. S. Fischer and J. Luecker, *Propagators and phase structure of Nf=2 and Nf=2+1 QCD*, Phys. Lett. B **718**, 1036 (2013), arXiv:1206.5191 [hep-ph].

[247] G. Eichmann, C. S. Fischer and C. A. Welzbacher, *Baryon effects on the location of QCD's critical end point*, Phys. Rev. D **93**, 034013 (2016), arXiv:1509.02082 [hep-ph].

[248] P. J. Gunkel, C. S. Fischer and P. Isserstedt, *Quarks and light (pseudo-)scalar mesons at finite chemical potential*, Eur. Phys. J. A **55**, 169 (2019), arXiv:1907.08110 [hep-ph].

[249] P. J. Gunkel and C. S. Fischer, *Masses and decay constants of (axial-)vector mesons at finite chemical potential*, Eur. Phys. J. A **57**, 147 (2021), arXiv:2012.01957 [hep-ph].

[250] C. S. Fischer, J. Luecker and J. A. Mueller, *Chiral and deconfinement phase transitions of two-flavour QCD at finite temperature and chemical potential*, Phys. Lett. B **702**, 438 (2011), arXiv:1104.1564 [hep-ph].

[251] C. S. Fischer and J. A. Mueller, *On critical scaling at the QCD N_f = 2 chiral phase transition*, Phys. Rev. D **84**, 054013 (2011), arXiv:1106.2700 [hep-ph].

[252] C. S. Fischer, L. Fister, J. Luecker and J. M. Pawlowski, *Polyakov loop potential at finite density*, Phys. Lett. B **732**, 273 (2014), arXiv:1306.6022 [hep-ph].

[253] C. S. Fischer, J. Luecker and J. M. Pawlowski, *Phase structure of QCD for heavy quarks*, Phys. Rev. D **91**, 014024 (2015), arXiv:1409.8462 [hep-ph].

[254] J. A. Müller, *A Dyson-Schwinger Approach to Finite Temperature QCD*, PhD thesis (Technische Universität Darmstadt, 2011).

[255] J. Lücker, *Chiral and deconfinement phase transitions in $N_f = 2$ and $N_f = 2 + 1$ quantum chromodynamics*, PhD thesis (Justus-Liebig-Universität Gießen, 2013).

[256] D. Müller, *QCD at finite density with Dyson-Schwinger equations*, PhD thesis (Technische Universität Darmstadt, 2013).

[257] P. Büscher, *Phase diagram of two-color QCD in a Dyson-Schwinger approach*, PhD thesis (Technische Universität Darmstadt, 2014).

[258] A. Maas, J. M. Pawlowski, L. von Smekal and D. Spielmann, *The Gluon propagator close to criticality*, Phys. Rev. D **85**, 034037 (2012), arXiv:1110.6340 [hep-lat].

[259] J. I. Skullerud et al., *Nonperturbative structure of the quark gluon vertex*, J. High. Energy Phys. **04**, 047 (2003), arXiv:hep-ph/0303176.

[260] J. Marques et al., *The quark propagator and quark-gluon vertex from lattice QCD at finite temperature*, Proc. Sci. **LATTICE2022**, 280 (2023), arXiv:2301.10607 [hep-lat].

[261] F. Gao and J. M. Pawlowski, *Phase structure of 2+1-flavour QCD and the magnetic equation of state*, Phys. Rev. D **105**, 094020 (2021), arXiv:2112.01395 [hep-ph].

[262] E. Eichten and F. Feinberg, *Dynamical Symmetry Breaking of Nonabelian Gauge Symmetries*, Phys. Rev. D **10**, 3254 (1974).

[263] R. Alkofer, C. S. Fischer, F. J. Llanes-Estrada and K. Schwenzer, *The Quark-gluon vertex in Landau gauge QCD: Its role in dynamical chiral symmetry breaking and quark confinement*, Ann. Phys. **324**, 106 (2009), arXiv:0804.3042 [hep-ph].

[264] I. L. Bogolubsky, E. M. Ilgenfritz, M. Muller-Preussker and A. Sternbeck, *Lattice gluodynamics computation of Landau gauge Green's functions in the deep infrared*, Phys. Lett. B **676**, 69 (2009), arXiv:0901.0736 [hep-lat].

[265] A. C. Aguilar, J. C. Cardona, M. N. Ferreira and J. Papavassiliou, *Non-Abelian Ball-Chiu vertex for arbitrary Euclidean momenta*, Phys. Rev. D **96**, 014029 (2017), arXiv:1610.06158 [hep-ph].

[266] O. Oliveira, T. Frederico and W. de Paula, *The soft-gluon limit and the infrared enhancement of the quark-gluon vertex*, Eur. Phys. J. C **80**, 484 (2020), arXiv:2006.04982 [hep-ph].

[267] L. Fister and J. M. Pawlowski, *Yang-Mills correlation functions at finite temperature*, arXiv:1112.5440 [hep-ph].

[268] A. K. Cyrol, M. Mitter, J. M. Pawlowski and N. Strodthoff, *Nonperturbative finite-temperature Yang-Mills theory*, Phys. Rev. D **97**, 054015 (2018), arXiv:1708.03482 [hep-ph].

[269] L. P. Kaptari, *Temperature Dependence of Gluon and Ghost Propagators in a Dyson-Schwinger Equations context*, arXiv:2212.07173 [hep-ph].

[270] P. Boucaud et al., *Quark propagator and vertex: Systematic corrections of hypercubic artifacts from lattice simulations*, Phys. Lett. B **575**, 256 (2003), arXiv:hep-lat/0307026.

[271] F. de Soto and C. Roiesnel, *On the reduction of hypercubic lattice artifacts*, J. High. Energy Phys. **09**, 007 (2007), arXiv:0705.3523 [hep-lat].

[272] J. Simeth et al., *Using NSPT for the Removal of Hypercubic Lattice Artifacts*, Proc. Sci. **LATTICE2014**, 294 (2015), arXiv:1501.06322 [hep-lat].

[273] C. S. Fischer, *Nonperturbative propagators, running coupling and dynamical mass generation in ghost - anti-ghost symmetric gauges in QCD*, PhD thesis (Eberhard Karls Universität Tübingen, 2003), arXiv:hep-ph/0304233.

[274] A. Cucchieri, A. Maas and T. Mendes, *Infrared properties of propagators in Landau-gauge pure Yang-Mills theory at finite temperature*, Phys. Rev. D **75**, 076003 (2007), arXiv:hep-lat/0702022.

[275] V. G. Bornyakov and V. K. Mitrjushkin, *Lattice QCD gluon propagators near transition temperature*, Int. J. Mod. Phys. A **27**, 1250050 (2012), arXiv:1103.0442 [hep-lat].

[276] R. Aouane et al., *Landau gauge gluon and ghost propagators at finite temperature from quenched lattice QCD*, Phys. Rev. D **85**, 034501 (2012), arXiv:1108.1735 [hep-lat].

[277] R. Bellwied et al., *The QCD phase diagram from analytic continuation*, Phys. Lett. B **751**, 559 (2015), arXiv:1507.07510 [hep-lat].

[278] C. Bonati et al., *Curvature of the pseudocritical line in QCD: Taylor expansion matches analytic continuation*, Phys. Rev. D **98**, 054510 (2018), arXiv:1805.02960 [hep-lat].

[279] K. Xu and M. Huang, *Zero-mode contribution and quantized first-order apparent phase transition in a droplet quark matter*, Phys. Rev. D **101**, 074001 (2020), arXiv:1903.08416 [hep-ph].

[280] P. Maris and P. C. Tandy, *Bethe-Salpeter study of vector meson masses and decay constants*, Phys. Rev. C **60**, 055214 (1999), arXiv:nucl-th/9905056.

[281] M. Asakawa and M. Kitazawa, *Fluctuations of conserved charges in relativistic heavy ion collisions: An introduction*, Prog. Part. Nucl. Phys. **90**, 299 (2016), arXiv:1512.05038 [nucl-th].

[282] V. Koch, *Hadronic Fluctuations and Correlations*, in *Relativistic Heavy Ion Physics* (Springer, 2010), arXiv:0810.2520 [nucl-th].

[283] F. Gao and Y.-x. Liu, *Interface Effect in QCD Phase Transitions via Dyson-Schwinger Equation Approach*, Phys. Rev. D **94**, 094030 (2016), arXiv:1609.08038 [hep-ph].

[284] J. I. Kapusta and C. Gale, *Finite-Temperature Field Theory: Principles and Applications*, Cambridge Monographs on Mathematical Physics (Cambridge University Press, 2011).

[285] R. Contant, *Phase structures of QCD and QCD-like theories*, PhD thesis (Karl-Franzens-Universität Graz, 2019).

[286] R. Bellwied et al., *Fluctuations and correlations in high temperature QCD*, Phys. Rev. D **92**, 114505 (2015), arXiv:1507.04627 [hep-lat].

[287] C. S. Fischer, D. Nickel and J. Wambach, *Hadronic unquenching effects in the quark propagator*, Phys. Rev. D **76**, 094009 (2007), arXiv:0705.4407 [hep-ph].

[288] C. S. Fischer and R. Williams, *Beyond the rainbow: Effects from pion back-coupling*, Phys. Rev. D **78**, 074006 (2008), arXiv:0808.3372 [hep-ph].

[289] C. S. Fischer, D. Nickel and R. Williams, *On Gribov's supercriticality picture of quark confinement*, Eur. Phys. J. C **60**, 47 (2009), arXiv:0807.3486 [hep-ph].

[290] B.-J. Schaefer, J. M. Pawlowski and J. Wambach, *Phase structure of the Polyakov–quark-meson model*, Phys. Rev. D **76**, 074023 (2007), arXiv:0704.3234 [hep-ph].

[291] V. Alonso, S. D. Vincenzo and L. Mondino, *On the boundary conditions for the Dirac equation*, Eur. J. Phys. **18**, 315 (1997).

[292] A. Chodos et al., *A New Extended Model of Hadrons*, Phys. Rev. D **9**, 3471 (1974).

[293] A. Chodos, R. L. Jaffe, K. Johnson and C. B. Thorn, *Baryon Structure in the Bag Theory*, Phys. Rev. D **10**, 2599 (1974).

[294] Z. Zhang, C. Shi and H. Zong, *Nambu-Jona-Lasinio model in a sphere*, Phys. Rev. D **101**, 043006 (2020), arXiv:1908.08671 [hep-ph].

[295] W. Greiner, S. Schramm and E. Stein, *Quantum Chromodynamics*, 3rd ed. (Springer, 2007).

[296] G. 't Hooft, *On the Phase Transition Towards Permanent Quark Confinement*, Nucl. Phys. B **138**, 1 (1978).

[297] A. M. Polyakov, *Thermal Properties of Gauge Fields and Quark Liberation*, Phys. Lett. B **72**, 477 (1978).

[298] K. Fukushima and V. Skokov, *Polyakov loop modeling for hot QCD*, Prog. Part. Nucl. Phys. **96**, 154 (2017), arXiv:1705.00718 [hep-ph].

[299] A. Roberge and N. Weiss, *Gauge Theories With Imaginary Chemical Potential and the Phases of QCD*, Nucl. Phys. B **275**, 734 (1986).

[300] C. Bonati et al., *Curvature of the chiral pseudocritical line in QCD: Continuum extrapolated results*, Phys. Rev. D **92**, 054503 (2015), arXiv:1507.03571 [hep-lat].

[301] C.-N. Yang and T. D. Lee, *Statistical theory of equations of state and phase transitions. 1. Theory of condensation*, Phys. Rev. **87**, 404 (1952).

[302] T. D. Lee and C.-N. Yang, *Statistical theory of equations of state and phase transitions. 2. Lattice gas and Ising model*, Phys. Rev. **87**, 410 (1952).

[303] M. E. Fisher, *Yang-Lee Edge Singularity and ϕ^3 Field Theory*, Phys. Rev. Lett. **40**, 1610 (1978).

[304] P. de Forcrand and O. Philipsen, *Constraining the QCD phase diagram by tricritical lines at imaginary chemical potential*, Phys. Rev. Lett. **105**, 152001 (2010), arXiv:1004.3144 [hep-lat].

[305] H. Saito et al. (WHOT-QCD), *Phase structure of finite temperature QCD in the heavy quark region*, Phys. Rev. D **84**, 054502 (2011), arXiv:1106.0974 [hep-lat].

[306] M. Fromm, J. Langelage, S. Lottini and O. Philipsen, *The QCD deconfinement transition for heavy quarks and all baryon chemical potentials*, J. High. Energy Phys. **01**, 042 (2012), arXiv:1111.4953 [hep-lat].

[307] S. Ejiri et al. (WHOT-QCD), *End point of the first-order phase transition of QCD in the heavy quark region by reweighting from quenched QCD*, Phys. Rev. D **101**, 054505 (2020), arXiv:1912.10500 [hep-lat].

[308] F. Cuteri, O. Philipsen, A. Schön and A. Sciarra, *Deconfinement critical point of lattice QCD with $N_f = 2$ Wilson fermions*, Phys. Rev. D **103**, 014513 (2021), arXiv:2009.14033 [hep-lat].

[309] A. Kiyohara, M. Kitazawa, S. Ejiri and K. Kanaya, *Finite-size scaling around the critical point in the heavy quark region of QCD*, Phys. Rev. D **104**, 114509 (2021), arXiv:2108.00118 [hep-lat].

[310] K. Kashiwa, R. D. Pisarski and V. V. Skokov, *Critical endpoint for deconfinement in matrix and other effective models*, Phys. Rev. D **85**, 114029 (2012), arXiv:1205.0545 [hep-ph].

[311] P. M. Lo, B. Friman and K. Redlich, *Polyakov loop fluctuations and deconfinement in the limit of heavy quarks*, Phys. Rev. D **90**, 074035 (2014), arXiv:1406.4050 [hep-ph].

[312] U. Reinosa, J. Serreau and M. Tissier, *Perturbative study of the QCD phase diagram for heavy quarks at nonzero chemical potential*, Phys. Rev. D **92**, 025021 (2015), arXiv:1504.02916 [hep-th].

[313] J. Maelger, U. Reinosa and J. Serreau, *Perturbative study of the QCD phase diagram for heavy quarks at nonzero chemical potential: Two-loop corrections*, Phys. Rev. D **97**, 074027 (2018), arXiv:1710.01930 [hep-ph].

[314] B. B. Brandt et al., *On the strength of the $U_A(1)$ anomaly at the chiral phase transition in $N_f = 2$ QCD*, J. High. Energy Phys. **12**, 158 (2016), arXiv:1608.06882 [hep-lat].

[315] A. Tomiya et al., *Evidence of effective axial U(1) symmetry restoration at high temperature QCD*, Phys. Rev. D **96**, 034509 (2017), arXiv:1612.01908 [hep-lat].

[316] S. Aoki et al. (JLQCD), *Role of the axial U(1) anomaly in the chiral susceptibility of QCD at high temperature*, Prog. Theor. Exp. Phys. **2022**, 023B05 (2022), arXiv:2103.05954 [hep-lat].

[317] A. Bazavov et al. (HotQCD), *The chiral transition and $U(1)_A$ symmetry restoration from lattice QCD using Domain Wall Fermions*, Phys. Rev. D **86**, 094503 (2012), arXiv:1205.3535 [hep-lat].

[318] M. I. Buchoff et al., *QCD chiral transition, U(1)A symmetry and the dirac spectrum using domain wall fermions*, Phys. Rev. D **89**, 054514 (2014), arXiv:1309.4149 [hep-lat].

[319] T. Bhattacharya et al., *QCD Phase Transition with Chiral Quarks and Physical Quark Masses*, Phys. Rev. Lett. **113**, 082001 (2014), arXiv:1402.5175 [hep-lat].

[320] V. Dick et al., *Microscopic origin of $U_A(1)$ symmetry violation in the high temperature phase of QCD*, Phys. Rev. D **91**, 094504 (2015), arXiv:1502.06190 [hep-lat].

[321] H. .-. Ding et al., *Correlated Dirac Eigenvalues and Axial Anomaly in Chiral Symmetric QCD*, Phys. Rev. Lett. **126**, 082001 (2021), arXiv:2010.14836 [hep-lat].

[322] O. Kaczmarek, L. Mazur and S. Sharma, *Eigenvalue spectra of QCD and the fate of UA(1) breaking towards the chiral limit*, Phys. Rev. D **104**, 094518 (2021), arXiv:2102.06136 [hep-lat].

[323] A. Butti, A. Pelissetto and E. Vicari, *On the nature of the finite temperature transition in QCD*, J. High. Energy Phys. **08**, 029 (2003), arXiv:hep-ph/0307036 [hep-ph].

[324] P. de Forcrand and M. D'Elia, *Continuum limit and universality of the Columbia plot*, Proc. Sci. **LATTICE2016**, 081 (2017), arXiv:1702.00330 [hep-lat].

[325] Y. Iwasaki, K. Kanaya, S. Kaya and T. Yoshie, *Scaling of chiral order parameter in two flavor QCD*, Phys. Rev. Lett. **78**, 179 (1997), arXiv:hep-lat/9609022 [hep-lat].

[326] M. D'Elia, A. Di Giacomo and C. Pica, *On the order of the deconfining transition in N(f) = 2 QCD*, Int. J. Mod. Phys. A **20**, 4579 (2005), arXiv:hep-lat/0408011 [hep-lat].

[327] M. D'Elia, A. Di Giacomo and C. Pica, *Two flavor QCD and confinement*, Phys. Rev. D **72**, 114510 (2005), arXiv:hep-lat/0503030 [hep-lat].

[328] J. B. Kogut and D. K. Sinclair, *Evidence for O(2) universality at the finite temperature transition for lattice QCD with 2 flavors of massless staggered quarks*, Phys. Rev. D **73**, 074512 (2006), arXiv:hep-lat/0603021 [hep-lat].

[329] C. Bonati et al., *Chiral phase transition in two-flavor QCD from an imaginary chemical potential*, Phys. Rev. D **90**, 074030 (2014), arXiv:1408.5086 [hep-lat].

[330] O. Philipsen and C. Pinke, *The $N_f = 2$ QCD chiral phase transition with Wilson fermions at zero and imaginary chemical potential*, Phys. Rev. D **93**, 114507 (2016), arXiv:1602.06129 [hep-lat].

[331] F. Cuteri, O. Philipsen and A. Sciarra, *QCD chiral phase transition from noninteger numbers of flavors*, Phys. Rev. D **97**, 114511 (2018), arXiv:1711.05658 [hep-lat].

[332] H. T. Ding et al., *Chiral phase transition of (2+1)-flavor QCD*, in 27th International Conference on Ultrarelativistic Nucleus-Nucleus Collisions (Quark Matter 2018) Venice, Italy, May 14-19, 2018 (2018), arXiv:1807.05727 [hep-lat].

[333] J. T. Lenaghan, *Influence of the U(1)(A) anomaly on the QCD phase transition*, Phys. Rev. D **63**, 037901 (2001), arXiv:hep-ph/0005330 [hep-ph].

[334] P. Kovacs and Z. Szep, *The critical surface of the $SU(3)_L x SU(3)_R$ chiral quark model at non-zero baryon density*, Phys. Rev. D **75**, 025015 (2007), arXiv:hep-ph/0611208 [hep-ph].

[335] K. Fukushima, *Phase diagrams in the three-flavor Nambu-Jona-Lasinio model with the Polyakov loop*, Phys. Rev. D **77**, 114028 (2008), arXiv:0803.3318 [hep-ph].

[336] B.-J. Schaefer and M. Wagner, *The Three-flavor chiral phase structure in hot and dense QCD matter*, Phys. Rev. D **79**, 014018 (2009), arXiv:0808.1491 [hep-ph].

[337] M. Mitter and B.-J. Schaefer, *Fluctuations and the axial anomaly with three quark flavors*, Phys. Rev. D **89**, 054027 (2014), arXiv:1308.3176 [hep-ph].

[338] M. Grahl and D. H. Rischke, *Functional renormalization group study of the two-flavor linear sigma model in the presence of the axial anomaly*, Phys. Rev. D **88**, 056014 (2013), arXiv:1307.2184 [hep-th].

[339] J. Eser, M. Grahl and D. H. Rischke, *Functional Renormalization Group Study of the Chiral Phase Transition Including Vector and Axial-vector Mesons*, Phys. Rev. D **92**, 096008 (2015), arXiv:1508.06928 [hep-ph].

[340] S. Resch, F. Rennecke and B.-J. Schaefer, *Mass sensitivity of the three-flavor chiral phase transition*, Phys. Rev. D **99**, 076005 (2017), arXiv:1712.07961 [hep-ph].

[341] J. Braun, L. M. Haas, F. Marhauser and J. M. Pawlowski, *Phase Structure of Two-Flavor QCD at Finite Chemical Potential*, Phys. Rev. Lett. **106**, 022002 (2011), arXiv:0908.0008 [hep-ph].

[342] J. Braun et al., *Chiral susceptibility in (2+1)-flavor QCD*, Phys. Rev. D **102**, 056010 (2020), arXiv:2003.13112 [hep-ph].

[343] F. Karsch, E. Laermann and C. Schmidt, *The Chiral critical point in three-flavor QCD*, Phys. Lett. B **520**, 41 (2001), arXiv:hep-lat/0107020 [hep-lat].

[344] F. Karsch et al., *Where is the chiral critical point in three flavor QCD?*, Nucl. Phys. Proc. Suppl. **129**, 614 (2004), arXiv:hep-lat/0309116 [hep-lat].

[345] P. de Forcrand, S. Kim and O. Philipsen, *A QCD chiral critical point at small chemical potential: Is it there or not?*, Proc. Sci. **LATTICE2007**, 178 (2007), arXiv:0711.0262 [hep-lat].

[346] H. .-. Ding et al., *Exploring phase diagram of $N_f = 3$ QCD at $\mu = 0$ with HISQ fermions*, Proc. Sci. **LATTICE2011**, 191 (2011), arXiv:1111.0185 [hep-lat].

[347] X.-Y. Jin et al., *Critical endpoint of the finite temperature phase transition for three flavor QCD*, Phys. Rev. D **91**, 014508 (2015), arXiv:1411.7461 [hep-lat].

[348] S. Takeda et al., *Update on Nf=3 finite temperature QCD phase structure with Wilson-Clover fermion action*, Proc. Sci. **LATTICE2016**, 384 (2017), arXiv:1612.05371 [hep-lat].

[349] A. Bazavov et al., *Chiral phase structure of three flavor QCD at vanishing baryon number density*, Phys. Rev. D **95**, 074505 (2017), arXiv:1701.03548 [hep-lat].

[350] F. Cuteri, O. Philipsen and A. Sciarra, *On the order of the QCD chiral phase transition for different numbers of quark flavours*, J. High. Energy Phys. **11**, 141 (2021), arXiv:2107.12739 [hep-lat].

[351] L. Dini et al., *Chiral phase transition in three-flavor QCD from lattice QCD*, Phys. Rev. D **105**, 034510 (2022), arXiv:2111.12599 [hep-lat].

[352] G. Fejos, *Second-order chiral phase transition in three-flavor quantum chromodynamics?*, Phys. Rev. D **105**, L071506 (2022), arXiv:2201.07909 [hep-ph].

[353] P. de Forcrand and O. Philipsen, *The Chiral critical line of N(f) = 2+1 QCD at zero and non-zero baryon density*, J. High. Energy Phys. **01**, 077 (2007), arXiv:hep-lat/0607017.

[354] H. Sanchis-Alepuz, C. S. Fischer and S. Kubrak, *Pion cloud effects on baryon masses*, Phys. Lett. B **733**, 151 (2014), arXiv:1401.3183 [hep-ph].

[355] D. T. Son and M. A. Stephanov, *Pion propagation near the QCD chiral phase transition*, Phys. Rev. Lett. **88**, 202302 (2002), arXiv:hep-ph/0111100 [hep-ph].

[356] P. Maris, C. D. Roberts, S. M. Schmidt and P. C. Tandy, *T - dependence of pseudoscalar and scalar correlations*, Phys. Rev. C **63**, 025202 (2001), arXiv:nucl-th/0001064 [nucl-th].

[357] P. Maris and C. D. Roberts, *Pi- and K meson Bethe-Salpeter amplitudes*, Phys. Rev. C **56**, 3369 (1997), arXiv:nucl-th/9708029 [nucl-th].

[358] P. Maris, C. D. Roberts and P. C. Tandy, *Pion mass and decay constant*, Phys. Lett. B **420**, 267 (1998), arXiv:nucl-th/9707003.

[359] H. Pagels and S. Stokar, *The Pion Decay Constant, Electromagnetic Form-Factor and Quark Electromagnetic Selfenergy in QCD*, Phys. Rev. D **20**, 2947 (1979).

[360] J. Gasser and G. R. S. Zarnauskas, *On the pion decay constant*, Phys. Lett. B **693**, 122 (2010), arXiv:1008.3479 [hep-ph].

[361] H. T. Ding et al. (HotQCD), *Chiral Phase Transition Temperature in (2+1)-Flavor QCD*, Phys. Rev. Lett. **123**, 062002 (2019), arXiv:1903.04801 [hep-lat].

[362] J. Braun, B. Klein and P. Piasecki, *On the scaling behavior of the chiral phase transition in QCD in finite and infinite volume*, Eur. Phys. J. C **71**, 1576 (2011), arXiv:1008.2155 [hep-ph].

[363] V. G. Bornyakov et al., *Probing the finite temperature phase transition with N(f) = 2 nonperturbatively improved Wilson fermions*, Phys. Rev. D **82**, 014504 (2010), arXiv:0910.2392 [hep-lat].

[364] J. Berges, N. Tetradis and C. Wetterich, *Nonperturbative renormalization flow in quantum field theory and statistical physics*, Phys. Rep. **363**, 223 (2002), arXiv:hep-ph/0005122 [hep-ph].

[365] B.-J. Schaefer and J. Wambach, *Susceptibilities near the QCD (tri)critical point*, Phys. Rev. D **75**, 085015 (2007), arXiv:hep-ph/0603256 [hep-ph].

[366] F. Rennecke and B.-J. Schaefer, *Fluctuation-induced modifications of the phase structure in (2+1)-flavor QCD*, Phys. Rev. D **96**, 016009 (2017), arXiv:1610.08748 [hep-ph].

[367] A. D'Ambrosio, O. Philipsen and R. Kaiser, *The chiral phase transition at non-zero imaginary baryon chemical potential for different numbers of quark flavours*, Proc. Sci. **LATTICE2022**, 172 (2023), arXiv:2212.03655 [hep-lat].

[368] R. Kubo, *Statistical mechanical theory of irreversible processes. 1. General theory and simple applications in magnetic and conduction problems*, J. Phys. Soc. Jap. **12**, 570 (1957).

[369] P. C. Martin and J. S. Schwinger, *Theory of many particle systems. 1.* Phys. Rev. **115**, 1342 (1959).

[370] J. M. Cornwall, R. Jackiw and E. Tomboulis, *Effective Action for Composite Operators*, Phys. Rev. D **10**, 2428 (1974).

[371] A. Cucchieri, *Gribov copies in the minimal Landau gauge: The Influence on gluon and ghost propagators*, Nucl. Phys. B **508**, 353 (1997), arXiv:hep-lat/9705005.

[372] P. J. Silva and O. Oliveira, *Gribov copies, lattice QCD and the gluon propagator*, Nucl. Phys. B **690**, 177 (2004), arXiv:hep-lat/0403026.

[373] A. Maas et al., *Strong-coupling study of the Gribov ambiguity in lattice Landau gauge*, Eur. Phys. J. C **68**, 183 (2010), arXiv:0912.4203 [hep-lat].

[374] C. S. Fischer, A. Maas and J. M. Pawlowski, *On the infrared behavior of Landau gauge Yang-Mills theory*, Ann. Phys. **324**, 2408 (2009), arXiv:0810.1987 [hep-ph].

[375] S. P. Klevansky, *The Nambu-Jona-Lasinio model of quantum chromodynamics*, Rev. Mod. Phys. **64**, 649 (1992).

[376] K. Fukushima, *Chiral effective model with the Polyakov loop*, Phys. Lett. B **591**, 277 (2004), arXiv:hep-ph/0310121.

[377] M. D. Scadron, G. Rupp and R. Delbourgo, *The quark-level linear σ model*, Fortsch. Phys. **61**, 994 (2013), arXiv:1309.5041 [hep-ph].

[378] N. Haque, M. G. Mustafa and M. Strickland, *Two-loop hard thermal loop pressure at finite temperature and chemical potential*, Phys. Rev. D **87**, 105007 (2013), arXiv:1212.1797 [hep-ph].

[379] K. G. Wilson, *Renormalization group and critical phenomena. 1. Renormalization group and the Kadanoff scaling picture*, Phys. Rev. B **4**, 3174 (1971).

[380] K. G. Wilson, *Renormalization group and critical phenomena. 2. Phase space cell analysis of critical behavior*, Phys. Rev. B **4**, 3184 (1971).

[381] C. Wetterich, *Exact evolution equation for the effective potential*, Phys. Lett. B **301**, 90 (1993), arXiv:1710.05815 [hep-th].

[382] J. M. Pawlowski, D. F. Litim, S. Nedelko and L. von Smekal, *Infrared behavior and fixed points in Landau gauge QCD*, Phys. Rev. Lett. **93**, 152002 (2004), arXiv:hep-th/0312324.

[383] H. Gies, *Introduction to the functional RG and applications to gauge theories*, Lect. Notes Phys. **852**, 287 (2012), arXiv:hep-ph/0611146.

[384] A. Wipf, *Statistical approach to quantum field theory: An introduction*, Vol. 864 (Springer, Heidelberg, 2013).

[385] A. K. Das, *Finite Temperature Field Theory* (World Scientific, New York, 1997).

[386] *Programming languages — C*, tech. rep. ISO/IEC 9899:1999 (International Organization for Standardization, Geneva, Switzerland, Dec. 1999).

[387] *GCC online documentation*, https://gcc.gnu.org/onlinedocs/ (visited on 2023-08-01).

[388] *GNU Scientific Library*, https://www.gnu.org/software/gsl/doc/html/ (visited on 2023-08-01).

[389] *CMake Reference Documentation*, https://cmake.org/cmake/help/latest/ (visited on 2023-08-01).

[390] *Python documentation*, https://docs.python.org/3/ (visited on 2023-08-01).

[391] *SciPy documentation*, https://docs.scipy.org/doc/scipy/ (visited on 2023-08-01).

[392] *NumPy Documentation*, https://numpy.org/doc/ (visited on 2023-08-01).

[393] *TeX Live documentation*, https://tug.org/texlive/doc.html (visited on 2023-08-01).

[394] *Matplotlib documentation*, https://matplotlib.org/stable/index.html (visited on 2023-08-01).

[395] *pgf – Create PostScript and PDF graphics in TeX*, https://ctan.org/pkg/pgf (visited on 2023-08-01).

[396] J. Ellis, *TikZ-Feynman: Feynman diagrams with TikZ*, Comput. Phys. Commun. **210**, 103 (2017), arXiv:1601.05437 [hep-ph].

[397] *Ubuntu*, https://ubuntu.com/ (visited on 2023-08-01).

[398] *Arch Linux*, https://archlinux.org/ (visited on 2023-08-01).

Acknowledgements

First and foremost, I am deeply grateful to my supervisor, Prof. Dr. Christian Fischer, who gave me the opportunity to work on these fascinating topics and provided me with both the necessary freedom and guidance whenever either was needed. Second, I want to thank Prof. Dr. Owe Philipsen for readily accepting to be my second referee. In addition, I gratefully acknowledge the assistance of and stimulating discussions with Prof. Dr. Lorenz von Smekal during my PhD Committee meetings as well as PD Dr. Bernd-Jochen Schaefer's collaboration and continuous interest in my work. Moreover, I would like to thank Prof. Dr. Jana Günther for interesting discussions and general collegiality.

From all of my colleagues, I am most obliged to Dr. Philipp Isserstedt who accompanied me throughout most of my PhD time and taught me everything useful to know about our framework. Without his collaboration, my work would only have been half as successful but twice as stressful. I am indebted to Milad Ghanbarpour, Joshua Hoffer, Dr. Philipp Isserstedt, Franziska Münster and Jonathan Yigzaw for carefully proof-reading parts of the manuscript. Furthermore, I cherish Franziska Münster's colourful advice and Joshua Hoffer's appreciation for my TikZ art.

I very fondly remember the beginning of my PhD time together with Milad Ghanbarpour and Dr. Dominik Schweitzer which was filled with physics, math, art and a lot of laughter. Particularly helpful to me during the time of writing up were insightful discussions with PD Dr. Markus Huber and Johannes Roth which I very much appreciate. I am thankful to my long-time office mate Dr. Konstantin Otto for many interesting chats about a wide range of topics as well as all past and present members of the institute whom I cannot thank by name. Additionally, I also want to extend my gratitude to the institute's secretaries – Monika Weingärtner, Ilka Sproates and the late Elke Jung – who helped with all sorts of bureaucratic and physics-unrelated troubles.

I would like to thank especially my family and also my friends for supporting me where they could and enduring me throughout my most demanding times. In particular, I want to express my deepest appreciation to Tom Brück whose friendship means the world to me and whose (occasionally unintended) wisdom never fails to brighten my mood. Special thanks should also go to a distinguished group of (former) physicists who started out as fellow students but have since become dear friends. Without them, I would not have been able to keep my (in)sanity in good times and bad, and our get-togethers are always something I am very much looking forward to.

This work has been supported by the Helmholtz Graduate School for Hadron and Ion Research (HGS-HIRe) for FAIR, the GSI Helmholtzzentrum für Schwerionenforschung, the Bundesministerium für Bildung und Forschung (BMBF, Federal Ministry of Education and Research) under Contract No. 05P18RGFCA and the Deutsche Forschungsgemeinschaft (DFG, German Research Foundation) through the Collaborative Research Center TransRegio CRC-TR 211 "Strong-interaction matter under extreme conditions".

Selbstständigkeitserklärung

Ich erkläre: Ich habe die vorgelegte Dissertation selbstständig und ohne unerlaubte fremde Hilfe und nur mit den Hilfen angefertigt, die ich in der Dissertation angegeben habe. Alle Textstellen, die wörtlich oder sinngemäß aus veröffentlichten Schriften entnommen sind, und alle Angaben, die auf mündlichen Auskünften beruhen, sind als solche kenntlich gemacht. Ich stimme einer evtl. Überprüfung meiner Dissertation durch eine Antiplagiat-Software zu. Bei den von mir durchgeführten und in der Dissertation erwähnten Untersuchungen habe ich die Grundsätze guter wissenschaftlicher Praxis, wie sie in der „Satzung der Justus-Liebig-Universität Gießen zur Sicherung guter wissenschaftlicher Praxis“ niedergelegt sind, eingehalten.

Gießen, den 22.09.2023

(Julian Bernhardt)